Dissertation

submitted to the
Combined Faculties for the Natural Sciences and for Mathematics
of the Ruperto-Carola University of Heidelberg, Germany
for the degree of
Doctor of Natural Sciences

Put forward by
Michael A. Blessenohl, M. Sc.
born in: Aachen
Oral examination: 2020-07-28

Fine-structure investigations in highly charged ions using spectroscopy in the vacuum ultraviolet regime

Referees: PD Dr. José R. Crespo López-Urrutia
PD Dr. Wolfgang Quint

Fine-structure investigations in highly charged ions using spectroscopy in the vacuum ultraviolet regime

Abstract

Spectroscopy of the fine structure of lithium-like ions allows for some of the best precision tests of quantum electrodynamics (QED) calculations. In this work, the fine-structure doublet of lithium-like nitrogen, oxygen, neon, and argon ions were studied. For neon, the results are of comparable accuracy to the best laboratory data found in literature. The here reported values for argon are the first laboratory results and more accurate than those of previous solar observations, and in good agreement with recent *ab initio* full-scale QED calculations. A related subject is the search for a possible variation of the fine-structure constant α. Two highly forbidden transitions in neodymium-like iridium are among the best-suited ones for this search. In a systematic study, for the final determination of the upper and lower levels, 68 previously unknown emission lines were found and assigned to this species, almost doubling the number of known transitions. For these purposes, a normal-incidence spectrometer was developed. A high-performance electron beam ion trap (and source) was co-developed and commissioned for TRIUMF (Vancouver); while record-breaking specifications were achieved with it, the reported vacuum ultraviolet (VUV) work was carried out using a similar system at MPIK Heidelberg.

Untersuchungen der Feinstruktur in hochgeladenen Ionen mittels Spektroskopie im Vakuum-Ultraviolettbereich

Zusammenfassung

Spektroskopie der Feinstruktur lithiumartiger Ionen stellt einen der präzisesten Tests quantenelektrodynamischer (QED) Berechnungen dar. In dieser Arbeit wurden die Feinstruktur-Dubletten lithiumartiger Stickstoff-, Sauerstoff-, Neon- und Argon-Ionen untersucht. Die Ergebnisse für Neon erreichen eine mit den besten Messwerten aus der Literatur vergleichbare Genauigkeit. Die hier für Argon ermittelten Werte sind die ersten Laborergebnisse und zudem in guter Übereinstimmung mit jüngsten, umfassenden, *ab initio* QED-Rechnungen. Ein damit verwandtes Thema ist die Suche nach einer möglichen Variation der Feinstrukturkonstante α. Zwei stark verbotene Übergänge in neodymartigem Iridium gehören zu den am besten geeigneten Kandidaten für diese Suche. In einer systematischen Untersuchung zur Bestimmung der oberen und unteren Terme wurden 68 bisher unbekannte Emissionslinien entdeckt und dieser Spezies zugeordnet. Zu diesen Zwecken wurde ein Spektrometer mit senkrechtem Lichteinfall entwickelt. Eine Elektronenstrahl-Ionenfalle (sowie -Quelle) wurde mitentwickelt und für TRIUMF in Vancouver in Betrieb genommen; während damit Rekordspezifikationen erreicht wurden, wurde die hier vorgestellte Arbeit im Vakuum-Ultraviolettbereich an einer ähnlichen Anlage am MPIK Heidelberg ausgeführt.

Contents

List of Acronyms **v**

1 Introduction **1**

2 Theory **9**
2.1 Atomic structure . . . 9
2.1.1 One-electron atom . . . 10
Non-relativistic solutions . . . 10
Relativistic considerations . . . 12
Effects of the nucleus . . . 13
2.1.2 Many-electron atoms . . . 13
Central field approximation . . . 13
Correlation effects . . . 15
2.2 Atomic structure codes . . . 17
2.2.1 Hartree-Fock . . . 17
2.2.2 Configuration interaction (CI) . . . 18
2.2.3 Coupled cluster (CC) . . . 18
2.2.4 Relativistic codes . . . 18
2.3 Quantum electrodynamics (QED) . . . 19
2.4 Interaction with external fields . . . 25
2.5 Electron-ion interactions . . . 26
2.5.1 Electron-impact ionisation . . . 26
2.5.2 Radiative recombination (RR) . . . 27
2.5.3 Dielectronic recombination (DR) . . . 29
2.5.4 Dither code . . . 30

3 Charge breeding of rare isotopes **31**
3.1 Introduction . . . 31
3.1.1 ARIEL facility at TRIUMF . . . 31
3.1.2 General concept of an EBIS charge breeder . . . 33
3.1.3 Electron beam ion trap (EBIT) . . . 33
3.2 CANREB EBIS . . . 36
3.2.1 Objectives . . . 36
3.2.2 Design of an EBIS charge breeder . . . 36
3.2.3 Magnet system . . . 36
3.2.4 Electron gun . . . 38
3.2.5 Trap setup . . . 39

3.2.6 Collector . . . 42
3.2.7 Ion optics . . . 42
3.2.8 Diagnostics of trapped ions . . . 44
High purity germanium detector (HPGe detector) . . . 44
Faraday cup . . . 44
Pickup ring . . . 45
3.3 Performance . . . 46
3.3.1 Electron-beam studies . . . 46
Space-charge potential . . . 47
Electron beam radius determination . . . 47
Trap capacity . . . 51
3.3.2 Injection and extraction studies . . . 51
Injection . . . 53
Extraction . . . 54
3.3.3 Outlook . . . 55

4 Spectroscopy **57**
4.1 3 m VUV grating spectrometer . . . 59
4.1.1 Optical design . . . 59
4.1.2 Mechanical design . . . 59
4.1.3 Micro-channel plate (MCP) detector . . . 60
4.1.4 Control and data acquisition system (DAQ) . . . 64
4.1.5 Performance . . . 65
4.1.6 Measurement schemes . . . 67
4.1.7 Data pre-processing . . . 70
Static mode . . . 70
Scanning mode . . . 71
4.2 EUV spectrometer . . . 75
4.2.1 Mechanical and optical design . . . 75
4.2.2 Charge-coupled device (CCD) . . . 75
4.2.3 Data pre-processing . . . 77

5 Fine-structure measurements **81**
5.1 Experimental parameters . . . 83
5.2 Data analysis . . . 83
5.2.1 Preparation . . . 83
5.2.2 Calibration . . . 84
5.3 Results . . . 89
5.3.1 Nitrogen ($Z = 7$) . . . 89
5.3.2 Oxygen ($Z = 8$) . . . 91
5.3.3 Neon ($Z = 10$) . . . 94
5.3.4 Argon ($Z = 18$) . . . 97
5.4 Summary . . . 99

6 Iridium spectroscopy **103**
6.1 FAC studies . . . 104
6.2 Experimental parameters . . . 107
6.2.1 Injection . . . 108
6.2.2 Charge-state verification . . . 108
6.2.3 EBIT parameters . . . 110
6.2.4 Additional systematics . . . 110
6.3 New spectral lines . . . 112
6.3.1 VUV results . . . 114
6.3.2 EUV results . . . 116
6.4 Comparison to theory . . . 119
6.5 Summary . . . 123

7 Summary and Outlook **127**

Bibliography **131**

Appendix **157**

A Methods in data analysis **157**
A.1 Linearisation of the MCP data . . . 157
A.2 Ballooning baseline algorithm . . . 159

B Supplementary material **163**
B.1 Fine-structure measurements . . . 163
B.1.1 Calibration lines . . . 163
B.1.2 Systematic studies on the oxygen deviation . . . 165
Comparison across different species . . . 165
Calibration function parameters . . . 170
B.2 Iridium spectroscopy . . . 171
B.2.1 Detailed energy scans . . . 171
B.2.2 Calibration lines in the extreme ultraviolet (EUV) range . . . 171
B.2.3 Complete list of known spectral lines of Ir^{17+} . . . 172

List of Acronyms

AC alternating current iii, 25

ADC analogue-to-digital converter iii, 64, 65, 70, 77, 157

ARIEL Advanced Rare Isotope Laboratory i, iii, 31, 32, 36, 53

ASG Max Planck Advanced Study Group iii

BESSY Berliner Elektronenspeicherring-Gesellschaft für Synchrotronstrahlung m.b.H. iii, 59, 65

BNL Brookhaven National Laboratory iii, 33

CAMP CFEL-ASG MultiPurpose chamber iii, 59

CANREB Canadian Rare Isotope Facility with Electron Beam Ion Source i, iii, 32, 36–39, 41, 43, 45, 46, 55, 57, 127, 151, 201

CBSIM charge breeding simulation iii, 30

CC coupled cluster i, iii, 18

CCD charge-coupled device ii, iii, 60, 65, 75–77, 79, 109, 152

CERN European Organization for Nuclear Research (acronym derived from the former French name: Conseil européen pour la recherche nucléaire) iii, 33

CFEL Center for Free Electron Laser Science iii

CI configuration interaction i, iii, 18, 19, 95, 103, 104, 106, 129

CI-DFS configuration-interaction Dirac-Fock-Sturm iii, 19, 20, 104, 106

CMB cosmic microwave background iii, 4, 5, 128

CODATA Committee on Data for Science and Technology iii, 2, 4

DAQ data acquisition system ii, iii, 64, 70, 71

DC direct current iii, 56

DESY Deutsches Elektronen-Synchrotron iii, 59

DLD delay line anode iii, 63

DR dielectronic recombination i, iii, 3, 29, 30, 35, 47, 49–53, 109, 151

EBIS Electron Beam Ion Source i, iii, 9, 26, 29–39, 41, 43–46, 51, 54, 55, 57, 104, 127, 151, 201

EBIT Electron Beam Ion Trap i, iii, 3, 7, 9, 26, 30, 31, 33, 35, 36, 40, 42, 44, 57, 58, 60, 62, 69, 81–83, 103, 104, 106–110, 123, 127–129, 152, 155

ECR Electron Cyclotron Resonance iii, 32

ECRIS Electron Cyclotron Resonance Ion Source iii, 32, 35

EUV extreme ultraviolet ii, iii, 3, 57, 58, 75–77, 79, 104, 108–110, 112, 114, 116, 118, 119, 123, 128, 152, 153, 155, 171

FAC flexible atomic code iii, 6, 9, 19, 104–107, 123

FLASH Free-Electron Laser in Hamburg iii, 36, 57–60, 65, 81, 104, 108–110, 123, 127–129, 152, 155

FSCC Fock space coupled cluster iii, 18, 104, 106

FWHM full width at half maximum iii, 83

HCI highly charged ions iii, 1, 2, 5, 6, 15, 26, 27, 35, 47, 54, 76, 127, 129

Heidelberg EBIT Heidelberg Electron Beam Ion Trap iii, 108, 109, 123

HIRES High Resolution Echelle Spectrometer iii, 4

HPGe detector high purity germanium detector ii, iii, 44, 47, 49

ISAC Isotope Separator and Accelerator iii, 32

MACOR Trademark of Corning Inc. for a machinable glass-ceramic iii, 39, 40, 155

MBPT many-body perturbation theory iii, 19

MCDF multi-configuration Dirac-Fock iii, 3, 19, 50

MCHF multi-configuration Hartree-Fock iii, 18

MCP micro-channel plate ii, iii, 60, 61, 63–71, 74, 109, 129, 130, 152, 153, 157–159

MOSFET metal-oxide-semiconductor field-effect transistor iii, 77

MPIK Max-Planck-Institut für Kernphysik e, iii, 31, 36, 57

NIM Nuclear Instrumentation Module iii, 64

NIST National Institute of Standards and Technology iii, 84–88, 92, 116, 163–166, 171, 172

NMR Nuclear Magnetic Resonance iii, 32

NRL U.S. Naval Research Lab iii, 97

NSCL National Superconducting Cyclotron Laboratory iii, 33, 36

OAO-3 Orbiting Astronomical Observatory 3 iii, 91

OFHC oxygen-free high thermal conductivity iii, 39, 40

PEEK polyether ether ketone iii, 39, 40

PTFE polytetrafluoroethylene (brand name Teflon by Chemours) iii, 39, 40, 155

QED quantum electrodynamics e, i, iii, 1–3, 7, 9, 12, 19–24, 81, 91, 94, 95, 97, 99–101, 127, 128, 151

RAON Rare isotope Accelerator complex for on-line experiment iii, 33

ROI region of interest iii, 70, 71, 73, 157, 158

RR radiative recombination i, iii, 27–30, 35, 48, 49, 151

SNR signal-to-noise ratio iii, 44, 75, 82, 165

TITAN TRIUMF's ion trap for atomic and nuclear science iii, 36

TOF time-of-flight iii, 53–56

TRAFS-3C Tel-Aviv Relativistic Atomic Fock Space coupled cluster code iii, 18

TRIUMF Canada's particle accelerator centre (acronym derived from the former name: Tri University Meson Facility) e, i, iii, 31, 33, 56, 127

UHV ultra-high vacuum iii, 39

UV ultraviolet iii, 63, 75

UVES Ultraviolet and Visual Echelle Spectrograph iii, 4

VLT Very Large Telescope iii, 4

VUV vacuum ultraviolet e, ii, iii, 7, 57–61, 63, 65, 67–69, 71, 73–75, 81, 85–88, 101, 104, 108, 110–112, 114, 116, 118, 119, 123–126, 129, 152, 153, 155, 163, 167–169, 171

CHAPTER 1

Introduction

Fine structure effects have been under extensive investigation in atomic physics since their discovery in the 19th century. Before going into details regarding this work, a short historical outline is given, highlighting major breakthroughs associated with this initially quite inconspicuous discovery as well as some of the advances made over the last decades.

While observing and cataloguing absorption lines in the spectrum of the sun in 1817, Fraunhofer catalogued a line he dubbed 'D' to be composed of two distinct lines [89]. In 1823 he found the same doublet of lines in an emission spectrum of candle light [90] that was identified originating from sodium by Kirchhoff during his time in Heidelberg in 1859 [116]. Finally, Michelson and Moreley found a splitting in the red line of the hydrogen Balmer series in 1887 using their interferometer [141] (initially built for proving the existence of a luminiferous æther). Not only did they first propose to use fine structure in metrology (as a length standard) but more importantly this discovery also inspired Sommerfeld, Dirac and others in the 1920s to develop a relativistic model of the hydrogen atom and relativistic quantum mechanics.

Improved experimental methods motivated Pasternack in 1938 to compile measurements on hydrogen, deuterium and singly charged helium from 1934 to 1937 [146]. He found a significant upward shift of the $1s^2 2s\ ^2S_{1/2}$ level with respect to the $1s^2 2p\ ^2P_{1/2}$ level of about $0.027\,\mathrm{cm}^{-1} \approx 3.3\,\mu\mathrm{eV}$, corresponding to $4 \times 10^{-5}\,\mathrm{nm}$. In 1947 Lamb and Retherford [125] were able to directly measure the microwave transition utilizing the much smaller decay rate of the metastable $^2P_{1/2}$ level and proved the non-degeneracy of both levels. Today, the shift of $l = 0$ levels in hydrogenic systems is known as the Lamb shift. This discrepancy could not be explained with any theory available at the time and sparked a whole new field in theoretical physics called quantum electrodynamics (QED).

So far, five Nobel prizes can be related to work on or stimulated by the discovery of fine structure: Michelson in 1907 for the spectrometer he used for the first observation of the fine-structure splitting in hydrogen; Schrödinger and Dirac in 1933 for the fully relativistic description of the hydrogen atom, Born in 1954 for his further development of relativistic quantum mechanics in atomic systems, Lamb in 1955 for his Doppler-free, direct measurement of the microwave transition in hydrogen; Tomonaga, Schwinger and Feynman in 1965 for their fundamental work in developing QED.

As soon as experimental methods were established to produce highly charged ions (HCIs) (ions stripped of at least half their electrons), precise measurements of the Lamb shift were conducted in hydrogen-like systems with high nuclear charges Z. Notably are sulphur [124], chlorine [46, 155], argon [25, 41, 124, 135], iron [42], nickel [26], krypton [180] and

uranium [27, 40, 98]. The most recent results for U^{91+} from 2005 confirm QED theory to a level of 2 % [98] in the strongest stationary electric fields found in nature. Due to the high accuracy of these calculations (they are expected to be better than the experimental data available), it has even been proposed to use hydrogenic systems as x-ray wavelength standards [120]. Similarly, helium-like systems have been investigated (sulphur [124], argon [1, 41, 46, 58, 123, 124, 133], titanium [49], iron [43, 124], copper [11], krypton [80, 108, 193] and uranium [40, 97]), offering potential insights into the interelectronic contributions to the binding energy.

$1s^2 2p\ ^2P_{1/2,3/2} \rightarrow 1s^2 2s\ ^2S_{1/2}$ transitions in lithium-like systems have the largest QED contributions of up to 15 % [120] having the best potential as benchmarks for calculations. A detailed discussion can be found in the next section.

While working on the relativistic description of atoms, Sommerfeld introduced a new, dimensionless quantity in 1916 referred to as the fine-structure constant. It represents the ratio of the velocity an electron bound to a proton has in its ground state in a Born-Sommerfeld atom to the speed of light in vacuum. The recommended value by the Committee on Data for Science and Technology (CODATA) is at the time of writing [74]:

$$\alpha = 77.297\,352\,569\,3(11) \times 10^{-3}\ (\approx 1/137) \tag{1.1}$$

Furthermore, it can be related to other physical constants such as the elementary charge e, the reduced Planck constant $\hbar$, and the electric constant ε_0.

$$\alpha = \frac{e^2}{4\pi\varepsilon_0\hbar c} \tag{1.2}$$

Precise modelling of the fine structure in lithium-like systems has applications in astrophysics [10, 87] and magnetically confined fusion plasmas [194]. Specifically, K-shell emissions in lithium-like ions are a valuable tool for diagnostics of hot plasmas.

Despite the low number of electrons, state-of-the-art *ab initio* QED calculations have reached comparable accuracy to experimental data only in the last few years. Before that, only interpolation of experimental data achieved sufficient predictive power. Availability of measurements of these systems therefore provides crucial benchmarks for the advancement of atomic structure calculations. These factors and the high sensitivity for QED effects have drawn a lot of attention to the lithium-like isoelectronic sequence and more highly charged ions have been investigated than for the hydrogen- and helium-like sequences. For $Z > 20$ these are scandium [129] iron [78], nickel [177], copper [79], zinc [177], silver [33], tin and xenon [84], gold [37], lead [36, 206], bismuth [2, 9, 37] and uranium [8, 37, 172].

As shown in Figure 1.1, the relative contributions of different effects change with the atomic number Z. While the one-loop QED effects, such as vacuum polarisation or self-energy are also present for low and medium values of Z, two-loop QED corrections become increasingly important for heavy elements [82]. Other effects are radiative interelectron QED interactions and relativistic effects such as the nuclear recoil [145]. They are explored in more detail in Section 2.3.

In the effort of transitioning from interpolation to full-scale QED calculations, an important step was Schweppe *et al.* [172] renewing interest in the topic of lithium-like

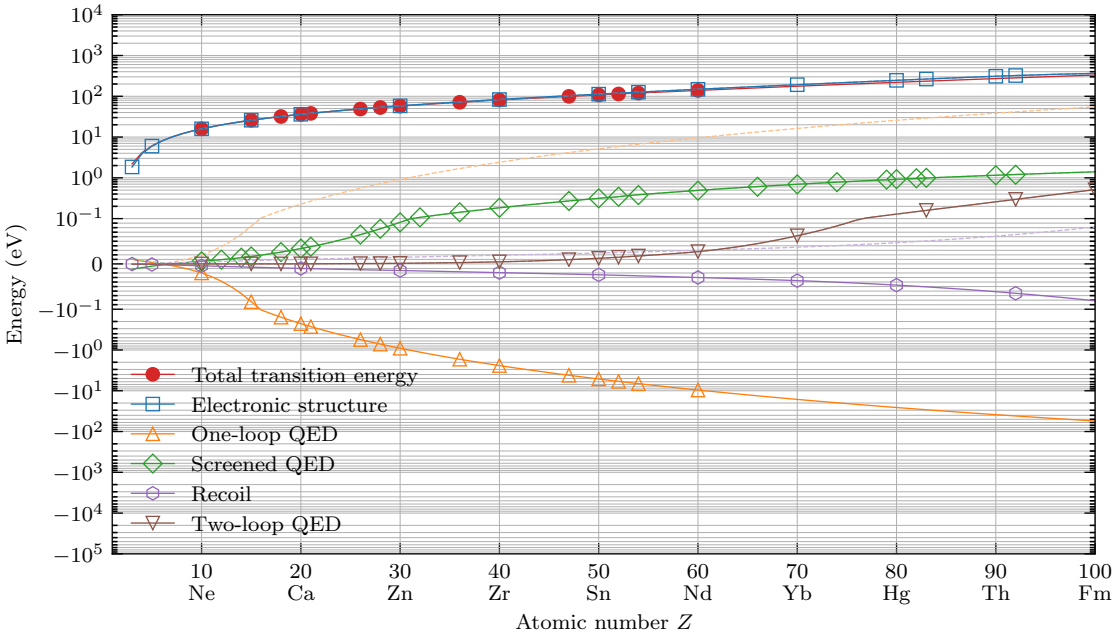

Figure 1.1: QED corrections for the fine-structure transition $1s^2 2p\ {}^2P_{1/2} \rightarrow 1s^2 2s\ {}^2S_{1/2}$ in Li-like ions for different values of the atomic number Z. For negative contributions to the total transition energy, dashed lines of the absolute value were added for magnitude comparison. Data adopted and interpolated from [118, 201]. Please note that the diagram is linear in the range from -10^{-1} eV to $+10^{-1}$ eV.

ions in 1991 by measuring the fine-structure splitting in uranium in beam-foil experiments. Beiersdorfer *et al.* supplemented data for bismuth in 1998 *et al.* using electron beam ion trap (EBIT) crystal spectroscopy [9] at an accuracy on the level of two-loop QED. Soon after, calculations were performed for the same ions [170, 200] and experiments on bismuth and uranium were improved and new data was added for gold by Brandau *et al.* using dielectronic recombination (DR) [37]. By 2005, lithium-like uranium was measured with even higher accuracy by means of EUV spectroscopy in an EBIT [8]. In 2006 Dong *et al.* added multi-configuration Dirac-Fock (MCDF) calculations to the picture [63] and non-perturbative two-loop QED effects were calculated by Yerokhin *et al.* [201]. The following year, these were improved [199] and a trend of investigating elements with moderate Z was initiated by Epp *et al.* by observing resonant laser excitation in iron [78]. One year later, scandium was studied by Lestinsky *et al.* using the DR method [129]. More recently, full QED calculations have been conducted by Kozhedub *et al.* [118] and wide ranges of Z and higher n levels were extensively calculated by Yerokhin *et al.* from 2012 to 2017 [202, 203]. For several lighter elements however, the most accurate data is still from observations of solar flares in the 1970s and has not been revisited in the laboratory. Additionally, there was some interest in doubly-excited states of these ions [160, 167].

A related topic emerged in 1937, when Dirac raised the question if the gravitational constant is really constant on cosmological time scales [59]. The ensuing discussion lead

to the idea that the fine-structure constant α might also change over time. In 1962 this was first proposed by Stanyukovich [176]. The ongoing discussion has received a growing interest recently [17–22, 86, 91, 92, 126, 158, 185, 189, 190, 195]. As opposed to the gravitational constant, changes of α do not conflict with the existence of life on earth in the Cambrian period as pointed out by Teller [181] and Gamow [91, 92]. Being dimensionless, it also enables very accurate testing without depending on the definition of a physical unit.

A few years after the suggestion of a possible variation of α, first experimental limits were published for a potential variation of the elementary charge e [65] by comparing the abundances of two naturally occurring isotopes of rhenium and osmium. Interest in the topic was renewed when absorption in gas clouds against background quasars was investigated using the High Resolution Echelle Spectrometer (HIRES) on the Keck I 10 m telescope and a small but significant deviation of $^{\Delta\alpha}/_{\alpha} = (-1.88 \pm 0.53) \times 10^{-5}$ was found for redshifts $z = {}^{\lambda_{\mathrm{obs}}}/_{\lambda_{\mathrm{lab}}} - 1$ of $1.0 < z < 1.6$ [190]. Additional data from the Ultraviolet and Visual Echelle Spectrograph (UVES) as well as the X-shooter instruments at the Very Large Telescope (VLT) confirmed the observation [189, 195, 196]. Due to the difference of about 45° in latitude between the two observatories, a spatial dipole distribution for $^{\Delta\alpha}/_{\alpha}$ could be deduced having the following parameters: amplitude $A = (0.72 \pm 0.16) \times 10^{-5}$, right ascension of (16.76 ± 1.17) h and declination of $-63.79° \pm 10.30°$. The significance of the deviation from a null result is 3.9σ [195]. Due to the direction it is referred to in some works as the 'Australian dipole'.

Given earths movement with respect to the cosmic microwave background (CMB), the orientation and amplitude of this dipole, the terrestrial variation over time can be estimated: α is expected to be increasing in the order of 10^{-20} to 10^{-19} every year [22]. While the earth orbit around the sun is estimated to cause a modulation in the order of 10^{-20}. For terrestrial measurements, such as precision spectroscopy of the splitting between $^2P_{3/2}$ and $^2P_{1/2}$ in systems with a single valence electron (see Chapter 5), experimental accuracy is by far not sufficient to date. Even for g-factor measurements that are currently used to determine the value of α CODATA 'only' recommends thirteen significant digits, even though these experiments are arguably among the highest-precision measurements in modern physics. Despite fine-structure splitting having a slightly higher sensitivity by being proportional to α^2, the astronomical quasar observations discussed above – dealing with much larger changes in the fine-structure constant – still required comparing doublets of different species in order to achieve significant accuracy [190].

Several other methods have been proposed for laboratory experiments [22, 185]. One of them is using isotope ratios of meteorites. But this approach is currently still lacking three orders of magnitude in accuracy. More promising is the investigation of the Oklo natural nuclear reactor in Gabon. In a uranium mine, a lower concentration of ^{235}U and typical products of nuclear reactors were found in some parts of the deposit. Geologists concluded that around two billion years ago – when the natural concentration of ^{235}U was high enough to sustain a nuclear chain reaction – multiple natural fission reactors were operating for a few million years in that deposit. It is suspected that water acted as neutron moderator and that each reactor was large enough so that the neutron escape rate was lower than their production. As in any uranium deposit, the isotopes ^{149}Sm and ^{155}Gd are present naturally and they are not among the decay products of the reactor.

But while it was running, ^{149}Sm was exposed to neutrons and the resonant capture cross section depends on the value of α. So the production rate of ^{155}Gd by neutron capture can be used to deduce a different value of the fine-structure constant for the time the reactor was active by studying the ratio of ^{149}Sm to ^{155}Gd present in the ore today. Recent studies indicate a non-zero difference in α of ${}^{\Delta\alpha}/_{\alpha} = -45^{+15}_{-7} \times 10^{-9}$ [126].

However, the best terrestrial constraints so far are given by comparison of optical clocks:

$$\frac{\dot{\alpha}}{\alpha} = (-1.6 \pm 2.3) \times 10^{-17}\,\mathrm{yr}^{-1} \tag{1.3}$$

$$\frac{\dot{\alpha}}{\alpha} = (-0.7 \pm 2.1) \times 10^{-17}\,\mathrm{yr}^{-1} \tag{1.4}$$

Where (1.3) uses a Hg^+/Al^+ clock comparison [158] and (1.4) was derived from all present clock comparisons and dysprosium measurements [93, 128]. As opposed to $\Delta\alpha$ denoting an absolute change in the fine-structure constant, $\dot{\alpha}$ represents the rate at which it is changing over time.

Although the comparison of optical clocks currently include a stationary value of the fine-structure constant within one sigma, there is some evidence that it is not the same everywhere at all times. However, in agreement with each other, both the Oklo reactor and optical clock data tend towards a decreasing value of α independently of each other while the prediction based on the Australian dipole suggests an increase over time [126]. So one of the assumptions – the dipole being stationary in time, with respect to the CMB, or it being monotonic – might not hold.

Fortunately, there is an ongoing effort to improve optical clocks, placing these variations just within reach for the next clock generations. There have been proposals to use a nuclear transition in ^{229}Th [147] that was found close to the optical regime around (149.7 ± 3.1) nm [173] and sensitive to the fine-structure constant [86].

Another idea is to use HCIs in optical clocks rather than singly charged ions. A limiting factor in accuracy of conventional clocks is that they are sensitive to the gravitation potential at the level of decimetres. So when improving accuracy by a few orders of magnitude, external perturbations such as the spatial extension of the trap and external magnetic fields become significant. HCIs on the other hand are more compact and therefore less sensitive to external perturbations [57, 66, 120, 204]. However, there are many challenges related to this idea: optical clocks rely on laser cooling and laser spectroscopy which requires the species to have suitable optical transitions in addition to the clock transition that are challenging to observe due to their low transition rates. Very recently, it has been demonstrated that this obstacle can be overcome in a cryogenic Paul trap by means of quantum logic spectroscopy [142]. A single Ar^{13+} ion ('spectroscopy ion') was trapped together with singly charged laser-cooled beryllium ions ('logic ion'). Once both species are sufficiently cold, they form a rigid lattice or string in the trap due to an equilibrium between attractive forces caused by the trapping potential and mutual repulsion of the ions. These so-called 'Coulomb crystals' allow for the spectroscopy ion to be cooled sympathetically. By interrogating short-lived transitions on a logic ion, the frequency of an optical transition in the HCI at 441 nm was measured with an uncertainty of less than 2 Hz (accuracy of

3×10^{-15}).

It should be noted that this was a first proof-of-principle experiment measuring an absolute frequency value and that accuracy is expected to improve. Furthermore, many transitions in HCI are a few orders of magnitude more sensitive to changes in the fine-structure constant than the ones in conventional clock ions [17]. Other requirements for suitable transitions are that they should be in the optical regime and have a very long lifetime resulting in a narrow line shape. There has been an ongoing search for the most sensitive species fulfilling these criteria.

Coulomb potentials acting on valence electrons in HCI are much stronger compared to neutral atoms. So the available transitions are shifted towards shorter wavelengths: the fine-structure transition $2p\ ^2P_{3/2} \rightarrow 2p\ ^2P_{1/2}$ for hydrogen-like uranium is in the x-ray regime (around 1.83 Å) while the same transition has a wavelength of 283 km in hydrogen (radio-frequency regime). Optical transitions between highly excited Rydberg states are broadened by competing x-ray transition branches, so the search for suitable optical transitions is constrained to fine or hyperfine structure, as well as ground states in species close to so-called 'level crossings'. The latter will be explored in more detail here.

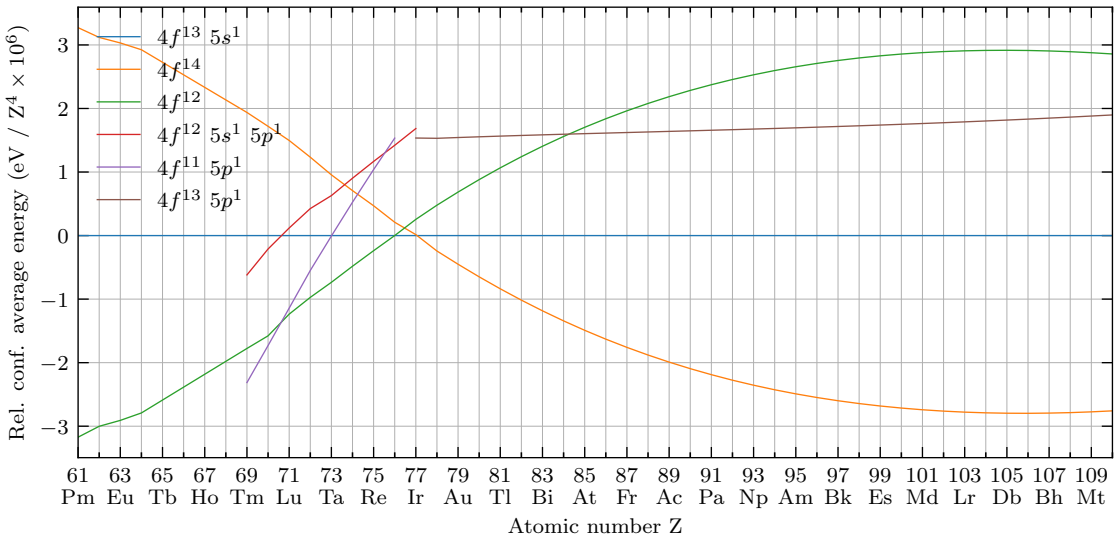

Figure 1.2: A few level crossings in the neodymium-like isoelectronic sequence. Structure calculations were performed using the flexible atomic code (FAC). For each Z, an average over all levels in the same configuration were calculated, the average energy of $4f^{13}5s^1$ was subtracted and the result scaled by $^{10^6}/_{Z^4}$. Not all configurations were calculated for every value of Z. Nevertheless, ten level crossings are shown here. For example the crossing of $4f^{13}5s^1$ and $4f^{14}$ around $Z^\star \approx 77$ or $4f^{12}$ and $4f^{14}$ at $Z^\star \approx 76.5$

Considering the ground states when sequentially removing electrons from a heavy atom, it transitions from Madelung ordering for the neutral atom to Coulomb ordering in the hydrogen-like system (see Section 2.1.2 for details of both ordering schemes). Accordingly, when keeping the number of electrons constant while increasing the atomic number Z, for some charge states along the sequence, pairs of configurations get very close in energy

before their order switches in the next step along the sequence. This phenomenon is referred to as level crossing. For the particular case of the neodymium-like sequence, this is shown in Figure 1.2.

In summary, there are two pressing issues involving fine structure. Firstly, despite a high interest in fine-structure transitions in lithium-like ions, which continues to be a valuable yardstick for modern atomic structure calculations based on QED, there still is a lack of laboratory measurements for many elements with medium values of Z that are particularly sensitive to higher-order interelectron interactions. Recently, Kozhedub *et al.* succeeded in calculating these up to third order [118]. Secondly, for high-precision measurements of the proposed variation of the fine-structure constant, many potential ion species have been investigated [17, 18, 20, 21, 67, 68, 70, 119, 163–165]. Amongst the most sensitive ones is neodymium-like Ir^{17+} [19] around the level crossing of $4f$ and $5s$. However, electron-electron correlation effects (see Section 2.1.2) are particularly hard to calculate in these systems. So a prerequisite for high-precision experiments with an α sensitive species (such as quantum logic spectroscopy) is detailed knowledge of the respective spectrum.

Both issues require spectroscopy in the vacuum ultraviolet (VUV) wavelength regime. In this work, a new 3 m normal-incidence spectrometer has been designed for EBIT experiments (see Chapter 4) that has unlocked the range of 40 nm to 140 nm and both issues have been addressed. The fine-structure splitting between the $1s^2 2p\ ^2P_{3/2}$ and $^2P_{1/2}$ levels has been studied along the lithium-like isoelectronic series for nitrogen, oxygen, neon and argon (see Chapter 5). Additionally, the spectrum of neodymium-like iridium was investigated using conventional spectroscopy methods in order to provide a better understanding of this species and eventually enable clock comparison experiments to study the variation of fundamental constants (see Chapter 5).

CHAPTER 2

Theory

Some aspects of theoretical atomic physics relevant to this work are discussed here. A more comprehensive overview can be found in any text book on the subject such as [38], [88] or [64].

The objective of atomic structure calculation is to determine energy levels with respect to the continuum and the corresponding wave functions as basis for additional calculations such as lifetimes of excited states or plasma modelling and the interpretation of experimental observations such as transition energies or rates.

In this work, it is used for the interpretation of spectroscopy data (Chapters 5 and 6). The observation of an individual spectral line offers only limited insight: a value for the transition energy, luminosity and polarisation on its own does not allow for identification of the corresponding atomic energy levels or species. Only when combined with additional information from other observations or calculations, lines can be identified (assignment to specific energy levels of the atom) or plasma parameters be deduced from ratios of emission line intensities. For the line identification processes found in the present work (see Chapter 6), calculation results from other works were used. Due to the limited range of levels available from more elaborate works, additional calculations were performed in this work using the flexible atomic code (FAC) [96]. A short overview of different atomic structure codes is provided in the following sections.

One of the most stringent tests of few-body bound-state QED structure calculations is observation of the fine-structure splitting of lithium-like systems. For the interpretation of the data presented in Chapter 5, a brief qualitative introduction to QED effects in these systems is given in Section 2.3. State-of-the-art QED calculation results from other works are given there for comparison with the experimental data.

All the data in the present work was recorded at electron beam ion source (EBIS) or EBIT devices (see Chapter 3 for a detailed description of these). So in all of the observations, plasma processes in charge-breeders such as these are a crucial aspect of the experiment. The most relevant ones are presented in Section 2.5.

2.1 Atomic structure

Before going into detail on the different codes and numerical methods, a more general introduction is given in the following. Most of the formula were adapted from [38].

2.1.1 One-electron atom

A natural starting point for atomic structure calculation is the most simple atomic system that is a one-electron (hydrogenic) atom. A non-relativistic solution can even be calculated analytically.

Non-relativistic solutions

For an atomic nucleus of charge Ze and an electron of charge e the Coulomb potential is given by

$$V(r) = -\frac{Ze^2}{(4\pi\varepsilon_0)\, r} \tag{2.1}$$

where ε_0 is the vacuum permittivity and r the distance between both particles.

By adding the kinetic energy in the centre-of-mass reference frame, a Hamiltonian can be formulated

$$\mathbf{H} = \frac{p^2}{2\mu} + V(r) \tag{2.2}$$

with p denoting the relative momentum and $\mu = \frac{m_\mathrm{e} M}{m_\mathrm{e}+M}$ representing the reduced mass using the electron and nucleus masses m_e and M respectively.

Switching to the centre-of-mass system in spherical polar coordinates, the Schrödinger equation in position representation

$$\left(-\frac{\hbar^2}{2\mu}\nabla^2 - \frac{Ze^2}{(4\pi\varepsilon_0)\, r}\right)(r) = E(r) \tag{2.3}$$

can be solved[1]. In this process three parameters arise that denote the eigenvalues and are interpreted as the principal (n), orbital (l) and magnetic quantum number (m_l). n can take on any positive integer number, while l is restricted to the values 0, 1, …$n-1$ and m_l to $-l$, $-l+1$, …$+l$. Due to historical reasons it is common practice to use code letters representing the values of n and l as given in Table 2.1.

However, the energy values that solve the Schrödinger equation for non-relativistic atoms only depend on the choice for the principal quantum number:

$$E_n = -\frac{Z^2}{2n^2}\left(\frac{e^2}{4\pi\varepsilon_0}\right)^2 \frac{\mu}{\hbar^2} \tag{2.4}$$

After replacing the spatial coordinate r with q, including the spin state as well, the solution for the electron wave function can be explicitly calculated by splitting it into a

1 A solution for parabolic coordinates does also exist but is not of relevance in this work.

Table 2.1: Code letters used for the principal and orbital quantum number values. Some of the letters for l were originally abbreviations for names of spectral line series but later more values were added alphabetically. The last column denotes the number of electrons that can be in a given subshell (double the degeneracy of l).

Numerical value	n	l	Original meaning	Max. no of electrons in l
0	-	s	sharp	2
1	K	p	precise	6
2	L	d	diffuse	10
3	M	f	fundamental	14
4	N	g		18
5	O	h		22
6	P	i		26
7	Q	k		30
8	R	l		34
9	S	m		38
10	T	n		42
11	U	o		46
12	V	p		50
13	W	r		54
14	X	t		58
15	Y	u		62
16	Z	v		66
17		w		70
18		x		74
19		y		78
20		z		82

radial ($R_{nl}(r)$), a spherically harmonic ($Y_{lm_l}(\theta,\phi)$) and a spin function ($\chi_{1/2,m_s}$)[2]:

$$(q) = R_{nl}(r)Y_{lm_l}(\theta,\phi)\chi_{1/2,m_s} \tag{2.5}$$

where $Y_{lm_l}(\theta,\phi)$ corresponds to the spherical harmonics:

2 Since the non-relativistic solution is degenerate in the electron spin, the spin function can be omitted at this stage. However, it is relevant for relativistic and many-electron atoms.

$$Y_{lm_l}(\theta,\phi) = \sqrt{\frac{2l+1}{4\pi}\frac{(l-m_l)!}{(l+m_l)!}} P_{lm_l}(\cos\theta) e^{\mathrm{i}m_l\phi} \tag{2.6}$$

$$R_n l(r) = -\left\{ \left(\frac{2Z}{na_\mu}\right)^3 \frac{(n-l-1)!}{2n\left[(n+l)!\right]^3} \right\}^{1/2} e^{-\rho/2}\rho^l L_{n+l}^{2l+1}(\rho) \tag{2.7}$$

using the associated Legendre polynomials $P_{lm_l}(\cos\theta)$, $\rho = \frac{2Z}{na_\mu}r$, the modified Bohr radius $a_\mu = \frac{(4\pi\varepsilon_0)\hbar^2}{\mu e^2} = a_0\frac{m}{\mu}$ and the associated Laguerre polynomials $L_{n+l}^{2l+1}(\rho)$.

For a single electron the spin function can only be one of the spinors $\left(\begin{smallmatrix}1\\0\end{smallmatrix}\right)$ or $\left(\begin{smallmatrix}0\\1\end{smallmatrix}\right)$.

Relativistic considerations

As early as 1887, experiments [141] indicated that this might not be the full picture to describe hydrogen atoms. Especially for larger values of Z relativistic effects become relevant, so that a more rigorous treatment is necessary. Most effects are taken into account by using the Dirac equation that can be solved for a single electron in a central field. To include changes in particle number, relativistic field theory is needed, though. However, in many cases it is sufficient to use perturbation theory to approximate the Dirac Hamiltonian up to the desired order:

$$\mathbf{H}_{\mathrm{Dirac}} = \underbrace{\frac{p^2}{2m_\mathrm{e}} + V(r)}_{\substack{\text{Non-relativistic}\\ \text{Hamiltonian}}} \underbrace{-\frac{p^4}{8m_\mathrm{e}^3c^2}}_{\substack{\text{Relativistic}\\ \text{correction of}\\ \text{the kinetic}\\ \text{energy}}} \underbrace{+\frac{1}{2m_\mathrm{e}^2c^2}\frac{1}{r}\frac{\mathrm{d}V}{\mathrm{d}r}\mathbf{L}\cdot\mathbf{S}}_{\text{Spin-orbit interaction}} \underbrace{+\frac{\pi\hbar^3}{2m_\mathrm{e}^2c} Z\alpha\delta(\mathbf{r})}_{\text{Darwin term}} \tag{2.8}$$

where c denotes the speed of light in vacuum, $\mathbf{L}$ and $\mathbf{S}$ are the orbital angular momentum and spin operator respectively. Finally, $\delta(\mathbf{r})$ is the three-dimensional delta distribution.

While the first two terms are identical to (2.2) with $\mu = {m_\mathrm{e}}$[3], there are additional terms for the relativistic corrections: $-\frac{p^4}{8m_\mathrm{e}^3c^2}$ is usually referred to as the relativistic correction to the kinetic energy and the last two terms represent the spin-orbit interaction and the Darwin term. The latter is a correction term only affecting s orbitals (due to the delta function). It slightly changes the effective potential around the nucleus taking into account the electrostatic interaction of the electron with the nucleus resulting in zitterbewegungen essentially smearing out the electron charge. Furthermore, it is proportional to the fine-structure constant α introduced on page 2.

These additional terms partly remove the degeneracy in n and introduce new quantum numbers $j = l + s$ (total angular momentum of the electron) and m_j (projection onto the z axis). j only takes the value $1/2$ for a one-electron system and $l = 0$. For $l \neq 0$, $j = l \pm 1/2$.

3 A relativistic treatment of the reduced mass is usually done in the framework of QED calculations (see Section 2.3).

Finally, m_j is in the range of $-j, -j+1, \ldots, +j$.

For $n > 1$ the energy levels are split, resulting in multiple spectral lines very close to each other. This effect is called fine structure. For hydrogen all three correction terms of the Dirac Hamiltonian (2.8) result in energy shifts of the same order of magnitude and the total shift is proportional to $Z^4\alpha^2$.

Effects of the nucleus

Although first observations of these effects in thallium and mercury spectra were published just a few years after the discovery of fine-structure splitting in 1892 [140], it took until 1935 for hypotheses to arise that these might be caused by a nuclear quadrupole moment.

Nuclei with a non-zero spin can couple to the angular momentum of the electron and therefore either remove degeneracy further and split a term into distinct levels, which is called hyperfine splitting, or shift the energy slightly, referred to as isotope shifts. If a mixture of different isotopes is emitting or absorbing light, this effect can also resemble a splitting.

To account for different isotopes, both mass and volume differences of the nucleus need to be considered. The first can be achieved by using the reduced mass as shown above. The latter is typically accounted for by modifying the Coulomb potential 2.1 of the nucleus by modelling the nucleus as a sphere with uniform charge distribution instead of a point-like object. Deviations from a point-like nucleus are most pronounced in subshells with large overlap between the nucleus and wave function such as the s orbitals.

New quantum numbers are introduced to calculate the hyperfine splitting, namely these are the nuclear spin quantum number I, the total angular momentum of the atom F with the corresponding operators $\mathbf{I}$ and $\mathbf{F} = \mathbf{I} + \mathbf{J}$. Values range from $|I - j|$ to $I + j$ for the latter. Degeneracy in F is removed by the hyperfine splitting that is approximately a factor of 2000 smaller than the fine-structure splitting.

So far, the nucleus was assumed to be a point charge. However, for heavy nuclei, this assumption breaks down and the size of the nucleus has to be taken into account. Usually one of the three models is used to modify the Coulomb potential: the homogeneously charged sphere, Fermi, or Gaussian charge distribution. All of these require an estimation of the nuclear radius, though.

2.1.2 Many-electron atoms

So far, only one-electron atomic systems were considered. Schrödinger equations for systems with N electrons cannot be solved exactly, so approximation methods are used that are very accurate in many cases.

Central field approximation

Starting point for all of these methods are two concepts: firstly, the independent-particle model introduces an effective field $V(r)$ for each individual electron, created by an infinitely heavy nucleus of charge Ze and the other $N - 1$ electrons. Secondly, the central field approximation assumes this potential can be separated into a spherically symmetric and asymmetric component. A very simple Hamiltonian in the independent-particle model is:

$$\mathbf{H}_{\mathrm{ip}} = \sum_{i=1}^{N} \left(-\frac{\hbar^2}{2m_{\mathrm{e}}} \nabla_{r_i}^2 - \frac{Ze^2}{(4\pi\varepsilon_0)\, r_i} \right) + \sum_{i<j=1}^{N} \frac{e^2}{(4\pi\varepsilon_0)\, r_{ij}} \tag{2.9}$$

where r_i is the coordinate of the electron i in the nucleus reference frame, $r_{ij} = |r_i - r_j|$ and the second summation is over all pairs of electrons.

Now the central-field approximation is employed and only the spherically symmetric component of the second sum in (2.9) is considered: $\sum_{i<j=1}^{N} \frac{e^2}{(4\pi\varepsilon_0) r_{ij}} \approx \sum_{i=1}^{N} S(r_i)$ where $S(r_i)$ is usually called the screening potential. The modified potential $V(r_i) = -\frac{Ze^2}{(4\pi\varepsilon_0) r_i} + S(r_i)$ should approach $-\frac{Ze^2}{(4\pi\varepsilon_0) r_i}$ for $r_i \to 0$ and $-\frac{(Z-N+1)e^2}{(4\pi\varepsilon_0) r_i}$ for $r_i \to \infty$. The small asymmetrical contributions can be dealt with at a later stage using perturbation theory by splitting the Hamiltonian into a symmetrical and asymmetrical part:

$$\mathbf{H}_{\mathrm{c}} = \left(\sum_{i=1}^{N} -\frac{\hbar^2}{2m_{\mathrm{e}}} \nabla_{r_i}^2 + V(r_i) \right) \tag{2.10}$$

$$= \sum_{i=1}^{N} h_i \tag{2.11}$$

$$\mathbf{H}_1 = \sum_{i<j=1}^{N} \frac{e^2}{(4\pi\varepsilon_0)\, r_{ij}} - \sum_{i=1}^{N} S(r_i) \tag{2.12}$$

$$\mathbf{H} = \mathbf{H}_{\mathrm{c}} + \mathbf{H}_1 \tag{2.13}$$

In the central field approximation, it is assumed, the perturbation can be neglected for now and the Schrödinger equation can be separated into a set of N equations:

$$\mathbf{H}_{\mathrm{cc}} = E_{\mathrm{cc}} \tag{2.14}$$

$$_{\mathrm{c}} = u_{a_1}(q_1) u_{a_2}(q_2) \dots u_{a_N}(q_N) \tag{2.15}$$

where a_i is referring to the set of quantum numbers related to the electron i: n_i, l_i, m_{l_i}, m_{s_i} and $u_{nlm_l}(q)$ correspond to the individual electron spin-orbitals. Each of these are solutions to an equation of the form $h_i u_{nlm_l m_s}(q) = E_{nl} u_{nlm_l m_s}(q)$ if normalised.

As for a single-electron system, the individual orbits can be represented and solved as in (2.5): $u_{nlm_l m_s}(q) = R_{nl}(r) Y_{lm_l}(\theta, \phi) \chi_{1/2,m_s}$ using a modified potential for $V(r)$ as outlined above.

Due to the Pauli exclusion principle and electrons being Fermions, each set of quantum numbers n, l and m_s can be only be occupied by a single electron (having spin quantum numbers m_s of $\pm 1/2$). In Table 2.1 this degeneracy is given for each value of l.

The spin function χ_{S,m_s} for multiple electrons can be composed by multiplying the spinors of each electron. Where the results are not eigenstates of $\mathbf{S}^2$, they are combined

using linear combinations. A more general formulation of the Pauli exclusion principle states that the wave function (q) must be antisymmetric ($(q) = -(q')$ where the coordinates for a pair of electrons in q are swapped in q'). So if $R_{nl}(r)Y_{lm_l}(\theta, \phi)$ is symmetric, only antisymmetric solutions for $\chi_{1/2,m_s}$ can be used and vice versa.

For a large number of electrons, this process is rather tedious. So in this representation, the so-called Slater determinant is used to enforce the Pauli principle:

$$_{\mathrm{c}} = \frac{1}{\sqrt{N!}} \begin{vmatrix} u_\alpha(q_1) & u_\beta(q_1) \cdots & u_\nu(q_1) \\ u_\alpha(q_2) & u_\beta(q_2) \cdots & u_\nu(q_2) \\ \vdots & & \\ u_\alpha(q_N) & u_\beta(q_N) \cdots & u_\nu(q_N) \end{vmatrix} \tag{2.16}$$

where α, β, …, ν represent all possible combinations of the quantum numbers n, l, m_l and m_s.

Most state-of-the-art atomic codes use better approximations than outlined above. A few of these methods are outlined in Section 2.2.

Correlation effects

When using the central field approximation in (2.9), not all of the electron-electron interactions are taken into account. So far, only their repulsion was considered. The term correlation effects usually refers to the interaction of electron spins and orbital momenta. We start by re-defining the one-electron operators $\mathbf{L}$ and $\mathbf{S}$ as $\mathbf{L} = \sum_{i=1}^{N} \mathbf{L}_i$ and $\mathbf{S} = \sum_{i=1}^{N} \mathbf{S}_i$. Then we add another term to (2.13):

$$\mathbf{H} = \mathbf{H}_{\mathrm{c}} + \mathbf{H}_1 + \mathbf{H}_2 \tag{2.17}$$

where, similar to the spin-orbit term in the one-electron case (2.8):

$$\mathbf{H}_2 = \sum_i \frac{1}{2m_{\mathrm{e}}^2 c^2} \frac{1}{r_i} \frac{\mathrm{d}V(r_i)}{\mathrm{d}r_i} \mathbf{L} \cdot \mathbf{S} \tag{2.18}$$

In order to solve this Hamiltonian using perturbation theory, it is important to determine the order in which to add $\mathbf{H}_1$ and $\mathbf{H}_2$ as perturbations. In discussing (2.9), we saw that $|\mathbf{H}_1|$ is proportional to Z. Furthermore, it can be shown that $|\mathbf{H}_2| \propto Z^4$ [38].

So for low and medium values of Z, it is safe to assume $|\mathbf{H}_1| \gg |\mathbf{H}_2|$. This case is dubbed Russel-Saunders or L-S coupling. For large values of Z and especially for HCIs, the opposite case $|\mathbf{H}_1| \ll |\mathbf{H}_2|$ can be applied, which is referred to as j-j coupling. However, for most atoms and ions both cases are approximations and if the coupling term and electrostatic correction are of similar importance, it is known as intermediate coupling.

L-S coupling First, $\mathbf{H}_{\mathrm{c}} + \mathbf{H}_1$ is calculated for a given electron configuration. For fully occupied (closed) subshells, there is only one solution. In partly occupied (open) subshells,

however, different energies are obtained for each possible value of $L = |l_1 - l_2|, |l_1 - l_2| + 1, \ldots, l_1 + l_2$ and $S = |s_1 - s_2|, |s_1 - s_2| + 1, \ldots, s_1 + s_2$. For more than two electrons, they are combined successively: all values for L and S are calculated by combining the first two electrons and then all of the possible values of L and S are combined with l_3 and s_3 individually. These solutions are called terms and are usually noted as ${}^{(2S+1)}L$ (i.e. ${}^3D$ for $L = 2$ and $S = 1$). If more than two electrons are in the same subshell, not all combinations for their quantum numbers m_{l_i} and m_{s_i} are compatible with the Pauli exclusion principle. By adding all variations up using $M_L = \sum_i m_{l_i}$ and $M_S = \sum_i m_{s_i}$, it can be seen which terms need to be excluded.

When adding the spin-orbit term $\mathbf{H} = \mathbf{H}_\mathrm{c} + \mathbf{H}_1 + \mathbf{H}_2$, the total Hamiltonian no longer commutes with $\mathbf{L}$ and $\mathbf{S}$, but it does commute with $\mathbf{J} = \mathbf{L} + \mathbf{S}$, causing the $(2L+1)(2S+1)$-fold degeneracy of the terms discussed in the previous paragraph to be partly removed. Possible values of J are $|L - S|, |L - S| + 1, \ldots, L + S$, causing the fine-structure splitting as already discussed for hydrogen in Section 2.1.1 on page 13. When including the value of J, the Russel-Saunders notation ${}^{(2S+1)}L_J$ for terms is obtained (i.e. ${}^3D_1$ for $L = 2$, $S = 1$ and $J = 1$).

Hund's rules are very useful empirical rules for the case of L-S coupling:

1. For a given configuration, the term with the largest value of S has the lowest energy. The energy of the other terms increases with decreasing value of S.
2. For a given value of S the term with the maximum value of L has the lowest energy.

j-j coupling In this case $\mathbf{H}_\mathrm{c} + \mathbf{H}_2$ is calculated as first step.

$$\mathbf{H}_\mathrm{c} + \mathbf{H}_2 = \sum_{i=1}^{N} h_i + \sum_{i=1}^{N} \frac{1}{2m_\mathrm{e}^2 c^2} \frac{1}{r_i} \frac{\mathrm{d}V(r_i)}{\mathrm{d}r_i} \tag{2.19}$$

$$= \sum_{i=1}^{N} h_i + \frac{1}{2m_\mathrm{e}^2 c^2} \frac{1}{r_i} \frac{\mathrm{d}V(r_i)}{\mathrm{d}r_i} \tag{2.20}$$

$$\tilde{h}_i = h_i + \frac{1}{2m_\mathrm{e}^2 c^2} \frac{1}{r_i} \frac{\mathrm{d}V(r_i)}{\mathrm{d}r_i} \tag{2.21}$$

So the first step partly removes the degeneracy of E_{nl} by splitting each level with $l \neq 0$ into two components E_{nlj} with $j = l \pm 1/2$. When using perturbation theory to calculate the full Hamiltonian $\mathbf{H}_\mathrm{c} + \mathbf{H}_2 + \mathbf{H}_1$, the degeneracy of each of these levels is further removed for all possible values for J that can be achieved by combining the individual values of j_i obeying the Pauli exclusion principle. These terms are usually denoted as $(j_1, j_2, \ldots, j_N)_J$.

Of course the number of terms and their degeneracy obtained for both coupling schemes is equivalent. In both cases, a degeneracy in $M_J = -J, -J + 1, \ldots, J$ remains for each term.

Ordering schemes In neutral atoms, subshell energies follow the 'Madelung rule' (also known as the 'aufbau principle'), where the ground state of an atom is obtained by

sequentially filling subshells starting with lowest values for $n+l$ prioritising lower values of n, when there are vacancies in different orbitals of same $n+l$ available. Up to $n=4$ this order is $1s, 2s, 2p, 3s, 3p, 4s, 3d, 4p, 5s, 4d, 5p, 6s, 4f, 5d, 6p, \ldots$.

In the j-j coupling regime (i. e. for hydrogen-like heavy ions) however, the ground state is determined by 'Coulomb ordering', where the orbits are ordered by principle quantum number n first and then by l resulting in $1s, 2s, 2p, 3s, 3p, 3d, 4s, 4p, 4d, 4f, \ldots$. The two schemes deviate from each other when adding the 19th electron after the subshell $3p$ is filled.

Similar to the coupling schemes, both methods are extreme cases and for many atomic systems the orbitals actually occupied in the ground state differ from both of these schemes. Along one isoelectronic sequence, configurations can therefore switch in order. See Figure 1.2 for examples of these level crossings along the neodymium-like sequence.

Clebsch-Gordan coefficients When coupling two spins $\chi_{j_1,m_{j,1}}$ and $\chi_{j_2,m_{j,2}}$, the resulting spin function in tensor product space $\chi_{j_1,m_{j,1};j_2,m_{j,2}} = \chi_{j_1,m_{j,1}} \otimes \chi_{j_2,m_{j,2}}$ will in general not be diagonal in the basis of J.

Clebsch-Gordan coefficients provide a unitary transformation into the eigenbasis in J and M_J:

$$\chi_{J,M_J,j_1,j_2} = \sum_{\substack{M_J=m_1+m_2 \\ m_1 \neq m_2}} C^{j_1\, j_2\, J}_{m_1\, m_2\, M_J} \chi_{j_1,m_{j,1};j_2,m_{j,2}} \tag{2.22}$$

so that

$$\mathbf{J}^2 \chi_{J,M_J,j_1,j_2} = J(J+1)\hbar^2 \chi_{J,M_J,j_1,j_2} \tag{2.23}$$

$$\mathbf{J}_z \chi_{J,M_J,j_1,j_2} = M_J \hbar \chi_{J,M_J,j_1,j_2} \tag{2.24}$$

The coefficients are tabulated for different basis sets in various textbooks.

2.2 Atomic structure codes

As discussed above, the calculation of atomic structure often requires approximation methods. Furthermore, limited computing resources need to be managed. Different atomic structure codes have been developed, representing alternative strategies to cope with these limitations. The formula in this section are derived from [64], [38] and publications on the individual codes mentioned in the text.

2.2.1 Hartree-Fock

We start from the independent particle Hamiltonian for multi-electron systems (2.9). But instead of separating a spherically symmetric part, a new potential $\mathscr{V}(q_i)$ is calculated based on the Slater determinant Φ (and therefore on the spin-orbitals $u_{a_i}(q_i)$; for details on the definition of this modified potential see [38]) yielding the Hartree-Fock equation:

$$\left[-\frac{1}{2}\nabla^2_{\mathbf{r}_i} + \mathscr{V}(q_i)\right] u_{a_i}(q_i) = E_{a_i} u_{a_i}(q_i) \tag{2.25}$$

which needs to be fulfilled by all the individual electron spin-orbitals. However, please note that this is not an eigenvalue equation, because $\mathscr{V}$ depends on $u_{a_i}(q_i)$. So instead of solving for the eigenvalues, the system of differential equations is numerically solved using the iterative self-consistent field approach: Starting from approximated individual spin-orbitals, $\mathscr{V}$ is calculated. This result is used in a second cycle to calculate more accurate spin-orbitals and so on, until convergence criteria are met. The final potential $\mathscr{V}$ is known as the self-consistent field of the atom.

A very important code in atomic physics based on this approach is the Cowan code [52] that includes features to fit intermediate results to experimental data for greater accuracy.

2.2.2 Configuration interaction (CI)

A major inaccuracy of the Hartree-Fock method is that correlations between the electrons (see Section 2.1.2) are only included in the sense that the Slater determinant is required to be antisymmetric. Other correlations can be taken into account by using a trial function composed of multiple Slater determinants,

$$\Phi = \sum_i c_i \Phi_i \tag{2.26}$$

where Φ_i are Slater determinants of different electronic configurations (the electrons occupy different orbitals) and the coefficients c_i are variational parameters.

Popular codes based on this approach are: SUPERSTRUCTURE [73], CIV3 [104] or multi-configuration Hartree-Fock (MCHF) [64, 85].

2.2.3 Coupled cluster (CC)

Rather than using a linear combination of Slater determinants as trial function, as for configuration interaction, an exponential operator can be used:

$$\Phi = \mathrm{e}^{\mathbf{T}} \Phi_0 \tag{2.27}$$

where the cluster operator $\mathbf{T} = \mathbf{T}_1 + \mathbf{T}_2 + \mathbf{T}_3 \ldots$ produces a linear combination of Slater determinants when acting on the reference wave function Φ_0.

Fock space coupled cluster (FSCC) codes such as the Tel-Aviv Relativistic Atomic Fock Space coupled cluster code (TRAFS-3C) [75–77, 112] are based on this approach.

2.2.4 Relativistic codes

Relativistic effects in numerical atomic structure calculation can be taken into account in different ways: Above, this was usually achieved by adding the Breit-Pauli approximation to the non-relativistic many-electron Hamiltonian using perturbation theory:

$$\mathbf{H}_{\mathrm{BP}} = \mathbf{H}_{\mathrm{ip}} + \mathbf{H}_{\mathrm{NFS}} + \mathbf{H}_{\mathrm{FS}} \tag{2.28}$$

where $\mathbf{H}_{\mathrm{ip}}$ is the non-relativistic Hamiltonian (2.9), $\mathbf{H}_{\mathrm{NFS}} = \mathbf{H}_{\mathrm{mass}} + \mathbf{H}_{\mathrm{Darwin}} + \mathbf{H}_{\mathrm{SSC}} + \mathbf{H}_{\mathrm{OO}}$ a term usually referred to as nonfine-structure Hamiltonian and composed of a relativistic mass correction, two-body Darwin terms, spin-spin contact term, and orbit-orbit interaction, while $\mathbf{H}_{\mathrm{FS}} = \mathbf{H}_{\mathrm{SO}} + \mathbf{H}_{\mathrm{SOO}} + \mathbf{H}_{\mathrm{SS}}$ contains terms for the nuclear spin-orbit interaction, spin-other-orbit and spin-spin term. Explicit formulas for these terms can be found in Chapter 21 of [64]. Other approximations can also be used to treat relativistic effects by perturbation theory such as Dirac-Coulomb or Dirac-Breit.

The second option is to use QED to solve the so-called Dirac-Coulomb-Breit Hamiltonian. The Breit-Pauli approach mentioned above can be viewed as a simplification of this approach by extending the non-relativistic Hamiltonian to include relativistic effects such as retardation of the electron-electron interaction up to relative order $(\alpha Z)^2$.

Codes including the complete retarded electron-electron interaction (i. e. by solving the full Dirac-Coulomb-Breit Hamiltonian) are referred to as fully relativistic. QED being a gauge theory, the Hamiltonian can be solved using different gauges and not all of the codes incorporate the full Coulomb gauge operator: some approximate it using the Breit or Gaunt operator (see Chapter 22 of [64]). Configuration interaction and coupled cluster can be combined both with perturbative and fully relativistic calculation. Popular codes are Multi-configuration Dirac-Fock (MCDF) by Grant *et al.* [94], AMBiT using the CI + MBPT ansatz [111], configuration-interaction Dirac-Fock-Sturm (CI-DFS) [184] or FAC [95, 96]. The latter was utilised for this work (i. e. for Figures 1.2 and 6.2).

2.3 Quantum electrodynamics (QED)

As mentioned in the introduction, QED effects cause an upward shift of about 3.3 µeV of the $2s_{1/2}$ level of hydrogen. From just describing a specific observation, QED has become a universal theory and one of the most accurately tested theories in physics. One of its predictions, the anomalous magnetic dipole moment of the electron, has been measured up to the level of 10^{-13} [100]. Due to the Lamb shift scaling with Z^4, compared to the energy of the levels scaling with Z^2, this effect is even more pronounced in heavier elements [64].

QED describes interactions of electrically charged particles with photons and is the first theory in full agreement with both quantum mechanics and special relativity. Details of the formalism are beyond the scope of this work. Instead, qualitative explanations as well as results from recent other works (mostly [118] and references therein) are summarised here.

Applied to atomic systems, QED is used to describe the interactions of electrons and the nucleus with themselves and each other by means of virtual particles giving rise to a multitude of corrections.

Here, only lithium-like ions are considered. They are similar to one-electron systems in the sense that they only have a single valence electron but due to the interaction with the two electrons in the $1s$ orbit, interelectron interactions are significant. This balance of the system being simple enough for calculation but showing all types of interactions makes

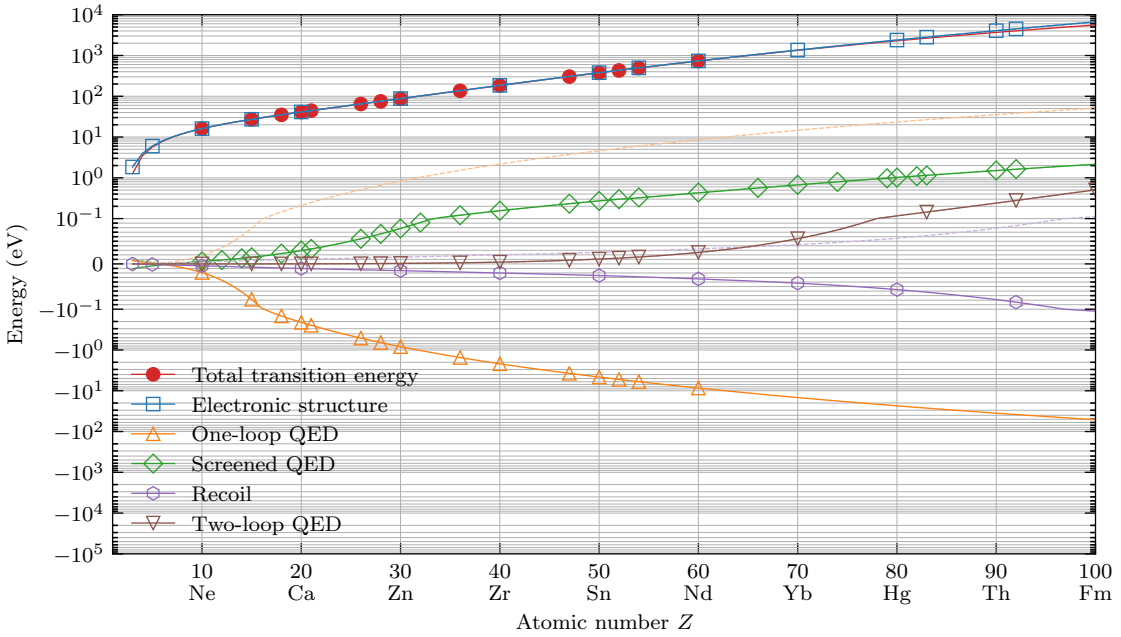

Figure 2.1: QED corrections for the fine-structure transition $1s^2 2p\ {}^2P_{3/2} \to 1s^2 2s\ {}^2S_{1/2}$ in Li-like ions for different values of the atomic number Z. For negative contributions to the total transition energy, dashed lines of the absolute value were added for magnitude comparison. Data adopted and interpolated from [118, 201].

lithium-like systems the ideal toy model for QED tests.

In Figure 1.1 of the introduction, corrections for the fine-structure transition $1s^2 2p\ {}^2P_{1/2} \to 1s^2 2s\ {}^2S_{1/2}$ were presented. The same corrections are shown in Figure 2.1 for the transition $1s^2 2p\ {}^2P_{3/2} \to 1s^2 2s\ {}^2S_{1/2}$. For the two transitions, the sign of each contribution is the same and differences are down to magnitude. For heavy elements, it can be seen that relativistic contributions are slightly more pronounced if the initial level is $1s^2 2p\ {}^2P_{3/2}$. The individual contributions will be explored in more detail here. Where applicable, a Fermi nuclear charge distribution was assumed.

Naturally, the largest contribution is the electronic structure since this includes the interaction of the electrons with the Coulomb potential in the QED framework. Kozhedub *et al.* calculated the structure using large-scale, fully relativistic CI-DFS calculations utilising the Breit approximation. It is usually expanded using scaling factors $\lambda = 1/Z$ to separate the electron-electron repulsion (scaling as Z) from the Coulomb field of the nucleus (scaling as Z^2). Figures 2.2 and 2.3 break the electron structure down into individual components. Relativistic contributions from Dirac terms of the Hamiltonian, one-, two-, and three-photon interelectronic interactions (corresponding to scaling parameters $\lambda = 1/Z$, $1/Z^2$, and $1/Z^3$ respectively), as well as an estimate for the higher orders are shown. The latter was obtained by subtracting the individually calculated orders from the total energy calculated using the Breit interaction using $\lambda = 1$.

By comparison of the two Figures, it is apparent that the ${}^2P_{3/2}$ level is affected much

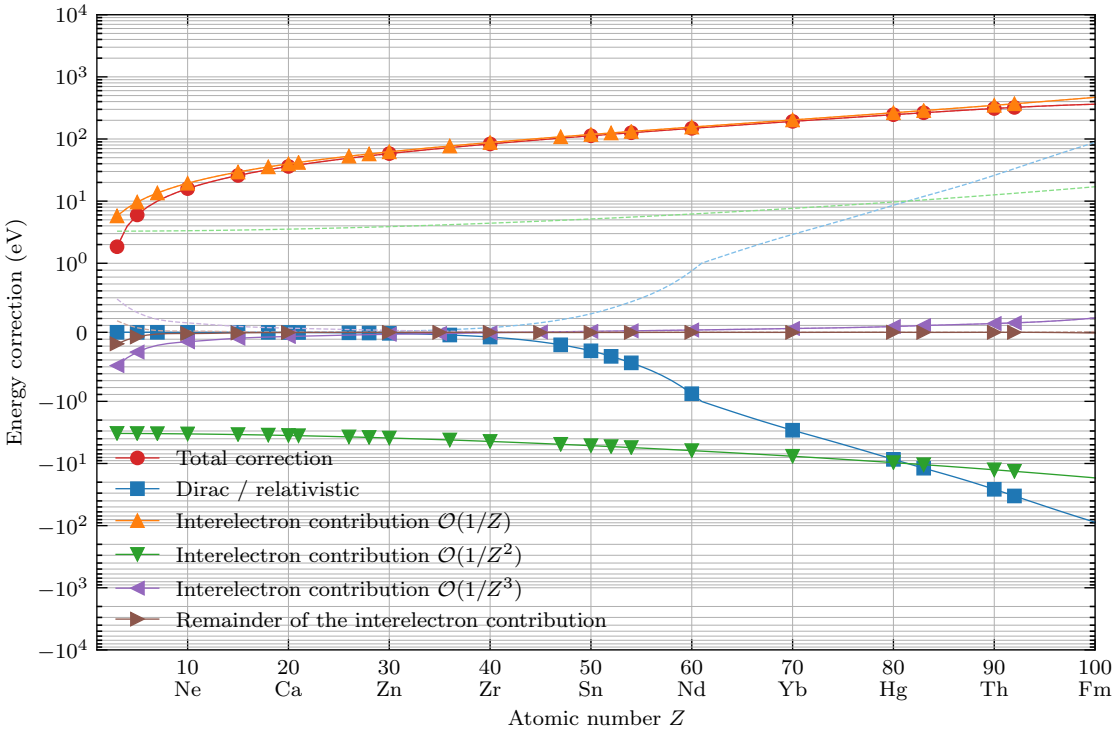

Figure 2.2: Electron structure contributions to $1s^2 2p\ ^2P_{1/2} \to 1s^2 2s\ ^2S_{1/2}$ for different values of Z. For negative contributions to the total transition energy, dashed lines of the absolute value were added for magnitude comparison. Data adopted and interpolated from [118].

stronger by relativistic effects. For $Z > 33$ these even becomes the dominant contribution. After all, this difference in the relativistic contributions partly removes degeneracy in j as discussed for the one-electron system.

The second largest contribution to the total transition energy are one-loop QED corrections. When quantising an electromagnetic field, the lowest energy state is non-zero (similar to a quantised harmonic oscillator) giving rise to virtual photons coupling to virtual electron-positron pairs (vacuum fluctuations) causing an electron in vacuum to perform rapid oscillatory motions. In a non-uniform field the electron can no longer be considered a point-like charge because the mean potential experienced by the particle is slightly different than the corresponding field at its mean position. Various interactions with virtual particles can be calculated. The simplest case is the emission and re-absorption of a single virtual photon (self-energy).

Usually the self-energy and vacuum polarisation are expanded in orders of (αZ), because the sequence converges after a few elements for small values of Z. For heavy ions, other methods are used, allowing the inclusion of higher order terms without explicit expansion. The vacuum polarisation can be separated into the Uehling and Wichmann-Kroll potentials. All of these contributions are shown in Figure 2.4 for the transition $1s^2 2p\ ^2P_{1/2} \to 1s^2 2s\ ^2S_{1/2}$.

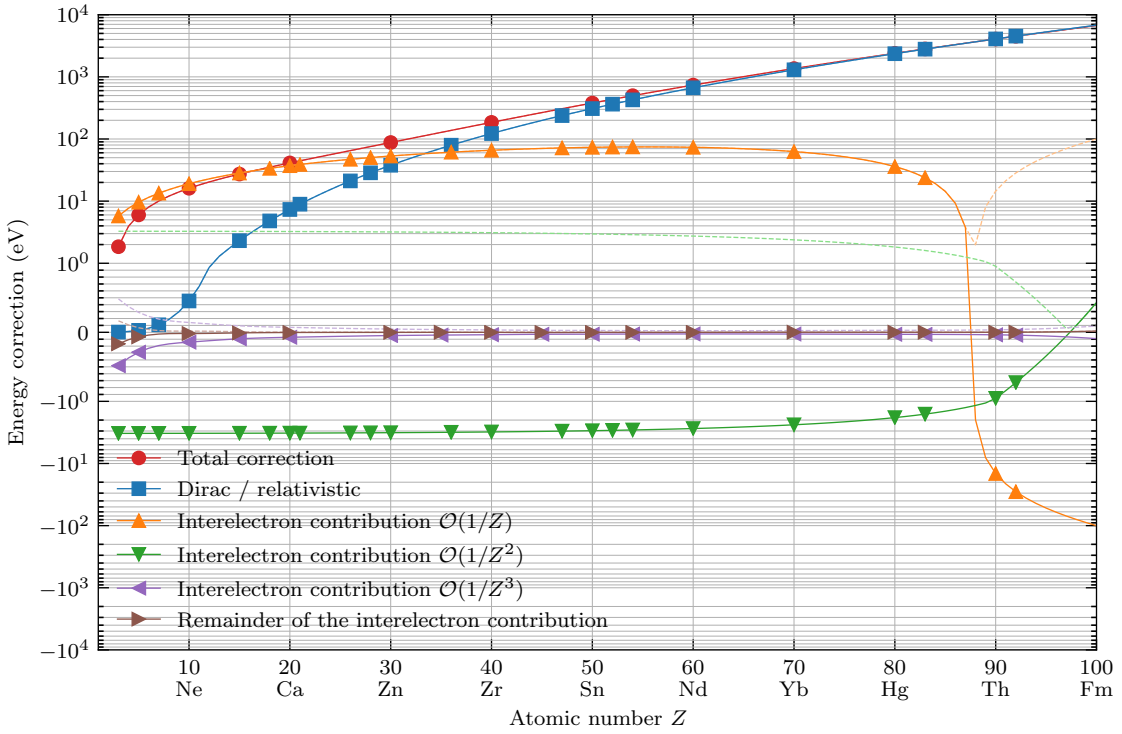

Figure 2.3: Electron structure contributions to $1s^2 2p\ ^2P_{3/2} \rightarrow 1s^2 2s\ ^2S_{1/2}$ for different values of Z. For negative contributions to the total transition energy, dashed lines of the absolute value were added for magnitude comparison. Data adopted and interpolated from [118].

One-loop QED contributions to the transition $1s^2 2p\ ^2P_{3/2} \rightarrow 1s^2 2s\ ^2S_{1/2}$ are not shown here due to their similarity (there are only minor differences in magnitude).

In lithium-like systems the two core-electrons screen the valence electron from some interactions. Coulomb-screening and interelectron photon exchange was taken into account in the calculation of the electronic structure given above up to second order. However, screening of one-loop QED effects also has to be taken into account. These can generally be regarded as second-order contributions in the expansion $(\alpha Z)^2$. But the values from Kozhedub *et al.* presented in Figure 2.5, partly take into account higher orders than just an expansion to second order would [118].

For the range of medium Z measured in this thesis, two-loop QED effects are negligible. For completeness, their total contribution is included in Figures 1.1 and 2.1 but these effects are not discussed in further detail here.

Finally, the nuclear recoil effect takes into account a finite mass of the nucleus. It is equivalent to the reduced mass in a non-relativistic calculation. This correction is considered to be beyond the Breit approximation calculation and is usually expanded in orders of m_e/M, $1/Z$, and αZ where M is the nuclear mass. The values from [118] provided here, are expanded in first order of m_e/M, all orders of $1/Z$, as well as one- and two-electron QED contributions. It can be seen in Figure 2.6 that the latter are most relevant to

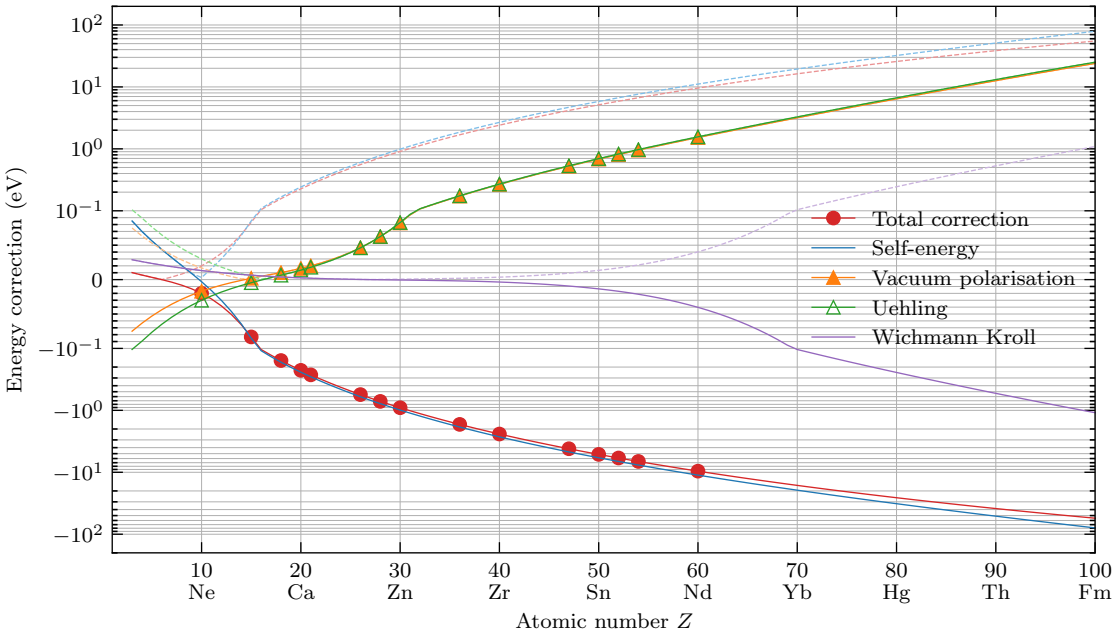

Figure 2.4: One-loop QED contributions to $1s^2 2p\ ^2P_{1/2} \to 1s^2 2s\ ^2S_{1/2}$ for different values of Z. For negative contributions to the total transition energy, dashed lines of the absolute value were added for magnitude comparison. Data adopted and interpolated from [6, 7, 118, 144]. For self-energy and Wichman-Kroll contributions, no symbols are shown because data points are available for atomic numbers in increments of one.

lithium-like ions with $Z > 40$.

In summary, the most relevant effects for lithium-like ions with $7 \leq Z \leq 18$ are the interelectron contributions up to third order, especially towards lower values of Z (third order about 0.9 %). Towards the end of the investigated range, relativistic effects are increasingly relevant for the transition $1s^2 2p\ ^2P_{3/2} \to 1s^2 2s\ ^2S_{1/2}$ at the level of up to 14 % (around 290 ppm for $^2P_{1/2} \to {}^2S_{1/2}$). One-loop QED and counteracting screening effect are also considerable (at the level of 0.4 %), while nuclear recoil is expected to be small (up to 200 ppm) and two-loop QED effects are negligible. When considering two or more photon interelectron interaction, one-loop QED effects and screening thereof as total QED effect, the resulting shift of the $1s^2 2p\ ^2P_{1/2} \to 1s^2 2s\ ^2S_{1/2}$ transition in argon attributed to QED is −3.7 eV or 11 %.

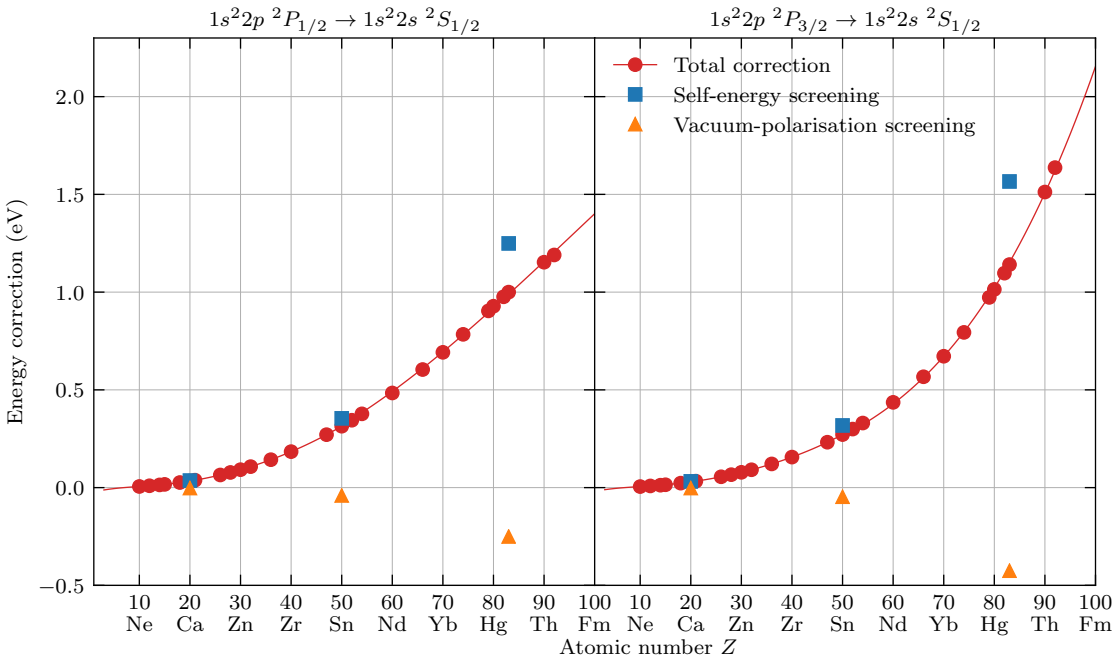

Figure 2.5: QED screening potential for different values of Z. Data adopted and interpolated from [118]. For self-energy and vacuum-polarisation contributions not enough data points were available for interpolation.

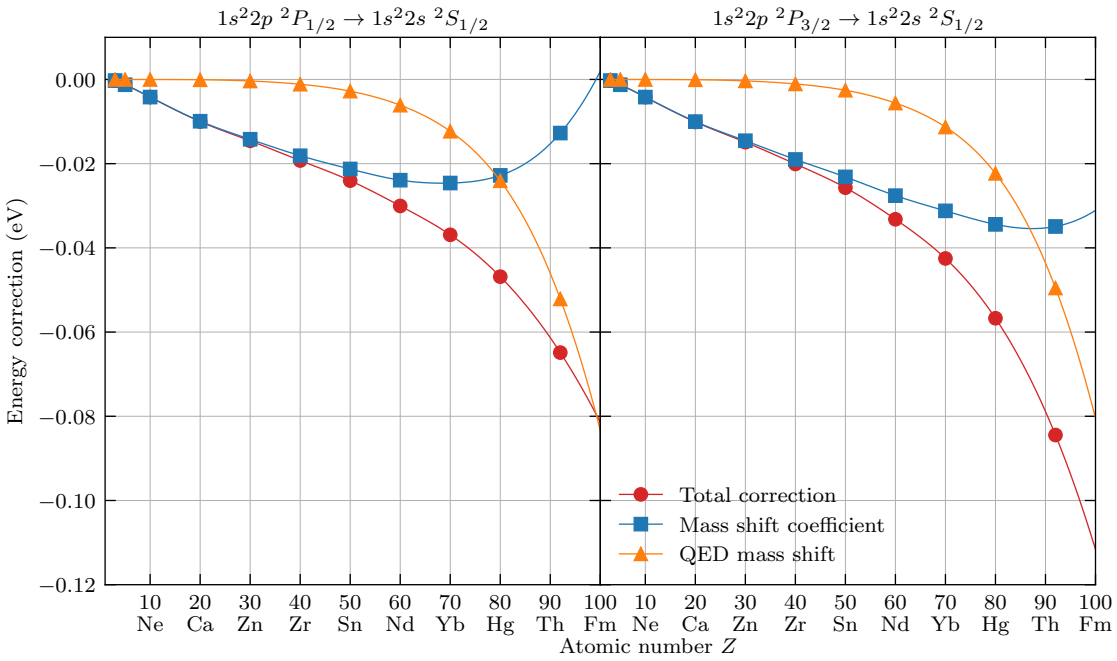

Figure 2.6: Nuclear recoil effect for different values of Z. Data adopted and interpolated from [118].

2.4 Interaction with external fields

For this work, only interactions of ions with external magnetic fields are relevant, namely for the identification of spectral lines of iridium. Nevertheless, it is worth mentioning that interactions with external electric fields are also an important topic in atomic physics. Both partly remove degeneracy in M_J: Levels with $\pm M_J$ are still degenerate, but levels with distinct absolute values of M_J have different energies. For weak external fields, the energy differences between the levels depend on the square of the field strength (quadratic Stark effect). In the strong-field regime the dependency becomes linear (linear Stark effect). Finally, level splitting due to a field with a time-dependent strength is referred to as the AC Stark effect. It is also worth mentioning that external electric fields also mix states of different parity so that transitions can be observed, which would otherwise be forbidden.

Similarly, degeneracy is partially removed when electrons or ions interact with an external magnetic field $\mathcal{B}$ (which is oriented along the z axis without loss of generality). This effect was first observed for sodium by Pieter Zeeman in 1896 [205]. The interpretation presented here was mostly adapted from [38]. Interaction with this external field gives rise to two additional terms in the Hamiltonian. For a N electron system with L-S coupling these are:

$$\sum_{i=1}^{N} \frac{\mu_\mathrm{B}}{\hbar} \left(\mathbf{L}_i + 2\mathbf{S}_i\right) \times \mathcal{B} = \sum_{i=1}^{N} \frac{\mu_\mathrm{B}}{\hbar} (\mathbf{L}_{z_i} + 2\mathbf{S}_{z_i}) \mathcal{B} \tag{2.29}$$

also known as the paramagnetic or linear term. The other one is called diamagnetic or quadratic:

$$\sum_{i=1}^{N} \frac{e^2}{8m_\mathrm{e}} \left(\mathcal{B} \times \mathbf{r}_i\right)^2 = \sum_{i=1}^{N} \frac{e^2}{8m_\mathrm{e}} \mathcal{B}^2 r_i^2 \sin^2\theta \tag{2.30}$$

Usually, only one of the two terms is considered and the other one is neglected. When the effect is observed in weak to moderate $\mathcal{B}$ fields, it is known as the linear Zeeman effect and (2.30) is usually neglected. Otherwise it is referred to as the quadratic Zeeman effect.

The linear case is further divided into three distinct situations:

1. For weak fields (up to $\mathrm{Z}^4\,\mathrm{T}$) the paramagnetic term discussed above is smaller than the spin-orbit interaction. This situation is called the anomalous Zeeman effect and by far the most relevant case for laboratory observations.
2. When both terms are of similar importance, it is referred to as the Paschen-Back effect.
3. Since first observations were made for $Z = 1$, where field strengths can be achieved in a laboratory environment that are much larger than the spin-orbit interaction, this case is called the normal Zeeman effect.

Field strengths of up to $10^4\,\mathrm{T}$ usually encountered in laboratories are moderate compared to some contexts in astrophysics. In these strong magnetic fields (about $10^4\,\mathrm{T}$ to $10^8\,\mathrm{T}$)

or in atomic systems with very high principal quantum number n (Rydberg atoms) the quadratic Zeeman effect can be observed which we will not discuss further. There is an even more extreme case for very strong fields, when the Coulomb potential of nucleus can be neglected.

All three cases of the linear Zeeman effect mentioned above, are discussed in more detail here:

1. For weak fields, degeneracy in J is removed by splitting every term by an energy of:

$$\Delta E = g\mu_{\mathrm{B}}\mathcal{B}M_J \tag{2.31}$$

where g is the Landé factor

$$g = 1 + \frac{J(J+1) + S(S+1) - L(L+1)}{2J(J+1)} \tag{2.32}$$

and the Bohr magneton $\mu_{\mathrm{B}} = \frac{e}{2m_{\mathrm{e}}}\hbar = 9.274\,010\,078\,3(28) \times 10^{-24}\,\mathrm{J\,T^{-1}}$ [74].

2. For intermediate field strengths (Paschen-Back effect) the additional splitting can be estimated by:

$$\Delta E = \mu_{\mathrm{B}}\mathcal{B}(M_L + 2M_S) + AM_LM_S \tag{2.33}$$

where $A = \bar{A}\hbar^2$ and $\bar{A}(\mathbf{LS})$ is the spin-orbit interaction.

3. Finally, for moderate magnetic field strengths (normal Zeeman effect) only $\Delta E = \mu_{\mathrm{B}}\mathcal{B}(M_L + 2M_S)$ is taken into account.

2.5 Electron-ion interactions

Most of the measurements presented in this work are based on highly charged ions in a plasma confined in the trap of an EBIT or EBIS interacting with an electron beam (see Chapter 3). Ion-ion interactions are also relevant: in particular charge exchange and thermalisation due to collisions. However, the electron density and relative kinetic energy in the interaction region favours electron-ion interactions. A few essential processes in these plasmas are presented here.

2.5.1 Electron-impact ionisation

Charge breeding in an EBIS is governed by electron impact ionisation. First efforts to explain this phenomena using theory were published by Thomson in 1912 [182] after he discovered the electron in 1897. Kinetic energy from a free electron is transferred to a bound electron during a collision. If it is sufficient to overcome the ionisation potential, the bound electron is ejected into the continuum. Assuming this leaves an inner-shell vacancy

in the ion, subsequent de-excitation can be detected by observing the photons emitted in this process.

Since 1912, there has been a struggle to predict cross-sections for the process. These efforts culminated in the 1960s, when Lotz was finally able to give a semi-empirical formula with predictive power by intra- and extrapolation to other elements and charge-states [131]:

$$\sigma_{\mathrm{EII}}(E) = \sum_{i=1}^{N} a_i q_i \frac{\ln \frac{E}{P_i}}{E P_i} \left(1 - b_i \, \mathrm{e}^{-c_i\left(\frac{E}{P_i}-1\right)}\right); \qquad E \geq P_N \tag{2.34}$$

where E is the energy of the incident electron, P_i is the binding energy of the ith subshell, q_i is the number of equivalent electrons in the same subshell, and a_i, b_i, c_i are empirical constants that need to be determined for the respective element and subshell. N should be chosen, so that $E \leq P_N$. Note that P_1 is equivalent to the ionisation potential here.

For $E \leq P_i$ the respective contribution to the cross section σ_i is zero. For larger energies the curve resembles the prediction from Bethe [24]: $\sigma_i(E) = (\ln E/P_i) \cdot P_i/E$ and has a maximum around $E_{\max} = 2.7P_i$ to $8P_i$. Generally this ratio is larger for atoms than for ions. In particular for HCIs this ratio can even go down to 2.3. For $E \gg P_i$ (2.34) can be simplified to $\sigma_i \approx a_i q_i \left(\ln \frac{E}{P_i}\right) / (E P_i) \sim \frac{\ln E}{E}$ [132].

2.5.2 Radiative recombination (RR)

In a plasma, the most relevant process counteracting electron-impact ionisation is radiative recombination that is shown in Figure 2.7: A free electron from the continuum is captured into a bound state by emission of a photon.

The total relativistic cross section equals that of the time-inverse process, called the photoelectric effect, first observed by Hertz and Hallwachs [103] and finally explained by Einstein [72].

First, a differential cross section for ionising an electron from a shell n with angular momentum j_n by an unpolarised photon with angular frequency ω is calculated [151, 152]

$$\frac{d\sigma_{\mathrm{ph}}}{d\Omega} = \frac{\alpha m_{\mathrm{e}} c^2}{4\hbar\omega} \frac{\lambda\!\!\!^{-2}_{\mathrm{c}}}{2(2j_n+1)} \sum_{\mu_n} \sum_{m_s} \sum_{\lambda} \left| M_{\mathbf{p},n}(m_s, \lambda, \mu_n) \right| \tag{2.35}$$

using the fine-structure constant α, the electron mass m_{e}, the speed of light in vacuum c, the reduced Planck constant $\hbar$, the Compton wavelength $\lambda\!\!\!^{-}_{\mathrm{c}}$, and the transition matrix elements $M_{\mathbf{p},n}$. The latter is averaged over the angular momentum projections for the ground state μ_n, the circular polarisation of the incoming photon $\lambda = \pm 1$ and the spin components of the emitted electron $m_s = \pm 1/2$.

Next, the emitted electron is described by Dirac spinors and the transition matrix elements $M_{\mathbf{p},n}$ are decomposed into spherical Bessel functions as explained in [107]:

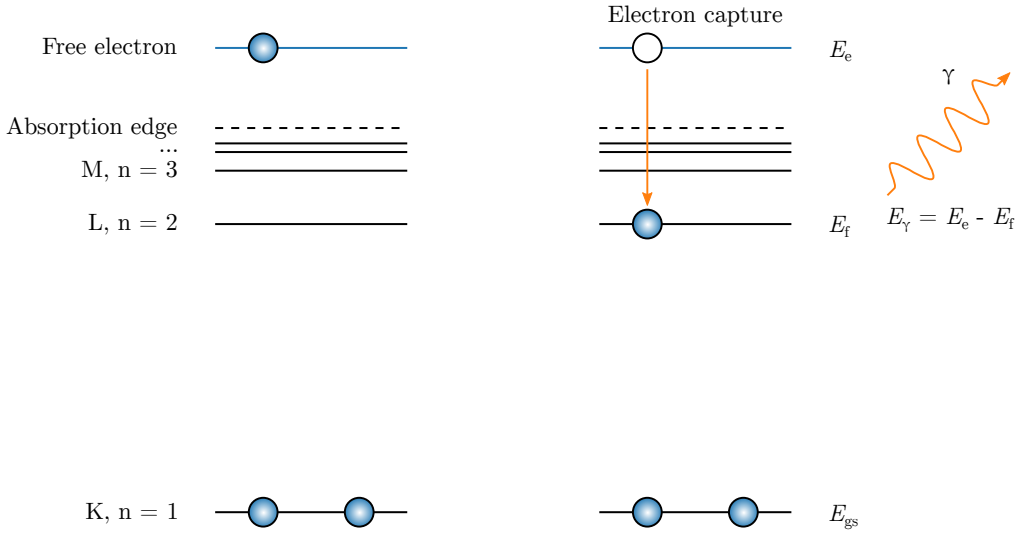

Figure 2.7: Schematic diagram of Radiative recombination. In this example, both states of the K shell are initially occupied and the free electron is captured into the L shell.

$$\sigma_{\mathrm{ph}} = \frac{8\alpha\pi^2 m_{\mathrm{e}} c^2}{\hbar\omega} \frac{\lambda\!\!\!^{-2}_{\mathrm{c}}}{2j_n + 1} \sum_{\mu_n} \sum_{\kappa} \left| \sum_{L} \mathrm{i}^L F^{\lambda=1}_{\mu_n}(L, \kappa) \right|^2 \tag{2.36}$$

introducing the imaginary unit i, as well as the relativistic angular momentum quantum number $\kappa_n = \pm(j_n + 1/2)$ and the total angular momentum quantum number L of the bound-state wave function. Explicit formulas to calculate $F^{\lambda}_{\mu_n}(L, \kappa)$, as well as tabulated numerical values for the K, L and M shells for hydrogen-like systems from hydrogen to copernicium are given in [106]. Furthermore, Ichihara gives a transformation coefficient to derive radiative recombination cross section for each electron from (2.36).

Finally, the total relativistic cross section for radiative recombination can be calculated:

$$\sigma_{\mathrm{RR}} = \frac{\sigma_{\mathrm{ph}}}{f_n(T_{\mathrm{e}}, |P_n|)} \tag{2.37}$$

with the kinetic energy of the electron T_{e} and the ionisation potential P_n, as well as:

$$f_n(T_{\mathrm{e}}, |P_n|) = \frac{\tilde{T}_{\mathrm{e}}^2 + 2\tilde{T}_{\mathrm{e}}}{\left(\tilde{T}_{\mathrm{e}} + \tilde{P}_n\right)^2} \tag{2.38}$$

where $\tilde{T}_{\mathrm{e}} = {}^{T_{\mathrm{e}}}/_{(m_{\mathrm{e}}c^2)}$ and $\tilde{P}_n = {}^{|P_n|}/_{(m_{\mathrm{e}}c^2)}$.

2.5.3 Dielectronic recombination (DR)

Electron capture does not necessarily result in the emission of a photon. When the excess energy is used, to excite a bound electron, the process is referred to as dielectronic recombination (DR).

As opposed to radiative recombination, this is a two-step process: first, a free electron is captured into a vacancy by simultaneous excitation of another electron bound to the same ion. When the sum of the kinetic energy of the electron and the potential energy of the level it is captured into equals the excitation energy, this process becomes resonant. Subsequently, the ion de-excites back to the ground state under emission of a photon. Both steps are illustrated in Figure 2.8. The time-inverse process is known as Auger effect and was discovered by Meitner in 1922 [138]. This legacy is still apparent in the notation for which shells are involved in the process: KLN DR refers to the process where a free electron is captured into the N shell under the excitation of an electron from the K to the L shell. KLN Auger decay would describe the time-inverse process: de-excitation of an L-shell electron to the K shell under ionisation of an N-shell electron.

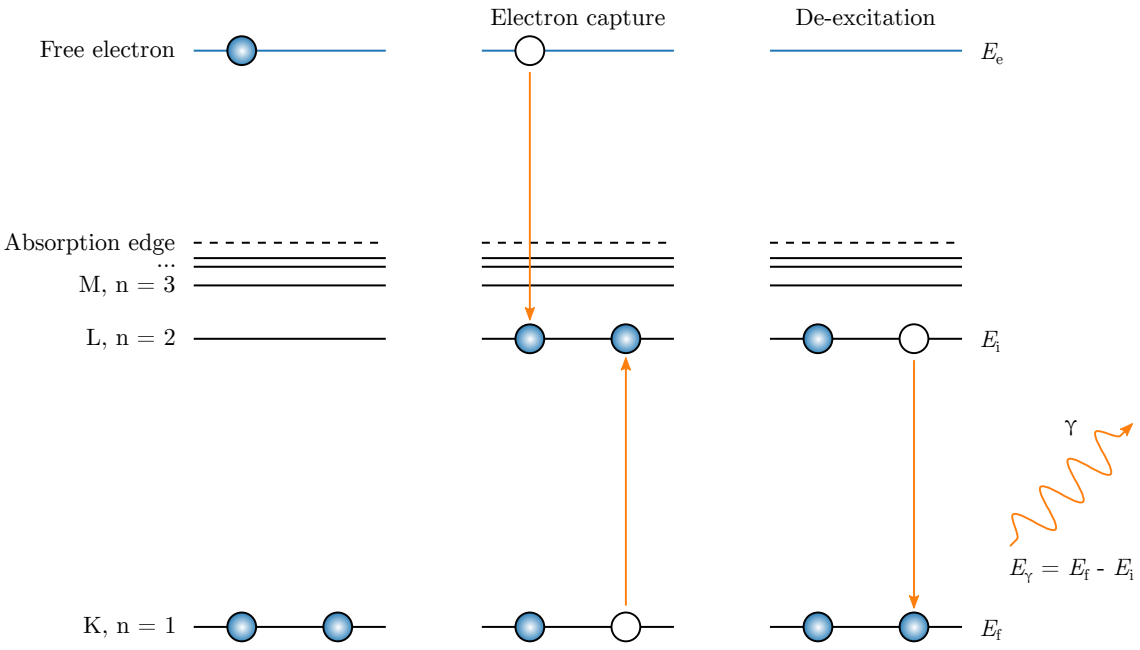

Figure 2.8: Schematic diagram of KLL Dielectronic recombination. A free electron is captured into the L shell under excitation of a K-shell electron into the L shell. In a second step one of the L shell electrons is de-excited to the ground state by emission of a photon. If the resonance condition $|E_e - E_f| = |E_f - E_i|$ is met, the cross section for electron capture is three orders of magnitude larger than for RR.

First signs of DR were discovered in the upper atmosphere in the 1940s [137], while laboratory measurements and the resonant nature of the process were observed in the 1980s [16, 60, 143]. Already one year later DR was studied in EBIS plasma [39].

2.5.4 Dither code

In Chapter 3, a novel EBIS charge breeder built and commissioned in the course of this work is presented. The temporal evolution of the ion-charge-state distribution is arguably the most important characteristic for charge breeders. Simulations in this work are based on the Dither code due to the extensive validation track record in EBIT experiments such as [148] but another popular choice is charge breeding simulation (CBSIM) [5].

Dither uses the Lotz formula given in (2.34) for electron impact ionisation. Being written in 1989, the code uses the approximation of Kim and Pratt [115] to calculate RR cross sections rather than the more rigorous approach by Ichihara *et al.* [107]. Cross sections for DR need to be supplied to the software by means of an external file in order to take this process into account. Charge exchange can often be neglected due to the low collision rate of trapped ions. However, for certain charge breeders collisions with background gas need to be taken into account. Dither assumes cold hydrogen as the only gas and uses recombination cross sections from an analytical expression from [109].

Starting with a given initial population of charge states, the set of coupled non-linear differential rate equations is numerically solved to deduce the temporal evolution. An example for such a simulation is shown in Figure 3.3.

CHAPTER 3

Charge breeding of rare isotopes

3.1 Introduction

The concept of charge breeding using an EBIS was first mentioned by Donets *et al.* on the 'First International Conference for Ion Sources' in Saclay in June 1969 [62]. Integrating this kind of charge-breeder into a cyclotron is proposed in the corresponding proceedings. Not only the development of EBIS-type charge breeders was set off by this publication, but it also laid the foundations for the remarkably fruitful EBIT research a few years later (see Section 3.1.3).

As main technical part of this dissertation, a new EBIS was designed, constructed and tested at the Max-Planck-Institut für Kernphysik (MPIK) together with Stepan Dobrodey, Renate Hubele, Thomas Baumann and Leigh Graham under the supervision of José R. Crespo López-Urrutia [61]. Currently the device is being commissioned as a charge breeder for heavy isotopes at TRIUMF in Vancouver. Finally, the largest cyclotron in the world will use an EBIS-type charge breeder. Admittedly, it will be located downstream in the facility and not be used as part of the injection, as suggested by Donets.

3.1.1 ARIEL facility at TRIUMF

TRIUMF is equipped with the worlds largest cyclotron. It can produce proton beams of up to 1 µA and 500 MeV. These beams are used for research in particle and nuclear physics, as well as life sciences. However the main cyclotron can only serve one beam line at a time and there is high demand for beam times. Therefore a new facility dubbed Advanced Rare Isotope Laboratory (ARIEL) is in construction since 2011. At its heart it features a 10 mA electron gun, a linear accelerator for 0.5 MeV [117] and two new target stations where the 0.5 MW electron beam is first converted into high energy photons by means of a converter target (i. e. liquid lead). These induce photo fission in the final production target made from uranium carbide, alkaline metals or actinides. Alternatively, a beam line from the main cyclotron will facilitate the use of proton beam on the production target. Although the overall cross section is lower for the electron beam driven fission, productivity can still be superior to that of the proton beam due to greater flux and higher fractional yields for the production of some neutron-rich heavy isotopes [44].

A big share of physics research at TRIUMF is geared towards neutron-rich nuclei. One potential application for ARIEL is production of the isotope ^{8}Li from a ^{9}Be target. Using the electron driver increases the yield over currently available rates. Beams of this species can be spin polarised by 80 % and implanted in a material sample. Subsequent β decay is anisotropic and may be employed to deduce electrical and/or magnetic properties of the sampled material by measuring the time dependency of the spin polarisation decay.

This so-called beta Nuclear magnetic resonance (β-NMR) is closely related to muon spin spectroscopy and ten orders of magnitude more sensitive than conventional NMR [179].

The rare isotopes evaporate from the target due to its heat. A laser is used to photo-ionize the isotopes, so that they can be accelerated towards the Canadian Rare Isotope Facility with Electron Beam Ion Source (CANREB), which is part of ARIEL project. Before the isotopes can be handed over to the existing post-accelerators leading to the experiments, referred to as Isotope Separator and Accelerator (ISAC-I and II), the beam needs to be separated from impurities, bunched and charge bred. The required mass-to-charge ratio of ISAC is $A/Q \approx 5 \ldots 7$. In accelerator facilities this can be achieved using EBIS devices, beam-foils and electron cyclotron resonance ion source (ECRIS).

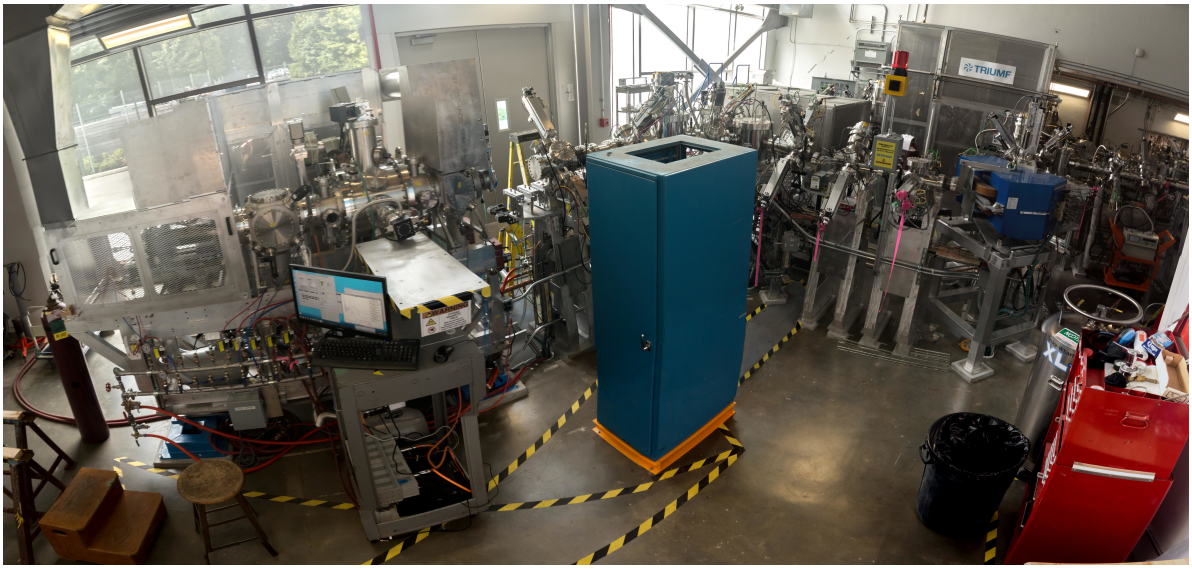

Figure 3.1: Panorama photograph of the CANREB hall taken on 28 June 2019. The EBIS is located to the left of the blue electronics rack. On the right both the radio-frequency cooler-buncher and the Nier spectrometer can be seen.

Stripper foils are very useful tools to produce highly charged ions. However, the ions need to be pre-accelerated. Often, this requires multiple stripping and acceleration stages, increasing cost, longitudinal and transverse emittances, as well as reducing overall efficiency [127]. Having an accelerator for a wide range of A/Q makes charge breeding for post-acceleration superfluous. Consequently, stripper foils are typically used to prepare highly charged ions for experiments rather than for post-acceleration.

ECR ion sources use microwaves to generate and heat a plasma in a low-pressure environment that is confined axially by a pair of solenoid coils and radially by a sextupole magnet. When an ion beam is sent through this plasma region, the ions can be ionised incrementally by electron-ion collisions. These charge breeders have a long tradition, are commercially available, can handle high ion beam currents and operate both in continuous and bunched mode. Compared to EBIS devices however, ECRIS contaminate the ion beam more because of the imperfect plasma confinement and subsequent interaction with the vacuum chamber walls. Moreover, transverse emittance is usually large and the plasma

conditions are not as well-known and finding the optimum set of parameters for new elements and charge states can be time consuming [127].

In recent years however, EBIS charge breeders have grown more popular due to high efficiency, fast and variable breeding times, small beam emittances and low levels of background ion species [127, 186, 191]. Laboratories having implemented EBIS charge breeders are: REXEBIS (CERN, Geneva, Switzerland), TITAN EBIT (TRIUMF, Vancouver, Canada), ReA EBIT (NSCL, East Lansing, USA), and CARIBU EBIS (Argonne National Laboratory, Lemont, USA). RISP EBIS (RAON, Daejeon, Korea) is not yet commissioned. RHIC EBIS (BNL, Upton, USA) could also be counted as a charge breeder currently in in operation. However, it serves as a synchrotron injector rather than a charge breeder for rare isotopes.

3.1.2 General concept of an EBIS charge breeder

An electron beam ion source uses electron impact ionisation to increase the charge of ions under investigation.

For efficient charge breeding, electron beams with high current densities are required [131]. A strong magnetic field is used to compress the beam emitted from a cathode in an electron gun. The electrons are dumped on a collector electrode that closes the electric circuit and returns them to the cathode power supply. Charged particles can only be injected and extracted along the axis of the magnetic field, requiring the collector to be a hollow cylinder. Along the magnetic field axis, voltages applied to at least three cylindrical electrodes—dubbed drift tubes—can be used to produce an electrostatic axial trapping potential for positively charged particles. The trap is completed radially by the negative space charge of the electron beam and the confinement due to the cyclotron motion caused by the magnetic field.

Up front, the continuous singly charged rare-isotope beam is cooled and bunched, so that each bunch can undergo the three consecutive steps injection, charge breeding and extraction: initially the gun-side drift tube is at a potential that reflects the incoming ion beam. After the ions have been transferred to the trapping region through the collector, the collector-side drift tube is raised to close the trap and capture the ion bunch. After charge-breeding the potential on the collector-side drift tube is lowered or the potential of the central drift tube is raised sufficiently so that the ions are extracted over-the-barrier. Figure 3.2 is a schematic diagram of the process.

Since the ion cloud is typically larger than the electron beam in the trap centre [130], it is an important factor, how much time the individual ions spend in the electron beam. While the kinetic energy of the electrons sets an upper boundary to the charge state, efficient charge breeding requires a good overlap, high current density and low background pressure. The latter two are the most important parameters for the design of a fast EBIS charge breeder. Higher current density generally leads to a better overlap due to the increased space charge of the electron beam.

3.1.3 Electron beam ion trap (EBIT)

Historically, electron beam ion traps (EBITs) were developed from electron beam ion sources (EBISes) and there is no fundamental difference between the two. Typically an

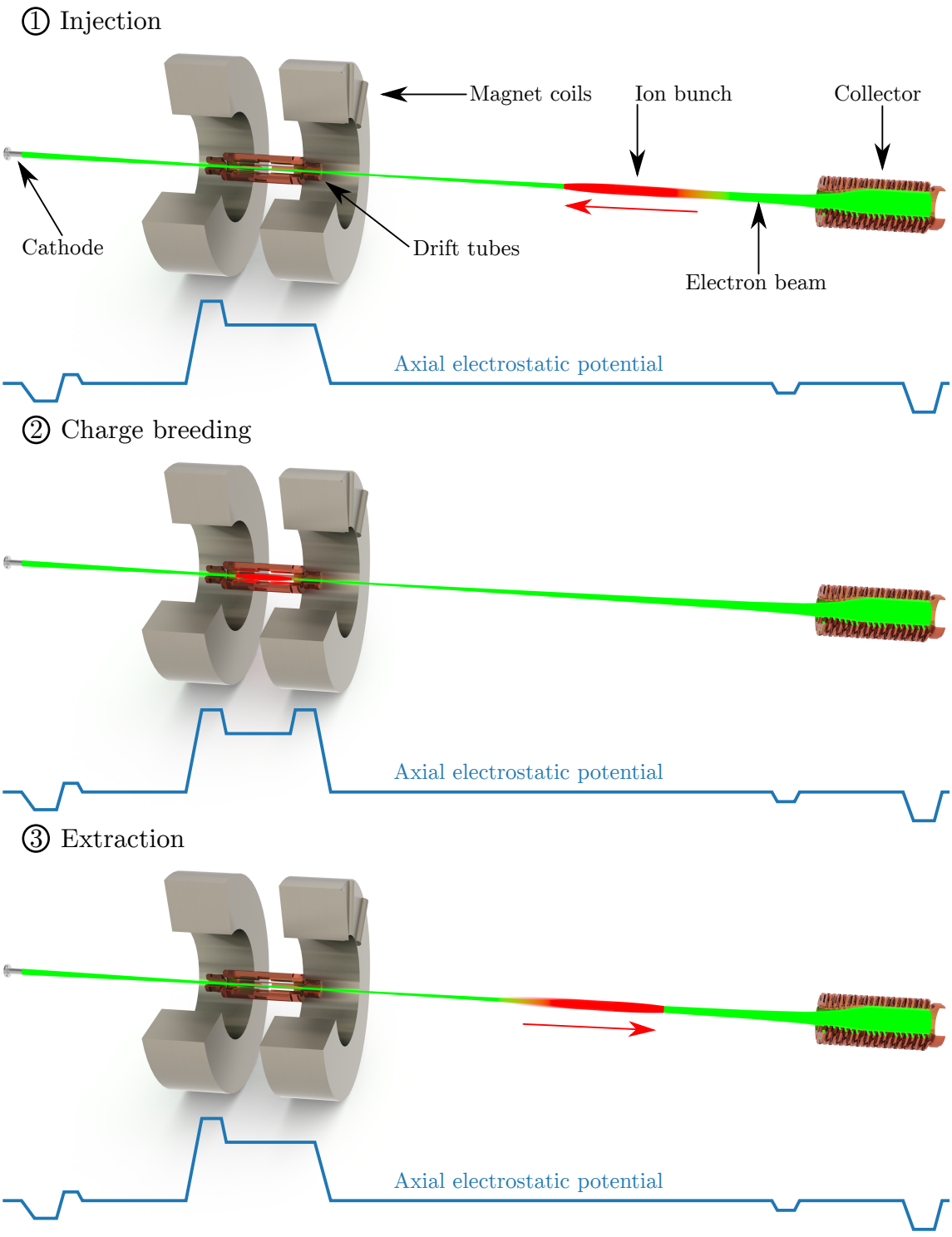

Figure 3.2: Schematic representation of an EBIS and the charge breeding process: superconducting coils produce a magnetic field that is used to compress the electron beam transmitted from the cathode to the collector. In the trap centre there are at least three drift tubes which can be used to form an axial electrostatic potential well. Furthermore the three phases of injection, charge breeding and extraction are shown here.

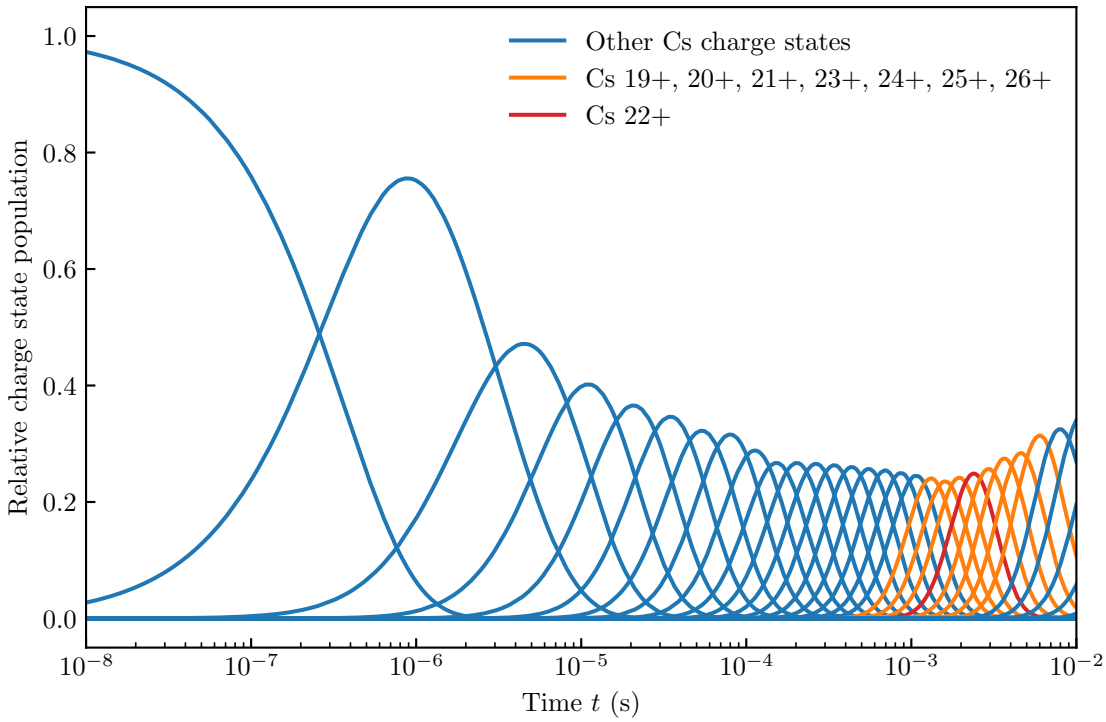

Figure 3.3: Time evolution of caesium ions during charge breeding. Simulation using the Dither code (see Section 2.5.4) and assuming the following parameters: beam energy of 2 keV, beam current of 500 mA, beam radius 100 µm, overlap of 80 % and a background pressure of 5×10^{-10} mbar. For a mass of 133 u the optimal charge state to achieve $^{A}/_{Q} \approx 6$ is 22, which is highlighted in red.

EBIT has a shorter trap length to avoid many instabilities that heat the ions and features a split pair magnet rather than a solenoid due to better optical access to the trap [130]. Typically, EBITs experiments are performed on ions being trapped within the device and EBIS experiments often involve observations of ions extracted from the apparatus. However, both types of measurements have been performed using either design.

Of particular interest are measurements involving electron impact ionisation and excitation, dielectronic recombination (DR), and radiative recombination (RR) usually studied as excitation energies and decay rates. HCIs can not only be investigated using the aforementioned charge breeding techniques of beam-foils and ECRIS but also by crossed-beam experiments and hot plasmas in fusion reactors.

Results from EBIT experiments have proven to be a vital contribution to diagnostics of fusion processes [12, 28, 175], interpretation of astrophysical observations [23, 150, 174], as well as atomic theory in general [9, 13, 79].

3.2 CANREB EBIS

The device built in the scope of this work will be the charge breeder for the ARIEL facility and integral part of CANREB, hence the name CANREB EBIS.

3.2.1 Objectives

Rare isotope beams envisioned at CANREB will arrive at the charge breeder in bunches of up to 10^6 singly or doubly charged ions at a repetition rate of not more than 100 Hz with a bunch length of less than 1 µs. Half-life of radioactive isotopes can be down to few milliseconds. Maximum ion beam energies will be 15 keV. 90 % of them should be trapped and more than 10 % should be in the desired charge state after breeding. The energy of the extracted bunch should be up to 14 keV $\times$ Q with a spread of less than 100 eV. Consequently, high electron beam currents are advantageous. Furthermore, the EBIS should be able to stretch the extracted bunch up to 1 ms. To ensure a low level of background ions in the extracted beam, a pressure in the trap of less than 10^{-12} mbar is required.

3.2.2 Design of an EBIS charge breeder

In addition of fulfilling the objectives lined out above (see 3.2.1), the design was based on EBIT devices previously designed and built at the MPIK in Heidelberg (namely HYPER-EBIT, TITAN EBIT and most recently FLASH-EBIT). EBITs are very similar to EBISes in the sense that they are charge breeding trapped ions. The decisive difference being that in EBITs the ions are investigated inside the trap while EBISes focus on extracting ions once they are charge-bred. The main feature therefore is a line-of-sight to the trap centre to do spectroscopy on the trapped ions. Optical access to the ions will be a valuable tool for non-destructive diagnostics for both the charge breeder and the ion bunches during operation, as will be demonstrated in section 3.3.1 below.

3.2.3 Magnet system

In order to achieve an unobstructed view to the trap centre, CANREB EBIS will be the second charge breeder at a rare-isotope facility with a split-pair superconducting magnet system. The first device utilising such a design was ReA EBIT at NSCL. Helmholtz coils are separated axially by their radius for ideal field homogeneity. Balancing that against spatial constraints and maximum field strength, the distance between the coils was chosen to be 1.23 radii.

Most other charge breeders currently in operation (listed in Section 3.1.1) feature a solenoid magnet system that is lower-cost and tends to have better field homogeneity. Disadvantages include worse pumping cross section and more intricate diagnostics of the charge breeding process.

The magnet system was built by Cryogenic Ltd. according to the specifications listed in Table 3.1 as a cryogen free system using a 2-stage (40 K and 4 K) Gifford-McMahon cryocooler. Seven radial viewports are available on the main magnet chamber. Three of them DN 160 CF and the remaining four DN 100 CF.

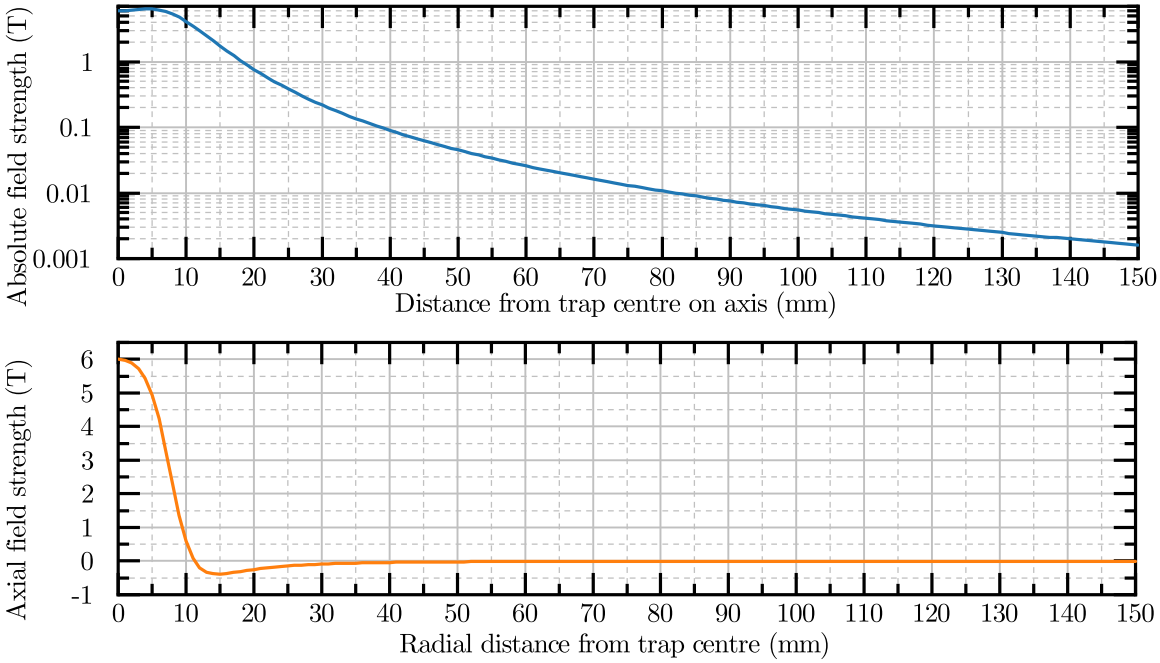

Figure 3.4: Stray magnetic field of the split-pair superconducting magnet as simulated by the manufacturer.

Table 3.1: Specification of the magnet system

Specification	Value
Split radial bores	50 mm
Axial bore	110 mm
Outer diameter	≈ 250 mm
Coil length	≈ 190 mm
Magnetic field	6 T
Homogeneity over central 10 mm[a]	0.3 %
Inductance	10 H
Stored energy	63 kJ
Force between magnet windings	18 t
Operating current	117 A

a This requirement was not fulfilled by the manufacturer. The homogeneity on axis was determined to be 6.0 % (see also Figure 3.4).

3.2.4 Electron gun

For short-lived radioactive isotopes, fast breeding times are of paramount importance. As outlined above in Section 3.1.2, this requires high current densities in the trap centre. Consequently the existing Heidelberg electron gun design was improved towards higher beam currents by choosing a larger diameter cathode (0.25 inch over 0.134 inch).

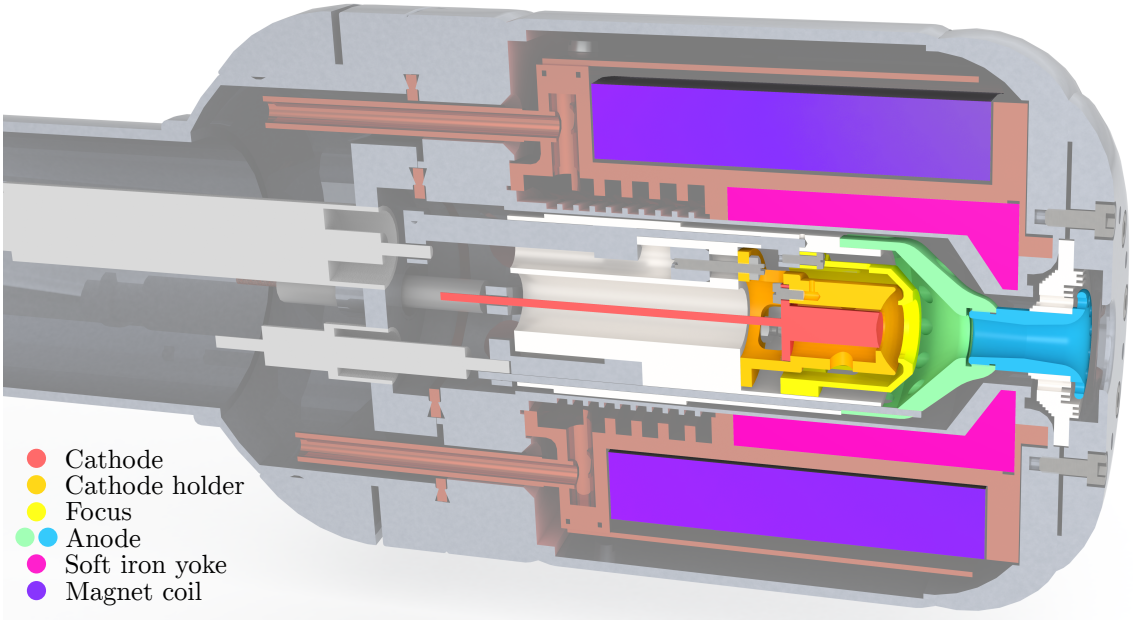

Figure 3.5: Sectional view of the CANREB EBIS electron gun. Electrons emitted from the cathode are accelerated using both the focus and anode electrode. As shown in the Figure, the anode segmented in two parts. The inner part is tapped so that both can be screwed together.

A sectional view of the resulting design is shown in Figure 3.5. As for previous designs, a Pierce geometry [149] and barium dispenser cathode were chosen. The emission surface is a tungsten matrix impregnated with barium-calcium-aluminate (BaO, CaO, Al_2O_3 in the ratio 6:1:2) and coated with a layer of osmium and ruthenium of 4000 Å . . . 6000 Å (this type of emission surface is dubbed type 612M). To achieve an angle of 67.5° between the emission surface and the 'cathode holder' (which acts as the Pierce cathode electrode) the radius of curvature on the emission surface was set to 10 mm. In analogy to the Pierce design, the "focus" electrode is used as the anode (the latter is used as a secondary anode).

Aside from the Pierce geometry, the semi-empirical optical theory of electron beams, as first formulated by Herrmann [102], was taken into account. As opposed to Brillouin flow that assumes a laminar flow for the beam, trajectories of representative electrons are treated as optical rays. The emission surface is thought of as an extended (light) source and transverse velocities are added to the particles by using a Maxwell-Boltzmann distribution, thereby including the temperature of the cathode into the model. A uniform charge density across the electron beam is assumed and optical aberrations are neglected.

Herrmann was able to estimate the minimum radius of an electron beam r_H in an external

magnetic field B from his model:

$$r_{\mathrm{H}} = r_{\mathrm{B}} \times \sqrt{\frac{1}{2} + \sqrt{\frac{1}{4} + \frac{8 m_{\mathrm{e}} k_{\mathrm{B}} T_{\mathrm{C}} r_{\mathrm{C}}^2}{\left(e B r_{\mathrm{B}}^2\right)^2} + \frac{B_{\mathrm{C}}^2 r_{\mathrm{C}}^4}{B^2 r_{\mathrm{B}}^4}}} \tag{3.1}$$

using the electron mass m_{e}, Boltzmann constant k_{B}, elementary charge e and, as parameters of the electron gun, the cathode temperature T_{C}, radius r_{C}, residual magnetic field on the emission surface B_{C}, and finally the Brillouin radius given by

$$r_{\mathrm{B}} = \sqrt{\frac{m_{\mathrm{e}} I}{\pi \varepsilon_0 \dot{z} e B^2}} \tag{3.2}$$

where I is the total beam current, ε_0 the vacuum permittivity, as well as the relativistic velocity along the propagation direction

$$\dot{z} = c_0 \sqrt{1 - \left(\frac{U e}{m_{\mathrm{e}} c_0^2} + 1\right)^{-2}} \tag{3.3}$$

with the speed of light c_0 and the acceleration potential U.

r_{H} can also be used to determine the mean current density $\bar{j} = {}^{I}/_{\pi r_{\mathrm{H}}^2}$. Since the maximum magnetic field B, as well as radius r_{C} and temperature T_{C} of the cathode are already constrained by design, the last important parameter is the residual magnetic field B_{C}. As demonstrated in Figure 3.6, the value should be kept below 1.0 mT to keep the current density in excess of 500 A cm^{-2}.

Consequently, the electron gun also features a water-cooled magnet coil and soft iron core that are used to generate a magnetic field of opposite polarity to the main magnet to cancel out the residual magnetic field on the emission surface. This so-called "bucking" coil was also subject to design improvements over previously made electron guns: a thicker wire of 4 mm by 2 mm (as opposed to 4 mm by 1 mm) coated with two layers of a polyester-THEIC based coating specified for 200 °C (Type W 210 DIN 46 416/DIN EN 60317-13) was used alongside an epoxy glue[1] with better thermal conductivity of 1.3260 W m^{-1} K^{-1}. Both changes are supposed to lower the operating temperature of the coil and thereby improving reliability and operational life of the magnet coil.

3.2.5 Trap setup

Constraints for designing the trapping region are limited material choices due to the cryogenic environment under ultra-high vacuum (UHV). Materials that were used include: oxygen-free high thermal conductivity (OFHC) copper, sapphire, stainless steel, polyether ether ketone (PEEK), aluminium, MACOR and polytetrafluoroethylene (PTFE). Most

1 Commercial name "OMEGABOND OB-200"

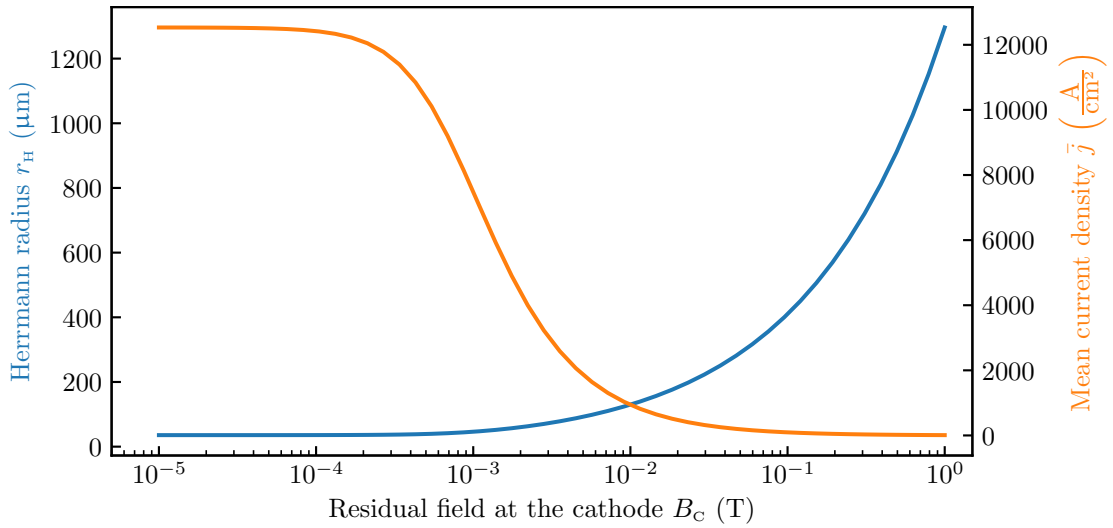

Figure 3.6: Herrmann radius and mean current density against residual magnetic field. T_C was assumed to be 1071.85 °C, for U and I typical values of 2 kV and 500 mA were used.

material choices revolve around the two main properties are electrical and thermal conductivity, a comparison in this respect is shown in Table 3.2. Additionally, a thin layer of commercially available vacuum grease ('Apiezon N') was introduced between interfaces where thermal conductivity is anticipated.

Table 3.2: Comparison of all materials used in the trap setup with respect to their thermal and electrical properties. MACOR is preferred over PTFE where rigidity is required.

	Thermal conductor		Thermal insulator
Electrical conductor	OFHC copper	aluminium	stainless steel
Electrical insulator	sapphire	MACOR, PTFE	PEEK

Compared to other EBIT devices built in Heidelberg, the trap setup did undergo a complete re-design. Most notably two more drift tubes were added for better control of the trap potential and thermal design was improved from serial to parallel cooling of the trap electrodes. Previous traps were an alternating stack of sapphire rings and electrodes, so heat from the central drift tube needed to be transferred through a sapphire to the adjacent drift tube and from there to the next one until the outermost drift tubes are reached where another sapphire and copper sheet is finally used to thermally link the outermost drift tube to the 4-K stage of the cold head.

Parallel cooling in the new design is achieved by sandwiching the drift tubes between two copper shells using three sapphires for each electrode (six for the central one). The heat is now transferred via sapphires to the upper copper shell which is thermally linked to the 4-K stage using another sapphire and OFHC copper band. A sectional view of this

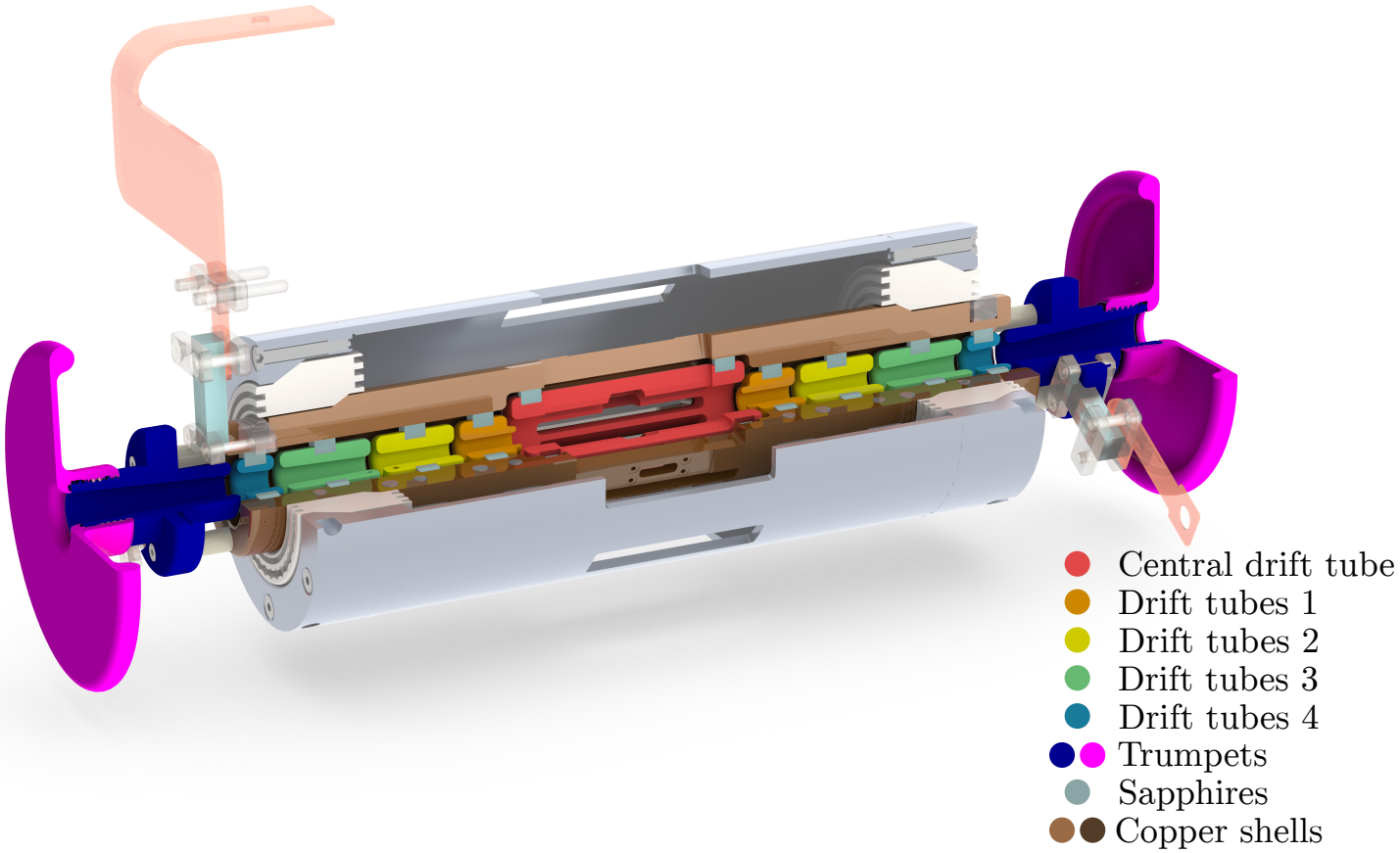

Figure 3.7: Sectional view of the CANREB EBIS trap centre. Drift tubes are symmetric around the central electrode. They are clamped in place by sapphire blocks and two copper shells. The outermost electrodes are called 'trumpets' due to their shape and consist of an inner and outer part. The latter is made from stainless steel for better thermal management. While the inner drift tubes are thermally connected to the 4 K stage of the cryocooler, the trumpets are linked to the 40 K stage. Thermal links via sapphire blocks and copper ribbons are shown transparent.

design is shown in Figure 3.7.

As in previous designs, there are two drift tubes to aid the transition from room-temperature to the 4-K environment. These are called “trumpets” due to their shape and consist of an outer and an inner part. The latter is made from copper and mounted on the outside of the copper shells holding the other trap electrodes and thermally linked to the 40-K stage of the cold head through a sapphire. The outer part is machined from stainless steel for better reflection of incident infrared radiation and is screwed onto the inner section.

Another feature adopted from other EBIT trap setups built in Heidelberg is the spark shield: an aluminium tube surrounding the copper shell and wirings that are mounted inside the magnet former. It prevents any high-voltage discharges to the superconducting magnet. Aluminium was chosen as material due to the more favourable magnetic properties and similar, yet larger linear thermal expansion coefficient compared to copper (Al: $23.1 \times 10^{-6}\,\mathrm{K}^{-1}$, Cu: $16.5 \times 10^{-6}\,\mathrm{K}^{-1}$).

3.2.6 Collector

After passing the trap setup, the electron beam is dumped onto the water-cooled collector electrode shown in figure 3.8. To prevent the electron beam from passing through the collector, an “extractor” electrode is used to create a potential barrier to reflect every remaining electron. To widen the beam, a magnet coil is utilised to cancel out the residual magnetic field from the main magnet. Despite the kinetic energy converted into heat on the collector electrode, secondary electrons can be produced on impact. To mitigate the risk of secondary electrons from leaving the collector in direction of the trap, the collector electrode is tapered towards that end and an additional “suppressor” electrode can be biased accordingly. Finally there are shields on both sides of the collector body called “front shield” and “back shield” to aid guiding the electron beam in and the ion bunches out.

A key improvement over existing designs was the collector coil: The same methods as for the electron gun were employed as described in Section 3.2.4 on page 39.

3.2.7 Ion optics

Located between the collector and trap setup, an additional set of electrodes is introduced for improved control over injection and extraction of the ion bunches. To maximize added control within the spatial constraints a so-called ‘Sikler’ lens [134] design was chosen. It is based on an Einzel lens, however the central electrode is split diagonally twice to add the functionality of a steerer for left-right and top-bottom adjustments of the focal position (see Figure 3.9).

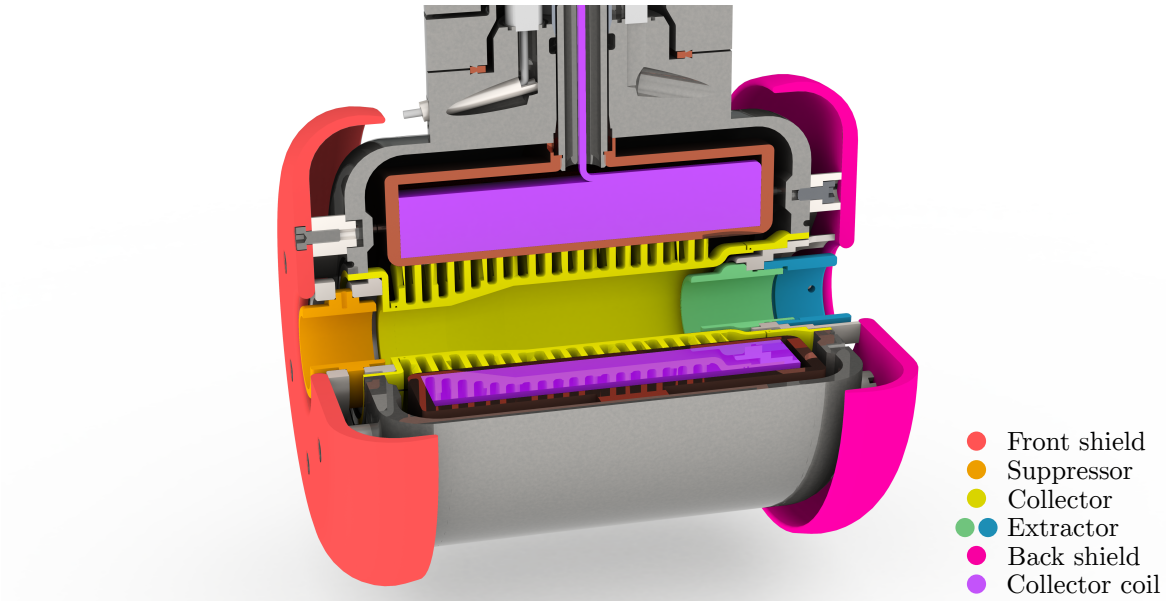

Figure 3.8: Sectional view of the CANREB EBIS collector. Cooling water is introduced through the 'neck' holding the collector in place from the top. It runs around the copper enclosure of the magnet coil, through the cooling ribs on the collector electrode and finally back to the top around the coil body. Front and back shield can be used to fine-tune the potentials to guide the electron or ion beam. Setting the extractor electrode to a respective potential ensures the electron beam cannot pass through the collector. Respectively, the suppressor can be utilised to repel secondary electrons.

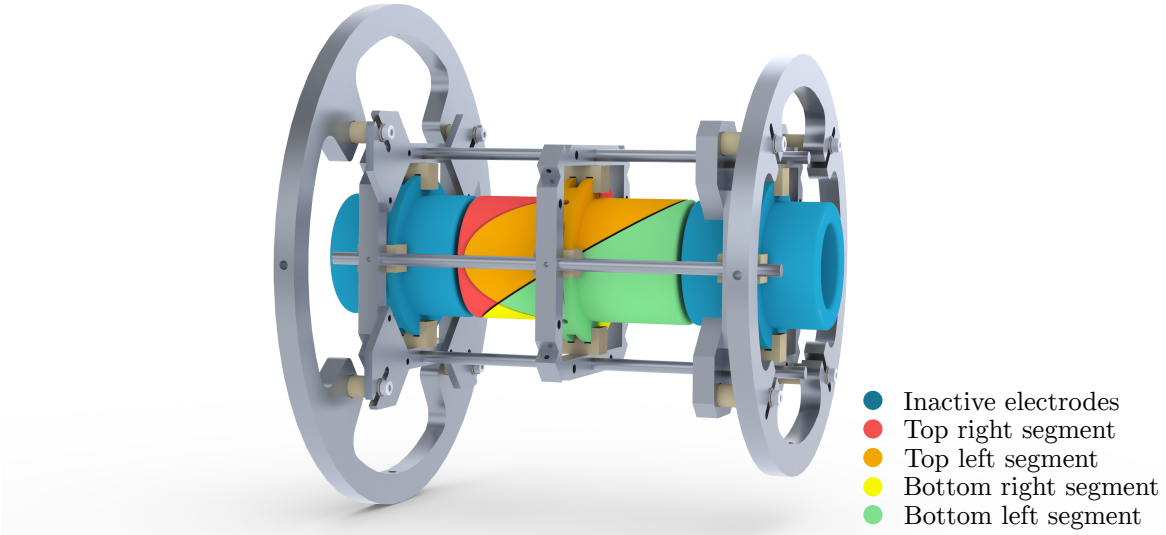

Figure 3.9: Three-dimensional model of the ion optics located in-between the trap (to the left) setup and the collector (to the right). Names of the individual segments designates the steering direction for positively charged particles moving through the lens if a negative potential is applied.

3.2.8 Diagnostics of trapped ions

A wide variety of diagnostic hardware has been used in conjunction with EBIS and EBIT devices. So this Chapter will focus on the hardware used in Section 3.3.1.

Data for charge breeding is mainly divided into two categories: photon and particle detection. The first category reveals information about atomic processes during charge breeding but could also be used to characterize radioactive γ decay of rare isotopes. Having a line-of-sight into the trap is a huge advantage for these techniques. Particle detection can be used to characterize the incoming or outgoing ion bunches as well as the electron beam. For the most part, this is a destructive measurement meaning that the bunch or beam is interrupted a the detector. A notable exception being the pickup ring discussed below. However, this information is required not only in the design and commissioning phase, but it is also indispensable for tuning the accelerator parameters during on-line operation.

High purity germanium detector (HPGe detector)

All photon measurements in this Chapter are performed using HPGe detectors that record time and energy for individual photons of approximately 2 keV to 800 keV (the exact range depends on the detector and beryllium window thickness). They are manufactured as semiconductor diodes using germanium as bulk material. Due to the low band gap of germanium, the detector is cooled in operation (typically using liquid nitrogen). Usually a p-i-n junction is used as diode, where i denotes an intrinsic layer. A schematic diagram of a PIN photodiode is shown in Figure 3.10. This additional structure has the two-fold advantage that a larger depletion zone is formed when a reverse bias is applied and that the breakdown voltage is higher which in turn further increases the size of the depletion zone. Whenever a photon with a kinetic energy larger than the band gap is absorbed in the depletion zone, first a single pair of charge carriers is formed. Since the kinetic energy of these is three orders of magnitude higher than the band gap, these can produce a cascade of secondary pairs of charge carriers causing a small current pulse. Using an integral charge sensitive preamplifier, which is also operating at cryogenic temperatures, this can be converted into a so-called tail pulse with an amplitude proportional to the energy of the incoming photon. Using a pulse shaping amplifier this signal is converted to a Gaussian pulse shape and the signal-to-noise ratio (SNR) is also further improved in this second amplification step. Finally these Gaussian pulses are digitized by a data acquisition system utilising a pulse-height analyser.

Faraday cup

A Faraday cup is a very basic detector for particles. At its heart, a metal hollow-body charges up when a beam of electrons or ions is impinged on its wall. By measuring the electric current during the discharge of the metal part, characteristics of the beam can be deducted (i. e. number of ions per time or bunch, temporal structure of the bunch and time-of-flight). When the Faraday cup can be moved mechanically, even some information about the spatial beam structure can be recovered.

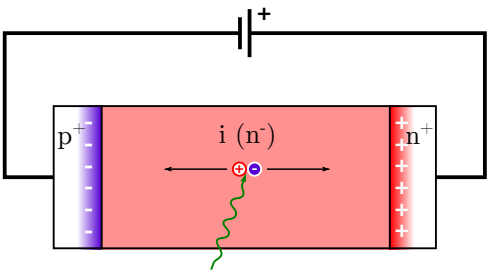

Figure 3.10: Schematic diagram of a reversed biased PIN photodiode biased. An x-ray photon (green sine wave) is absorbed in the depletion zone of the diode creating a pair of charge carriers that are accelerated towards the p or n doped region respectively. Due to the high kinetic energy these charge carriers cause a cascade of secondary charge carriers being transferred from a valence to a conduction band (not shown).

Pickup ring

A hollow metal cylinder creates a field-free region in vacuum. In turn this causes mirror charges in the cylinder whenever charged particles move through it. This principle can be exploited for a non-destructive particle detection. Similar to a Faraday cup, the pickup ring is encased by a grounded electrode. So when a bunch passes through the ring, the induced mirror currents can be recorded. A downside in comparison to a Faraday cup is that it can only detect bunched beams of charged particles and a calibration is required to deduce the absolute beam current.

A schematic section for a Faraday cup and pickup ring are given in Figure 3.11.

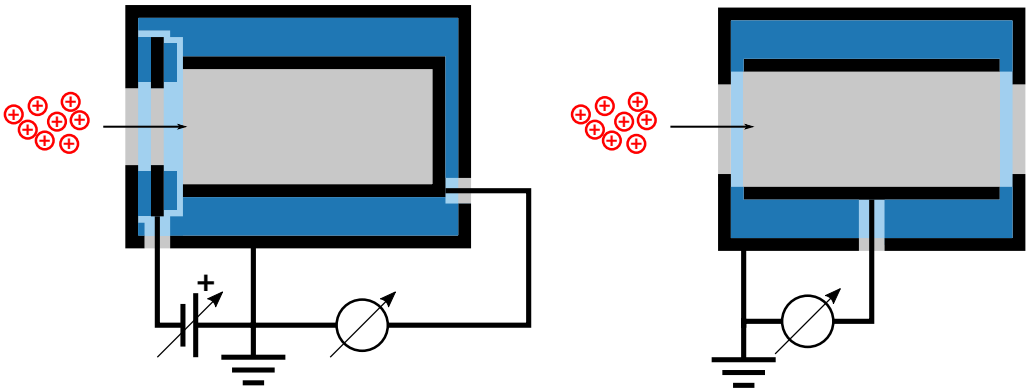

(a) Faraday cup **(b)** Pickup ring

Figure 3.11: Schematic cross section of a Faraday cup and pickup ring. Electrically conducting material is shown in black, isolators are indicated in blue. Usually Faraday cups feature a ring shaped suppressor electrode around the open end to prevent secondary electrons from leaving the cup and a grounded case around the whole assembly to have a well-defined capacity for an accurate current measurement. A pickup ring consists of a cylindrical electrode surrounded by grounded case. When the ion bunch moves through, a mirror current can be detected.

3.3 Performance

During commissioning, electron beams of up to 1 A were demonstrated [29], making CANREB EBIS one of the most powerful EBIS charge breeders in the world. However, in this test the current was not limited by design or operating parameters of the machine but by the cathode power supply, so the maximum beam current could readily be surpassed by upgrading commercially available components outside the vacuum. But even without further upgrades the intended breeding times as outlined in Section 3.2.1 are well within reach using the current densities demonstrated here.

3.3.1 Electron-beam studies

One of the first measurements to characterise the performance of the electron gun was a perveance determination the measurement is also discussed in [188]. In charged particle beams, this measure characterises how space-charge dominated beam propagation is. While the potential on the focus and anode electrode was kept at 0 V, voltage on the cathode was increased while the beam current was measured. It was assumed the emission is characterised by the emission law

$$I_\mathrm{b} = A \times (U_\mathrm{cath} - U_0)^P \,. \tag{3.4}$$

Using A, U_0 and P as free parameters this function was fitted to the experimental data yielded a perveance A of $(4.11 \pm 0.04) \times 10^{-6}\,\mathrm{A/V}^P$ or 4.1 µPerv, $U_0 = (15 \pm 1)$ V and $P = 1.491 \pm 0.001$. Both these results and the data are shown in Figure 3.12.

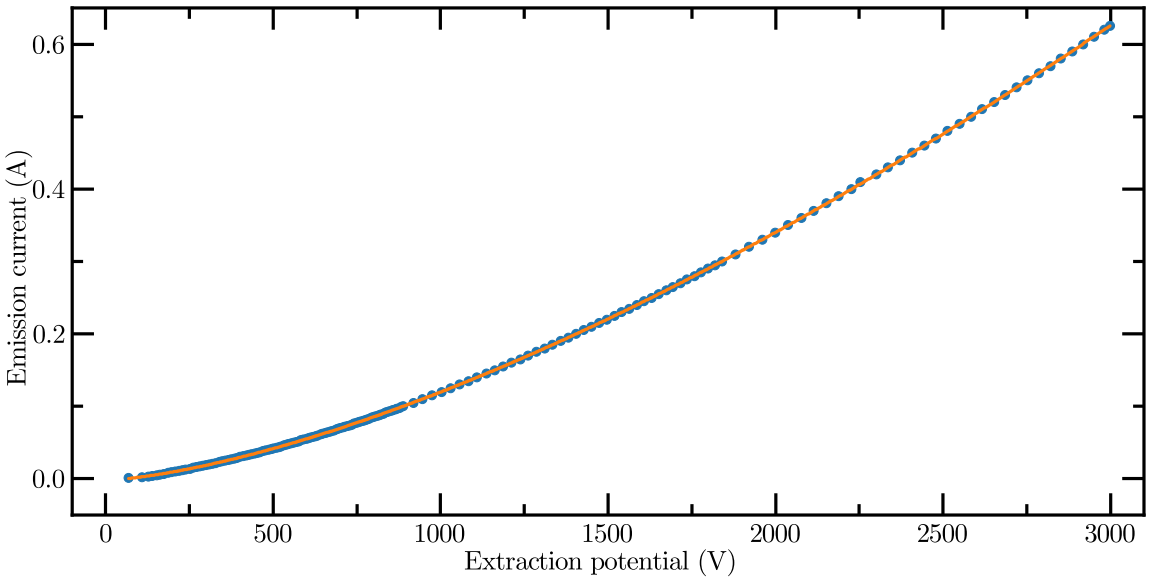

Figure 3.12: Perveance measurement to characterise the electron gun. Focus and anode potential was kept at 0 V while the cathode voltage was varied. Points represent data, the solid line is a result of the power-law (see Formula 3.4) fit yielding 4.1 µPerv.

Space-charge potential

An important, yet elusive characteristic of the electron beam is its space-charge potential. Direct measurement requires a dedicated device in the cryogenic environment of the trap that potentially also affects the beam. So the preferred way to measure space-charge potentials is an indirect one: to observe spectra of ions inside the trap. However, this method bears the challenge to separate the space-charge potential of the electron beam from the so-called space-charge compensation which is caused by the positively charged ion cloud. As a consequence of varying the beam current, the space-charge potential and compensation changes. A first characterisation of this effect was also investigated in [188] by trapping barium and tungsten ions emitted from the heated cathode. Subsequently, they are ionised by electron impact ionisation and capture of free electrons can be observed as photons emitted form radiative recombination using a HPGe detector. When varying the electron beam current, space-charge is affected and the observed photon energy is changing. This effect is presented in Figure 3.13.

For a more accurate determination of space charge, dielectronic recombination (DR) (see Section 2.5.3) can be used. In these measurements, electron beam energy is varied while an x-ray spectrum is recorded. Whenever the kinetic energy of the electrons (including space-charge contributions) matches the resonance energy, count rate increases drastically. So the need for a precise photon energy measurement is waived. Since the resonance energies are well-known from theory, recording both the count rate and acceleration potential is sufficient: by comparison of data with a synthetic spectrum, a total value for the space-charge potential can be derived (see Figure 3.14).

Furthermore, a temporal evolution of the DR resonances can be used to separate contributions from the electron beam and ions. At the arbitrary time $t_0 = 0$, all ions are dumped from the trap by inverting the axial potential well. Utilising a continuous injection of neutral ions such as argon, ions accumulate in the trap over time, slowly shifting the beam energies at which the resonance maxima occur towards lower values until an equilibrium for capture and loss of ions is reached. Immediately after t_0 there are no ions in the trap, so the only space-charge contribution is from the electron beam. However, the photon count rate on the resonance is also zero but the value can be reconstructed by extrapolating the temporal evolution of the excitation energies to t_0. A convenient way to represent data from such a measurement is shown in Figure 3.15.

For $I_\mathrm{b} = 64\,\mathrm{mA}$ the measurement suggests a space-charge compensation of $\approx 160\,\mathrm{eV}$ caused by the HCI. As already determined above, the total space-charge potential including contributions of the electron beam and HCIs is 47 eV. This yields $\approx 207\,\mathrm{eV}$ of space-charge caused by the electron beam only.

Electron beam radius determination

For an infinitely long, cylindrical electron beam with uniform charge density ρ_e, the electrostatic potential Φ is given by Poisson's equation

$$\vec{\nabla}^2 \Phi = -\frac{\rho_\mathrm{e}}{\varepsilon_0} \tag{3.5}$$

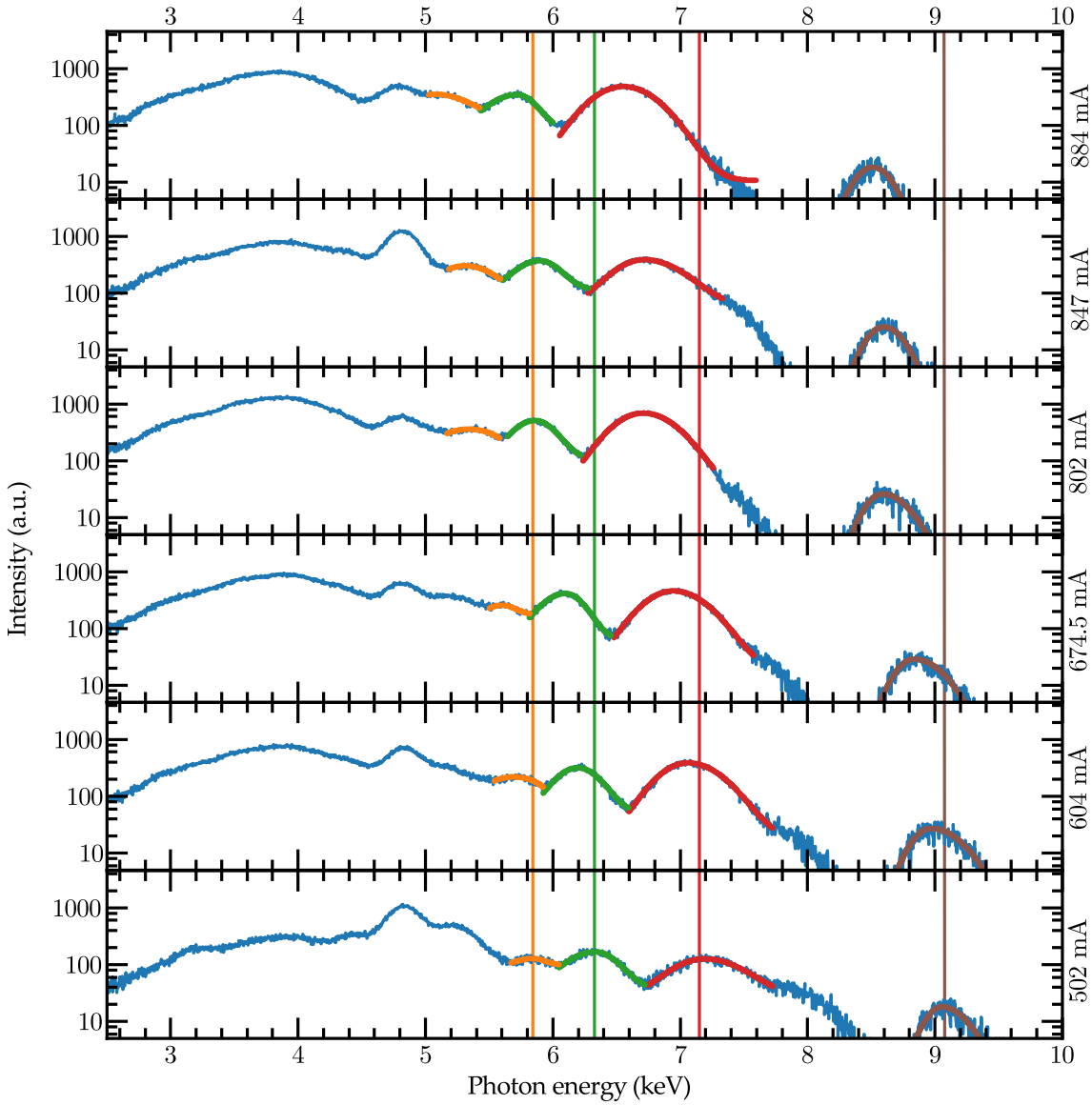

Figure 3.13: X-ray spectra of radiative recombination (RR) (see Section 2.5.2) in barium and tungsten ions for varying electron beam current. Due to space-charge effects, the kinetic energy of the electrons depends on the beam current. Since the energy of photons emitted due to recombination is equal to the kinetic energy of the electrons and the (fixed) ionisation potential of the level, the same emission peak appears at another photon energy for a different beam current. For comparison, coloured lines indicate the maxima positions of the respective peak in the spectrum recorded at 520 mA. All of the coloured peaks can be identified as RR into the $n = 3$, 4, 5, and 6 (brown, red, green and orange respectively) shell of tungsten.

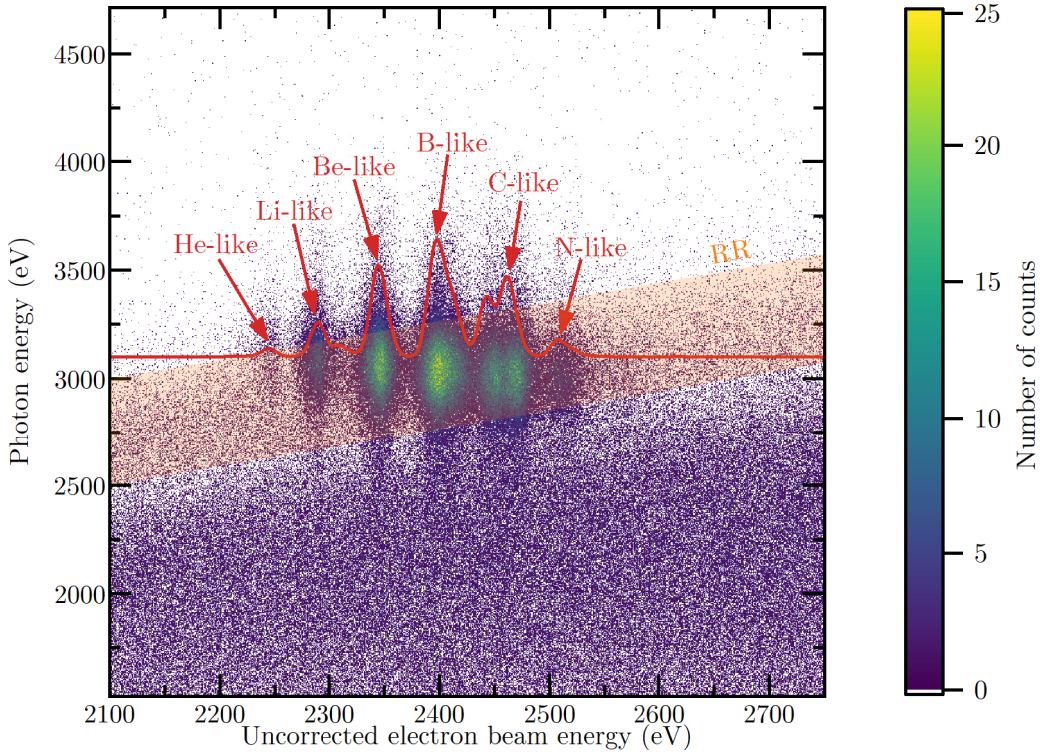

Figure 3.14: KLL dr spectrum of argon: A HPGe detector detector was used for the data acquisition. Individual photons and their respective energy were measured in coincidence with the acceleration potential applied (the potential was varied from 2100 V to 2750 V). A two-dimensional histogram was constructed using this data. A slanted band of events is caused by RR (highlighted by an orange trapezoid). A synthetic DR spectrum is shown as a solid red line. Arrows indicate where certain ion species contribute most to the respective resonance peak. The synthetic spectrum was shifted by 47 eV towards lower energies to match the experimental data. Concurrently this value corresponds to the absolute space-charge potential derived from this measurement for a beam current of $I_\mathrm{b} = 64\,\mathrm{mA}$. The data presented here has previously been published in [29].

where ε_0 corresponds to the permittivity of vacuum. Using cylindrical symmetry, this equation can be simplified to

$$\frac{1}{r}\frac{\partial}{\partial r}\left(r\frac{\partial}{\partial r}\Phi\right) = -\frac{\rho_\mathrm{e}}{\varepsilon_0} \tag{3.6}$$

that can be solved for the radius coordinate r being smaller or larger than the electron beam r_e:

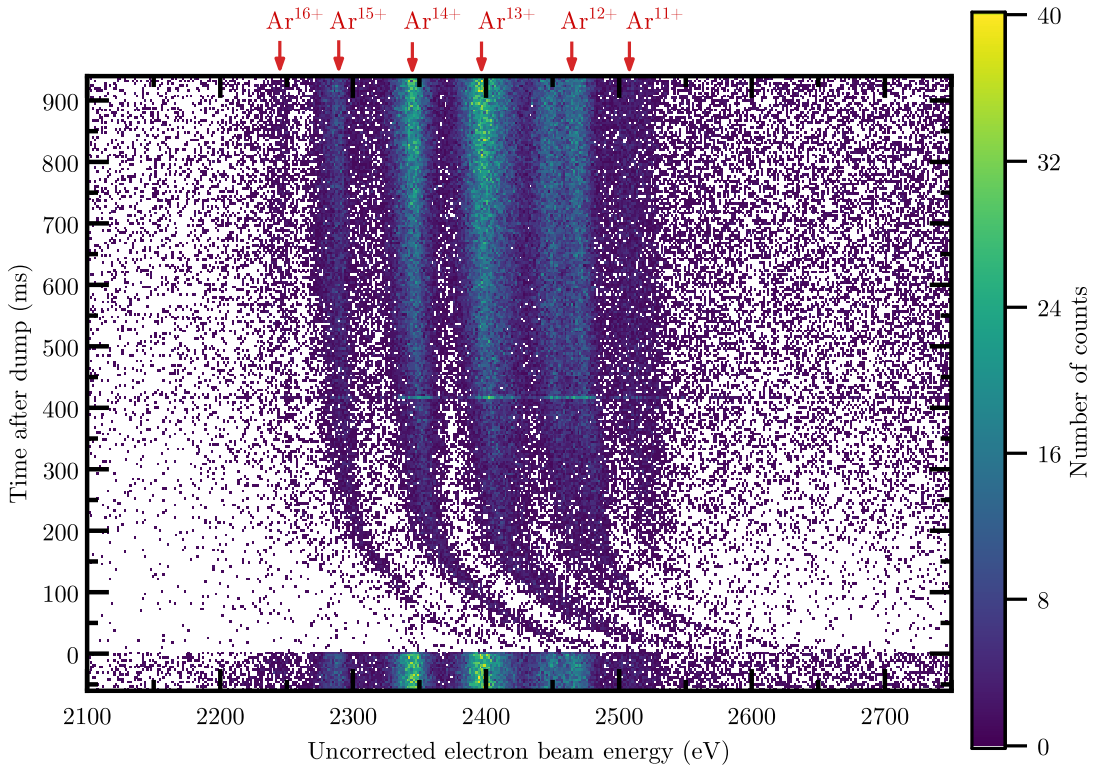

Figure 3.15: Temporal evolution of an argon dr spectrum over time. To cover all of the histogram, the trap is dumped periodically while the electron beam energy is continuously changed. Events are only accepted for the histogram if the photon energy is around 3.1 keV (Kα of argon). The data presented here has previously been published in [29].

$$\Phi(r) = \begin{cases} \Phi_\mathrm{D} + \Phi_0 \left(\frac{r^2}{r_\mathrm{e}^2} + \ln \frac{r_\mathrm{e}^2}{r_\mathrm{D}^2} - 1 \right), & r \leq r_\mathrm{e} \\ \Phi_\mathrm{D} + \Phi_0 \ln \frac{r^2}{r_\mathrm{D}^2}, & r \geq r_\mathrm{e} \end{cases} \tag{3.7}$$

Where the inner radius of the central drift tube $r_\mathrm{D} = 7\,\mathrm{mm}$, the electrostatic potentials $\Phi_\mathrm{D} = \Phi(r_\mathrm{D})$ and $\Phi_0 = \Phi(r_0)$ were introduced. Φ_0 only depends on the linear charge density along the electron beam:

$$\Phi_0 = \frac{1}{4\pi\varepsilon_0} \times \frac{I_\mathrm{b}}{\dot{z}} \tag{3.8}$$

MCDF calculations yield a DR resonance energy of $E_\mathrm{res} = 2303\,\mathrm{eV}$ for Ar^{14+} which can be used to estimate the relativistic velocities of the electrons using Eq. 3.3 yielding $\dot{z} = 2.84 \times 10^7\,\mathrm{m/s}$ and therefore $\Phi_0 = 20\,\mathrm{V}$.

Figure 3.15 indicates an acceleration potential of $E_\mathrm{D} \approx 2500\,\mathrm{eV}$ immediately after

dumping the trap contents for the same Ar^{14+} DR resonance. Plugging these values into Eq. 3.7 for $r = 0$ and solving for r_e:

$$2303\,\mathrm{V} = \Phi(0\,\mathrm{m}) = \Phi_D + \Phi_0 \left(\ln \frac{r_e^2}{r_D^2} - 1 \right) \tag{3.9}$$

$$r_e = r_D \sqrt{e^{\frac{2303\,\mathrm{V} - \Phi_D}{\Phi_0} + 1}} \tag{3.10}$$

$$r_e \approx 7\,\mathrm{mm} \sqrt{e^{\frac{-200\,\mathrm{V}}{20\,\mathrm{V}} + 1}} \tag{3.11}$$

$$r_e \approx 75\,\mu\mathrm{m} \tag{3.12}$$

Using Herrmann theory (see Eq. 3.1 in Section 3.2.4), this experimental value and additional parameters given by the setup ($T_C = 1350\,\mathrm{K}$, $r_C = 3.175\,\mathrm{mm}$ and $B = 6\,\mathrm{T}$) can be used to estimate the residual magnetic field on the cathode $B_C = 3.3\,\mathrm{mT}$. The aforementioned radius of 75 µm at 64 mA yields a current density of $360\,\mathrm{A/cm^2}$. Extrapolating this to beam currents of 1 A results in a current density of $5500\,\mathrm{A/cm^2}$.

Trap capacity

From these measurements, a value for the total trap capacity, as well as the ion production rate can be determined. Please note that the trap capacity depends on the trapping potential so the value derived here is depending on operating parameters of the EBIS. First, the number of electrons inside the trap at any given time is derived to be $1 \times 10^9\,e$ (in addition to $\dot{z}$ and I_b from the previous Section, the trap length of 78 mm is used). As previously mentioned, the maximum space-charge compensation by the ions was found to be 76.5 % corresponding to a total trap capacity of approximately 56×10^6 Ar ions (assuming an average charge of $13.5\,e$ per ion), which is well within the objectives outlined in Section 3.2.1 even for $I_b = 64\,\mathrm{mA}$.

Instead of using the space-charge compensation in equilibrium, the slope can be used to investigate the trap filling rate. Please note that these measurements were performed using the neutral gas injection instead of injecting positively charged ions through the collector. In principle neutral atoms are harder to capture since they are not attracted to the electron beam and overlap is a more important factor for neutral beams. Therefore additional studies were performed using different injection pressures, which are shown in Figure 3.16. Due to an electron beam current of 125 mA, the resonances appear at a slightly different beam energy as in Figure 3.15.

From this graph, a total trap capacity of $2.14 \times 10^9\,e$ can be deduced for this specific set of operating parameters and the slopes correspond to ion build-up rates of $3.97 \times 10^5\,Ar^{12+}/\mathrm{ms}$, $1.05 \times 10^6\,Ar^{12+}/\mathrm{ms}$, and $1.87 \times 10^6\,Ar^{12+}/\mathrm{ms}$ respectively. Indicating a higher injection pressure leads to the trap filling up faster albeit the charge distribution favouring lower charge states.

3.3.2 Injection and extraction studies

All above measurements were performed using offline injection of neutral atoms, additional tests of injection and extraction were performed with charged ions. An important aspect

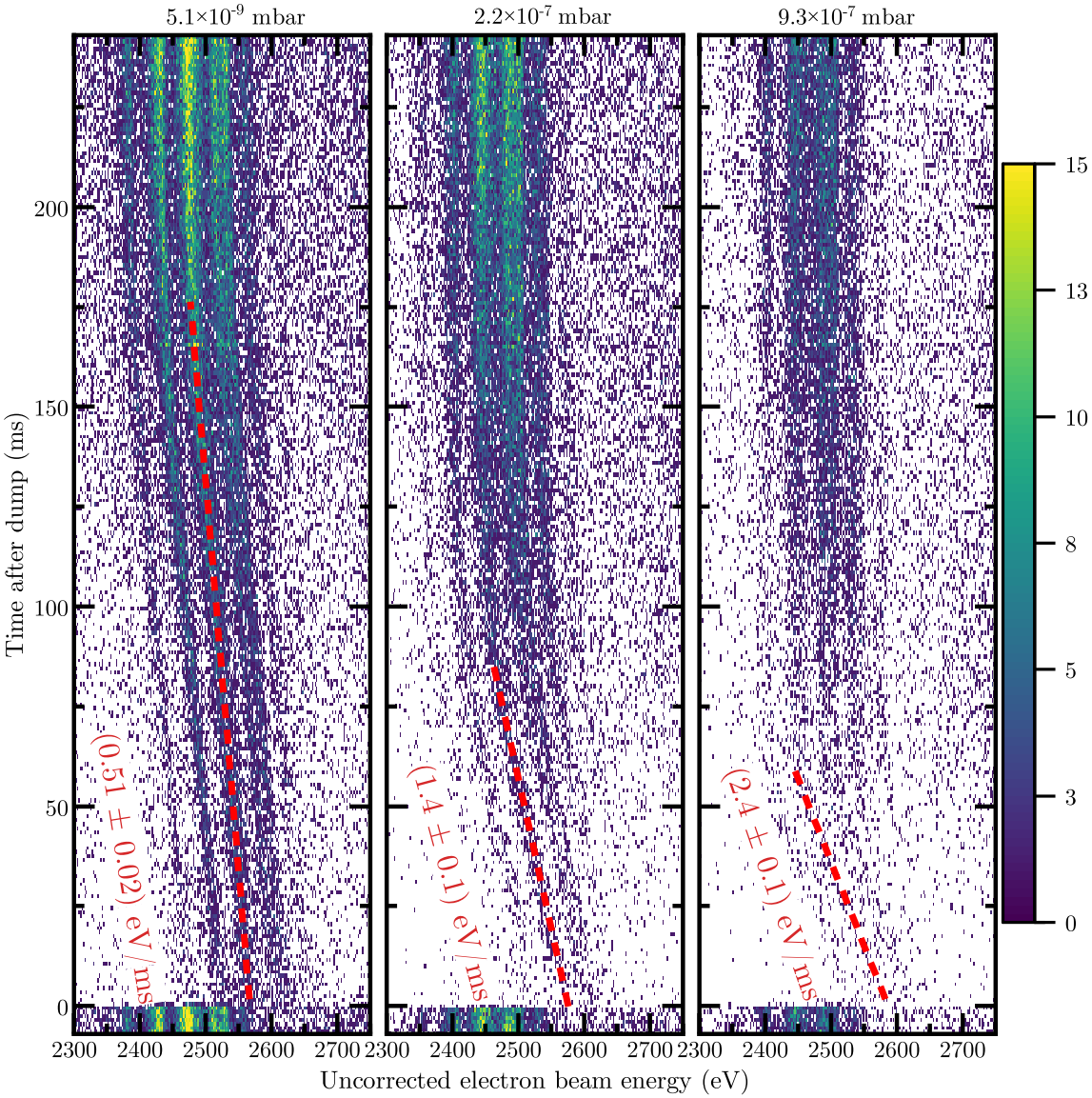

Figure 3.16: Temporal evolution of argon DR spectra over time for injection pressures of 5.1×10^{-9} mbar, 2.2×10^{-7} mbar and 9.3×10^{-7} mbar respectively. Red dashed lines indicates the temporal change of the resonance energy for Ar^{13+}. Slopes are denoted next to the lines. The data presented here has previously been published in [29].

of the commissioning phase in Heidelberg were injection and extraction tests since this will be the normal mode of operation as part of the ARIEL facility. Both processes require switching drift tube potentials quickly which was implemented by using two high voltage power supplies connected to a push-pull switch manufactured by Behlke with a rise time of $\approx 20\,\mathrm{ns}$.

Injection

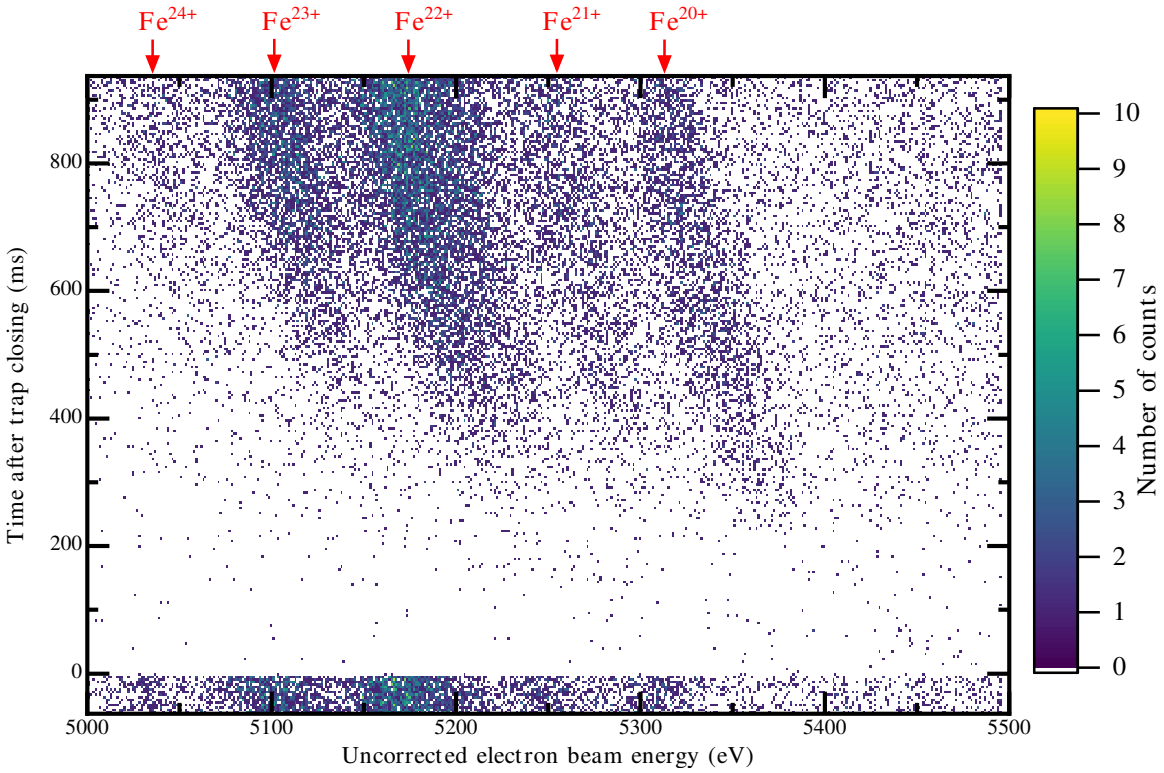

Figure 3.17: Temporal evolution of dielectronic recombination in iron injected from the laser ion source. Parameters for the measurement are $B = 6\,\mathrm{T}$, $I_b = 200\,\mathrm{mA}$ at $U = 5000\,\mathrm{eV}$ to $5500\,\mathrm{eV}$. After dumping the trap content and triggering the laser pulse of the external laser ion source at $t = 0\,\mathrm{ms}$, a build-up of KLL resonances for helium- to carbon-like iron was observed. Due to the trap filling up over time, these shift towards lower energies. The data presented here has previously been published in [29].

Injection of singly charged ions was performed using an external laser ion source. Pulses at 532 nm with durations of 9 ns, and energies of 15 mJ were focused onto a metal disk (in this case iron) generating a plasma plume. 3.75 µs after the laser pulse, these ions were accelerated by means of a voltage pulse of 3 kV applied to two grids at a distance of 10 mm. To capture the ions in the trap, the collector-side drift tube potential was lowered temporarily. Time delay between triggering the laser pulse and switching the drift tubes was found to be ideal around 18 µs, roughly corresponding to the time-of-flight (TOF) for the distance of 1.4 m from the laser ion source to the trap centre.

Verification of successful injection is provided by recording DR spectra using the same

semi-conducting detector used in the previous section. In Figure 3.17, the temporal evolution of the injection and charge-breeding process is shown. Saturation due to space-charge compensation is reached much later compared to the argon measurements above. Bunches emitted from the laser ion source can be steered and focused by the ion optics between collector and trap described in Section 3.2.7. However, there was an electrical fault during the measurement, so all elements were of the optics were grounded and overlap between the incoming ion beam and electron beam is insufficient for optimal trapping. Nonetheless, this data indicates that the device is capable of trapping and charge-breeding ions even under unfavourable conditions.

Extraction

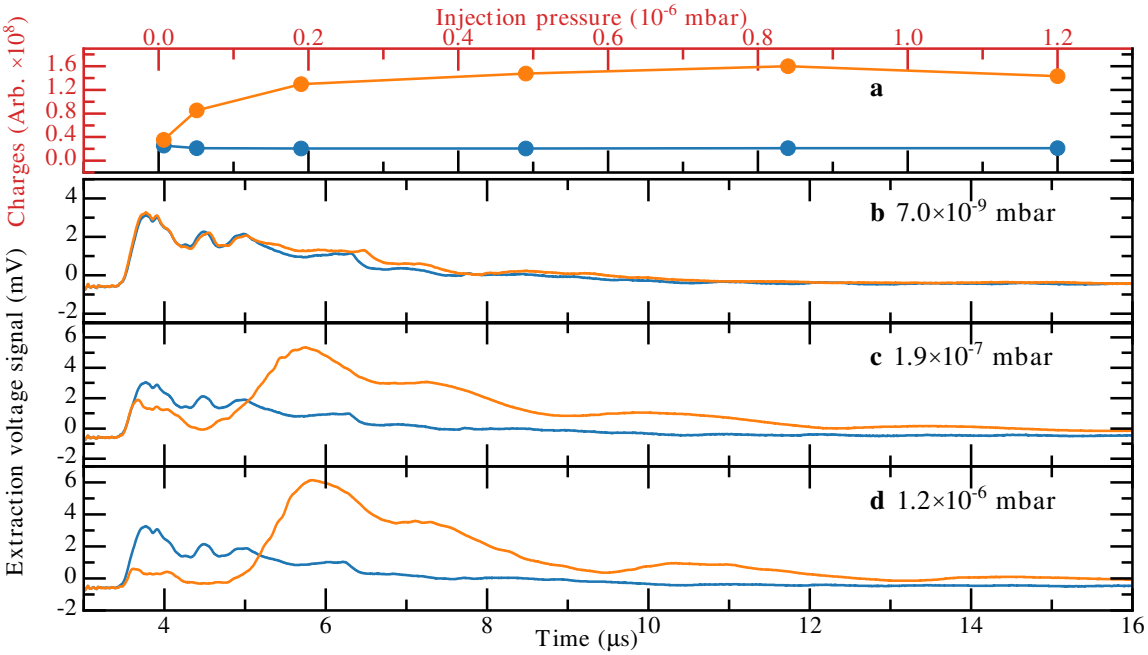

Figure 3.18: Extraction currents of argon ions for different injection pressures. **a** shows the number of ions extracted ions in the TOF region 5 µs to 8 µs for each pressure measured (including those shown in spectra **b** – **d**). Data shown in orange was recorded with the neutral gas injection on, while blue data points were recorded without. Pressure values refer to the second stage of the injection system. The data presented here has previously been published in [29].

Extraction was characterised using both a Faraday cup and a pickup ring (see Section 3.2.8) at around 600 mm from the trap centre. To determine the yield, a digital storage oscilloscope recorded traces of ion current per time. The voltage drop across a 500 Ω resistor connected to the Faraday cup was recorded as scans over the following parameters: neutral gas injection pressure, energy of the electron beam, and trap depth.

Parameters for EBIS operation were similar to the injection measurements above: $B = 6\,\mathrm{T}$, $I_b = 200\,\mathrm{mA}$ at $U = 5000\,\mathrm{eV}$. Argon HCIs were bred in the EBIS and regularly extracted either by lowering the potential barrier or by increasing the trap potential to a

value higher than the barrier on the collector side.

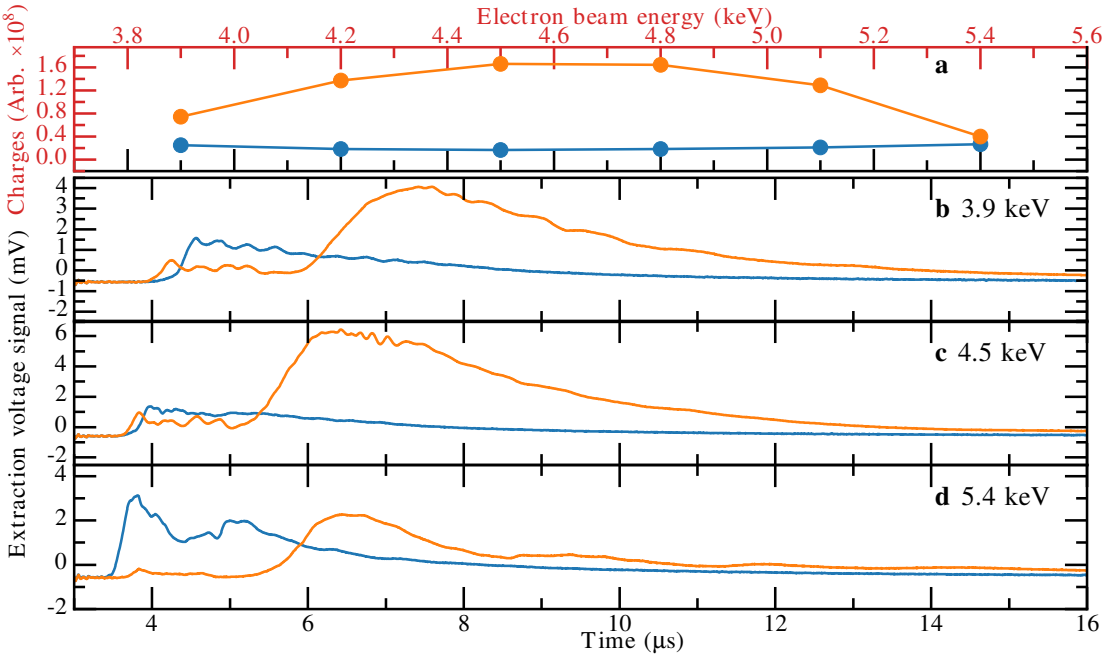

Figure 3.19: Extraction of ar ions for different beam energies. **a** shows the number of ions extracted ions in the TOF region 5.2 µs to 10 µs for each pressure measured (including those shown in spectra **b** – **d**). Data shown in orange was recorded with the neutral gas injection on, while blue data points correspond to a closed injection.

Extracted ions in dependence of the neutral gas injection pressure is shown in Figure 3.18. Panels **b** and **c** show a broad peak at approximately 6 µs. Integrating the current over a 4 µs time interval around the highest peak yields $\approx 10^8$ ions per bunch (assuming a charge-state distribution of $Ar^{10+} \ldots Ar^{16+}$).

A scan over the beam energy (Figure 3.19) reveals that there is a maximum ion yield around 4.5 keV to 4.8 keV. Comparing the individual traces shown in panels **b** – **d**, one can see that ions around the optimum beam energy arrive approximately 1.5 µs earlier than for the lowest energies considered in this measurement indicating that the ions are breed into higher charge-states.

Studying the dependency of the ion yield on the trap depth in volt is shown in Figure 3.20. Deeper traps favour heavier ions and therefore have a higher yield. However, the TOF resolution of the individual charge-states degrades, so that they become almost indistinguishable in panel **d**.

3.3.3 Outlook

Comparing data shown in this Chapter with the requirements for CANREB EBIS presented in Section 3.2.1, there are no indications for a major problem in operation: a trap capacity of 10^9 elementary charges is sufficient to trap the required 90 % out of a bunch of 10^6 ions of charge 1+ or 2+. Current densities of up to 5000 A/cm^2 were demonstrated which is sufficient for breeding 10 % of a rare-isotope bunch to a mass-to-charge ration of

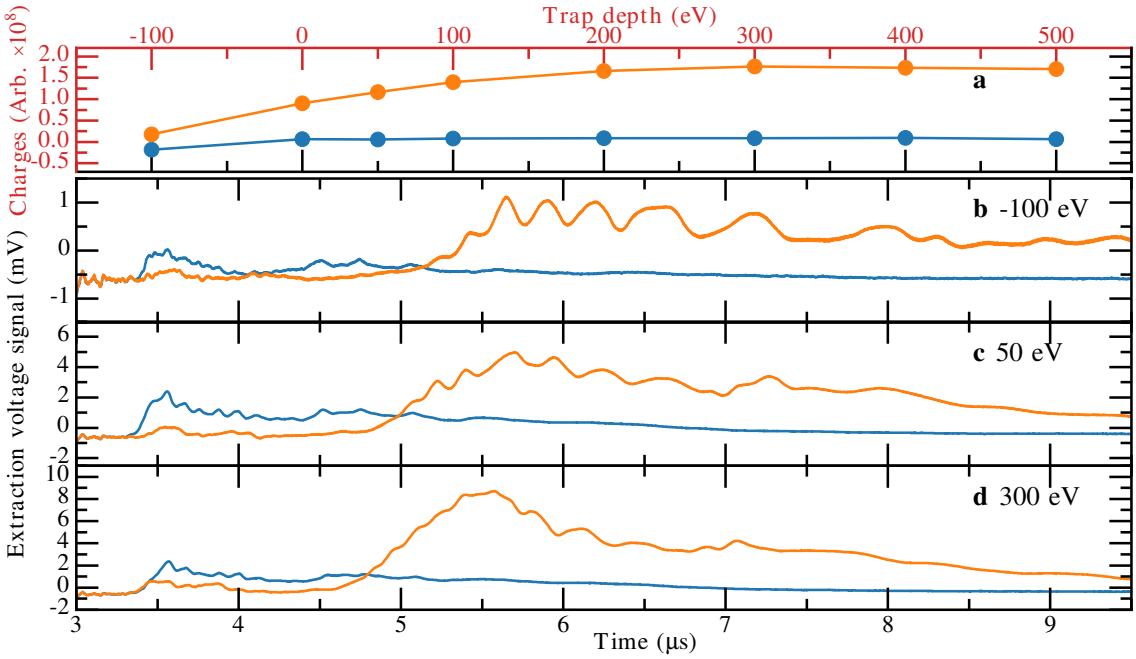

Figure 3.20: Extraction of ar ions for different trap depths. **a** shows the number of ions extracted ions in the TOF region 5 µs to 8 µs for each pressure measured (including those shown in spectra **b** – **d**). Data shown in orange was recorded with the neutral gas injection on, while blue data points correspond to a closed injection. The data presented here has previously been published in [29].

approximately 7 in a few milliseconds.

Upgrade to high-voltage operation at up to 15 keV – to match the incoming ion beam energies – is still an ongoing upgrade at TRIUMF. Due to the strict safety regulations it was agreed that this is done on-site after shipping to Vancouver. A full optimisation of the parameters will only be possible after final installation at the beam line. However, it will be an ongoing process of iterative improvements throughout the operation of the device.

Especially the beam current demonstrated to be 1 A DC is a very promising specification. Furthermore, visible access of the trap centre is a rare, yet particularly interesting feature for a charge breeder due to the potential for on-line optimisation using non-destructive measurements of photons emitted from the trap centre.

CHAPTER 4

Spectroscopy

The measurements the following two Chapters was recorded at the MPIK in Heidelberg using FLASH-EBIT quipped with two spectrometers. There are many similarities to the CANREB EBIS design described in Chapter 3. More details on the EBIT can be found in Chapter 3 of [81] while the following two Sections focus on the spectrometers attached to it.

Strictly speaking, the term VUV is defined as 10 nm to 200 nm and EUV as 10 nm to 121 nm. Spectroscopy performed in this work falls in the overlap region while using two different instruments. One is a more compact setup sensitive to photons from 5 nm to 40 nm that is called 'EUV spectrometer' in this work (as opposed to the name used in the original work on the instrument [3, 4]). The other one has an arm length of 3 m and is most sensitive from 40 nm to 140 nm. To emphasise the slightly different ranges both spectrometers operate in, the latter device is dubbed 'VUV spectrometer'.

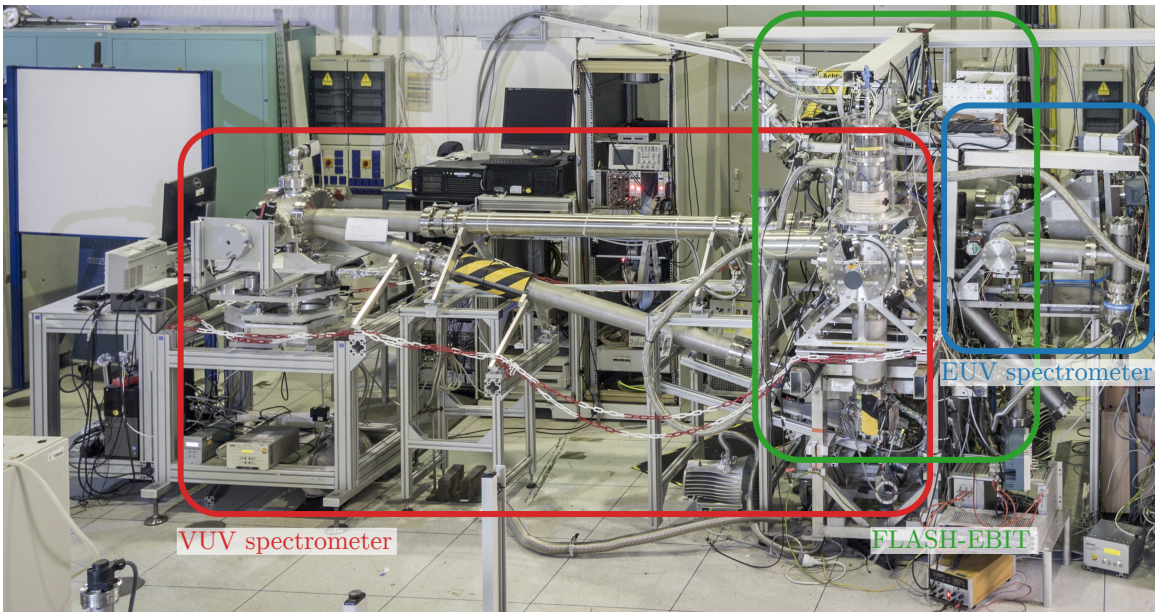

Figure 4.1: Side view of the EUV and VUV spectrometer attached to FLASH-EBIT. The latter is shown in front view from the collector side, so the electron beam is perpendicularly emerging from the drawing plane.

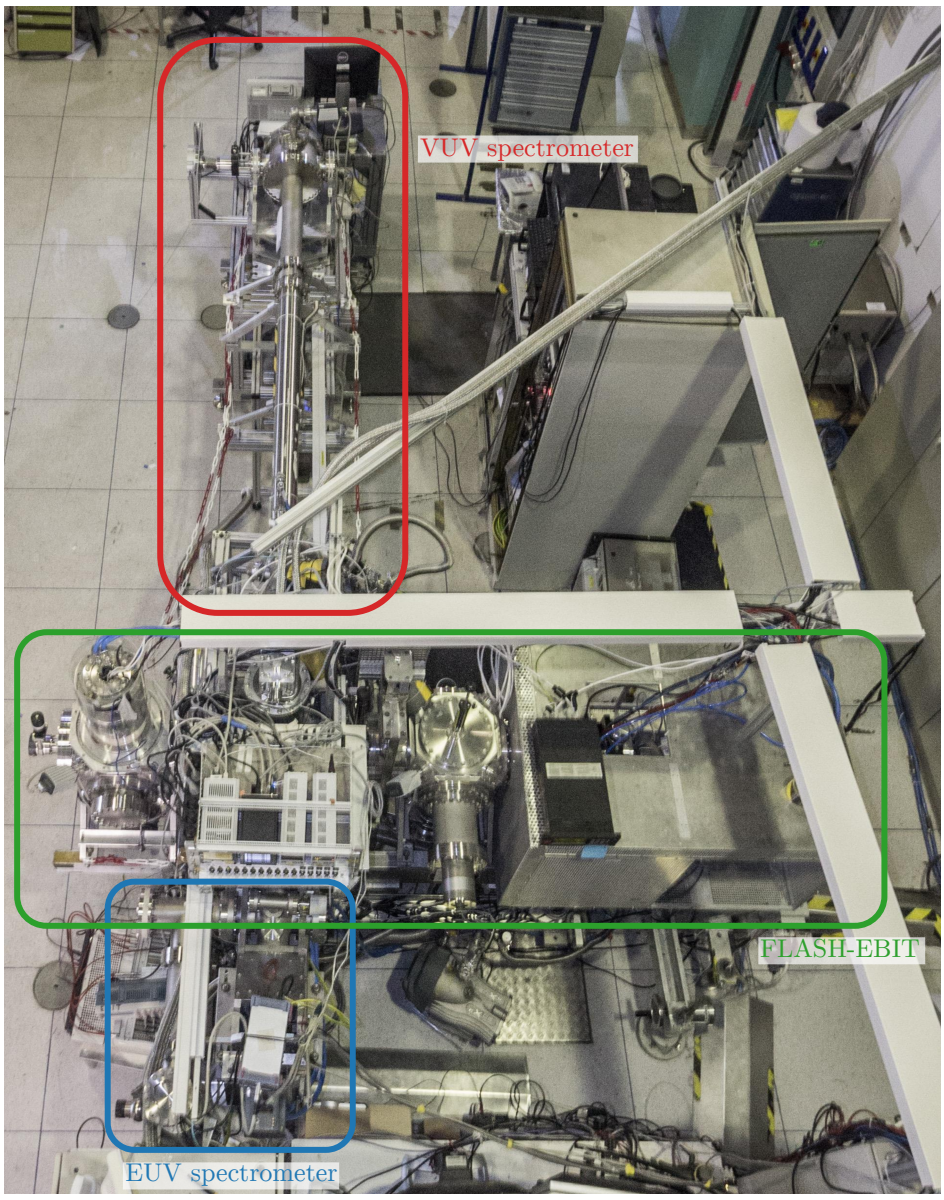

Figure 4.2: Bird's-eye view of FLASH-EBIT, EUV and VUV spectrometer. The electron gun manipulator is encased by the Faraday cage on the right. Between the two spectrometers magnet and the trap centre is located and finally, the collector chamber is on the left.

4.1 3 m VUV grating spectrometer

A first version of this instrument is presented in the author's master thesis [30] where it was used in conjunction with the CFEL-ASG MultiPurpose chamber (CAMP) [178] for multiple beam times at a Free-Electron Laser in Hamburg (FLASH) beamline at Deutsches Elektronen-Synchrotron (DESY) (i. e. see [139] for results). However, the setup was significantly improved during the course of this work. So the current setup and data analysis is described in full detail here.

4.1.1 Optical design

A major challenge in designing optics for the VUV regime is that there are no lenses available and normal reflectivity is low (typically less than 30 %) compared to optics for visible light. Using grazing incidence at angles of a few degrees, higher reflectivity can in principle be achieved. However, this drastically increases the size and therefore cost of optical elements to achieve the same solid angle. So when limited light intensity is available, it is usually desirable to have as few optical elements as possible.

One of the simplest reflective spectrometer was published by Rowland [159]. It features a concave reflective grating with a radius of curvature R (resulting in a focal length of $R/2$). One can draw a so-called Rowland circle with diameter R tangentially to the grating so that its centre is located on the grating surface normal. If the point-like light source (or entrance slit) is located on this Rowland circle, the light is re-focused onto another position on the same circle. This is illustrated in Figure 4.3.

The angle of reflection φ_n for a specific spectral mode and wavelength can be calculated using the grating equation

$$n \times \lambda = g \times (\sin(\varphi) + \sin(\varphi_n)) \tag{4.1}$$

where n is an integer representing the propagation-mode of interest, λ the wavelength, g the distance from the centre of one ruling to the centre of the adjacent ruling and φ the angle of incidence.

Determination of the focal position can be achieved geometrically, once the Rowland circle and angle of reflection are known, by finding the intersection of the reflected beam with the Rowland circle.

4.1.2 Mechanical design

As the term vacuum ultraviolet indicates, this type of radiation is absorbed by air, so the spectrometer needs to be *in vacuo*.

A set of diffraction gratings was recovered from the Berliner Elektronenspeicherring-Gesellschaft für Synchrotronstrahlung m.b.H. (BESSY) cyclotron 3 m normal incidence monochromator. They are glass-blanks of 150 mm diameter, radius of curvature $R = 3000\,\text{mm}$ with a slope error $\sigma_\text{R} < 0.4''$. The one that was used throughout this work is platinum coated, has 2400 l/mm and a blaze wavelength of $\lambda_\text{opt} = 80\,\text{nm}$ [154].

Due to the available gratings, normal-incidence (Rowland) configuration with an arm length of 3 m was chosen for the spectrometer. Maximum light-efficiency is achieved by using the ion cloud as a cylindrical light source without focusing optics or entrance slit.

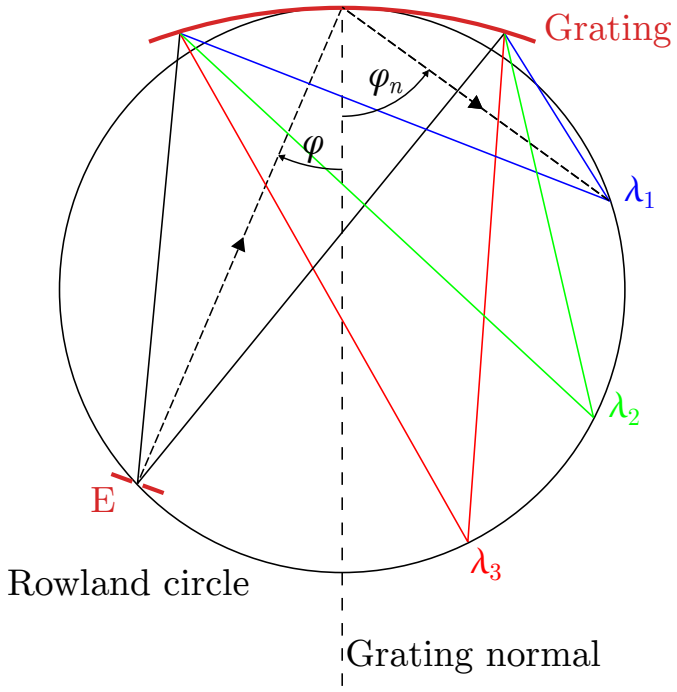

Figure 4.3: Schematic diagram of Rowland geometry adapted from [168]. Rulings and entrance slit E are perpendicular to the drawing plane. λ_1, λ_2 and λ_3 indicate where the focal positions of the spectrometer are located. Radius of curvature of the grating R is the same as the diameter of the Rowland circle.

Spatial constraints due to the dimensions of the FLASH-EBIT lead to the choice of a fixed angle of 15° between incident and reflected light. To observe different spectral ranges, the grating is rotated with respect to the incident light. The detector was placed on a linear manipulator stage below the trap within the support structure for the EBIT (see Figure 4.4). When the grating is rotated, the detector moves along the Rowland circle and therefore it needs be moved closer to the grating or away from it to stay in the focal plane.

Precise rotation in a vacuum is facilitated by using a ferro-magnetic fluid rotary feed-through. A shaft connected to the grating holder is sealed by a ferrofluid held in place by a magnetic field. On the vacuum side, unlubricated ball bearings facilitate precise positioning. At atmosphere off-the-shelf hardware can be used for actuation (see Figures 4.5 and 4.6). A Newport URS75BPP rotation stage was used for positioning and a Heidenhain RON 905 rotary encoder for precise measurement of the grating angle.

4.1.3 Micro-channel plate (MCP) detector

VUV radiation can be detected using a multitude of detectors such as charge-coupled devices (CCDs) (see Section 4.2.2), photodiodes, and photomultiplier tubes. Position-sensitive detectors are preferred since they reduce acquisition time drastically compared to a spectrometer with exit slit and detector without spacial resolution. Due to the small spectral range covered at a specific grating angle, only a few lines can be observed at once. So the grating was rotated continuously during some measurements to cover a larger

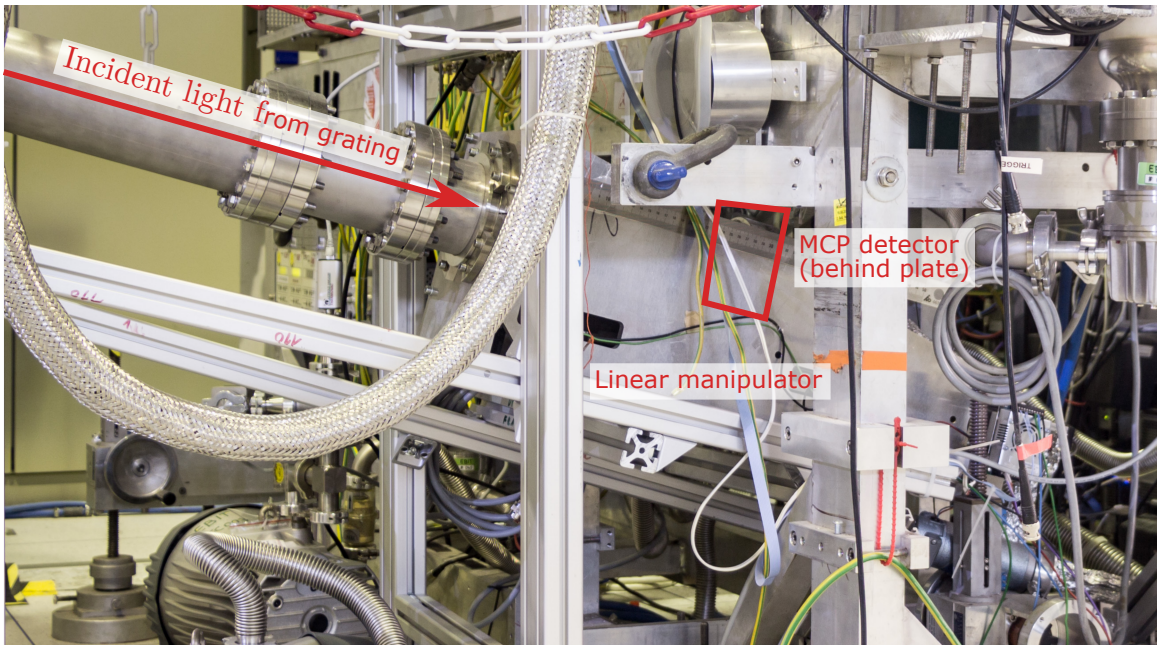

Figure 4.4: Detailed photograph of the linear stage for the micro-channel plate (MCP) detector. It was motorised using a stepper motor Trinamic PD-109-57. With a rate of approximately 1 Hz the grating angle is read, the corresponding focal position determined and the MCP moved respectively. The detector is located behind the metal side plate of the linear manipulator.

spectral range. For these acquisitions, timing information is crucial for data analysis. Consequently, a MCP is the detector of choice. Additionally it has the advantage of being 'solar blind', meaning visible background light i. e. from pressure gauges does not contribute to the dark count rate.

Assembly of an MCP starts by pushing soluble glass fibres ('cores') into hollow glass fibres ('channels') made from another type of glass. These billets are individually drawn to produce thin fibres that are combined into stacks which are drawn again. Multiple drawn stacks are fused together into a capsule (also called 'boule') that are edge ground and polished into blanks. After more processing, the soluble cores are etched away leaving a glass disc with a regular pattern of small holes. Typical diameter for the channels is 12.5 µm and the distance is 15 µm centre to centre. Also the channels are often oriented at an angle of 8° to 15° with respect to the surface normal ('bias angle'). In some MCPs the channels are curved within the glass plate. Treating the blanks with hot hydrogen atmosphere chemically forms a thin semi-conducting surface layer in the channels. Finally, both flat sides of the disc are vacuum-metallized so that a high-voltage can be applied across the plate. A schematic representation of such a finished MCP is shown in Fig. 4.7.

MCPs are versatile detectors; they can be used to detect particles such as electrons, ions or photons. Furthermore, they can be used in spatially and/or time resolved detectors. When an incident photon impacts a channel wall, one or more electrons are released due to the photoelectric effect. When a voltage is applied across the plate, the electron is

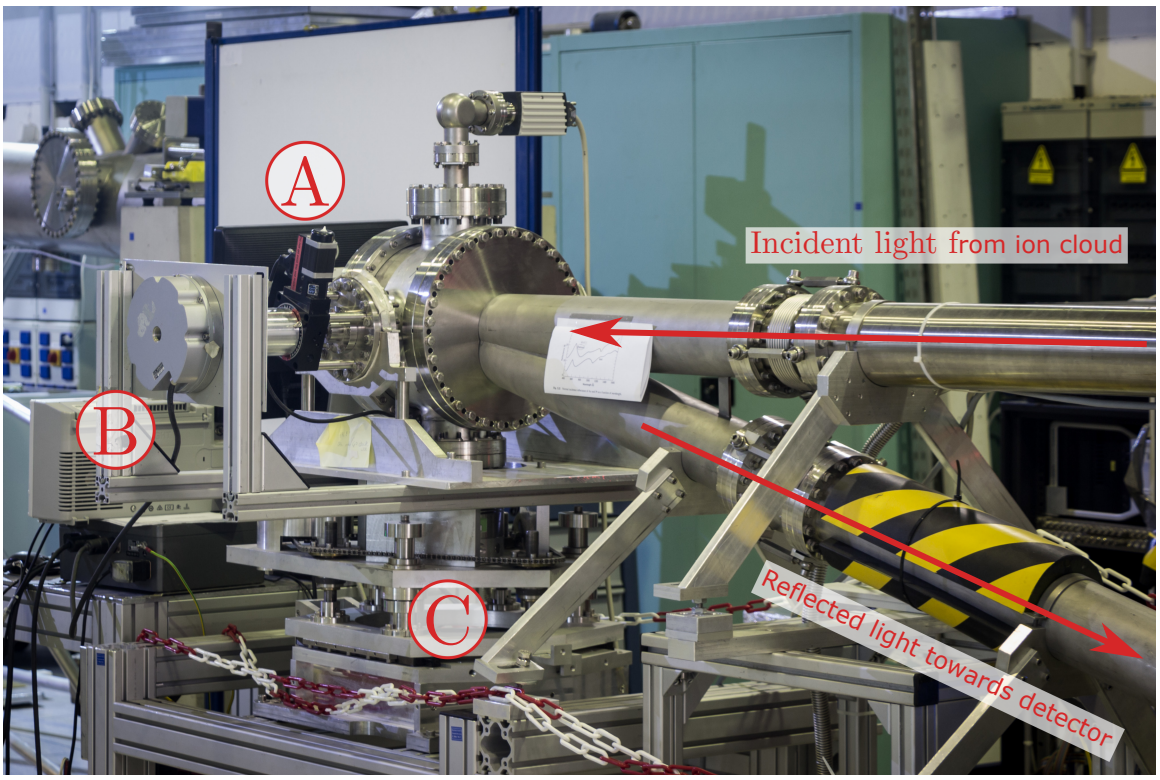

Figure 4.5: Detailed photograph of the grating chamber. 'A' is the rotation stage used to actuate and 'B' the rotary encoder to accurately measure the grating angle. 'C' is a mechanism for aligning the height of the grating with respect to the EBIT.

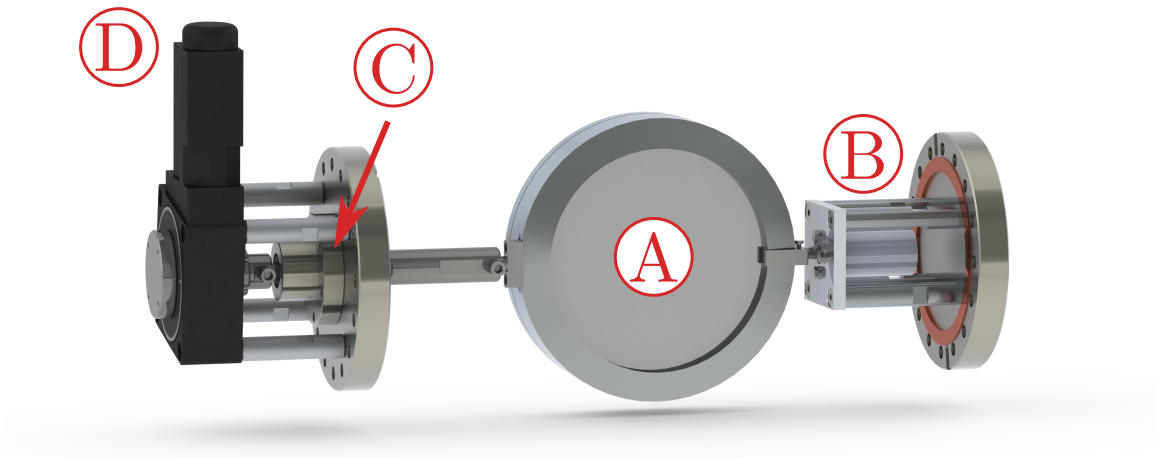

Figure 4.6: Rendered image of the grating mount. 'A' is the grating, 'B' the in-vacuum bearing, 'C' the ferro-magnetic fluid feedthrough and 'D' the rotation stage unit including the stepper motor to rotate the grating. Compare to Figure 4.5 for a photograph of the closed vacuum chamber. Rotary encoder for angle measurement is not shown.

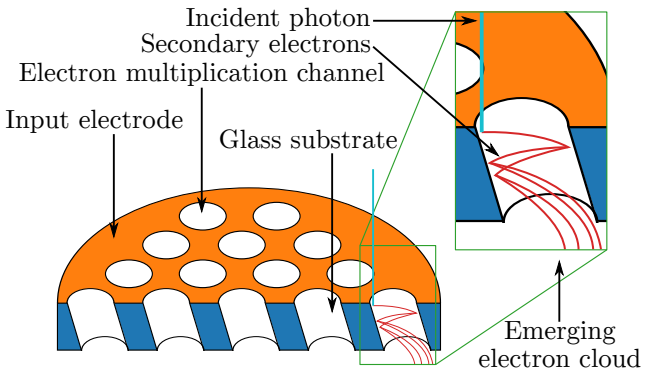

Figure 4.7: Schematic diagram of a micro-channel plate. When a photon of sufficient energy impinges on a micro-channel wall, it can cause emission of an electron. An acceleration potential between the input and output electrode (the latter is located on the bottom face) increases its kinetic energy to facilitate emission of secondary electrons. After several multiplication steps, an electron cloud is emitted from the channel on the output face.

accelerated towards the positive potential. Due to the channel being at an angle, the electron has a good chance of hitting the channel wall again at a higher kinetic energy. Therefore, secondary electrons are released from the channel wall. This process happens several times so that a single ultraviolet (UV) photon is converted into an electron cloud being released from the positive face of the MCP. So each individual channel effectively acts as a photomultiplier tube.

To improve efficiency for longer wavelengths, coatings or photo cathodes can be added to the system. For higher yields, multiple MCPs can be combined using alternating channel angles (i. e. two in 'chevron' configuration or three as a 'Z stack').

Depending on the use case there are multiple options for detecting the electron cloud. In night vision applications typically a phosphor screen is utilized. When spatial information is not needed, a simple metal plate anode can be used. For this work both spatial and timing information is required. Two popular methods of achieving this are delay line anodes (DLDs) or wedge-and-strip anodes. The first type is presented in Figure 4.8. Usually it is comprised of two bare copper wires on top of each other and a plate to collect all electrons that missed the wires. One of them is later used to deduce the x coordinate of the event, the other one for the y coordinate. An electron cloud impinging on a wire causes a local negative charge. The electrons repelling each other splits the signal into two counterpropagating current pulses. Both ends of the wires are connected to a data acquisition system and either the time delay or the difference in pulse shape can be recorded to analyse where the electron cloud was collected.

The data presented in this work was recorded using a bare (uncoated) chevron stack MCP supplied by RoentDek Handels GmbH (model DLD40EP). It has an active diameter of 45 mm, thickness of 1.5 mm, channel diameter of 25 µm, spacing of 32 µm and bias angle of 8°. It features a DLD with a spatial resolution of better than 0.1 mm, overall linearity of 0.3 mm, temporal resolution better than 0.2 ns and a multi-hit dead time of 10 ns to 20 ns.

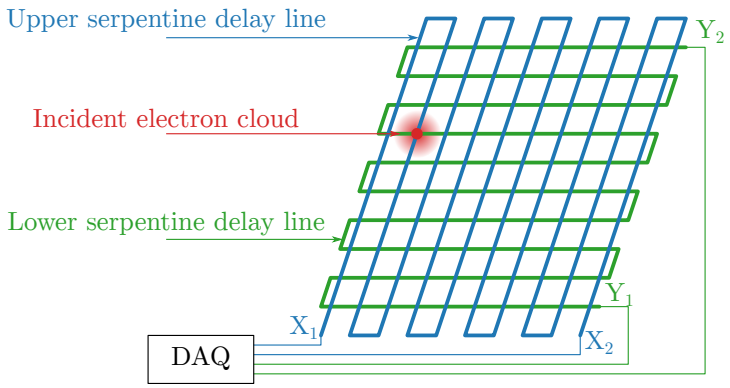

Figure 4.8: Schematic diagram of a delay line anode. Due to the electrons repelling each other after being collected by the wires, two current pulses are counterpropagating. Either the time delay or the pulse shapes are analysed by the data acquisition system (DAQ). A pulse travelling further broadens more so that pulse height or width give an indication where along the wires it originated. A time delay measurement usually requires one of the signals being shifted in time so that one of the two pulses can always act as a start pulse.

4.1.4 Control and data acquisition system (DAQ)

Two computers are involved in the data acquisition: a spectrometer control and a dedicated data acquisition computer. Both record data that is used in the analysis. Using Ethernet they can be remote controlled. To scan a wavelength range the control computer is communicating with a Newport SMC100BPP motion controller to drive the Newport URS75BPP rotation stage. Continuously, the Trinamic PD-109-57 focus motor is moving the linear stage to keep the MCP detector in the focal plane.

Events detected on the MCP delay line are amplified using a RoentDek DLA-TR6 differential amplifier. Nuclear Instrumentation Module (NIM) pulses X_2 and Y_2 are delayed using an Ortec GG8020 to ensure they always arrive later than X_1 and Y_1, respectively. Their time delay is measured in coincidence using a 13 bit FAST ComTec Timing analogue-to-digital converter (ADC) 7072T in conjunction with the Multiparameter Multichannel Analyzer System (MPA-3) of the same brand connected to the data acquisition computer.

Guaranteed accuracy of the rotation stage is only $0.015° = 15\,\text{mdeg}$, so it is mechanically connected to a Heidenhain RON 905 rotary encoder with one absolute position and 36 000 incremental impulses per rotation. Readout is performed by a Heidenhain AWE 1024 interpolating 1024-fold for a final resolution of better than 0.000 001° or 25 bit.

This level of accuracy is not compatible with the MPA-3 system, so the angle is recorded separately on the spectrometer control computer and combined with the MCP data in post-analysis. However, this requires synchronisation between both systems. The AWE 1024 features a mode of operation where an external logic pulse is used to trigger conversion and storage of the current angle ('storage pulse'), followed by asynchronous read-out of the stored value via GPIB interface. So a Stanford Research Systems DS345 function generator, configured by the spectrometer control computer, is used to generate a 20 Hz square-wave signal as trigger. The same signal is fed into an ADC channel of the MPA-3 data acquisition system. An overview of the most important components used to acquire a

VUV spectrum is shown in Figure 4.9.

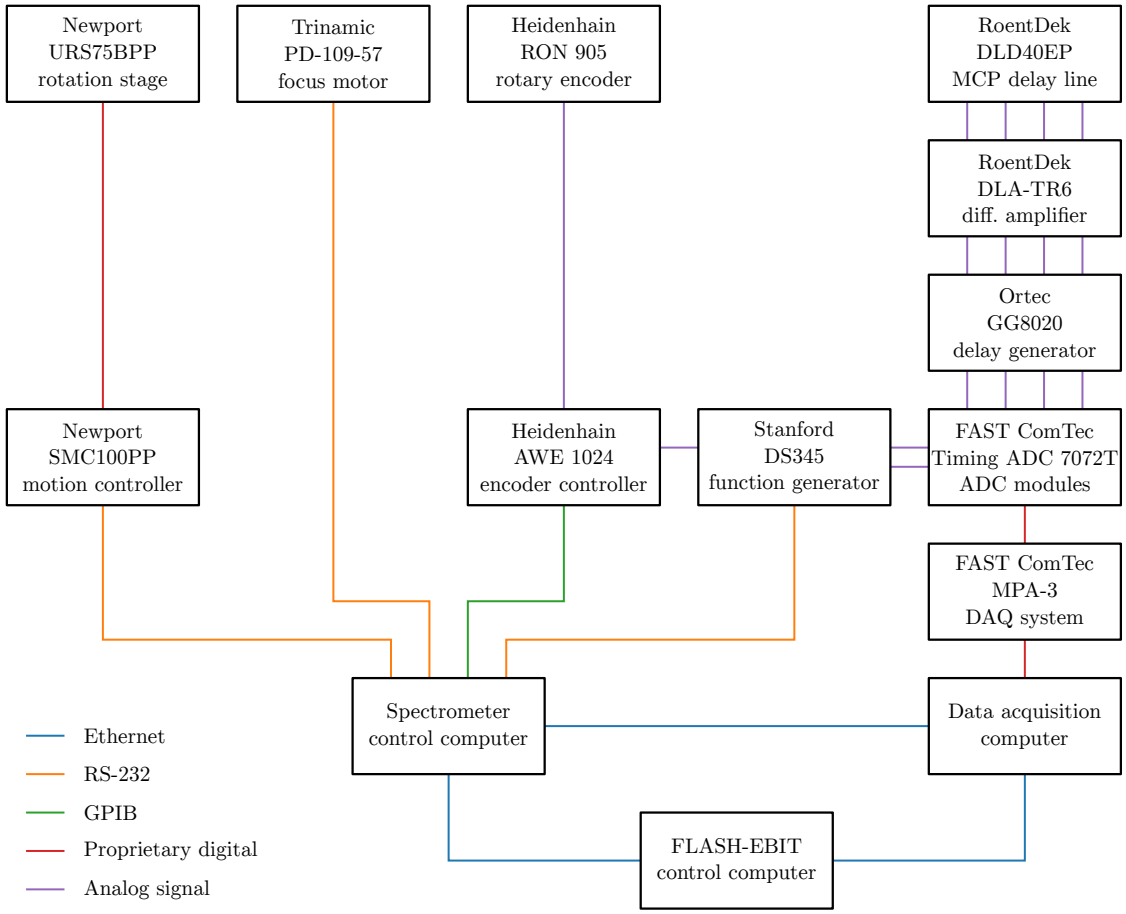

Figure 4.9: Scheme of the VUV control and data acquisition system. All of the control tasks are handled by the spectrometer control computer but both record data to generate a VUV spectrum in post-processing. Synchronisation between the systems is achieved using a function generator to trigger a grating angle measurement and the MPA-3 ADC that also records each events on the MCP detector.

4.1.5 Performance

When evaluating performance of a spectrometer, the first import characteristic that comes to mind is resolution. However, sensitivity was also an important factor, since the objective of this work is the search for weak transition lines.

As mentioned earlier, the same gratings and some parts of the setup have been used in previous experiments at FLASH and BESSY demonstrating that a resolution of more than 44 500 can be achieved using that grating [30, 139, 154]. However, these setups used a collimated light source (by means of an entrance slit/hole or Kirkpatrick-Baez mirror) as well as a CCD detector with better spatial resolution (13.5 µm compared to 100 µm).

Since the photon flux available was much lower for the experiments presented here, some

of the resolution was sacrificed by not introducing a slit in order to maximize sensitivity. Additionally, the solid angle was increased by upgrading the vacuum tubes from an inner diameter of 38 mm to 100 mm. It is now estimated to be $\Omega \approx 9.3 \times 10^{-4}$ sr.

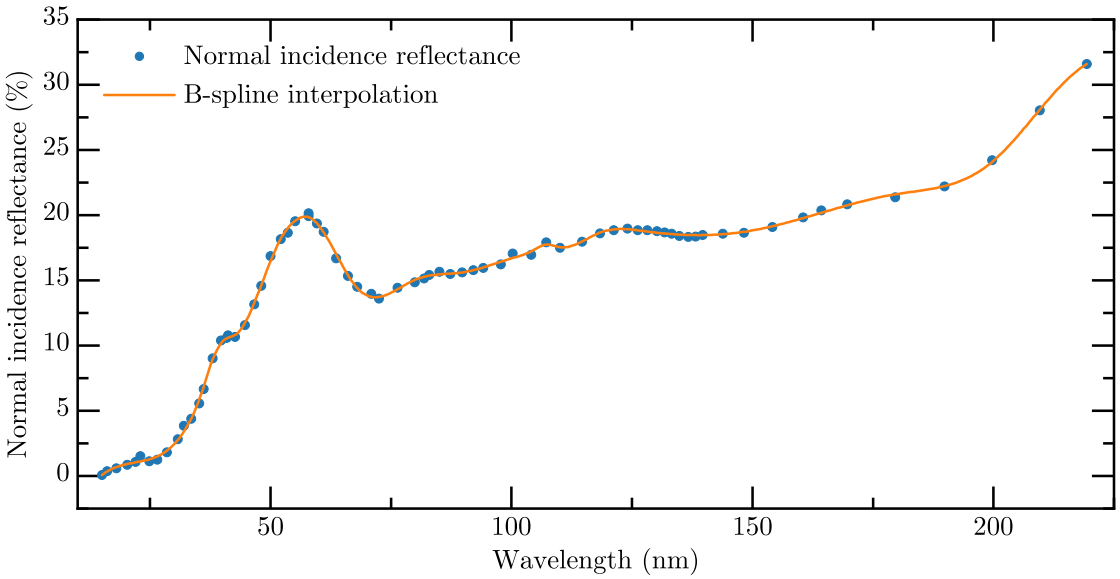

Figure 4.10: Reflectance of fused silica coated with platinum at room temperature in normal incidence. The data was extracted from [105] and interpolated.

Other factors affecting sensitivity are the efficiency of the grating and detector. There is no data available for this particular grating or MCP, so it was estimated using literature values. A reflectance curve for platinum coated fused silica was used from [105] (see Figure 4.10). By heating the substrate during coating, a higher reflectance and more durable surface could be obtained. However, gratings are typically coated at room temperature because heating can potentially harm the ruling. So the reflectance for surfaces coated at room temperature were used. For the diffraction efficiency of blazed gratings, a formula from literature was evaluated [48]:

$$I(\beta) = k \operatorname{sinc}^2 \left[n\rho \left(\cos\varphi - \frac{\sin\varphi}{\tan\frac{\alpha+\beta}{2}} \right) \right] \tag{4.2}$$

where α and β are the angles of the incident and reflected light respectively. φ represents the blaze angle, n is an integer number representing the spectral order,

$$k = \min\left(\frac{\cos\beta\cos(\alpha-\varphi)}{\cos\alpha\cos(\beta-\varphi)}, 1 \right) \qquad \text{and} \tag{4.3}$$

$$\rho = \begin{cases} \frac{\cos\alpha}{\cos(\alpha-\varphi)} & \alpha \geq \varphi \\ \cos\varphi & \alpha < \varphi \end{cases} \tag{4.4}$$

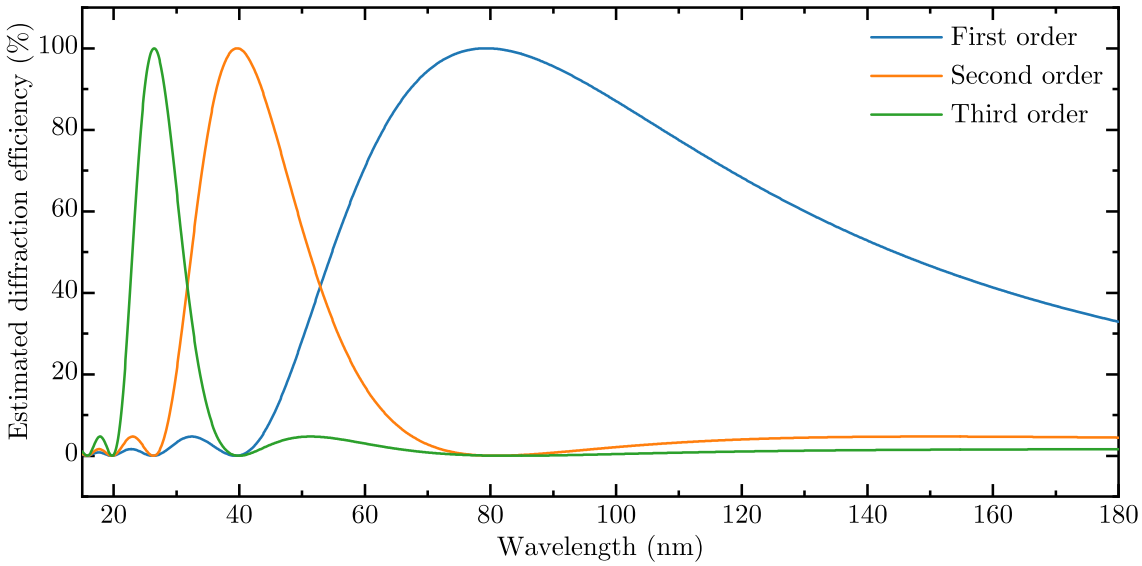

Figure 4.11: Estimated diffraction efficiencies for the first three spectral orders using a scalar theory derived from first principles [48]. These are not taking into account polarisation nor the radius of curvature. For now, a reflectance of 100 % was assumed. The combined efficiencies is shown in Figure 4.13.

Finally, the detector quantum efficiency was assumed to be that of a bare MCP photocathode i. e. measured by [136] (see Figure 4.12).

These parameters (reflectance, diffraction and quantum efficiency) were multiplied to obtain the estimated overall spectrometer efficiency presented in Figure 4.13. This is neglecting the dependence of the reflectance on the actual angle of incidence. Highest sensitivity of more than 1.1 % is achieved in the wavelength range of 50 nm to 120 nm. Below 30 nm the limiting factor is grating reflectance and above 130 nm the MCP quantum efficiency.

4.1.6 Measurement schemes

Different schemes were used to operate the spectrometer: Either a ‘static mode’, where the grating was moved to the desired angle before taking data or a ‘scanning mode’, where the grating angle was changed during acquisition. Due to the large dispersion and relatively small detector diameter the spectral range covered in the former mode is limited to approximately 4 nm. So scanning has the advantage that the spectral range can be any subset of the full range of the spectrometer. However, this mode requires a more intricate data pre-processing (see next section).

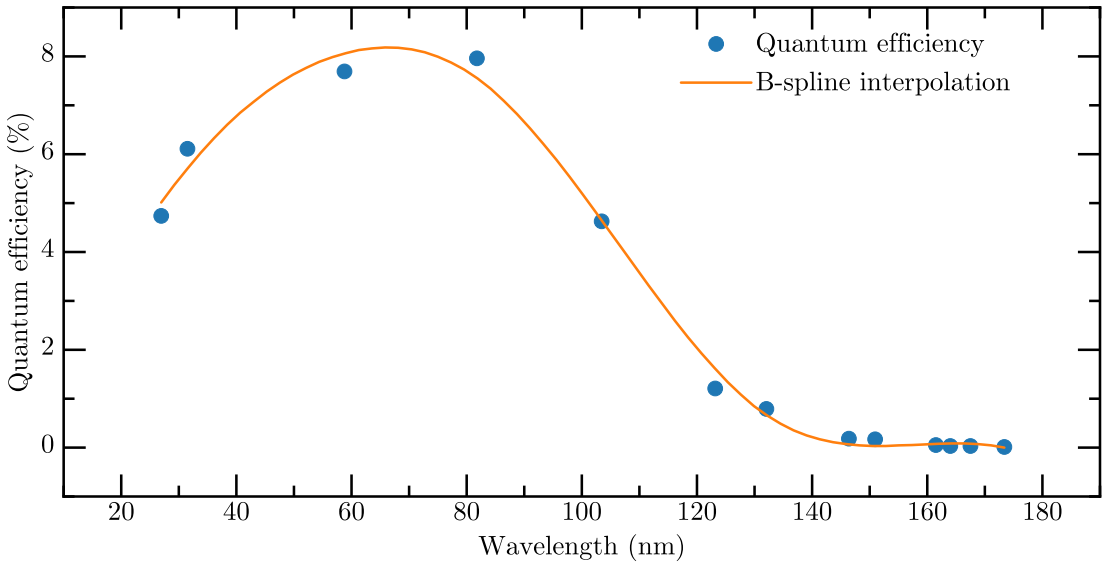

Figure 4.12: Quantum efficiency of an uncoated MCP photocathode such as the one used in this work. The data was extracted from [136] and interpolated.

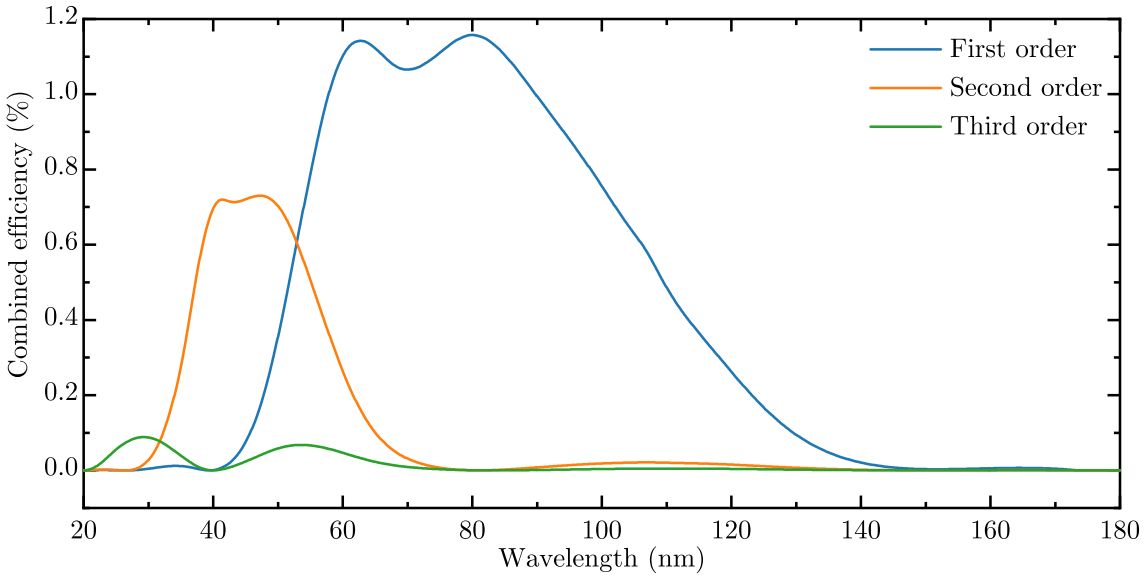

Figure 4.13: Estimated combined efficiencies for the VUV spectrometer taking into account reflectance and diffraction efficiency of the grating as well as the detector quantum efficiency. Reflectance is assumed to be in normal incidence while the diffraction efficiency was calculated based on the angle of reflection.

When changing the grating angle during a measurement, synchronisation between the angular data and the time stamps of events on the MCP detector is required as described on page 64. In addition to the 20 Hz trigger pulses for the angle readout, two distinct kind of auxiliary pulse sequences can be generated:

- A 'start/stop sequence' that is a 3 s burst of a frequency modulated square wave of 100 Hz to 300 Hz followed by a pause of 3.5 s. The amplitude of the square wave is 0 V to 5 V and the modulation wave form is a ramp of 20 Hz. This sequence is shown in Figure 4.14.
- A 'synchronisation sequence' using an amplitude of 2.45 V to 2.55 V (effectively a fixed output voltage not triggering the angle encoder but the data acquisition system) for the duration of 0.25 s.

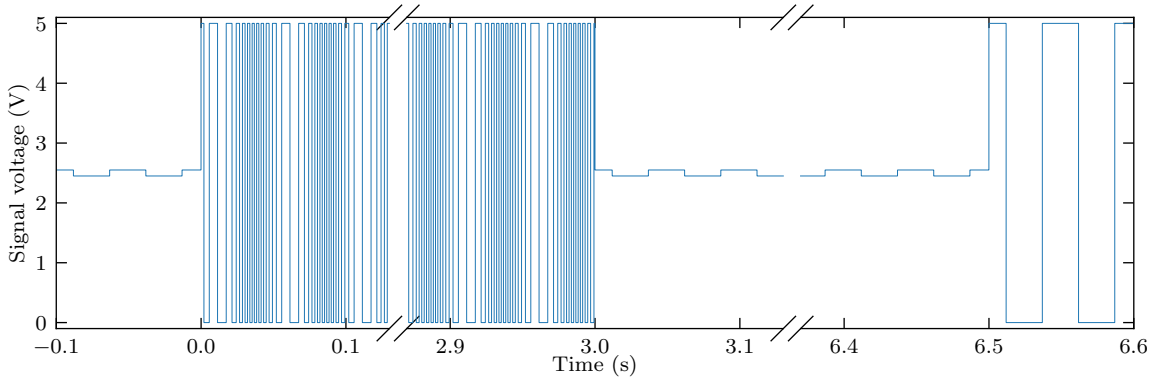

Figure 4.14: 'start/stop sequence' used for the synchronisation of the VUV spectrometer. At time $t = 0$ s, a burst of 3 s of a frequency modulated square wave is initiated. After a consequent pause of 3.5 s, the 20 Hz square wave triggering the readout of the grating angle is started.

A scanning mode measurement is initiated by generating a start/stop sequence before scanning the full spectral range a few times in succession over the course of a few hours to a day. When the end of the scan range is reached, the grating speed is changed, so that the grating is moving back to the lower end of the range in a couple of minutes. For some of the measurements, a synchronisation sequence was sent after scanning the grating angle for a fixed amount of time before moving the grating back to the zero order position that was consequently scanned at the same angular velocity as the main scan. Before moving back to the position where the scan was interrupted, another synchronisation sequence is generated. When the desired number of scans is finished, a second start/stop sequence is recorded.

When the grating is rotated, the focal position is changing slightly. To enable long-term acquisition in scanning mode, the detector is kept in focus using the linear manipulator mentioned earlier. To determine the focus positions for the complete spectral range, oxygen was injected into and trapped in the EBIT. Fluorescence lines from electron impact ionisation were observed at various, fixed grating angles and the position of the MCP

detector was manually optimised for minimum line width. These detector positions were interpolated for the full range of grating angles using a third-order polynomial function. During a measurement, this lookup table is used to continually adjust the focus motor position to keep the detector in focus.

4.1.7 Data pre-processing

Data analysis was implemented in Python unless otherwise noted. In this section, a graph of count rate against grating angle is extracted from raw data. We will start with data recorded in static mode before adding another layer of complexity for the analysis of spectra recorded in scanning mode.

Static mode

MCP data is recorded by the MPA-3 DAQ system into `.lst` files native to this system. These are binary files written in a sequential manner in blocks of varying length making it very inefficient to skip or extract data from arbitrary positions in the file. So the first step of data analysis is to convert the `.lst` file into a more prevalent data format allowing for random access. HDF5 is a very popular format for storage of tensors ('data sets') that can be organized in a tree-like structure of nested 'groups'. The data can efficiently be read and written at random positions and can hold annotations. There are open-source libraries and viewers available for all major programming languages and operating systems. An efficient converter was implemented in C for converting `.lst` files of several GB to a `.hdf5` file in a matter of seconds to minutes. The converter can also be used for other types of measurements utilizing the MPA-3 system since the conversion is without loss of information: All the ADC data is copied into a group called `EVENT` containing three data sets:

- `EVENT/adcnumbers` contains a single column with the numbers of all ADCs active during the measurement.
- `EVENT/adcdata` is a matrix with columns for each active ADCs and a row for each event. If a channel was triggered in this event, it contains the value (number 0 to 8191) and 65535 otherwise.
- `EVENT/adctimes` contains a single column with the same number of rows as the `EVENT/adcdata` matrix. It holds the time in millisecond for each event since the start of the measurement.

During analysis, more data is added to the file.

The pre-processing steps are presented in Figure 4.15 and described here.

First, A mask is created to extract all data relevant for analysis. In particular, only events are selected, where both coordinates (named X and Y) are present. Also a circular ROI, defined by its centre coordinates and radius, is applied to exclude events close to the rim of the MCP since there are significant distortions.

At this point, the data can be represented by a list of three-dimensional vectors (timestamp, X and Y coordinate). Applying a rotation matrix, the spatial coordinates are rotated by 78.3° counterclockwise compensating for the orientation at which the detector is mounted.

A lookup table is used to flatten out any non-linearities along the dispersive axis caused by the delay-line anode or DAQ system. The process of determining this lookup table is described in the Appendix A.1.

The last conversion of the dispersive axis coordinate is into a grating angle. Strictly speaking, this step is not necessary in static mode if suitable calibration data is available. However, having a comparable axis is very useful for transferring and compare data or calibrations.

Finally, a histogram is compiled with respect to the grating angle using a given bin size (usually 0.3 mdeg was used). Weighing factors are employed to assure the round shape of the ROI and exposure time is comparable for each bin.

Scanning mode

Conversion of the input file, application of the ROI, rotation and distortion correction are identical to the static mode. However, after these steps an additional step is required to correlate each MCP event with an angle measurement of the rotary encoder.

An additional file has to be provided for this measurement scheme: a `.db` file created by the spectrometer control computer in the SQLite database format contains a table called `RON` with two columns named `tstamp` and `angle`. Timestamps from the first column are used to match event times from the HDF5 file discussed earlier. Synchronisation events are stored in the database using a negative angle value (valid angles are in the value range of 0.0° to 360.0° and therefore always positive). Using the time in ms since the last start/stop or synchronisation sequence and since the last synchronisation event in the angles table respectively, the closest angle measurement in time is determined for each event on the MCP.

Now, there are four values per event (timestamp, angle, X and Y coordinate). However, the angle is not the full picture yet: since the detector extends along the dispersion axis, it detects photons of more than one wavelength reflected under slightly different angles. So when the grating is rotating, the spectral lines move across the detector. This needs to be taken into account by converting each event coordinate oriented along the dispersion axis into an angle offset. This 'dispersion correction' is then added to the grating angle of the respective event. The process is applied to an exemplary spectrum in Figure 4.16.

During data analysis, this is achieved by calculating a dispersion in units of degrees per MCP coordinate using a pre-determined polynomial of third order depending on the grating angle (the dispersion changes slightly along the spectral range of the spectrometer).

The parameters for this polynomial are pre-determined by recording a spectrum, generating a 2D histogram for grating angle against the coordinate on the MCP along the dispersion direction. In this spectrogram every spectral line are slanted. Their slope is aforementioned dispersion in units of degrees per MCP coordinate at that specific angle. The value is determined for various angles across the whole range, and a cubic function fitted to the values to interpolate it to values grating angles, where no intense line was available to determine the slope.

After correcting the angles for the dispersion, a histogram with respect to the angle is compiled (a bin size of 0.3 mdeg was used). Finally, this histogram is corrected for the exposure time and shape of the ROI. During a scan, the grating is not moving completely

smoothly but in discrete steps of the stepper motor called ‘micro steps’ that are transformed to even smaller steps by gears of the rotation stage. So for each timestamp in the encoder database, the exposure time is added to all the relevant bins for that particular grating angle using the full weight at the centre of the region of interest and decreasing towards the rim of it. Dividing the histogram by this exposure map yields the pre-processed spectrum in scanning mode.

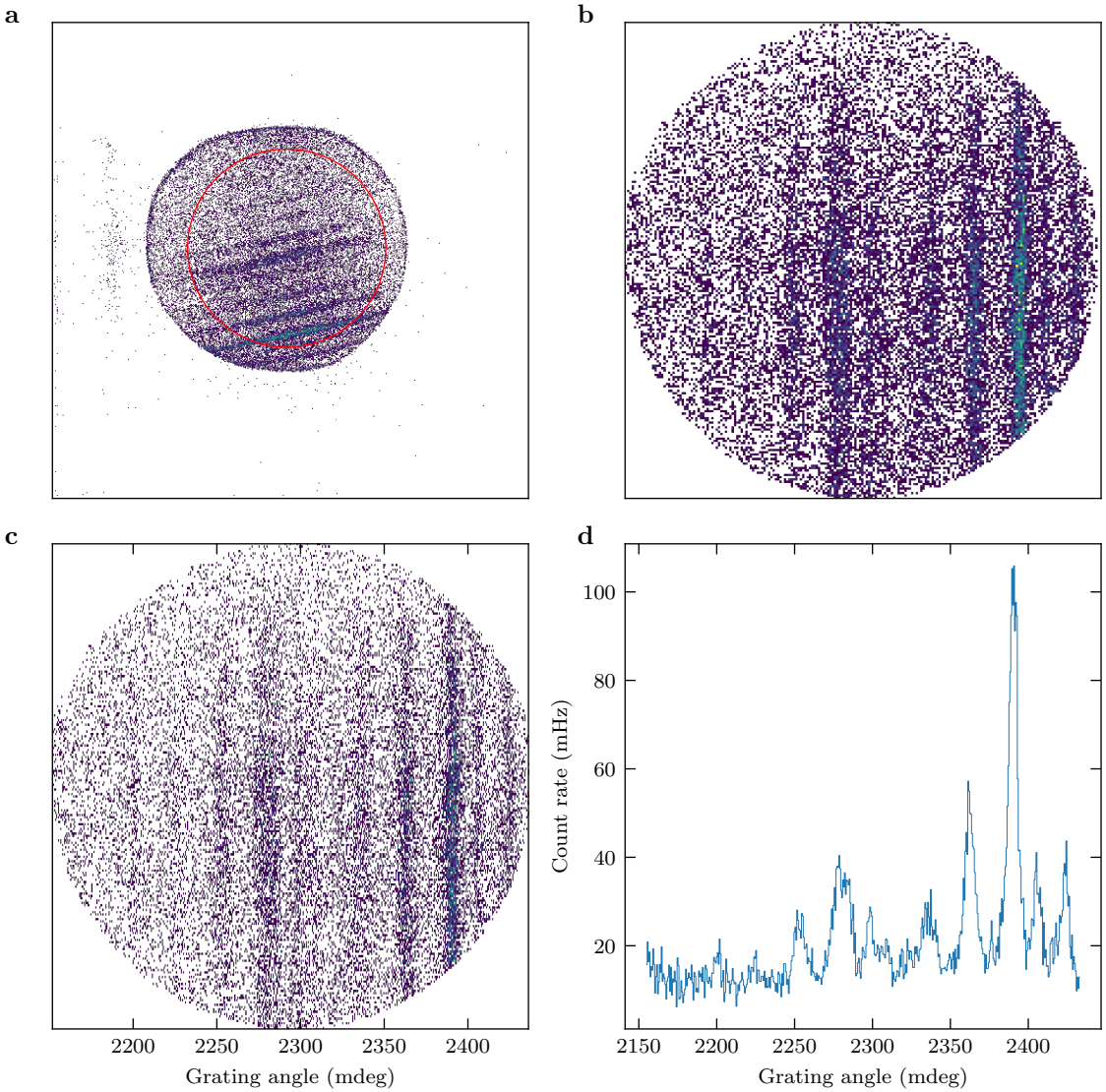

Figure 4.15: Pre-processing scheme for the VUV spectrometer in static mode. An exemplary raw data set is shown in Subfigure **a** together with the circular region of interest (ROI). After masking the data, rotating and linearising it, a 2D histogram was compiled for illustrating this intermediate step (**b**). The coordinate of the dispersive axis is consequently converted to a grating angle, simplifying calibration during analysis. After compensating non-linearities of the detector using a lookup-table (Appendix A.1), a 2D histogram is compiled (**c**). Finally, intensities are normalised with respect to exposure time and the circular shape of the ROI before being projected (**d**). For illustration purposes, Subfigures **a** and **b** were binned 16-fold and the dispersive axis in **c** and **d** a bin size of 0.6 mdeg was used.

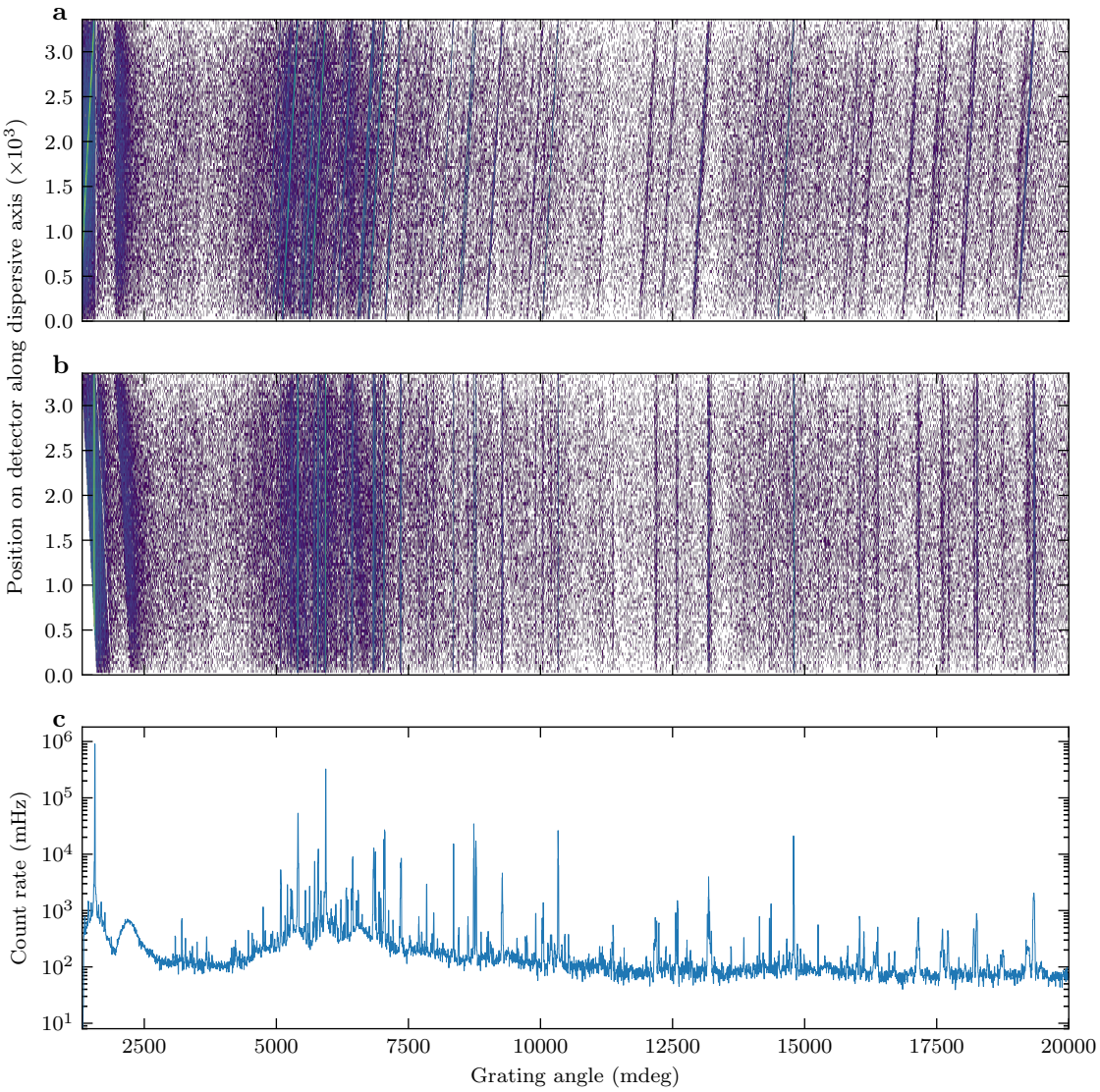

Figure 4.16: Pre-processing scheme for the VUV spectrometer in scanning mode demonstrated for an oxygen spectrum. A two-dimensional histogram is shown in Subfigure **a**, where each detector event was binned according to the closest angle measurement in time and position along the dispersive axis. It can be seen that the line moves across the detector from bottom to top as the grating angle is increased. So the measured angle for each event is corrected using the coordinate along the dispersive axis. This dispersion factor changes slightly across the spectral range and is therefore calculated using a cubic function in the grating angle. The same spectrum is shown after applying the dispersion correction (**b**). Finally, the spectrogram is projected after exposure correction (**c**). For illustration a more coarse binning was used in this graph: 32-fold along the dispersive axis and 5 mdeg for the grating angle. The strongest peak around 1.6° corresponds the image of the ion cloud (zero order) and the end of the scanning range is in this case 20° ≈ 260 nm. Between the zero order and the first spectral lines, a broader feature can be seen in **a**. As opposed to a direct reflection, it does not move across the detector when the grating angle is varied. So it is assumed to be a diffuse reflection of the zero order, illuminating the sensitive area of the MCP for a certain range of grating angles. Analysis of this particular spectrum is presented in Figure 5.3.

4.2 EUV spectrometer

Unlike the VUV normal-incidence spectrometer described above, the grazing-incidence flat-field EUV spectrometer was used in previous measurements. Since it was presented in detail in [3, 4], this Section will be brief and focus on different influences on the signal-to-noise ratio (SNR) and improvements to the data analysis process introduced during these measurements.

4.2.1 Mechanical and optical design

Central to both the mechanical and optical design is the diffraction grating. It is an concave, grazing-incidence, flat-field grating manufactured by Hitachi [101]. By varying the ridge distance and curving them across the surface of the grating, it has a flat focal plane (as opposed to a curved one as for the Rowland configuration described in 4.1.1). For optimal reflectivity in the UV and soft x-ray regime, it uses shallow reflection angles with respect to the surface and is coated with gold. The design should suppress any coma or spherical aberrations. Important parameters are:

- Physical dimensions: 40 mm × 70 mm × 12 mm (width × length × height)
- Line density: 1200 lines/mm
- Radius of curvature: 13 450 mm
- Blaze angle: 1.9°
- Incident angle: 87° (against grating normal)
- Optimal angles of reflected light: 75.61° to 83.04° (against grating normal)
- Optimal wavelength range: 5 nm to 25 nm

It is worth noting that wavelengths of up to 40 nm can easily be observed, even if the blaze angle is not ideal for these reflection angles.

A rendered section of the spectrometer is shown in Figure 4.17. There is no window nor slit between the trap centre and the CCD, so the whole spectrometer is under vacuum. The grating is mounted on a tilt-shift stage that can be manipulated from outside the vacuum by micrometer screws. An edge-welded bellow is used so that the camera can be re-positioned for focusing or to change the wavelength regime observed. Since the sensor has a height of 27.6 mm, a range of approximately 7.25 nm can be observed at once.

4.2.2 Charge-coupled device (CCD)

A CCD is a grid of photo-sensitive surfaces (so-called 'pixel') accumulating electric charge proportional to the amount of incident light during exposure. Consequently, the charge is electronically read out by a charge-sensitive amplifier. Typically the signal is converted pixel by pixel. Commercially available sensors have pixel dimensions in the order of a few to tens of micrometers and in the order of 1 000 000 pixel per sensor.

For these experiments a commercial back-illuminated windowless CCD by Andor (Model DO436 - BN - 9DQ) was used. Featuring a resolution of 2048 × 2048, square pixel of 13.5 µm in size.

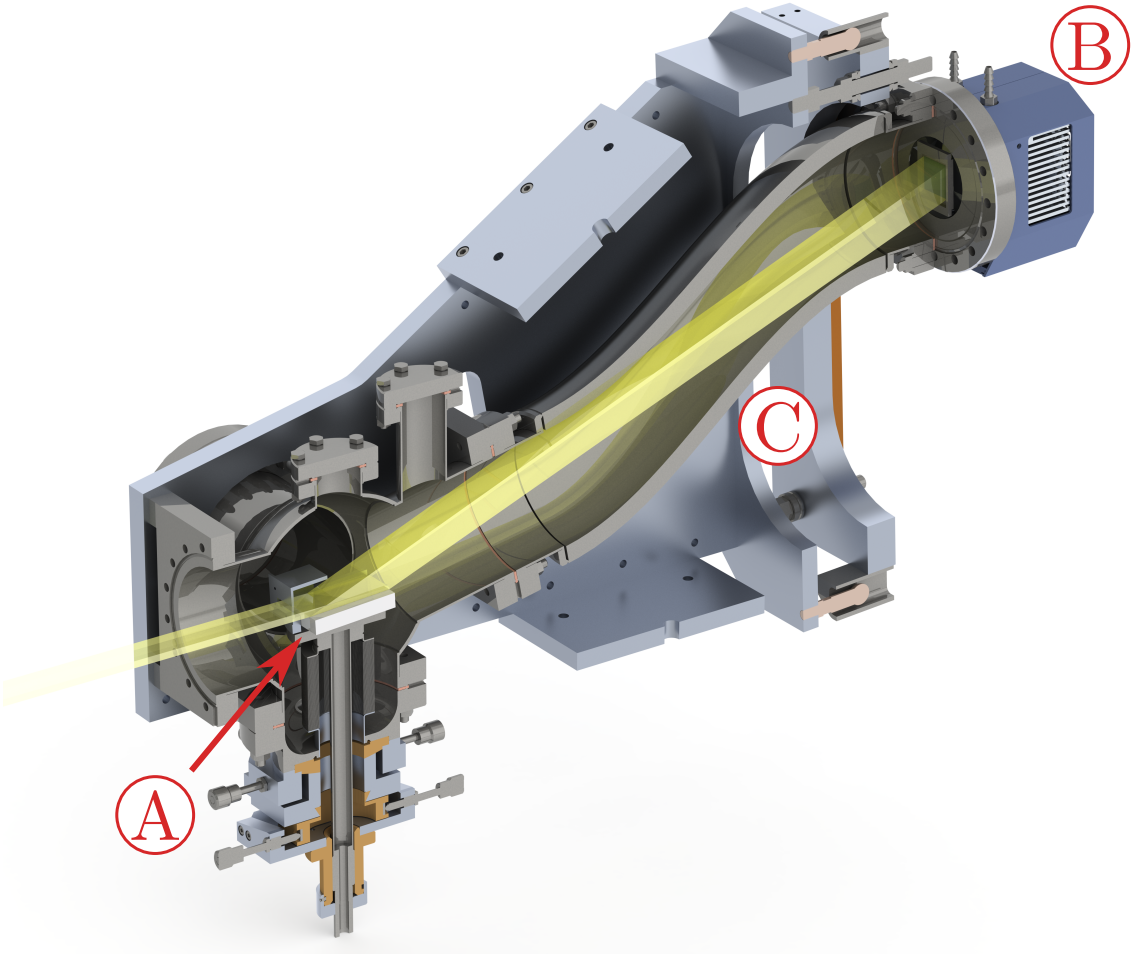

Figure 4.17: Section of the flat-field EUV spectrometer. Light emitted by the trapped HCIs propagates from left to right. 'A' denotes the grating located on a tilt-shift stage for alignment. A symbolic light beam from the the trap centre, reflected by the grating and being detected by the CCD sensor 'B' is indicated as yellow beam. By means of the edge-welded bellow at 'C' and the tilt-shift manipulator at the back of the device, the sensor position can be adapted for the spectral range of interest and focused. In this figure the camera is at the upper maximum position of the travel range covering a wavelengths of about 32.75 nm to 40 nm.

Several aspects need to be taken into account to optimize signal to noise of a CCD sensor: for the signal strength, quantum efficiency is a key factor. For photons observed in this work (30 eV to 60 eV) it approximately increases linearly with photon energy from 20 % to 30 %. Secondly, there are cosmic particles, predominantly muons that can charge up a group of close-by pixel. These need to be discarded before data analysis. Especially for exposure times of several minutes or longer and when binning is used (see next Paragraph), these events can be a hassle. Finally, imperfections of the detector need to be accounted for: some individual pixel always charge up during exposure (so-called 'hot pixel') and some are significantly less sensitive (referred to as 'dead pixel').

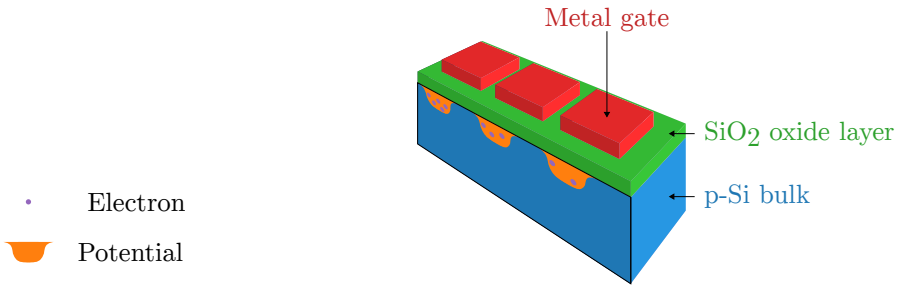

Figure 4.18: Schematic diagram of a CCD sensor. Before exposure, the silicon substrate is biased with respect to the metal gates to form a deep depletion zone in the p doped bulk under the metal oxide layer. Consequently, the metal gates are biased at a positive potential causing a potential well to form under the metal-oxide layer similar to the channel in a MOSFET. Photons impinging on the depletion zone can create electron-hole pairs and the electrons are attracted to the potential well under the closest gate electrode. For read out, the charges can be moved from one pixel to an adjacent one by switching the potentials of the respective gates.

In addition to signal imperfections, there are different noise effects that need to be balanced: Firstly, the read-out process is a noisy analogue-to-digital conversion process. For this CCD two ADCs are available. A fast one, converting individual pixel charges into a digital signal at 1 MHz with a typical noise of 7.5 electrons per conversion and a slower one operating at 31 kHz with a noise level of 2.5 electrons. These values include noise caused by the ADC itself as well as the read-out process. For this work, the low-noise mode was always selected. Further measures to reduce this kind of noise is to not read the charge stored on the pixel individually but in groups called bins. Since the charges are added up before conversion, the read-out noise is distributed over all the pixel in the same bin. However, this reduces spatial resolution and increases the risk of loosing signal due to cosmics.

Secondly, there is thermal noise (also known as dark current) that is caused by pair production in the bulk or depletion zone. This can be mitigated by cooling the sensor down. For this work, a three-stage thermoelectric heat pump connected to cooling water supply of the building was used to reach an operating temperature of −69 °C resulting in a dark current of approximately 0.003 electrons per pixel per second. At maximum resolution (no binning) and low-noise settings for readout, the dark current surpasses the read-out noise for exposure times of approximately 14 min.

Finally, a gain can be selected corresponding to certain ratios of electrons per count. These are: gain values 1 and 2 correspond to 2, 16 to 1.4 and 32 to 0.7 electrons per count.

4.2.3 Data pre-processing

Before the actual analysis of the data, there are several steps of pre-processing required. During the measurement, images are recorded as binary files using the proprietary Andor Solis software. These SIF image files contain metadata such as the settings and the actual image as a two-dimensional array of 16 bit integers.

After importing the raw images in Python, a mask for pixel containing cosmics is generated. Since there are many image files that should contain the same spectral lines,

this can be achieved using a histogram analysis: for each pixel, a mean value and its standard deviation is calculated. Every image, where the value of this pixel is larger than a threshold factor times the standard deviation, it is considered to be a cosmic in that particular image. For a large number of images, this threshold factor can be fairly large (i.e. 5). For a small number of images, there are more sophisticated algorithms available such as the one proposed by Pych [153]. It takes advantage of the fact that spectra should be self-similar along one axis and analyse the histograms of subsections of the image.

A pre-determined mask for the locations of dead and hot pixel as well as lines with non-linear sensitivity is applied before the counts are divided by the exposure time and a mean value is calculated over all the images. A mean value is used rather than adding the images up to account for masking due to cosmic events. Instead of replacing the value for a masked pixel, it is not considered when calculating the average.

Finally, the mean image is projected along the non-dispersive axis. To account for small alignment inaccuracies, each line is shifted by a number of pixel calculated using a linear function. In order to determine this shift parameter, a trial image is projected for all shift values within a certain range. The shift value resulting in the largest maximum in the projection is then used as the best shift. This requires at least one spectral line in the trial image.

All steps of the preprocessing are shown in Figure 4.19. A square root of each individual pixel of the raw data is used as uncertainty and each pre-processing step performed on the data has an equivalent processing step on the two-dimensional array of uncertainties, so that the final result are two one-dimensional arrays containing the projected spectrum and respective uncertainties.

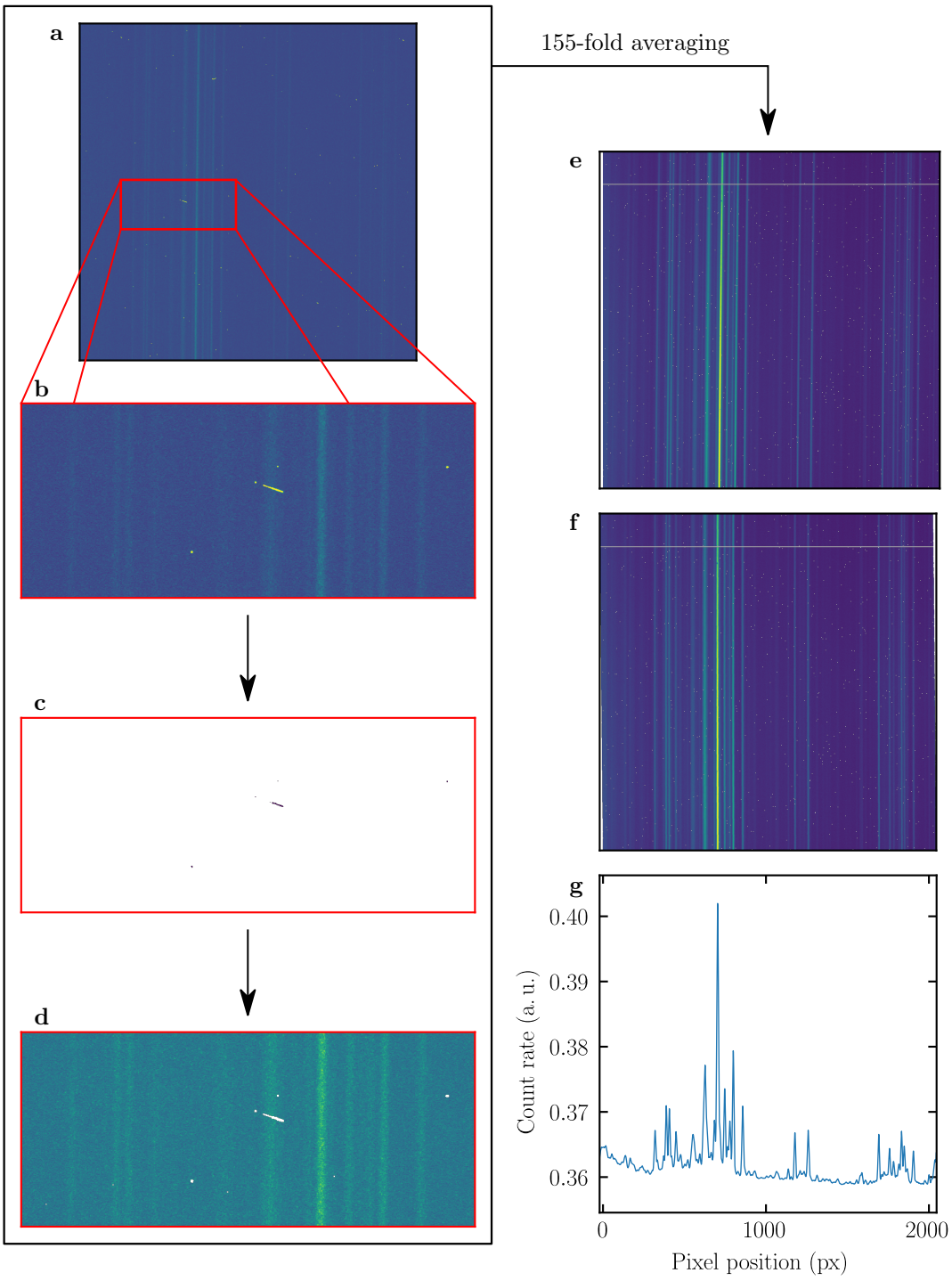

Figure 4.19: Pre-processing of EUV spectra. Subfigure **a** is a raw image acquired, using the CCD camera. (**b**) A small part of the image is magnified to show the cosmic removal process. (**c**) A mask for removing cosmics and bad pixel is derived from the data. (**d**) The cleaned up image now contains blank spots. All the steps shown in the box are repeated for each individual image of the same spectrum. (**e**) Consequently, the mean value is calculated for each pixel over all available images (in this example 155). (**f**) Lines of pixel are shifted with respect to each other, so that spectral lines are now straight along the non-dispersive direction. Please note the blank wedges on the bottom left and upper right corner of the spectrogram. (**g**) Final one-dimensional projection of the spectrum.

CHAPTER 5

Fine-structure measurements

As discussed on page 2, full-scale *ab initio* QED calculations of the fine-structure splitting in lithium-like ions have achieved comparable accuracy to experimental data in the last decade. Due to its high sensitivity to the full palette of QED effects despite a relatively simple structure with only one valence electron, this species offers a high-precision benchmark for few-body bound state QED, stimulating a demand for ever more precise experimental data. In the past, this isoelectronic sequence has been investigated for high nuclear charges Z. However, as shown in Section 2.1.1, QED contributions are also significant for low to medium atomic numbers.

In the present work, new data is provided for fine-structure splitting in the range of low to medium Z. Specifically, the lowest-lying splitting between $1s^2 2p\ ^2P_{1/2} \rightarrow 1s^2 2s\ ^2S_{1/2}$ and $1s^2 2p\ ^2P_{3/2} \rightarrow 1s^2 2s\ ^2S_{1/2}$ was studied (see Figure 5.1).

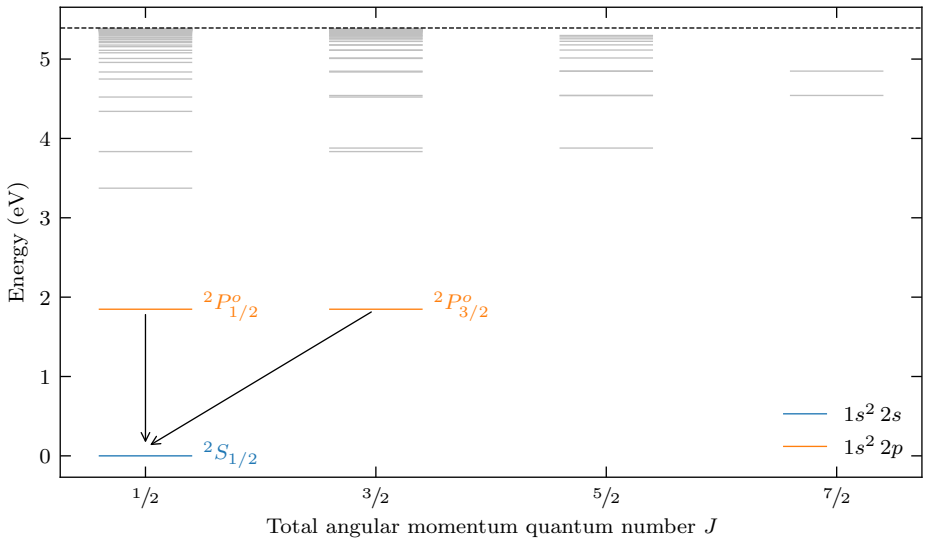

Figure 5.1: Level scheme for lithium. The ionisation threshold is represented by a dashed black line. Transitions investigated in this chapter (the fine structure doublet) are indicated by arrows.

All measurements were conducted at FLASH-EBIT (see Chapter 3 for details on this kind of apparatuses) in conjunction with the 3 m normal-incidence VUV spectrometer (described in detail in Section 4.1). The element of interest was injected into the trap in gaseous form and ionised sequentially to the lithium-like charge state by means of electron

impact ionisation. Plasma processes in the trap also provide excitation – mainly through scattering with electrons – for the detection of subsequent fluorescence. Calibration was achieved using known spectral lines within the same spectrum.

As discussed in Section 4.1.5, a rather high photon flux is needed for a decent signal-to-noise ratio (SNR). This requires a sufficient amount of ions in the trap favouring gas injection over other methods such as an external laser ion source (see Section 3.3.2). Consequently, gaseous elements were investigated due to the ease of handling them. Nitrogen, oxygen, neon and argon ($Z = 7, 8, 10$ and 18 respectively) were injected successfully. Despite the doublet of fine-structure lines being just outside the sensitive range of the instrument, carbon was also injected in the form of methane but no clear signal was observed.

Generally, impurities are not an issue in EBIT measurements. However, for a few specific electron beam energies ideal for the respective contamination, these have been observed in the past. Barium or tungsten emitted from the heated cathode, the constituents of air leaking into the chamber, as well as traces of helium from the cryocooler have been observed in previous measurements. For the low beam energies employed in this work, oxygen was found as an impurity in the trap for most of the fine-structure measurements (with the exception of argon) as well as for the iridium spectroscopy presented in the next chapter. One strategy to mitigate impurities, is the to optimise axial trapping potentials established by the voltages applied to the drift tubes.

There are voltages that can be applied to the individual drift tubes shaping the potential along the axis within the trap and there is a trap bias voltage applied to all of the drift tubes by means of a single power supply. For bias voltages of more than 200 V, the oxygen impurity is repelled by the positive potential. So most likely, it originates either from atoms crossing the electron beam outside the trapping region or it is released in the form of ions at the hot cathode or the collector. On the other hand, this observation is opposing the idea that oxygen is injected as impurity alongside the gas of interest.

When the species under investigation has a mass similar to the impurity (as for nitrogen), it can be cumbersome to get a good SNR. As discussed in Section 3.3.1 the capacity of the trap is limited, so the impurity can supersede the species of interest. Using the (positive) trap bias rather than the (negative) cathode bias voltage to accelerate the electron beam reduces the maximum beam current and therefore the trap capacity.

Another technique to suppress impurities is to raise the central drift tube potential in regular intervals ('inverting' the trap) for a short time to dump all ions from the trap. Although the species of interest is also affected by the dump, it accumulates much faster in the trap faster than the impurity due to the continuous gas injection. So in measurements averaging over time, this technique improves the signal overall.

Despite these efforts, it was not possible to remove oxygen completely for the nitrogen measurements, so these spectra were also used for determining the oxygen fine-structure during analysis.

In some spectra, evidence of neutral helium was found. However, since there are only few emission lines within the spectral range and the observed lines were weak, no countermeasures were required.

5.1 Experimental parameters

For each element, the spectrometer was moved to a fixed grating angle around the position of the fine-structure lines. Data was acquired and compared for open and closed gas injection to identify lines originating from the species of interest. Consequently, the trap and electron beam parameters were carefully optimised for signal strength and oxygen suppression (see Table 5.1 for the results).

Table 5.1: Optimal EBIT parameters for fine-structure measurements. Nitrogen and oxygen were typically measured using the same settings, for dedicated oxygen measurements, the dump was not used. Trap potentials are given as voltages for the three central trap electrodes from gun to collector side.

	N and O	Ne	Ar
Cathode bias (V)	−200	−500	−1375
Trap (V)	20-0-25	160-0-160	75-0-60
Trap bias (V)	50	0	200
Beam energy (eV)	250	500	1575
Beam current (mA)	20	45	175
Dump	1 s every 10 s	1 s every 15 s	2 s every 30 min

After optimisation, a few spectra were recorded per element in scanning mode (see Section 4.1.6) yielding a total exposure time of a few days per element.

Oxygen data was acquired using eight exposures with multiple scans each, amounting to a total exposure time of about 190 h. Some of these measurements were shared with nitrogen. In total, 166 h of data distributed across seven measurements were available for this species. For neon, a little less than 110 h across three datasets were successfully acquired, while argon was found to have more signal, so three measurements with a total acquisition time of 66 h were sufficient.

5.2 Data analysis

After pre-processing the data according to Section 4.1.7, the fine-structure splitting was obtained using the procedure described here.

5.2.1 Preparation

As per Section 4.1.6, a scan of the complete spectral range was broken down into multiple smaller ranges. Between these, a scan of the zero-order line was performed. Over the course of multiple hours, the line positions can move slightly due to long-term drifts. One cause for these shifts was identified to be correlated to changes in ambient temperature resulting in thermal expansion of the apparatus. Assuming the position of the zero-order line should be the same throughout an acquisition, measurements where significant shifts of ≈ 0.04 nm or more compared to the initial zero-order scan were found, were not included in final data analysis. For comparison, a typical full width at half maximum (FWHM) for a spectral line is about 0.03 nm. In each measurement, the complete spectral range was scanned multiple times.

In each scan, there are typically dozens of lines. Manually fitting thousands of peaks is

a very time consuming task. So finding and fitting peaks in a spectrum was automated and the results manually checked before using them for calibration. First, a baseline was found using the algorithm described in Section A.2, then the function `find_peaks` from the Python package `scipy.signal` was used to compile a list of maxima positions. Finally, each peak was individually fitted using a Gaussian.

5.2.2 Calibration

Each measurement was independently calibrated using data from the National Institute of Standards and Technology (NIST) Standard Reference Database version 5.7 [122] presented in Table B.1 in the appendix.

A cubic function $f(x) = ax^3 + bx^2 + cx + d$ was used to calibrate the dispersive axis (recorded as grating angle) into units of nm. To get an accurate estimate of the calibration uncertainty, this was done as a two-step process: First, an unweighted fit was used to get an approximation of the calibration function $f_1(x)$. This result was differentiated with respect to x giving the dispersion for any grating angle. By multiplying this value with the uncertainties for the line positions obtained when fitting the individual peaks in the spectrum with Gaussian functions, uncertainties in y are calculated for each data point. It is safe to assume that the uncertainty due to the line fit is independent of the wavelength uncertainties in the NIST atomic spectra database, so they can be added using the root sum squared:

$$\Delta y_i = \sqrt{\left(\left.\frac{\mathrm{d}f_1(x)}{\mathrm{d}x}\right|_{x=\mu_i} \Delta\mu_i\right)^2 + (\Delta\lambda_{\mathrm{NIST}})^2} \tag{5.1}$$

These combined values are used as weights in a second fit of the cubic polynomial resulting in the final calibration function. The covariance matrix also obtained by the fit is used in conjunction with the degrees of freedom to calculate a 1σ confidence band. For each species, one measurement and the respective calibration is presented in Figures 5.2, 5.3, 5.4 and 5.5.

Unless otherwise noted, wavelength or transition energy uncertainties in the following are given as the root sum square of the uncertainty arising from the determination of the maximum position for the respective line and the mean of the calibration fit residua.

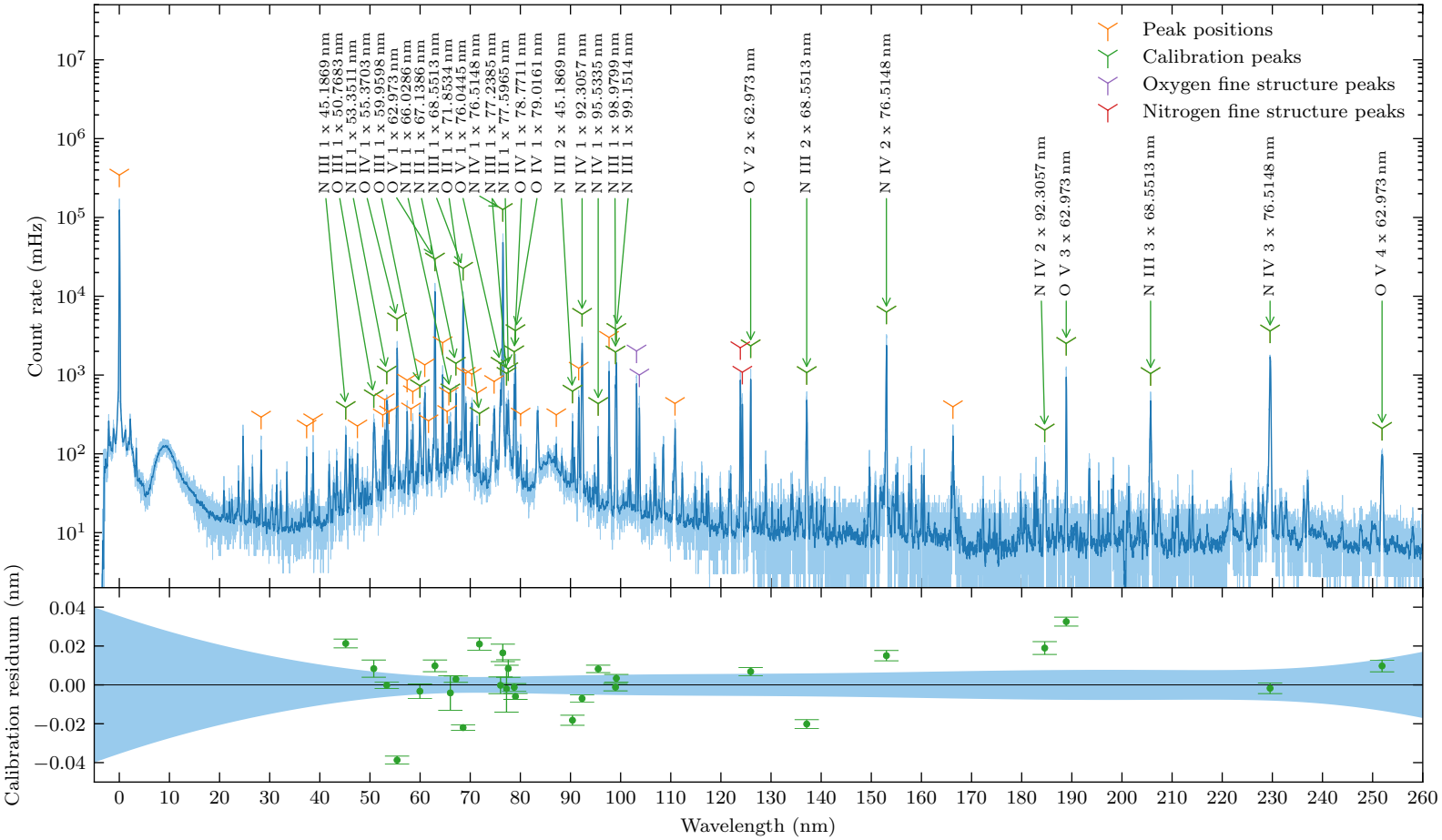

Figure 5.2: VUV spectrum of nitrogen. The upper part presents the complete spectral range. For better visibility, a moving average (dark blue line) was applied to the raw data (light blue line). All individually fitted peaks are indicated by Y shaped markers. Every peak used for calibration is annotated in the upper part by its species, spectral order and NIST wavelength. In the lower part of the Figure, residua for the calibration peaks are shown in relation to the 68.27 % confidence band of the fit result.

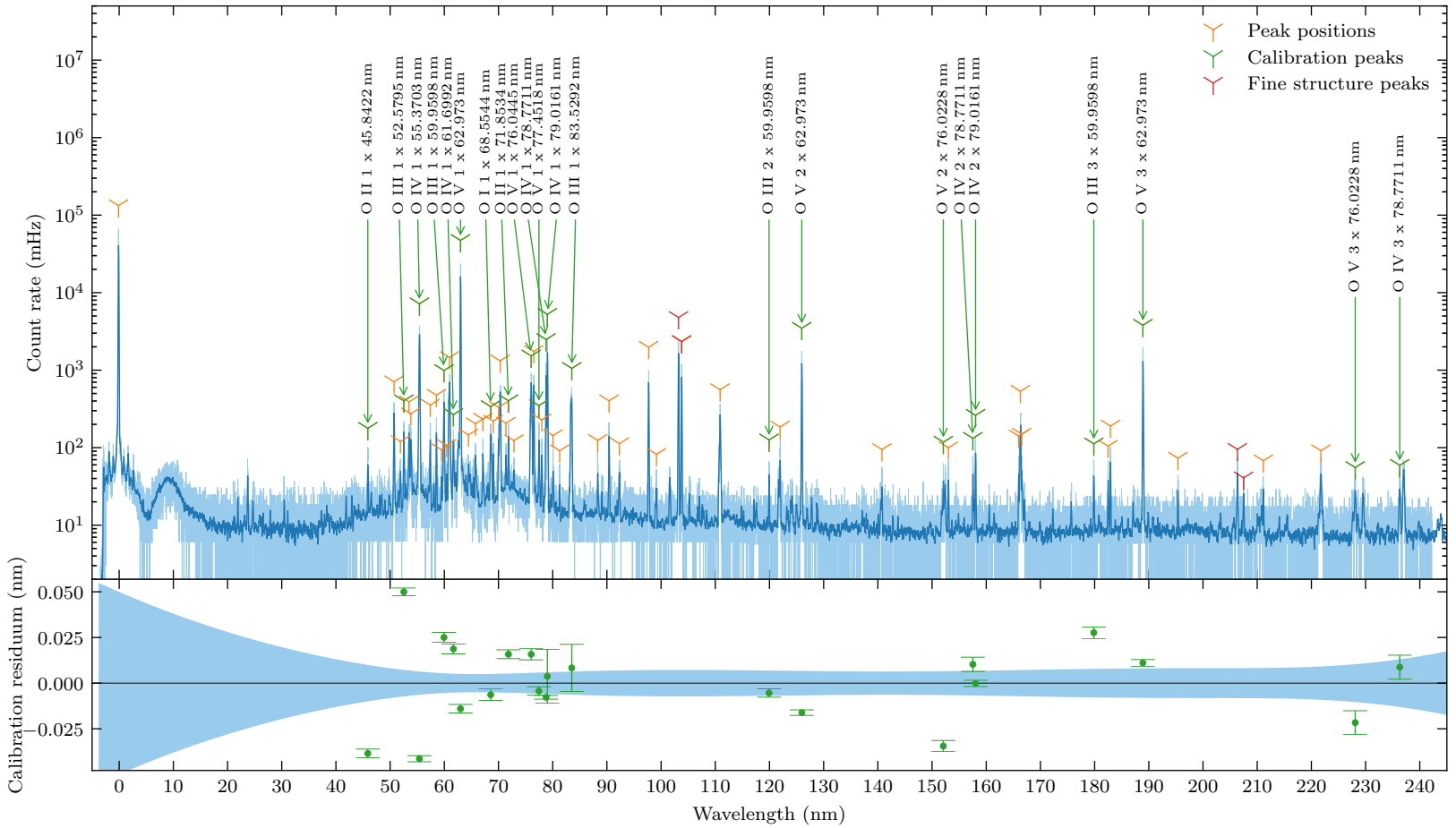

Figure 5.3: VUV spectrum of oxygen. The upper part presents the complete spectral range. For better visibility, a moving average (dark blue line) was applied to the raw data (light blue line). All individually fitted peaks are indicated by Y shaped markers. Every peak used for calibration is annotated in the upper part by its species, spectral order and NIST wavelength. In the lower part of the Figure, residua for the calibration peaks are shown in relation to the 68.27 % confidence band of the fit result.

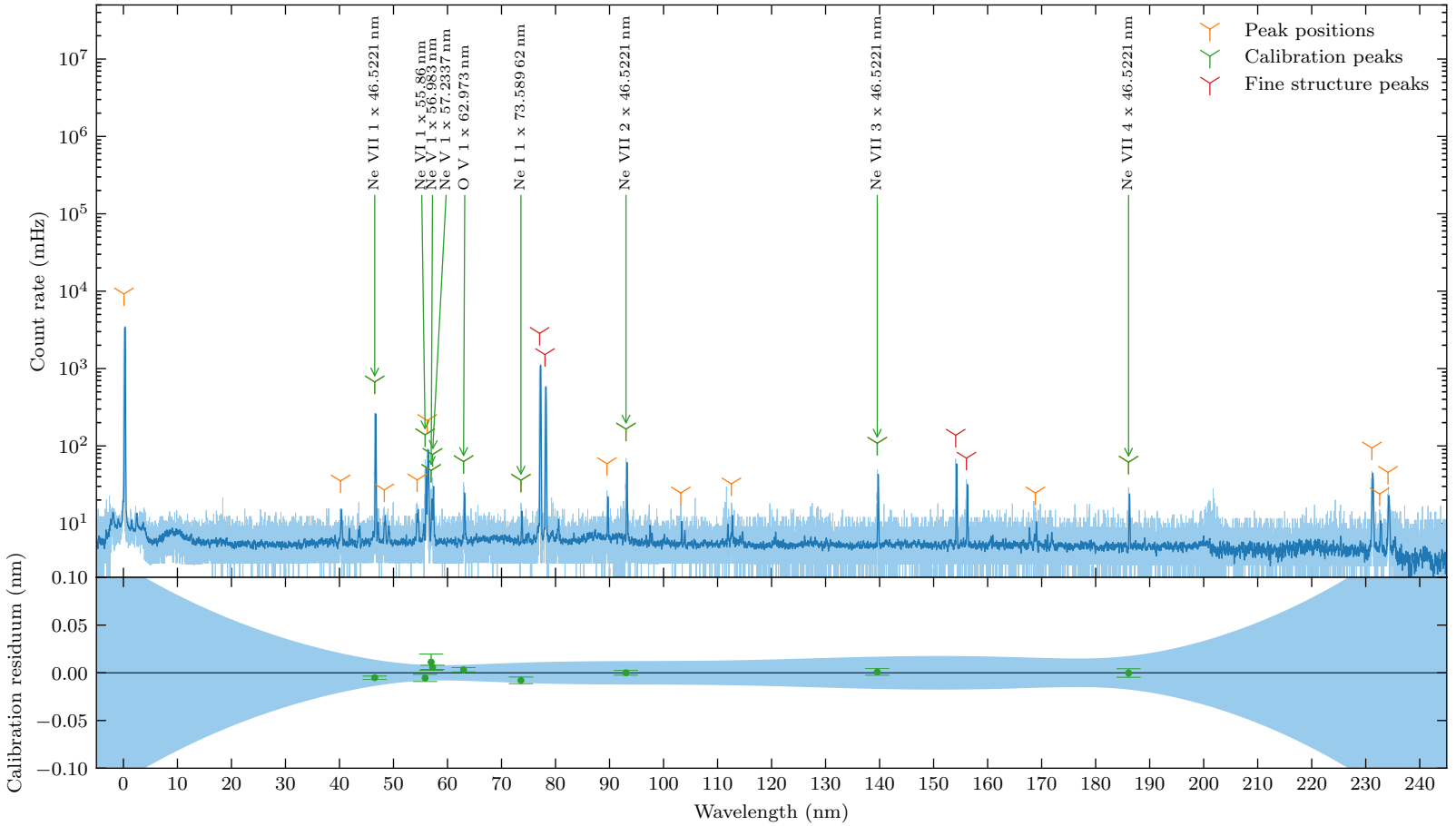

Figure 5.4: VUV spectrum of neon. The upper part presents the complete spectral range. For better visibility, a moving average (dark blue line) was applied to the raw data (light blue line). All individually fitted peaks are indicated by Y shaped markers. Every peak used for calibration is annotated in the upper part by its species, spectral order and NIST wavelength. In the lower part of the Figure, residua for the calibration peaks are shown in relation to the 68.27 % confidence band of the fit result.

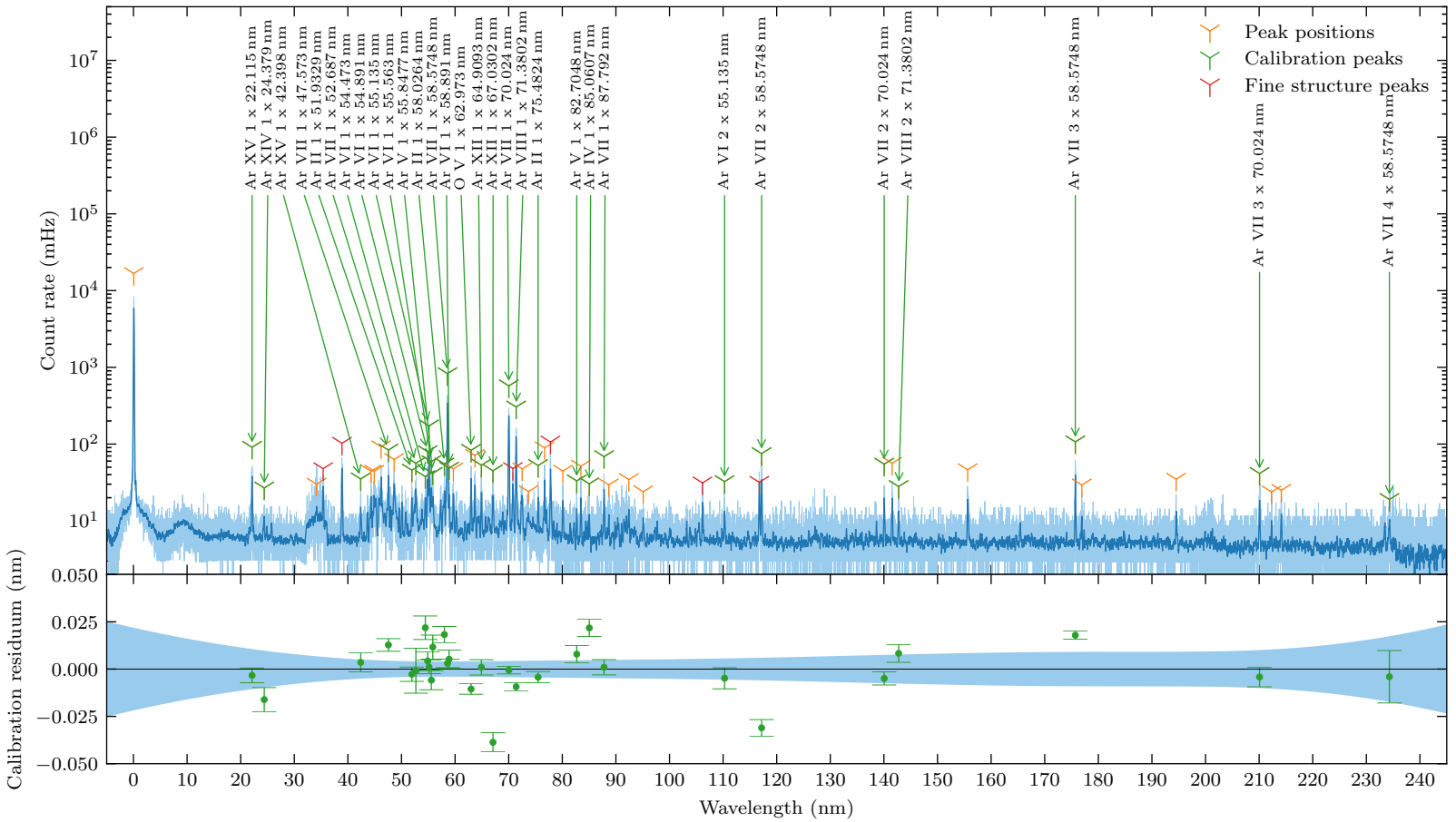

Figure 5.5: VUV spectrum of argon. The upper part presents the complete spectral range. For better visibility, a moving average (dark blue line) was applied to the raw data (light blue line). All individually fitted peaks are indicated by Y shaped markers. Every peak used for calibration is annotated in the upper part by its species, spectral order and NIST wavelength. In the lower part of the Figure, residua for the calibration peaks are shown in relation to the 68.27 % confidence band of the fit result.

5.3 Results

Before summarising the results, each species is discussed individually.

5.3.1 Nitrogen ($Z = 7$)

As mentioned in Section 5.1, oxygen impurities were most prominent in nitrogen spectra due to their similarity in mass and charge. So while injecting nitrogen gas, most spectra also contained oxygen lines and for some, the fine-structure lines of oxygen were also determined in spectra with nitrogen injection. So in Figure 5.2 fine-structure peaks for both species are marked.

Seven measurements denoted as 'N 1' to 'N 7' were performed over several weeks and calibrated separately yielding slightly different values for the two fine-structure peaks in N V shown in Figure 5.6. A weighed average was calculated using the individual uncertainties as weights, resulting in the values of 123.8737(45) nm and 124.2716(45) nm.

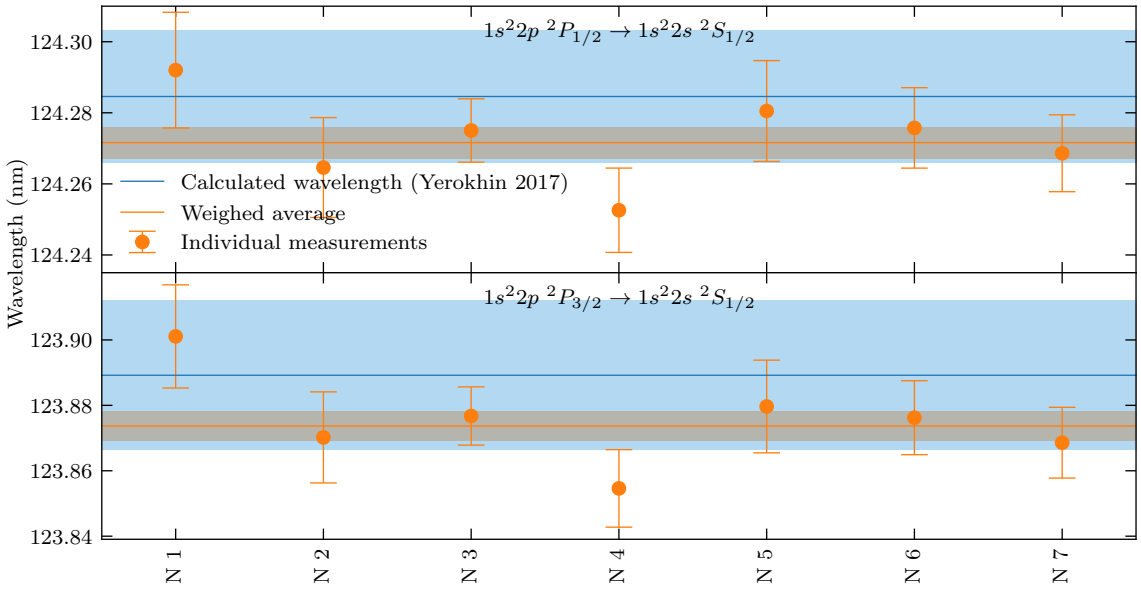

Figure 5.6: Fine-structure results for nitrogen. Wavelengths were determined for all seven measurements individually. Error bars represent the individual uncertainty that was also used to calculate the weighed average (shown as orange band in the background). For comparison the most recent theory calculation by Yerokhin *et al.* [203] is presented.

A comparison of the numerical values with other results from literature is given in Table 5.2 and a visual representation thereof is presented in Figure 5.7.

The nitrogen 'lithium doublet' was first observed in 1924 by Bowen and Millikan [34]. Ten years later, a systematic study was reported by Edlén using a high-voltage vacuum spark and a grazing-incidence vacuum spectrograph [71]. It took until 1963 for the doublet to be revisited by Bockasten *et al.* [32] due to the increased interest in plasma diagnostics in fusion reactors. Nitrogen was added in small quantities to the hydrogen gas of the fusion reactor SCEPTRE IV. The resulting emission lines were detected using a 3 m

Table 5.2: Comparison of nitrogen results with values available from literature.

Upper level	$1s^2 2p\ ^2P_{3/2}$ Wavelength (nm)	$1s^2 2p\ ^2P_{1/2}$ Wavelength (nm)
Other experimental work:		
Edlén (1934) [71]	123.8800(10)	124.2778(10)
Bockasten (1963) [32]	123.8805(10)	124.2803(10)
Hallin (1966) [99]	123.8821(10)	124.2804(10)
This work	123.8737(45)	124.2716(45)
Calculations:		
Yerokhin (2017) [203]	123.889(23)	124.285(19)
Kim (1991) [114]	123.8712	124.2699

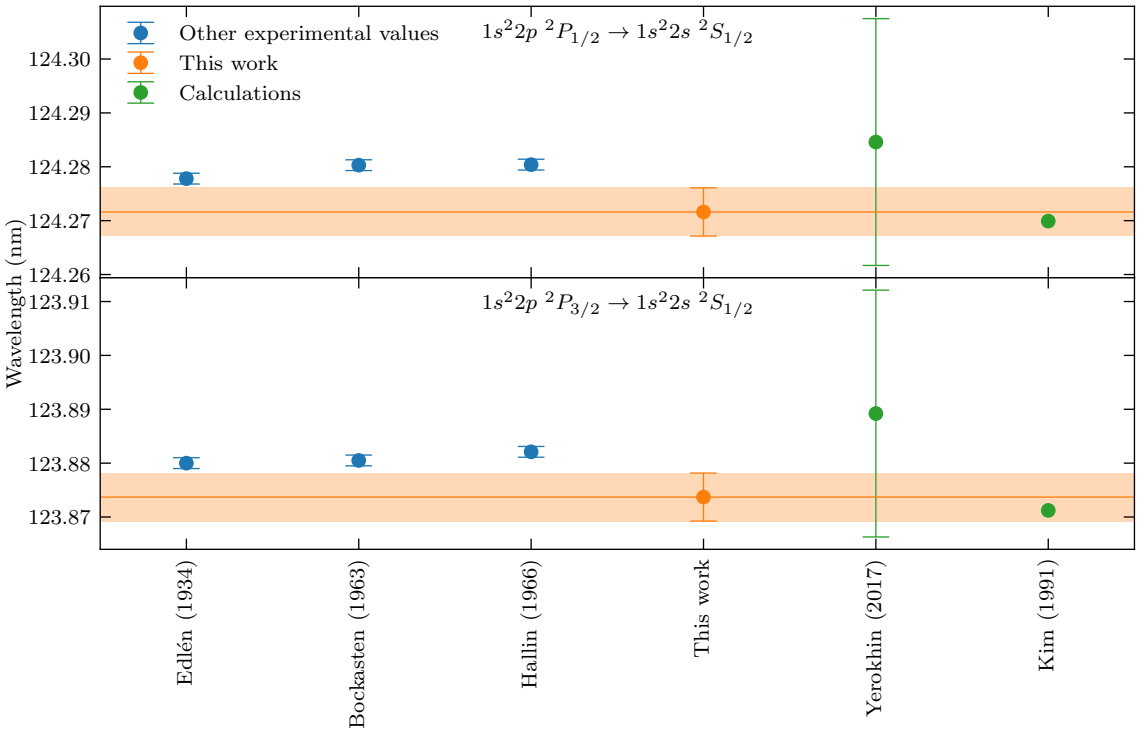

Figure 5.7: Comparison of the results for nitrogen with data found in literature. The error bar for this work represents the combined uncertainty. For Kim *et al.* no uncertainty is available.

normal-incidence vacuum spectrometer (Hilger E793). The values reported by Hallin a few years later used the same spectrograph but in conjunction with a theta-pinch discharge chamber [99].

It should be noted that the two results from fusion reactors are not completely independent measurements since they were done using the same instrument and Hallin was a co-author on the value reported by Bockasten *et al.* Furthermore, there is a significant disparity of 2.5σ between the value reported by Edlén and the fusion reactors for the transition $1s^2 2p\ ^2P_{1/2} \rightarrow 1s^2 2s\ ^2S_{1/2}$. A similar level of disagreement is found when comparing the values for the other fine-structure transition reported by Hallin and Edlén. This will be explored in more detail when discussing oxygen data of the same authors. In summary, although the uncertainties for the values reported here are larger than in previous experiments and these are just within 2σ, agreement of the present work with the other values is still better than their mutual agreement.

When comparing the results with calculations by Yerokhin *et al.* [203] and Kim *et al.* [114] good agreement and a better accuracy is found for this work. However, it should be noted that Yerokhin *et al.* was not conducting full-scale QED calculations but focussing on the calculation of doubly excited states. Therefore, the uncertainties provided in that work are quite large. For Kim *et al.* no uncertainty was available.

The level of accuracy in the present corresponds to 0.36 meV. Calculations by Yerokhin *et al.* [203] indicate contributions to the $^2P_{1/2}$ level for the Breit interaction of 3.81 meV. The mass shift (specific and normal mass shift) is −2.59 meV, and QED contributions are estimated to be −3.27 meV, so the experimental accuracy relative to the combined QED contributions is 17.6 %.

5.3.2 Oxygen ($Z = 8$)

Data analysis for oxygen was quite similar to that of nitrogen with the exception that in addition to three dedicated oxygen spectra recorded with gas injection (see Figure 5.3), five nitrogen spectra were used to determine the oxygen fine-structure splitting. A visual representation of the results and the weighed average is presented in Figure 5.8.

As for nitrogen, the 'lithium doublet' in oxygen was first observed by Bowen and Millikan but two years later, in 1926 [35]. The same doublet was investigated in the systematic study by Edlén mentioned in the discussion of nitrogen [71]. In 1963, Bockasten *et al.* [32] also published a value alongside their nitrogen value. Similarly to the nitrogen data, the values were reported to be slightly higher than the previous result. However, in this case, the accuracy was claimed to be slightly better, resulting in a disagreement of 3.3σ for the $^2P_{3/2} \rightarrow {}^2S_{1/2}$ transition.

Lithium-like oxygen is present in interstellar gas clouds and this disparity became apparent, when inconsistencies arose for the data analysis of the Copernicus (Orbiting Astronomical Observatory 3 (OAO-3)) satellite observations [110]: unexpectedly many of the observed radial gas velocities were negative when using the more recent value by Bockasten *et al.* Consequently, calibration of the spectrometer aboard the spacecraft and the reliability of the two existing laboratory measurements were questioned. This debate lead to further spectroscopic studies. Most notably by Ryabtsev [161] using a 6.65 m spectrometer in conjunction with two different light sources: a triggered glancing spark and

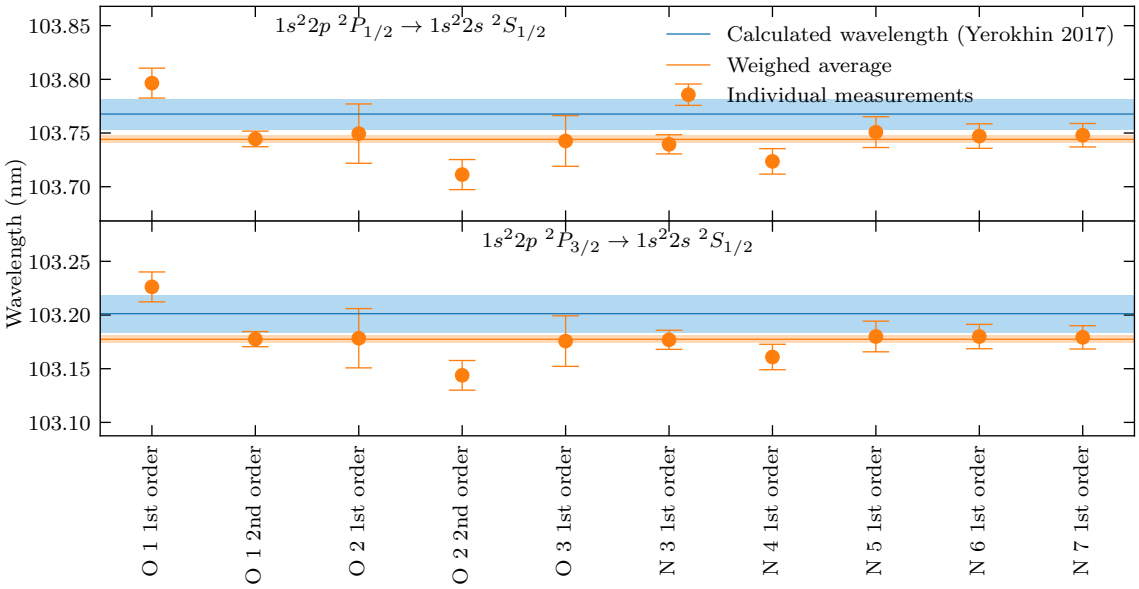

Figure 5.8: Fine-structure results for oxygen. Wavelengths were determined for all measurements individually. Error bars represent the individual uncertainty that was also used to calculate the weighed average (shown as orange band in the background). The element symbol in the labels of the x axis represent the gas being injected during the measurement. Orders refer to the spectral order which was used for wavelength determination. For comparison a calculation by Yerokhin *et al.* [203] is presented.

a three-electrode spark, Brown [45] analysed data from another measurement [183] utilising a Hinteregger condensed capillary discharge lamp and a 3 m grazing-incidence Hilger spectrograph. Finally, Kaufman and Martin [113] used sliding-spark and triggered-spark sources, as well as a 10.7 m normal-incidence spectrometer at NIST that are believed to be the most reliable values. However, all the values recorded after 1963 are significantly lower than the ones reported by Bockasten *et al.* which might be an indication for a systematic upward shift in the data reported by Bockasten *et al.* and Hallin for nitrogen. This could either be explained by the use of a fusion reactor as light source, or the spectrometer that was used in both measurements.

A comparison of the numerical values for oxygen can be found in Table 5.3 and a visual representation in Figure 5.9. Although the uncertainty is slightly lower for oxygen as compared to nitrogen, considerably more precise experimental values exist in literature. Additionally, the values reported here are considerably lower than other results from experiments or calculations. As to why this is the case, remains an open question.

First of all, the effect does not appear to be entirely linear; when comparing the fine-structure splitting (as opposed to the absolute transition energies), the present work has the lowest value: 66.01 meV, 65.79 meV, 65.89 meV, 65.86 meV, and 65.93 meV (same order as Table 5.3) compared to 65.64 meV in this work.

A misidentification in the calibration process is also unlikely due to Figure 5.8 showing

Table 5.3: Comparison of oxygen results with values available from literature.

Upper level	$1s^2 2p\ ^2P_{3/2}$ Wavelength (nm)	$1s^2 2p\ ^2P_{1/2}$ Wavelength (nm)
Other experimental work:		
Edlén (1934) [71]	103.1912(10)	103.7613(10)
Bockasten (1963) [32]	103.194 50(50)	103.762 70(50)
Ryabtsev (1975) [161]	103.192 40(50)	103.761 40(50)
Brown (1980) [45]	103.192 90(50)	103.761 70(50)
Kaufman (1989) [113]	103.192 60(50)	103.762 00(50)
This work	103.1774(37)	103.7441(37)
Calculations:		
Wang (2019) [187]	103.194 95(86)	103.763 14(87)
Yerokhin (2017) [203]	103.201(18)	103.768(14)
Kim (1991) [114]	103.187 46	103.757 04

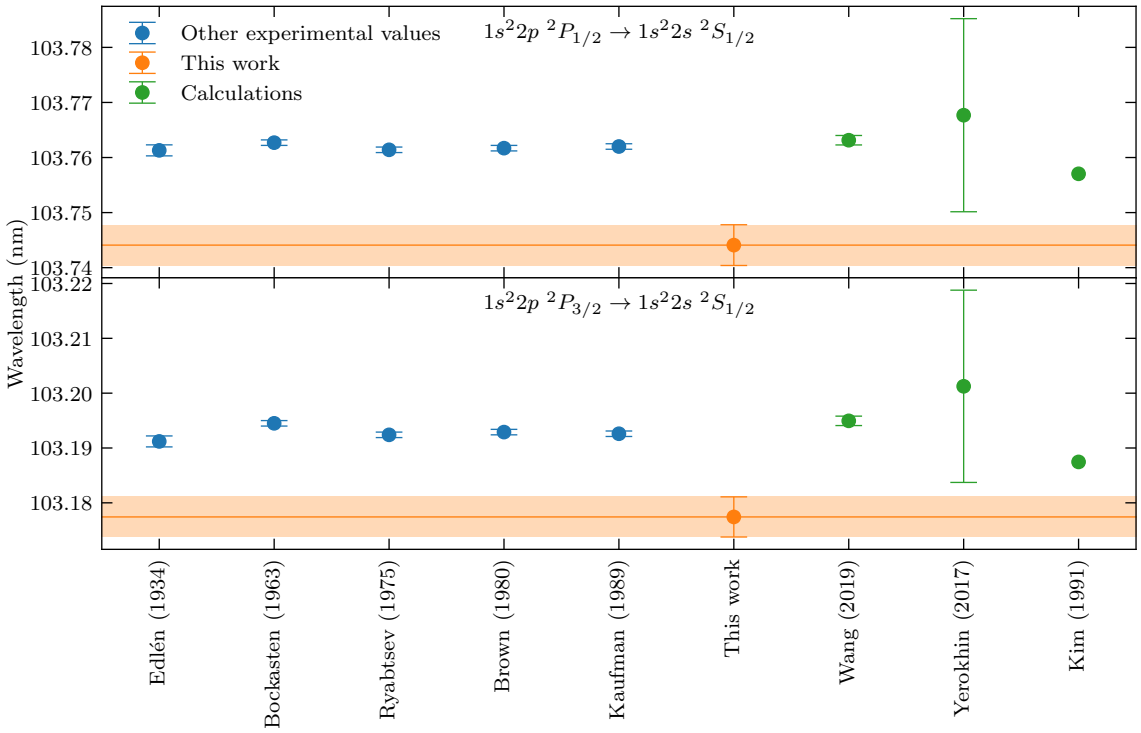

Figure 5.9: Comparison of the results for oxygen with data found in literature. The error bar for this work represents the combined uncertainty. For Kim *et al.* no uncertainty is available.

no systematic deviation between dedicated oxygen measurements calibrated using predominantly oxygen lines and the combined spectra with nitrogen (where known transitions in nitrogen were used for calibration). A more detailed comparison of the oxygen lines present in the spectra of neon and argon can be found in Section B.1.2 in the appendix. For the nitrogen data, also a small discrepancy in comparison to previous experiments is observed towards lower values. However, for nitrogen there is good agreement with theory and disagreement between the literature values is even larger than the disparity to the present work. Furthermore, when considering the difference to values found in literature against wavelength, no smooth dependency was found for these four values. Edlén published a table of calibration lines along with the fine-structure wavelengths [71]. Of the 24 oxygen lines used in the present work, eight are shared with the calibration in said work that reduces the risk of having chosen inaccurately known calibration lines.

Various effects could cause a systematic shift of different charge states or species with respect to each other. When investigating helium for example, the spectrum of He I is slightly shifted with respect to the spectrum of He II. However, this can be attributed to the atomic beam of the gas injection being at an angle of 45° with respect to the line-of-sight of the spectrometer. Due to the neutral atoms not being attracted by the trapping potential, their thermal velocity is high enough for the lifetime of the excited states to slightly shift the centre of luminosity with respect to that of the ion cloud. However, independent of the cause for such a shift, the calibration residua presented in Figures 5.2 and 5.3 should also suffer from this effect and a systematic deviation should be seen when compared to the residua of other species. This is not the case.

Since the spectrometer does not use a slit, each spectral lines is a convolution of the natural line width with an optical image of the ion cloud. So the observed line widths should be a good indicator for systematic effects on the geometrical shape of the ion cloud. However, no trend was found for line widths of nitrogen or oxygen lines, as well as low charge states compared to highly charged ions.

Albeit the systematic deviation being not yet understood, the values reported here are within 1.7σ of the uncertainty stated by Yerokhin *et al.* So a few magnitudes of corrections in the calculation of the $^2P_{1/2}$ level are provided here. The uncertainty not including the systematic effect discussed above, is 0.45 meV. The Breit interaction is predicted to be of 6.80 meV, the mass shift (again the sum of the specific and normal mass shift) is −3.13 meV, and combined QED effects are −5.71 meV. However, due to the disparity with other experimental values in literature, a systemic uncertainty of approximately 1.28 meV would be more appropriate. So due to the systematic effect, a comparison with QED calculations is less accurate than for nitrogen despite the larger nuclear charge and relative accuracy of the spectrometer being expected to be better.

5.3.3 Neon ($Z = 10$)

As for nitrogen and oxygen, all the independently derived wavelengths are presented in Figure 5.10 first. Then, the weighed average is compared to literature values in Table 5.4 and Figure 5.11.

Due to the ionisation potential of 207.27 eV [121] required for lithium-like neon, the first observation of the fine-structure doublet was reported much later than for nitrogen

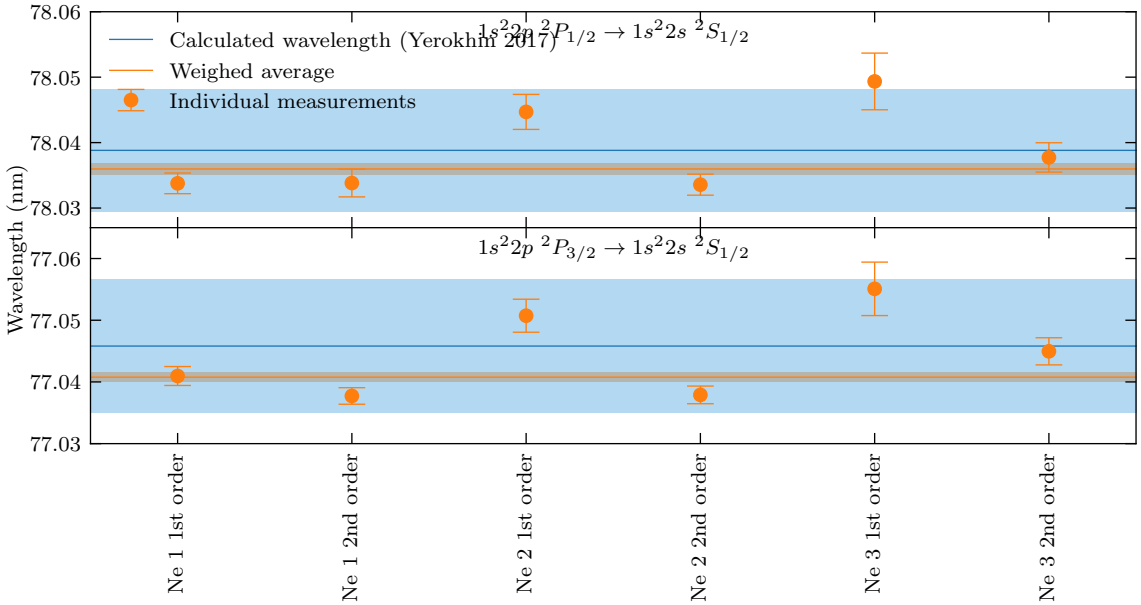

Figure 5.10: Fine-structure results for neon. Wavelengths were determined for all measurements individually. Error bars represent the individual uncertainty that was also used to calculate the weighed average (shown as orange band in the background). Orders refer to the spectral order which was used for wavelength determination. For comparison the most recent theory calculation by Yerokhin *et al.* [203] is presented.

and oxygen by Fawcett *et al.* in 1961 [83] using trace elements introduced into a high-temperature deuterium plasma in the Zeta reactor and a 3 m normal-incidence vacuum spectrograph. Two years later, Bockasten *et al.* confirmed the value using the same setup as described for nitrogen and oxygen [32].

Both previous observations agree well with each other. However, the values reported here agrees well with the first value by Fawcett *et al.* but for the transition $1s^2 2p\ ^2P_{1/2} \rightarrow 1s^2 2s\ ^2S_{1/2}$, there is a significant discrepancy of 4.25σ to the value reported by Bockasten *et al.* Considering the discrepancies of the values they reported for nitrogen and oxygen with other data as well as their significant discrepancy with calculations such as the most accurate one to date by Kozhedub *et al.* [118], there is a strong indication that their estimated uncertainty might be to small. The uncertainties reported here are of comparable magnitude to theirs but there is much better agreement with most recent calculations available as far as uncertainties are given for the calculated values. None are available for Chen and Cheng as well as Kim *et al.* [50, 114].

For $Z = 10$, more calculations are available than for the other elements studied in the present work. Blundell [31] used relativistic many-body perturbation theory and introduced *ab initio* calculations of the QED screening potential. Chen and Cheng [50] supplemented rigorous QED with relativistic CI calculations. But most notably, Kozhedub *et al.* provides the calculated value with the smallest uncertainty and is in good agreement with the

Table 5.4: Comparison of neon results with values available from literature.

Upper level	$1s^2 2p\ ^2P_{3/2}$ Wavelength (nm)	$1s^2 2p\ ^2P_{1/2}$ Wavelength (nm)
Other experimental work:		
Fawcett (1961) [83]	77.042(3)	78.034(3)
Bockasten (1963) [32]	77.040 90(50)	78.0324(10)
This work	77.040 77(73)	78.035 97(84)
Calculations:		
Yerokhin (2017) [203]	77.046(11)	78.0388(94)
Sapirstein (2011) [171]	77.0423(48)	78.0364(49)
Kozhedub (2010) [118]	77.0414(19)	78.0349(20)
Chen (1995) [50]	77.040 88	78.032 45
Blundell (1993) [31]	77.0418(24)	78.0339(25)
Kim (1991) [114]	77.039 82	78.032 95

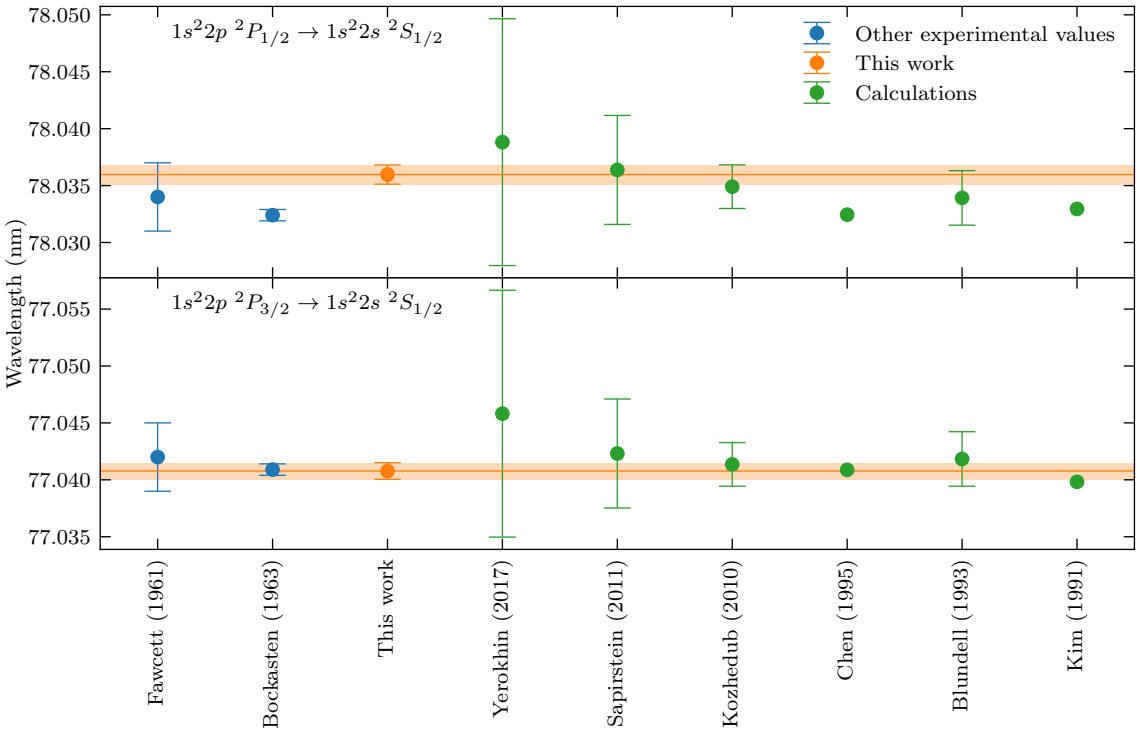

Figure 5.11: Comparison of the results for neon with data found in literature. The error bar for this work represents the combined uncertainty. For Chen and Cheng as well as Kim *et al.* no uncertainties are available.

present work. More detail on this calculation is provided in Section 2.1.1. Sapirstein and Cheng calculated one- and two-photon diagrams at an unprecedented level and applied the two-loop Lamb shift at a later stage. Additionally, three-photon diagrams were estimated [171].

The reported uncertainty of 0.17 meV on the transition $1s^2 2p\ ^2P_{1/2} \rightarrow 1s^2 2s\ ^2S_{1/2}$ is sensitive to the Breit interaction of 17.2 meV, the nuclear recoil of −4.2 meV and the one-loop QED effect in the magnitude of −20.0 meV (as well as the screening thereof being about 5.8 meV). For the combined QED effect, this corresponds to a relative sensitivity of 1.2 % [118, 203].

5.3.4 Argon ($Z = 18$)

All the independently derived wavelengths are presented in Figure 5.12. The weighed average is compared to literature values in Table 5.5 and in Figure 5.13.

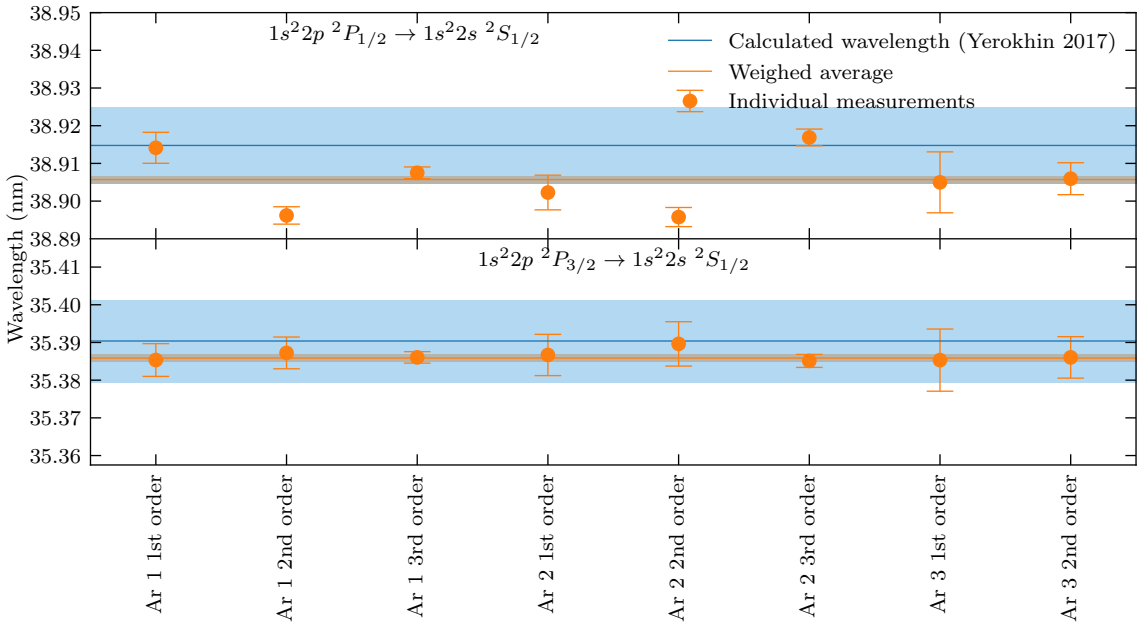

Figure 5.12: Fine-structure results for argon. Wavelengths were determined for all measurements individually. Error bars represent the individual uncertainty that was also used to calculate the weighed average (shown as orange band in the background). Orders refer to the spectral order which was used for wavelength determination. For comparison the most recent theory calculation by Yerokhin and Surzhykov [202] is presented.

As opposed to nitrogen, oxygen and neon, there is no laboratory data available for argon yet. So instead, solar observations during the Skylab mission are given for comparison. Two solar flares were observed on 15 June and 9 August 1973 using the NRL spectroheliograph. The spectra were analysed by Widing and Purcell [192], Sandlin *et al.* [169], and Dere [56]. Widing and Purcell are claiming the highest accuracy.

Considering the spread of these values with respect to each other, agreement is quite good with the exception of the value provided by Sandlin *et al.* [169]. When comparing

Table 5.5: Comparison of argon results with values available from literature.

Upper level	$1s^2 2p\ ^2P_{3/2}$ Wavelength (nm)	$1s^2 2p\ ^2P_{1/2}$ Wavelength (nm)
Other experimental work:		
Widing (1976) [169]	35.3880(20)	38.9110(20)
Sandlin (1976) [192]	35.3920(30)	38.9140(30)
Dere (1978) [56]	35.3840(30)	38.9080(30)
This work	35.3859(10)	38.905 72(94)
Calculations:		
Yerokhin (2012) [202]	35.390(11)	38.9148(100)
Sapirstein (2011) [171]	35.3866(10)	38.9055(12)
Kozhedub (2010) [118]	35.385 84(61)	38.906 40(61)
Blundell (1993) [31]	35.3846(10)	38.9055(12)
Kim (1991) [114]	35.387 33	38.908 38

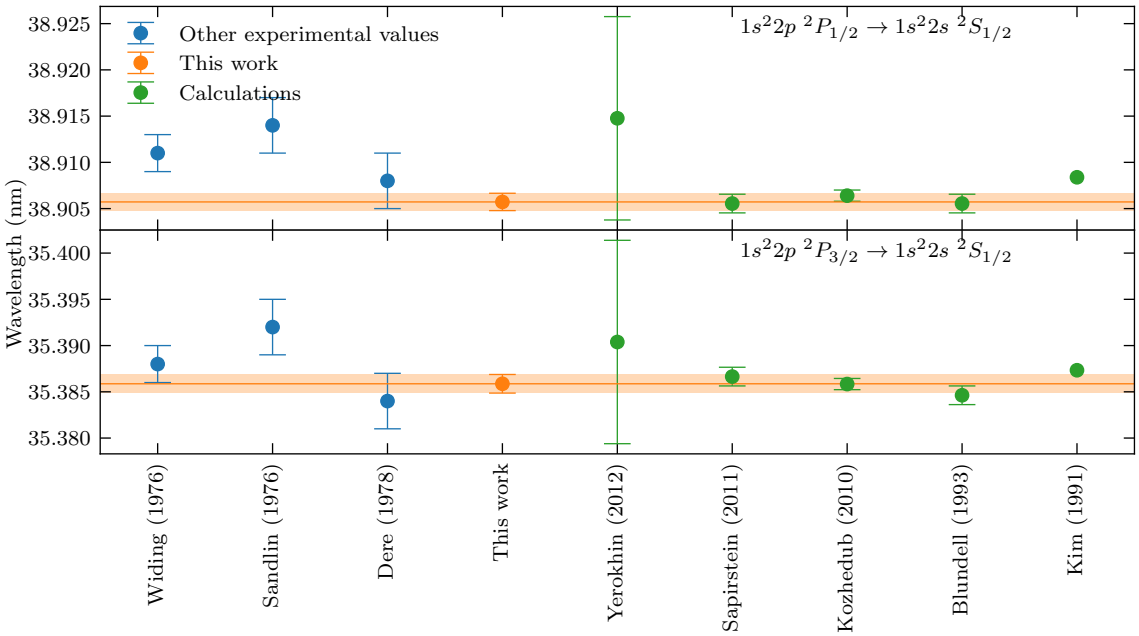

Figure 5.13: Comparison of the results for argon with data found in literature. The error bar for this work represents the combined uncertainty. For Kim *et al.* no uncertainties are available.

the values presented in this work to data based on calculations, no disparity can be found from the values published in the last decade. It should be noted that the solar Ar XVI $^2P_{3/2}$ line is blended with a transition line of Fe XV.

In terms of theory, see Section 5.3.3 for details, since the data available is from the same sources with the exception of Yerokhin and Surzhykov [202]. However, the latter is very similar to Yerokhin *et al.* [203] with the exception of different ranges of Z being calculated.

In summary, the values reported here are the first laboratory observation of the fine-structure doublet of argon. Furthermore, it is the most accurate value to date and in excellent agreement with the most recent *ab initio* QED calculations.

The reported uncertainty of 0.77 meV on the transition $1s^22p\ ^2P_{1/2} \rightarrow 1s^22s\ ^2S_{1/2}$ is sensitive to the Breit interaction of 154 meV, a nuclear recoil of −8.2 meV and a one-loop QED effect in the magnitude of −157 meV (as well as the screening thereof being about 26 meV). For the combined QED effect, this corresponds to a relative sensitivity of 0.59 %.

5.4 Summary

The lack of experimental data for the fine-structure doublets of $1s^22p\ ^2P_{1/2} \rightarrow 1s^22s\ ^2S_{1/2}$ and $1s^22p\ ^2P_{3/2} \rightarrow 1s^22s\ ^2S_{1/2}$ for moderate nuclear charges Z has been addressed in the present. The elements nitrogen, oxygen, neon and argon have successfully been observed (for wavelengths, see Table 5.6, for energies Table 7.1).

Table 5.6: Fine structure doublets of neon and argon reported in this work.

Upper level	$1s^22p\ ^2P_{3/2}$ Wavelength (nm)	$1s^22p\ ^2P_{1/2}$ Wavelength (nm)
Nitrogen ($Z = 7$)	123.8737(45)	124.2716(45)
Oxygen ($Z = 8$)	103.1774(37)	103.7441(37)
Neon ($Z = 10$)	77.040 77(73)	78.035 97(84)
Argon ($Z = 18$)	35.3859(10)	38.905 72(94)

For nitrogen, only three laboratory measurements have been available. Even the most recent one was published more than half a century ago. Since there are significant mutual discrepancies between these and with the values reported here (on the level of 2σ), further investigation is required. However, the results of the present work are the only ones in agreement with both of the calculations by Yerokhin *et al.* [203] and Kim *et al.* [114].

Oxygen on the other hand has previously been studied in more detail due to its relevance for astronomy. There is quite a significant disagreement to the values reported here. For a more detailed discussion see page 92 and Section B.1.2 in the appendix.

For neon, the new values are of comparable accuracy to the best experimental data found in literature by Bockasten *et al.* [32]. It should be noted, though, that the wavelengths presented in their work deviate significantly from other values found in literature for oxygen, nitrogen, and neon, so the claimed accuracy is probably overestimated. Furthermore, for the present work, a better agreement with calculations and the only other laboratory result available (Fawcett and Purcell [83]) was found.

Finally, for lithium-like argon, both the first observations in a laboratory and the most

accurate values so far are presented here. Previous solar observations have been limited in accuracy due to the Ar XVI $1s^2 2p\ ^2P_{3/2} \rightarrow 1s^2 2s\ ^2S_{1/2}$ emission line being blended with Fe XV. Reasonable agreement has been found with these previous experiments and excellent agreement with the most recent state-of-the-art QED calculations is reported.

It is worth mentioning that a lot of data on fine-structure splitting in other charge-states of argon is available in literature. Hydrogen-like argon has been measured a few times from 1983 to 2014 [25, 41, 124, 135], helium-like argon was even measured in 2018 [1, 41, 46, 58, 123, 124, 133] together with the beryllium-like [133] charge state.

In terms of precision tests for QED calculations, a comparison of the accuracy reported here with different contributions to the calculated energies is shown in Tables 5.7 and 5.8. Overall, the most accurate transition energy reported in this work is $^2P_{3/2} \rightarrow {}^2S_{1/2}$ in lithium-like neon at a level of 0.15 eV corresponding to 9.5 ppm. However, due to QED effects being more pronounced at higher nuclear charges, the most accurate test of these effects was found in the transition $^2P_{1/2} \rightarrow {}^2S_{1/2}$ in lithium-like argon that was tested to the level of 0.59 %.

Table 5.7: Accuracy of the results reported in this work compared to calculated contributions to the transition energies for $^2P_{3/2} \rightarrow {}^2S_{1/2}$ ([203] was used for N, O, and Ne, as well as [202] for Ar) in units of meV.

	N	O	Ne	Ar
Breit interaction	−2.0	−3.1	−5.9	−20
Mass shift	−2.6	−3.1	−4.2	−8.2
QED	−3.1	−5.4	−13	−125
Level of accuracy	0.36	0.45	0.15	0.99

Table 5.8: Accuracy of the results reported in this work compared to calculated contributions to the transition energies for $^2P_{1/2} \rightarrow {}^2S_{1/2}$ ([203] was used for N, O, and Ne, as well as [202] for Ar) in units of meV.

	N	O	Ne	Ar
Breit interaction	3.8	6.8	17.3	154
Mass shift	−2.6	−3.1	−4.2	−8.2
QED	−3.3	−5.7	−14	−133
Level of accuracy	0.36	0.45	0.17	0.77

In comparison to the calculations along the isoelectronic sequence, good agreement was found with Yerokhin *et al.*, Yerokhin and Surzhykov, Sapirstein and Cheng, Kozhedub *et al.*, and Blundell for all atomic charges Z. Although there is no uncertainty stated for the values provided by Chen and Cheng as well as Kim *et al.*, there is reasonable agreement at a similar level as compared to Yerokhin *et al.* The only significant discrepancy was with respect to Wang and Yan. Since the comparison can only be made for oxygen, however, this can probably be attributed to the systematic effect observed in oxygen which is discussed in more detail in Section 5.3.2.

In conclusion, it was demonstrated that accurate QED benchmarks can be performed

for ions in the range of $Z = 7$ to 18 along the lithium-like isoelectronic sequence and that reliable laboratory data is sparse in the VUV wavelength regime. The most recent measurement available in literature for comparison to the present work was Kaufman and Martin from 1989 [113]. On the other hand, there are quite recent *ab initio* full-scale QED calculations claiming similar or better accuracy as the data presented here. Namely, these are Wang and Yan [187] for oxygen and Kozhedub *et al.* [118] for argon from 2019 and 2010 respectively. Both calculations demonstrate the urgent need for better experimental data in order to benchmark future improvements to few-body bound-state QED calculations at the highest level of accuracy. Improvements in structure calculation will allow for better predictions in more complex atomic systems and eventually improve plasma diagnostics in astronomy and fusion reactors.

CHAPTER 6

Iridium spectroscopy

After Berengut *et al.* [19] suggested neodymium-like iridium for testing the variation of fundamental constants (see page 3), it has been an ongoing effort for both experiment and theory to understand the corresponding level scheme and spectrum.

EBIT experiments are well suited for the study of highly charged iridium: the ionisation potential of around 406.3 eV [47] is well within the capabilities even of compact devices. Furthermore, permanent interaction with the electron beam provides plenty of excitation processes for core-excitation that is required for subsequent detection of florescence.

As discussed in the introduction, Ir^{17+} is close to the $4f$-$5s$ level crossing. It is suspected that $4f^{13}5s^1$ is the ground state. Other configurations with levels very close to the ground state are $4f^{12}5s^2$ and $4f^{14}$. A Grotrian diagram of these configurations is given in Figure 6.1. All of the observed transitions that have been identified so far, are also presented there.

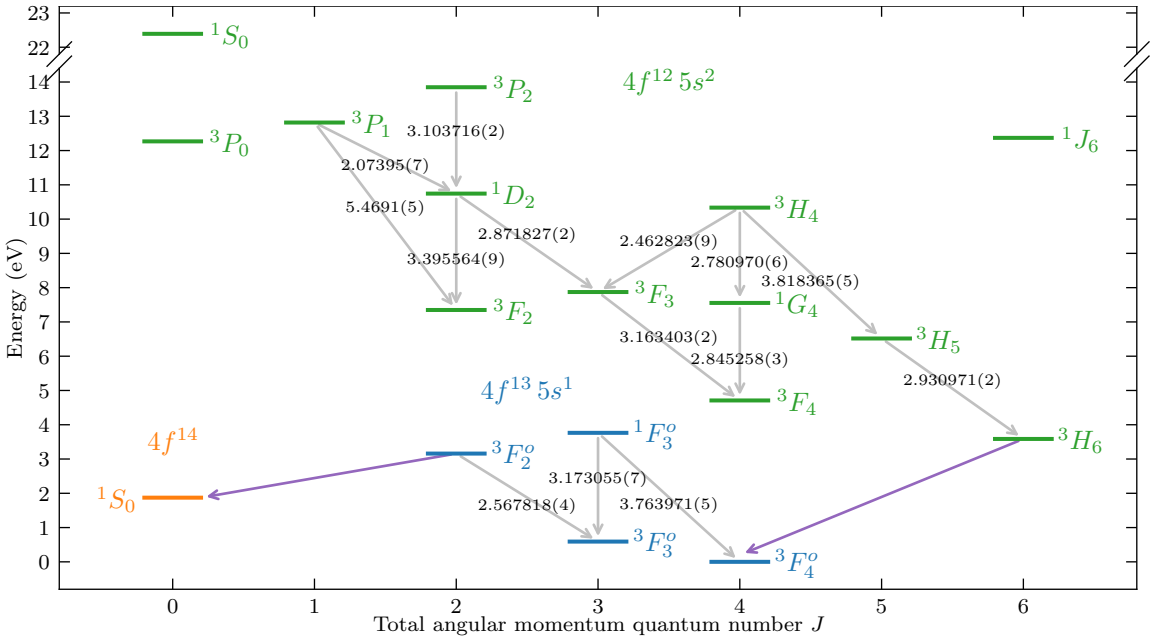

Figure 6.1: Grotrian diagram of Ir^{17+} near the ground state. Gray arrows indicate experimentally confirmed transitions [15, 197]. Otherwise CI calculations by Cheung *et al.* [51] were used to set energies in the diagram. Transition proposed for fine-structure variation experiments are shown in purple.

Very promising candidates for narrow transitions in the optical regime is one from the $4f^{12}5s^{2\,3}H_6$ level to the ground state $4f^{13}5s^{1\,3}F_4^o$ that could be induced by hyperfine mixing with $4f^{12}5s^{2\,3}H_5$ resulting in a forbidden M2/E3 transition. The most abundant isotope ^{193}Ir has a nuclear spin of $I = 3/2$ facilitating hyperfine transitions. Highest sensitivity can be achieved by comparing this transition with another one from $4f^{13}5s^{1\,3}F_2^o$ to $4f^{14\,1}S_0$. It is suspected, the forbidden E3 transition is enabled by mixing with the $4f^{13}5s^{2\,1}P_3$ state. Both transitions have opposite signs in their dependence on the fine-structure constant, so comparing the two combines their sensitivities. Compared to the Hg^+ and Al^+ clock comparison experiment mentioned in the introduction, a combination of the two iridium lines provides a 12.8-fold increase in sensitivity [19, 69, 158].

Other transitions, such as $4f^{12}5s^{2\,3}F_2$ to $4f^{14\,1}S_0$ are expected to offer higher sensitivities but in practice these could be broadened by competing E1 decay channels [19].

Specifically addressing the slow, forbidden transitions i. e. using quantum logic spectroscopy [142] requires dedicated laser systems and good knowledge about the exact transition energies. However, due to their low transition rates, a direct observation using conventional spectroscopy methods is not feasible. So other transitions linking the relevant levels need to be found and identified.

In the last years, Windberger *et al.* and Bekker *et al.* [14, 15, 197, 198] have found and identified lines. These are shown in Figure 6.1. However, an important yet elusive quantity, is the energy separation between the three configurations $4f^{13}5s^1$, $4f^{12}5s^2$ and $4f^{14}$. Especially the former two are particularly challenging to calculate due to their $4f$ holes. Very recent advances in computational methods allowed to include the $4d$ shell into the valence space in CI calculations [51]. These improved predictions place them 0.12 eV to 0.74 eV higher than the most elaborate approaches utilised so far (Cowan code [166], CI [19], CI-DFS [197] and FSCC [197]).

This places many interconfiguration transitions in the VUV range. Especially the ones with the highest expected intensities. Aforementioned experimental efforts were based on earlier calculations and have therefore focussed on optical (229 nm to 403 nm) and EUV (16 nm to 23 nm) spectroscopy.

For this work, the new 3 m VUV spectrometer described in Section 4.1 was used at FLASH-EBIT and new spectral lines were found in this range (see Section 6.3). Systematic studies in preparation of the experiment are discussed in Section 6.2. Finally, the new data is compared with calculations in Section 6.4. A general introduction to the operation of EBIS/EBIT devices can be found in Section 3.1.2.

6.1 FAC studies

To aid the line identification process, calculations have been conducted in the course of this work using the flexible atomic code (FAC). The main objective was to supplement data for higher-energy configurations, since these are not available from previous, more elaborate calculations. Especially when considering energies of the newly found EUV transitions (see Table 6.4) of 30.8 eV to 41.1 eV, these are well outside the range of previously calculated levels.

In Figure 6.2 a Grotrian diagram is provided of all levels up to 100 eV extending the scope to the configurations $4f^{12}\,5s^1\,5p^1$, $4f^{11}\,5p^1$, and $4f^{13}\,5p^1$.

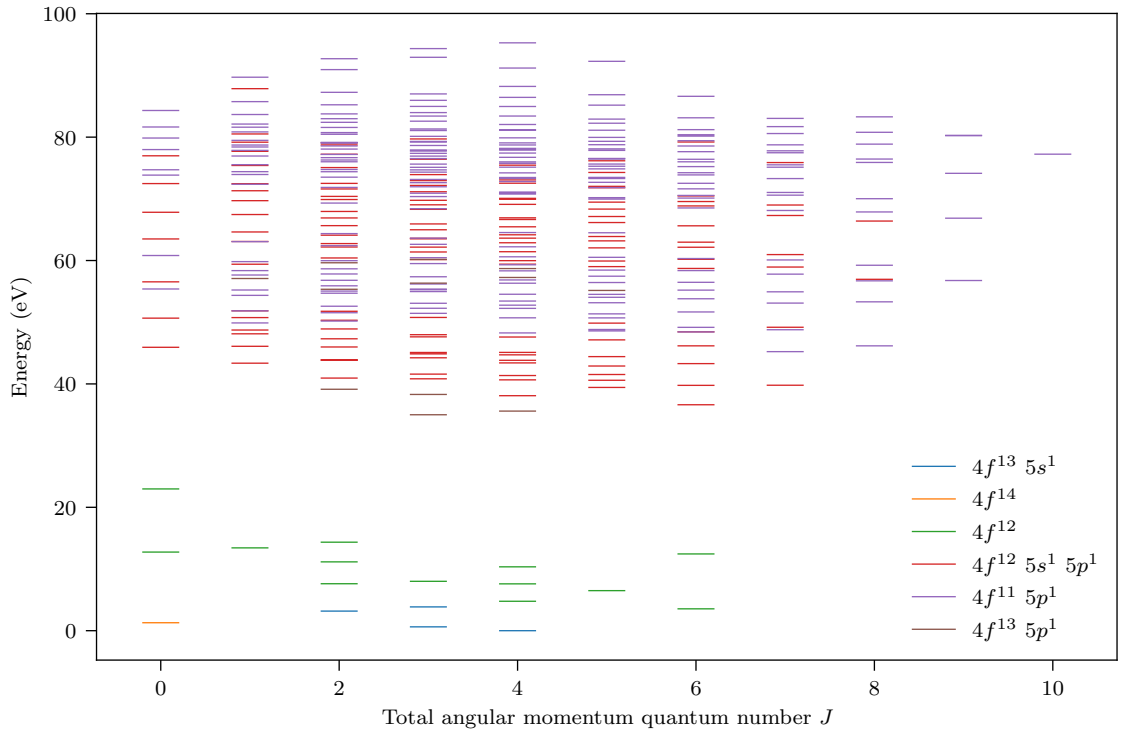

Figure 6.2: Extended Grotrian diagram of neodymium-like iridium. All levels up to 100 eV are shown here (410 levels in total).

So far, no lines have been found experimentally in the range between 25.4 eV to 30.1 eV even though this spectral range has been investigated. When consulting Figure 6.2, this could be explained by the gap between the manifold of levels ranging from 0 eV to 22.4 eV and the second one from ≈ 38 eV to 95 eV. It is safe to assume that electron impact ionisation is populating levels at random for the energy range discussed here. However, de-excitation is not random but a cascade down into the ground state or a metastable level that results in transitions closer to the ground state being more intense due to their higher population. Inelastic electron-ion collisions can also de-populate metastable states either by electron impact excitation or by radiationless de-excitation.

As for many other atomic structure codes, an important input parameter for FAC calculations is which configurations to include in the calculation. For this work, a semi-empirical approach was used by first running a set of 1988 calculations, where only the configurations $4f^{13}\,5s^1$, $4f^{12}\,5s^2$ and one additional level obtained using the Aufbau principle was included (see Section 2.1.2). From these results, configurations were ranked by how close calculated transitions were to the experimental values. Finally, a new calculation was done, including the 50 most significant configurations at the same time. This two-step approach has the advantage that the first step of many computationally less expensive calculations can be run in parallel on a cluster. Parallelisation is limited for a single, complex FAC calculation due to the use of shared memory for the inter-process communication

limiting computation to a single node.

Including the 50 most relevant configurations according to this method yielded results in agreement with more elaborate calculations at the level of 0.3 eV. It should be noted, however, that only the three lowest-lying configurations can be compared and that two of these have transitions used in the optimisation procedure. So it could well be that accuracy for levels in other configurations is not improved by this method. But for $4f^{13}\,5s^1$, $4f^{12}\,5s^2$ and $4f^{14}$ the disparity to the more elaborate calculations is much lower compared to previous FAC results (see Table 6.1).

Table 6.1: Comparison of different calculation results of the lowest levels in Ir^{17+}. All values are given in eV.

Conf.	Term	CI [51]	FSCC [197]	CI-DFS [197]	Cowan [197]	FAC [197]	FAC this work
$4f^{13}\,5s^1$	$^3F^o_4$	0	0	0	0	0	0
	$^3F^o_3$	0.592	0.578	0.604	0.525	0.599	0.623
	$^3F^o_2$	3.123	3.119	3.105	3.246	3.180	3.176
	$^1F^o_3$	3.768	3.744	3.788	3.796	3.821	3.857
$4f^{14}$	$^1S_0$	1.535	1.686	0.871	0.700	7.396	1.290
$4f^{12}\,5s^2$	$^3H_6$	3.755	3.003	3.641	4.215	8.843	3.544
	$^3F_4$	4.905	4.159	4.748	5.249	10.043	4.770
	$^3H_5$	6.670	5.912	6.530	7.249	11.912	6.493
	$^3F_2$	7.616	6.820	7.479	7.911	12.930	7.613
	$^1G_4$	7.719	6.970	7.556	8.237	13.007	7.593
	$^3F_3$	8.081	7.291	7.916	8.558	13.418	8.004
	$^3H_4$	10.480	9.737	10.285	11.109	15.870	10.352
	$^1D_2$	11.068	10.219	10.943	11.391	16.558	11.156
	$^1J_6$	12.539	11.638	12.627	12.605	17.820	12.442
	$^3P_0$	—	11.656	12.351	12.540	18.050	12.743
	$^3P_1$	—	12.326	13.141	13.382	18.832	13.425
	$^3P_2$	—	13.327	14.044	22.070	19.830	14.346
	$^1S_0$	—	21.684	23.031	—	28.220	22.979

The semi-empirical results presented here are very close to the most recent *ab initio* results by Cheung *et al.* [51]. The choice of configurations included in the FAC calculation is critical for accurate results. Prior to selecting configurations as described above, a smaller set of configurations was used for a rigorous test of the effects of correlation: all possible combinations of any number of these were used to calculate the level structure. When comparing the results with experimental data, it was found that including or excluding specific configuration individually as opposed to sets of them together were minute.

In addition to energy levels, calculations can also be used to derive radiative decay rates (see [51]). Line intensities in a plasma such as the one in an EBIT are determined by the product of the upper level populations and aforementioned rate. So in addition to the energy levels and radiative transition rates, collisional-radiative modelling is required to

estimate these populations by means of a rate matrix and population vector. See Figure 6.3 for such a calculation on the Ir^{17+} level scheme.

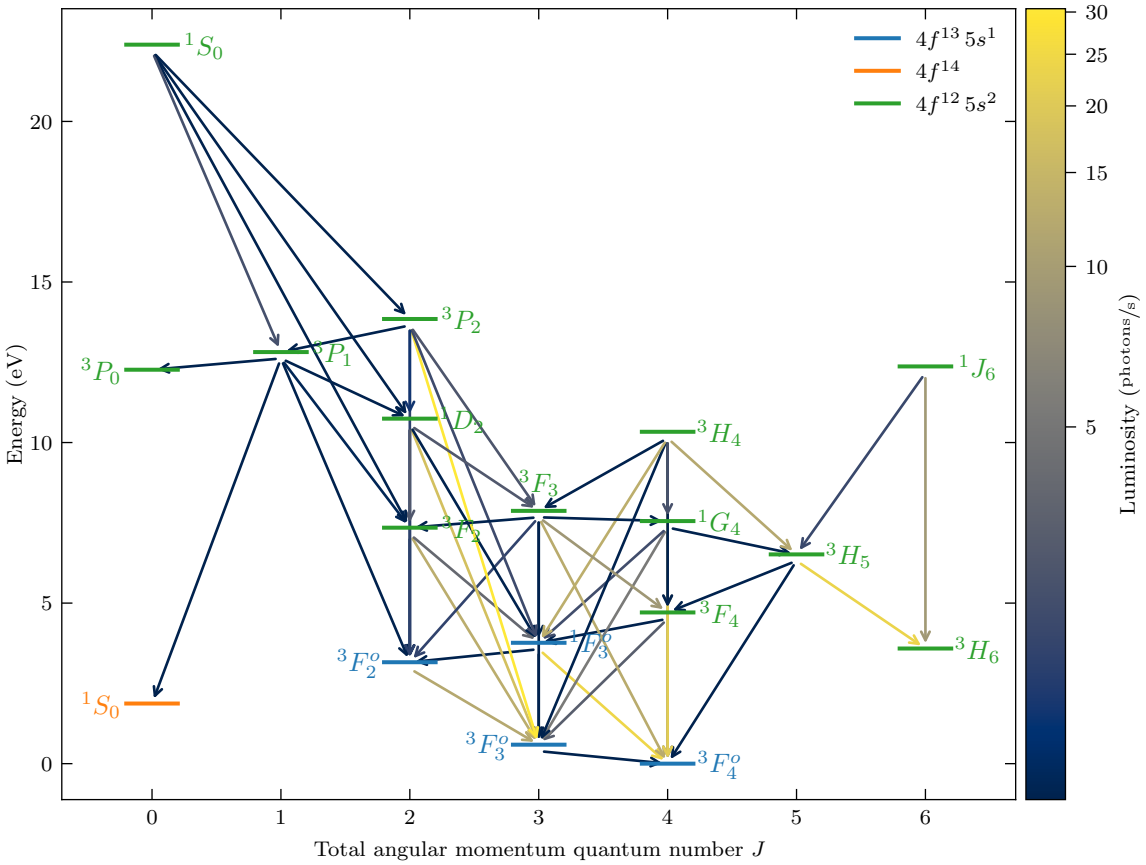

Figure 6.3: Transition rates as calculated using the collisional-radiative modelling code in FAC. Energy levels are the same as in Figure 6.1 while luminosities were used from the collisional-radiative modelling presented in [15]. Only transitions with a luminosity of more than 0.01 photons/s are shown.

When comparing line luminosities in Figure 6.3 with transition rates found in [51] it is apparent that there are discrepancies which can not be attributed to the population of the upper level. For example, Cheung *et al.* expect the transitions $^3H_4 \rightarrow {}^3F_3^o$ and $^3H_4 \rightarrow {}^3F_4^o$ to be the strongest interconfiguration ones. However, the latter is much weaker according to the FAC data. Since both transitions originate from the same level, the upper level population is the same and cannot explain the discrepancy. Collisional-radiative modelling based on the improved FAC structure calculation presented above has not been realised. Calculating transition rates and collisional excitation cross sections is a prerequisite but not yet feasible for the number of levels that need to be included.

6.2 Experimental parameters

A key challenge when performing spectroscopy of EBIT plasmas often is the simultaneous presence of many different charge states in the trap. So systematic approaches are required

to attribute spectral lines to the correct charge state. These are explained in the following. Furthermore, previous experiments were performed at the Heidelberg Electron Beam Ion Trap (Heidelberg EBIT). Due to the size of the 3 m VUV instrument and spatial constraints around that EBIT, it was not feasible to perform measurements in this new spectral range at the same device. So the established parameters needed to be adapted for this work at FLASH-EBIT.

6.2.1 Injection

Neodymium-like iridium was obtained by subjecting a metal-organic compound with low vapour pressure to vacuum. As in previous experiments, a powder of methylcyclopentadienyl(1,5-cyclooctadiene)iridium (CAS number 132644-88-3) was used. After evaporation, the gas is expanded through a needle valve, two differentially pumped vacuum chambers and multiple slits into the trap, where it is ionised by electron impact ionisation.

Due to the low solid-angle of the spectrometer compared to the spectroscopy performed in previous works, this setup was improved by adding the capability to align the needle valve with the line-of-sight to the trap without the need for venting neither the injection system nor the trap. To aid evaporation, the injection system vacuum chamber was also heated in initial measurements. However, only a minor increase in signal strength was seen at the cost of an increase in impurities and chemical degradation of the powder, so that it needed to be replenished more often. Causing disruptions of the long-term data acquisition, heating the injection system was abandoned for the final measurements presented here.

6.2.2 Charge-state verification

Once iridium atoms have reached the trap, electron impact ionisation is sequentially increasing the charge state until electron capture and ionisation processes are in equilibrium (see Section 2.5.4). The most relevant parameters to control the final charge state distribution during an experiment are the electron beam energy and current. Another key aspect is the magnetic field that is kept at the maximum value for most experiments to facilitate ideal compression of the electron beam. However, Heidelberg EBIT differs from FLASH-EBIT in some key aspects, including the magnetic field (8 T in the former apparatus and 6 T in the latter), gun and trap design. These result in a slightly different space-charge potential for the same electron beam parameters (see Section 3.3.1), so the ideal parameters for the production of neodymium-like iridium needed to be found by comparison with previous experiments.

Since some of the data presented in [14] and [15] was acquired using the compact EUV spectrometer (description in Section 4.2), a direct comparison was realized by using this instrument at FLASH-EBIT. EUV data from the same device was matched to verify the charge state composition of the plasma. New data from the spectrometer was also used to optimise injection of the iridium compound and to monitor contamination by other elements.

The difference in space charge is compensated by using a different acceleration potential for the electron beam. To determine the ideal values, EUV spectra were acquired while incrementally raising the voltage. These spectra are assembled into a two-dimensional spectrogram where the abscissa represents wavelength and the ordinate electron beam energy.

See Figure 6.4 **b** for the result. Please note some of the differences to DR measurements such as the one shown in Figure 3.13: the beam current is changed incrementally rather than continuously due to the CCD sensor being limited to read-out after completion of the exposure time (as opposed to the MCP, where timestamps are available for individual events). Furthermore, the axes assignment is switched by convention.

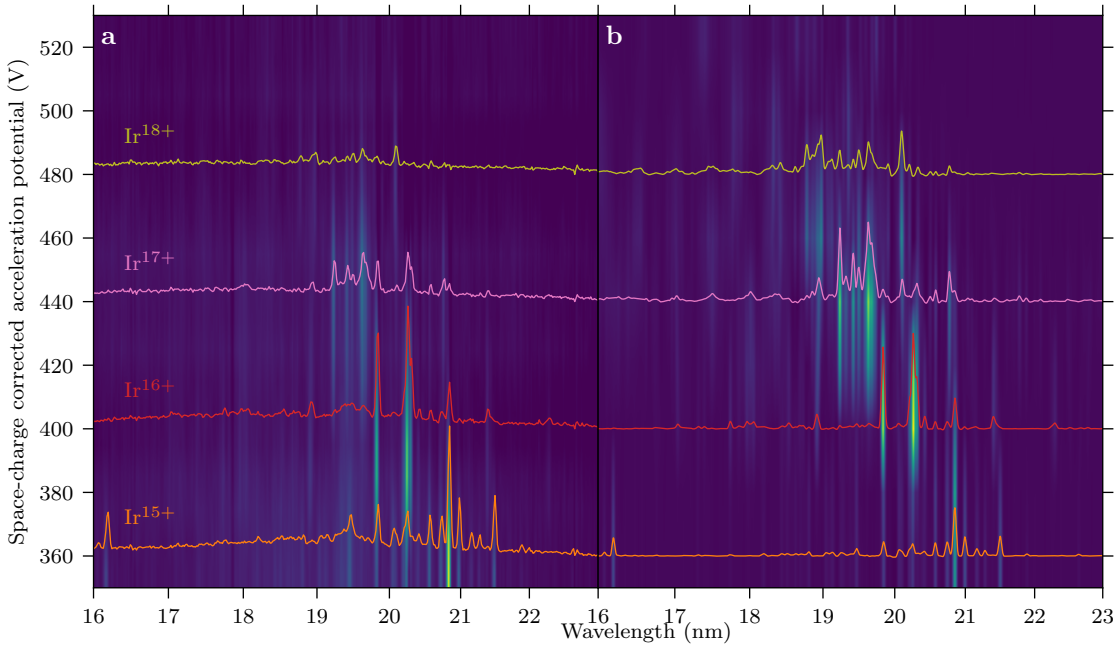

Figure 6.4: Charge-state verification for iridium. EUV spectra were acquired for different electron beam energies and assembled into a spectrogram. The dataset presented in **a** was acquired by Bekker *et al.* (see Figure 4.8 of [14]) at the Heidelberg EBIT. Individual spectra at the ideal energies for the respective charge state are also shown the spectrogram. **b** was acquired at FLASH-EBIT using different parameters. The dominant ion species can be identified by matching the spectra. Linear interpolation along the ordinate and baseline subtraction was used for visualisation.

Spectra in Figure 6.4 were recorded in the known EUV range with the highest beam current allowing for stable electron beam for each acceleration energy. These datasets were pre-processed and projected as described in Section 4.2.3 before being assembled into the two-dimensional spectrogram presented here. As the electron beam energy increases, fluorescence of Ir^{17+} emerges around the ionisation potential of 406.3 eV [47], peaks at approximately 440 V and, with the onset of fluorescence of Ir^{18+} around the same energy, reduces in intensity, before vanishing completely around 500 V. For the diagram, acceleration energies were reduced by 90 V, so that the onset of fluorescence matches calculated ionisation potentials in order to compensate the space-charge potential.

Bekker *et al.* assembled a similar diagram in Figure 4.8 of [15]. This data is also shown in Figure 6.4. From comparison it was deduced that lines attributed to the neodymium-like charge-state of iridium are most pronounced for a space-charge corrected

acceleration potential of $U_{\text{beam}} = 440\,\text{V}$ (corresponding to an uncorrected acceleration energy of $U_{\text{acc}} = 530\,\text{V}$). Not all plasma parameters could be reproduced, however: in direct comparison, some relative differences in intensity between the ion species can be seen. Nevertheless, the charge states can clearly be identified.

6.2.3 EBIT parameters

After identifying the correct charge state, other EBIT parameters were optimised for maximum signal intensity using the strongest EUV and VUV lines. The most relevant being the shape of the trap potential. There are nine drift tubes available to which voltages can be applied. Additionally, all of them can be biased by an offset voltage. The optimised set of parameters can be found in Table 6.2.

Table 6.2: Optimal parameters determined for Ir^{17+} spectroscopy at FLASH-EBIT.

Cathode bias (V)	−440
Anode voltage (V)	160
Trap (V)	0-30-0
Trap bias (V)	0 to 150
Beam energy (eV)	470 to 620
Beam current (mA)	30

As for the fine-structure measurements, oxygen was initially observed as impurity in the trap (see page 82). Due to the difference in mass between iridium and oxygen, beam energies being higher than 470 eV, and the slightly inverted trap configuration, the most intense oxygen lines were barely above the signal-to-noise level after optimisation even without dumping the trap in regular intervals. Furthermore, spectral lines of oxygen do not display the characteristic dependency on the electron beam energy observed for neodymium-like iridium. Even though the misidentification of an oxygen line as iridium is highly unlikely, the impurity was carefully monitored.

6.2.4 Additional systematics

Calibration was performed before attributing individual spectral lines to a specific charge state. As mentioned in the last section, oxygen was observed as impurity in the trap and for the actual measurement, trap potentials were optimised to suppress contamination. For calibration however, the opposite was done: while iridium was injected into the EBIT, the trap was optimised for highest intensity in the strongest emission line of O^{4+} at $(62.973 \pm 0.005)\,\text{nm}$. A combined spectrum of iridium and oxygen was recorded at an acceleration potential of $U_{\text{acc}} = 495\,\text{V}$ (see Figure 6.5) and compared to a spectrum optimised for a clean iridium signal at $U_{\text{acc}} = 490\,\text{V}$ to prevent misidentification of calibration peaks. Similar to the procedure presented in Section 5.2.2, the calibration fit was performed twice. In a first fit, statistically correct weights were attained for the second run, so that a confidence band can be calculated for the complete spectral range. The combined spectra and calibration is shown in Figure 6.5.

Uncertainties given for peak positions are the root sum square of the confidence band at the respective wavelength and the uncertainty of the peak position as per the Gaussian fit.

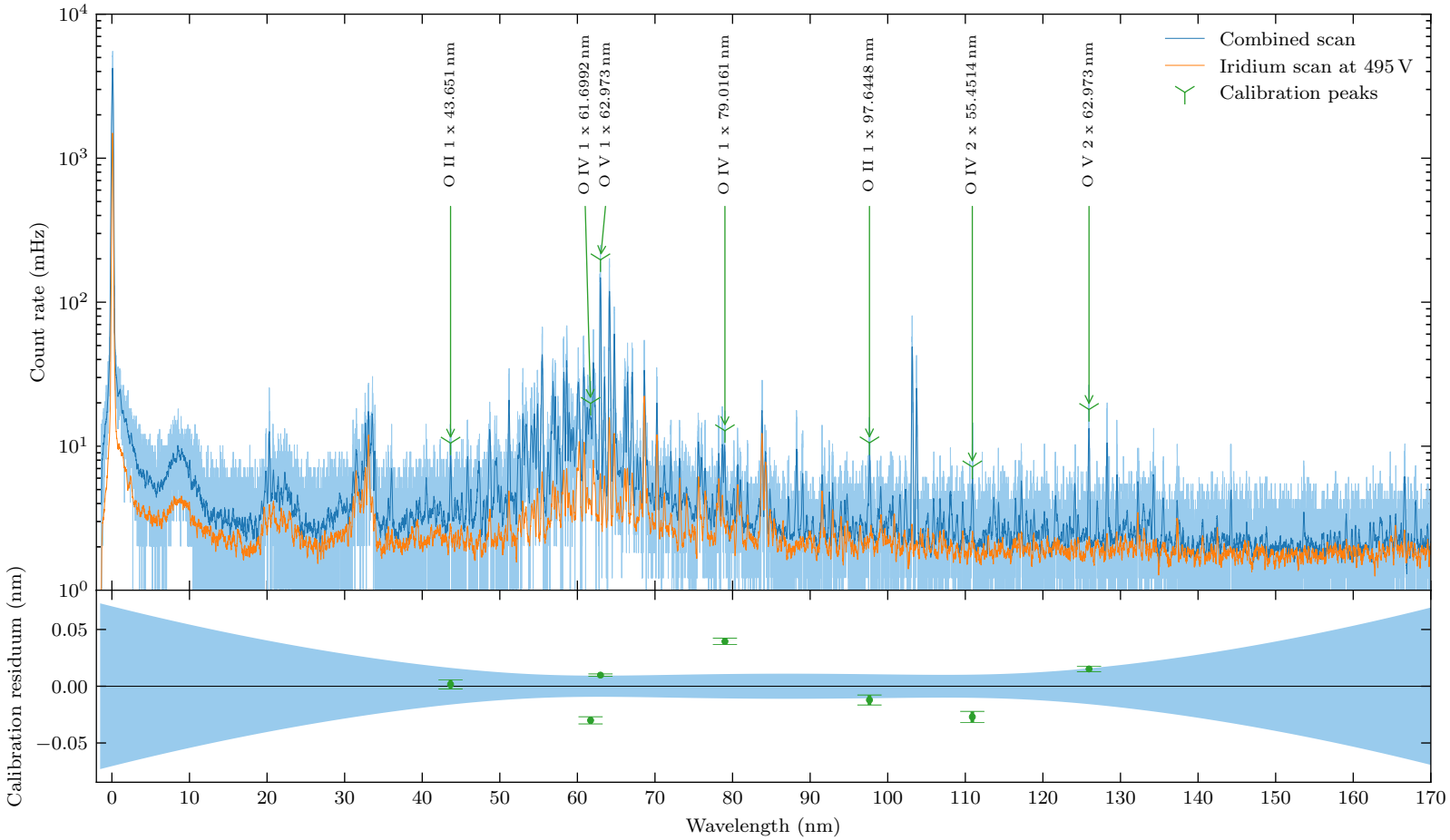

Figure 6.5: Combined VUV spectrum of iridium and oxygen used for calibration. Additionally, a clean iridium spectrum recorded at a similar beam energy is shown. For the combined scan, raw data is shown in light blue, otherwise the spectra are smoothed for visualisation. Calibration peaks are indicated in the upper part of the graph, while the lower part shows their residua and the 68.27 % confidence band of the fitted cubic function.

Apart from the oxygen impurity mentioned above, no additional impurities were found. The VUV spectrum of oxygen was well known at the time of data acquisition. As systematic checks, both the EUV spectrum was checked for unknown emission lines by comparison with previous iridium measurements. Furthermore, a scan of the full spectral range of the VUV spectrometer was performed using the same experimental parameters but without injecting iridium into the trap. No unknown spectral lines were found in this data, nor in EUV data acquired simultaneously.

6.3 New spectral lines

As for the EUV spectra discussed above, it is expected that the VUV spectrum acquired at the acceleration potential of $U_{\mathrm{acc}} = 530\,\mathrm{V}$, which was found to be ideal for Ir^{17+}, also contains lines of Ir^{15+}, Ir^{16+} and Ir^{18+}. So in order to separate them, the acceleration potential was varied in steps of 10 V from 470 V to 620 V. After a line was found in the spectrum of 530 V, the intensity was plotted against the acceleration potential in order to assign it to a specific charge state.

In the VUV regime, iridium has low fluorescence intensities requiring long acquisition times of approximately one hour per grating angle and acceleration energy. In Section 4.1.6 two different modes of operation were presented for the VUV spectrometer: a scanning mode covering a wide spectral range and a static mode limited to a spectral range of about 4 nm per acquisition. Scanning the complete range of the instrument of 180 nm for 15 different acceleration energies at a rate of $4\,\mathrm{nm\,h^{-1}}$ would result in a total acquisition time of 675 hours (about one month). There are long term drifts in signal intensity due to chemical degradation of the metal-organic compound but intensity ratios are crucial for charge state identification. So it was decided to run a single scan of the complete spectral range at 530 V to aid calibration and identify regions with spectral lines, before switching to static mode by moving the grating to a spectral region of interest and recording 15 spectra at different acceleration potentials while keeping the grating angle stationary.

Before spectral lines are accepted as a potential Ir^{17+} transition, their intensity for different acceleration potentials is compared to that of the EUV lines already identified as neodymium-like iridium discussed in Section 6.2.2.

This scheme reduces acquisition time by not investigating spectral regions without potential candidates for transitions and, more importantly, reduces relative changes in intensity caused by long-term drifts by recording the same spectral region at all acceleration potentials within 16 h. Nonetheless, every potential emission line of iridium is investigated, due to the initial scan of the complete spectral range. The overview scan and all spectral ranges investigated in more detail are presented in Figure 6.6.

It should be noted that a few weeks into the measurement, a turobomolecular vacuum pump on the injection system failed. Due to the differential pumping system, the pressure was sufficiently low to continue the measurement. In post-analysis, contaminations were found in the spectra that only appear in data recorded after the hardware malfunction. Due to the redundancy (overlap between the investigated spectral regions) preventing misidentifications and the impurity not being impacted by changes in electron beam energy, some of these detailed energy scans were included in the analysis presented here. The following ranges were recorded after the incident: 87.73 nm (see Figure B.33), 96.12 nm

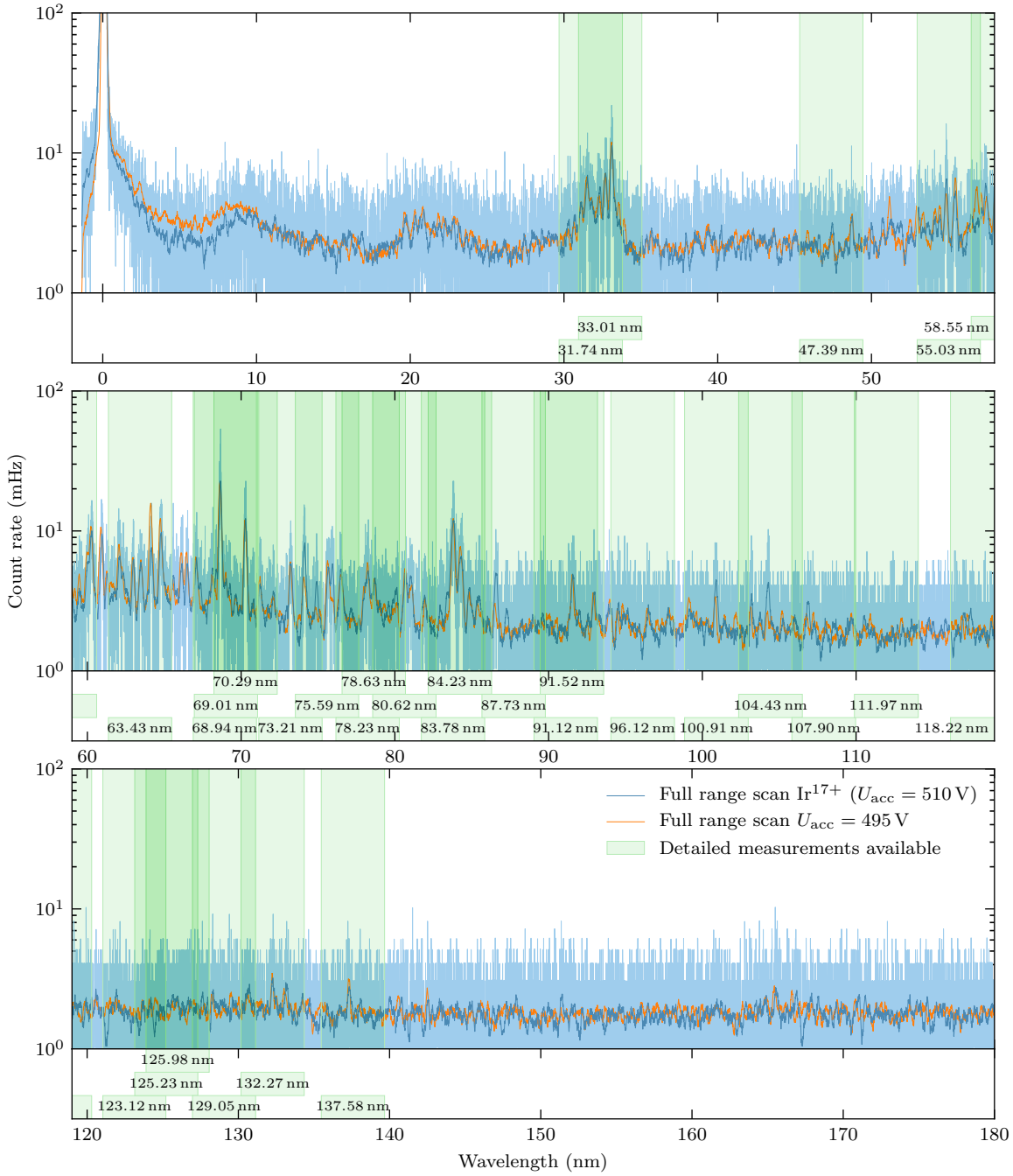

Figure 6.6: Full-range scan of neodymium-like iridium. Raw data is shown in light blue, otherwise the spectra are smoothed for visualisation. As reference to the calibration shown in Figure 6.5, the same scan at $U_{acc} = 495\,V$ is also presented here. Spectral ranges, where a detailed energy scan is available are shaded in green. Additionally, a box below the spectrum is indicating the central wavelength of the respective range.

(B.39), 100.91 nm (B.41), 104.43 nm (B.43), 107.90 nm (B.45), 137.58 nm (not included in the analysis), 123.12 nm, 125.98 nm (B.51), and 129.05 nm.

6.3.1 VUV results

Analysis of the initial full-range scan rose interest in a detailed investigation of 31 spectral ranges (these are also indicated in Figure 6.6). Of these, an exemplary spectrum is discussed here (Figures 6.7 and 6.8). The other ones can be found in Appendix B.2.

After the individual spectra were pre-processed according to Section 4.1.7, they were calibrated using the method described above and assembled into a two-dimensional spectrogram displaying wavelength against electron beam energy. Before a peak finding algorithm was applied to the spectra recorded at 490 V, 530 V, 570 V, and 610 V (correspond to the ideal energies for measuring Ir^{16+}, Ir^{17+}, Ir^{18+}, and Ir^{19+} respectively), the spectrograms were smoothed using a Gaussian filter, a baseline subtraction was performed based on the algorithm described in Appendix A.2 and four spectra closest to the ideal beam energy were averaged to improve the signal-to-noise ratio. Since the peak finding algorithm operated on a one-dimensional spectrum, this list of peak positions was not discriminating different charge states: i. e. a peak found in the spectrum at 530 eV could also be due to a transition in Ir^{16+} or Ir^{18+}. So two-dimensional Gaussian functions were fitted to the data. Initially only one Gaussian was used at the energy with maximum intensity. Where the fit did not converge or the the parameters were out of a plausible range, the fit was repeated using a linear combination of two or more two-dimensional Gaussian functions until convergence was achieved.

Results for all of the detailed energy scans were compared and duplicates were removed by averaging where multiple measurements covered the same spectral line. In total 140 lines were successfully fitted (without duplicates). Of these, 56 were attributed to Ir^{17+}. A list of these lines is given in Table 6.3. To distinguish lines found in the VUV range from lines found in the EUV (see next Section), they are denoted as 'V1', 'V2' and so on. Numbers not appearing in the list were attributed to another charge state of iridium.

Table 6.3: New spectral lines found for neodymium-like iridium in the VUV range. λ denotes the wavelength of the line, E the transition energy, I the amplitude, and σ is the Gaussian line width. The unit mHz refers to the count rate across the detector and a bin size of 0.3 mdeg $\approx$ 0.0012 nm. The last column is a references to the figure of the detailed energy scan the respective line was found in.

	λ (nm)	E (eV)	I (mHz)	σ (nm)	Detailed scan
Line V2	30.731(27)	40.345(35)	4.05	0.0571	B.5
Line V3	30.964(26)	40.042(34)	3.34	0.0427	B.5
Line V6	32.167(26)	38.543(31)	1.31	0.0889	B.5
Line V19	48.717(12)	25.4499(62)	5.38	0.0296	B.7
Line V26	54.1916(98)	22.8789(41)	3.60	0.0709	B.9
Line V29	54.9065(93)	22.5810(38)	14.84	0.0401	B.9
Line V33	56.5100(90)	21.9402(35)	10.03	0.0560	B.9
Line V36	57.3993(88)	21.6003(33)	13.93	0.0553	B.11
Line V38	58.0096(86)	21.3731(32)	27.73	0.0304	B.11

Table 6.3 continued

	λ (nm)	E (eV)	I (mHz)	σ (nm)	Detailed scan
Line V40	59.0102(95)	21.0106(34)	2.06	0.1160	B.11
Line V44	62.0924(90)	19.9677(29)	10.11	0.0695	B.13
Line V48	63.4215(83)	19.5492(26)	8.54	0.0672	B.13
Line V52	64.859(90)	19.116(27)	3.27	0.2208	B.13
Line V55	67.1265(90)	18.4702(25)	9.47	0.0799	B.15
Line V56	67.3572(85)	18.4070(23)	8.22	0.0679	B.15 and B.17
Line V57	67.9319(86)	18.2512(23)	7.49	0.0412	B.15 and B.17
Line V59	68.3754(86)	18.1329(23)	16.53	0.0359	B.15
Line V61	68.3832(86)	18.1308(23)	17.68	0.0363	B.17 and B.19
Line V62	69.2596(87)	17.9014(22)	7.24	0.0575	B.15, B.17, and B.19
Line V63	69.611(12)	17.8111(30)	2.30	0.1708	B.19
Line V64	70.0072(88)	17.7102(22)	4.28	0.0313	B.15, B.17, and B.19
Line V68	70.3505(88)	17.6238(22)	9.42	0.0332	B.15 and B.19
Line V70	70.7255(89)	17.5303(22)	3.27	0.0530	B.15, B.17, and B.19
Line V74	72.1295(90)	17.1891(22)	12.05	0.0376	B.19 and B.21
Line V77	73.3123(93)	16.9118(22)	3.99	0.0458	B.21
Line V79	74.1041(92)	16.7311(21)	27.04	0.0379	B.21
Line V80	74.9165(93)	16.5497(21)	13.88	0.0385	B.21 and B.23
Line V82	75.9073(94)	16.3336(20)	16.91	0.0413	B.23
Line V84	76.5360(96)	16.1995(20)	5.86	0.0642	B.23 and B.25
Line V85	77.1691(96)	16.0666(20)	2.44	0.0362	B.23 and B.27
Line V89	78.4882(96)	15.7965(19)	6.59	0.0323	B.25 and B.27
Line V91	78.8750(97)	15.7191(19)	4.27	0.0485	B.25, B.27, and B.29
Line V93	79.5693(97)	15.5819(19)	5.92	0.0389	B.25, B.27, and B.29
Line V94	80.0180(98)	15.4945(19)	10.25	0.0365	B.25, B.27, and B.29
Line V97	80.9440(98)	15.3173(19)	12.72	0.0310	B.29
Line V99	81.7068(99)	15.1743(18)	3.38	0.0290	B.29
Line V101	82.9999(99)	14.9379(18)	5.28	0.0342	6.7 and B.31
Line V102	83.4146(99)	14.8636(18)	10.16	0.0333	6.7 and B.31
Line V103	83.684(10)	14.8156(18)	20.98	0.0413	6.7 and B.31
Line V105	84.116(10)	14.7396(17)	10.29	0.0306	6.7 and B.31
Line V107	84.787(10)	14.6229(17)	4.74	0.0288	B.31
Line V109	85.328(10)	14.5302(17)	8.94	0.0352	6.7 and B.31
Line V110	85.697(10)	14.4678(17)	4.39	0.0326	B.31
Line V111	86.514(10)	14.3311(17)	17.96	0.0424	B.33
Line V114	89.598(10)	13.8378(16)	2.27	0.0619	B.33, B.35, and B.37
Line V117	92.5669(99)	13.3940(14)	3.32	0.0358	B.35 and B.37
Line V118	94.372(10)	13.1378(14)	0.98	0.0472	B.39
Line V119	95.1586(98)	13.0292(13)	4.99	0.0454	B.39
Line V120	99.3781(95)	12.4760(12)	3.30	0.0342	B.41

Table 6.3 continued

	λ (nm)	E (eV)	I (mHz)	σ (nm)	Detailed scan
Line V123	100.8492(93)	12.2940(11)	15.27	0.0353	B.41
Line V124	104.2361(91)	11.8946(10)	13.09	0.0346	B.43
Line V125	105.9458(90)	11.7026(10)	5.23	0.0386	B.43 and B.45
Line V127	106.9240(90)	11.595 55(98)	3.47	0.0306	B.45
Line V129	110.5331(91)	11.216 92(93)	5.64	0.0367	B.47
Line V132	116.271(11)	10.663 40(97)	2.54	0.0391	B.49
Line V137	124.180(14)	9.9842(11)	0.79	0.0510	B.51

Using this data in conjunction with the wavelength dependent sensitivity of the spectrometer and its solid angle, synthetic spectra were composed that can be found in Figures 6.11, 6.12, and 6.13.

6.3.2 EUV results

Based on predictions by atomic structure calculations, previous works by Bekker *et al.* only investigated the EUV range from 16 nm to 23 nm. However, the initial scan of the full VUV spectral range (see Figure 6.6 and lines V2, V3 and V6 in Table 6.3) indicated potential emission lines around 30 nm that are at the lower end of the sensitivity range of the VUV instrument (see Figure 4.13) but well within spectral range for the compact EUV spectrometer. So the camera position of the latter was adjusted to this range and data was acquired alongside the static mode VUV acquisition. The same range measured by both instruments independently is shown in Figure 6.9.

Furthermore, this facilitates a direct comparison of both instruments. It should be noted, though, that exposure time was vastly different in this example. The 3 m VUV spectrometer acquired data for 15 h in total while data from the compact EUV spectrometer was averaged over a total of about 500 h.

A separate calibration was performed by injecting iron in the form of the metal-organic substance iron pentacarbonyl into the trap immediately after the iridium measurement was finished. A scan of the same beam energies was performed and fluorescence of the charge states Fe^{8+} to Fe^{16+} was observed. Due to the abundance of highly charged iron in astrophysical plasma, it has many well-known emission lines that can be used for calibration. In Figure 6.10 this data is presented in conjunction with residua of the calibration fit. A list of calibration lines adopted from the NIST atomic spectra database [122] can be found in the appendix (see Table B.4).

As uncertainty, the mean value of the residua was used. After attaining initial guesses for peak positions in the iridium spectra shown in Figure 6.9 **a** (after smoothing and baseline subtraction, a peak finding algorithm was used) Gaussian functions were fitted for each peak in every electron beam energy. Not counting multiple occurrences of the same spectral line at different energies, 65 lines were found in total, of which 15 were attributed to the neodymium-like charge state according to their intensity curve in dependency of the electron beam energy. All of these are shown in Table 6.4. Uncertainties therein are root sum square values of the uncertainty in the peak fit and calibration uncertainty.

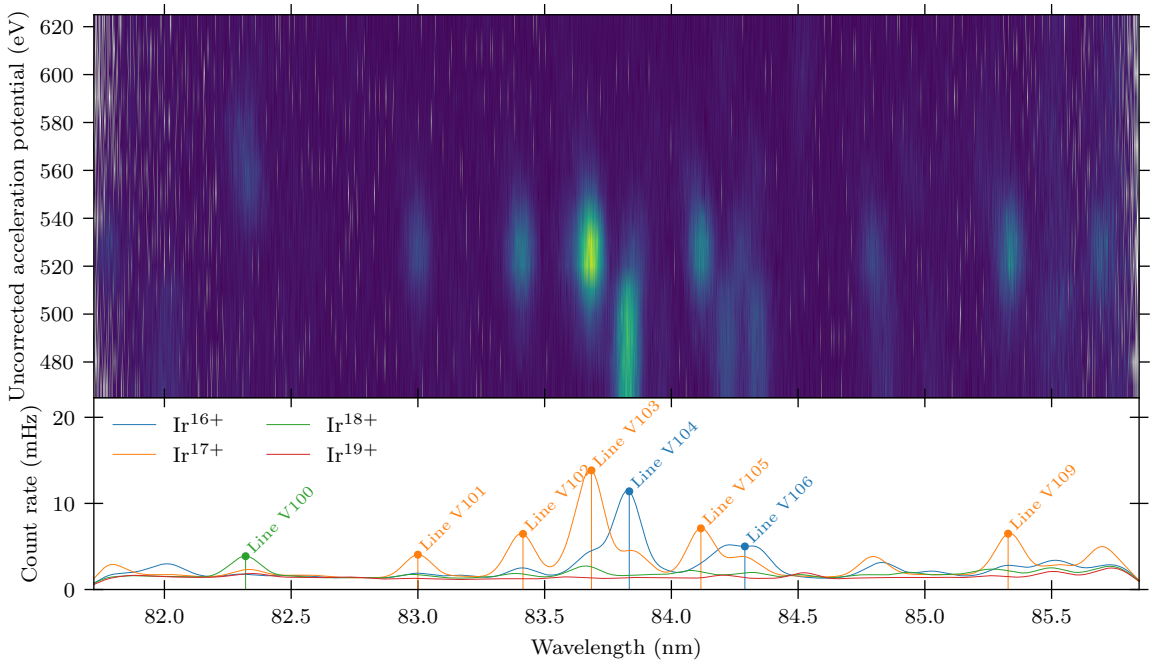

Figure 6.7: Detailed energy scan of iridium around 83.78 nm. The upper part showing the two-dimensional spectrogram, while individual smoothed spectra at beam energies of 490 V, 530 V, 570 V, and 610 V are shown in the lower part. These values correspond to the ideal energies for measuring Ir^{16+}, Ir^{17+}, Ir^{18+}, and Ir^{19+} respectively. Sections through the data along the beam energy axis at the peak positions marked in the lower part can be found in Figure 6.8.

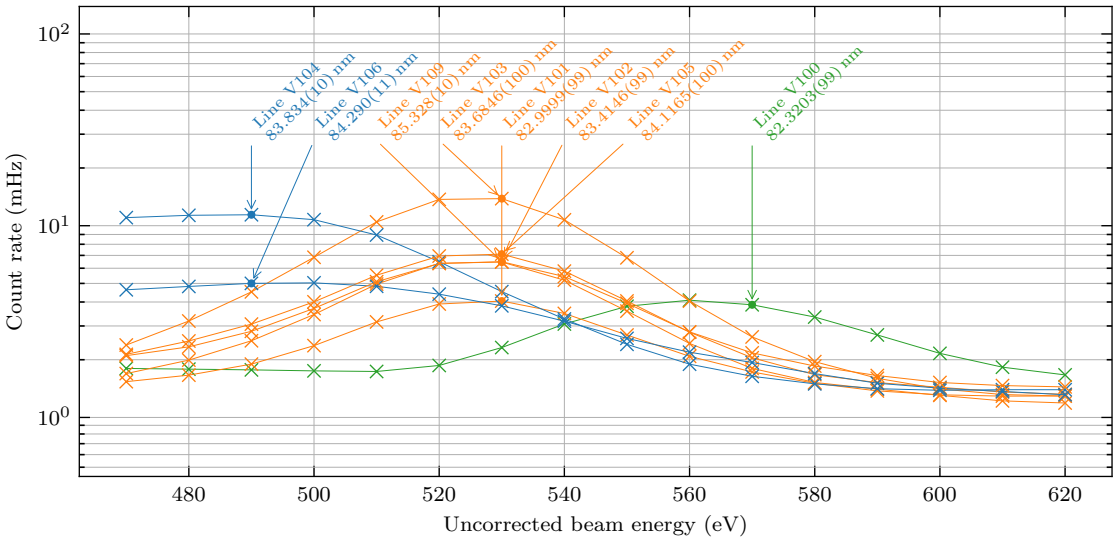

Figure 6.8: Peak intensities of the lines found in Figure 6.7 plotted against beam energy.

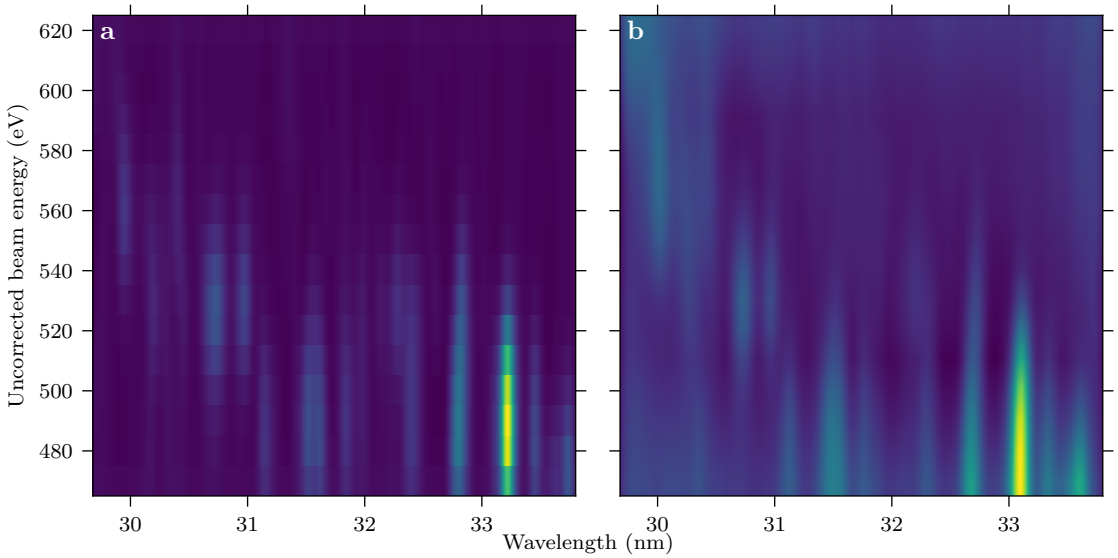

Figure 6.9: Direct comparison of the EUV and VUV spectrometer. **a** was recorded using the compact EUV spectrometer, while the data in **b** is adopted from Figure B.5. The data of the VUV spectrometer was smoothed, a background subtraction was performed and it was cropped to the same spectral range as available from the EUV spectrometer (raw VUV data is shown in Figure B.5).

Table 6.4: New spectral lines found for neodymium-like iridium in the EUV range. Please note that the intensities are detector count rates and therefore differ for the EUV and VUV spectrometer.

	λ (nm)	Energy (eV)	I (mHz)
Line E6	30.1340(23)	41.1443(32)	0.0593
Line E7	30.2291(25)	41.0175(34)	0.0329
Line E9	30.3850(44)	40.8043(58)	0.0532
Line E10	30.5084(28)	40.6394(37)	0.1838
Line E11	30.6453(22)	40.4579(29)	0.2838
Line E12	30.8825(23)	40.1471(30)	0.1545
Line E23	31.9991(36)	38.7461(43)	0.3200
Line E24	32.1406(23)	38.5755(28)	0.1047
Line E29	32.4560(36)	38.2007(42)	0.0968
Line E41	35.0890(31)	35.3342(31)	0.0271
Line E48	37.5364(28)	33.0304(24)	0.0078
Line E49	37.5390(28)	33.0281(24)	0.0193
Line E51	37.9416(31)	32.6776(27)	0.0396
Line E63	39.7908(44)	31.1590(34)	0.0272
Line E65	40.1605(31)	30.8722(24)	0.0459

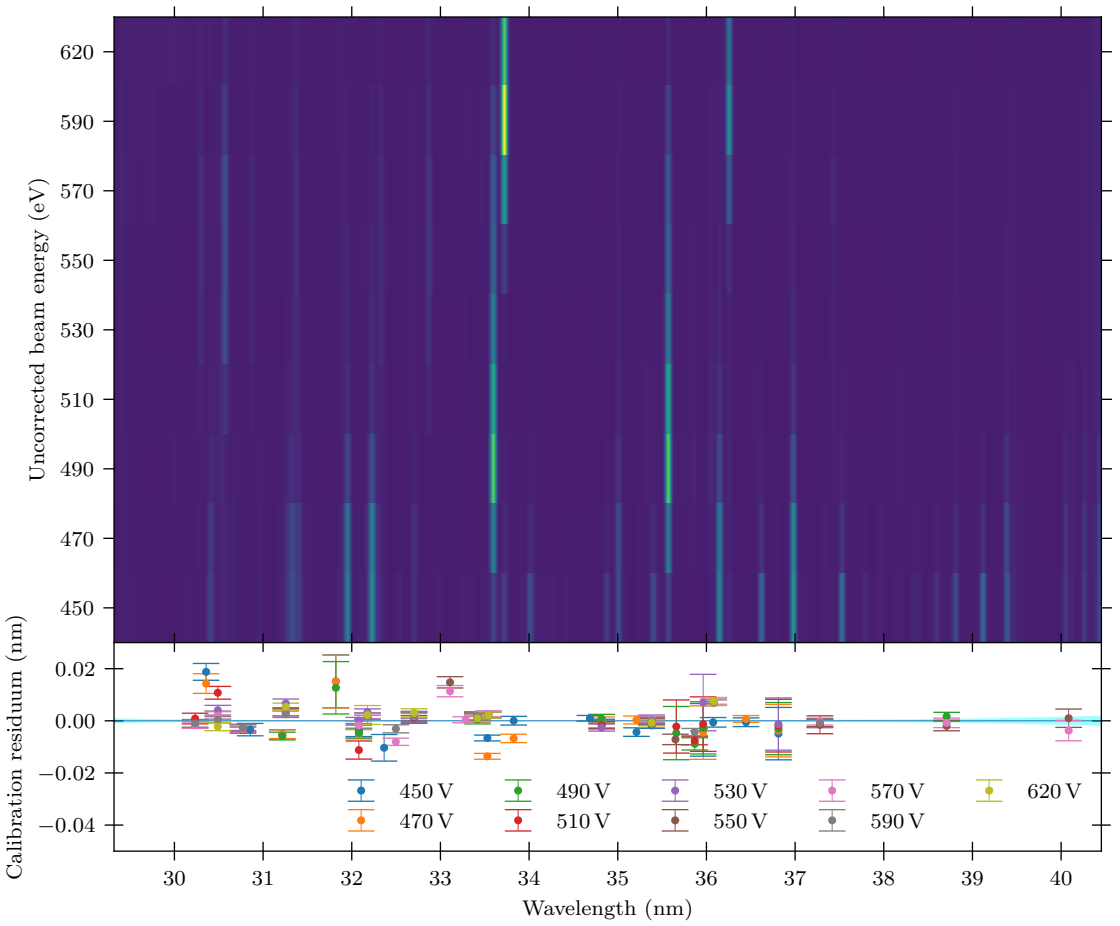

Figure 6.10: Electron beam energy scan in the EUV range with iron injection. In the lower part, calibration residua are shown in conjunction with the confidence band of the calibration fit. Calibration peaks were fitted for individual electron beam energies. However, calibration was performed as a combined fit including all calibration lines.

The VUV line V6 can easily be matched to the EUV line E24. However, for Lines E11 and E12 with V2 and V3 respectively, there is a disparity of $\approx 3\sigma$. It should be noted, though, that these line are just at the lower end of the sensitive range, the acquisition time available for the VUV spectrometer was much shorter and furthermore, the calibration was extrapolated for these three lines (43.6 nm was the calibration line with lowest wavelength; see Figure 6.5). So for further analysis, Lines E11, E12, and E23 are used instead of Lines V2, V3, and V6. Gaussian line width is narrower on the EUV spectrometer by a factor of ≈ 17.

6.4 Comparison to theory

After new emission lines have been found and attributed to Ir^{17+}, the next logical step is identifying the corresponding transitions and levels involved, so the energy of the respective

terms can be improved in accuracy.

However, for neodymium-like iridium this is a non-trivial task, since predictions from atomic structure calculation are only available for a limited number of levels and even these have large uncertainties. Previous successful identifications in this ion species have relied on three different methods:

1. It is expected for fine-structure transitions to scale smoothly with the atomic number Z (i. e. see [17, 19, 20, 57, 66, 68, 114, 163, 164, 204]). So it is assumed, a scaling law of $E_i(Z) = A_i + B_i(Z - Z_{\mathrm{mean}}) + C_i(Z - Z_{\mathrm{mean}})^2$ can be applied, where spectra are available for other elements along the isoelectronic sequence. First, a set of lines is obtained by picking a single line from each of the spectra. A set of parameters A_i, B_i and C_i is obtained by fitting the scaling law to this set of lines. After repeating this procedure for every possible combination of lines, all sets with implausibly large residuals are rejected. By comparing the remaining experimentally obtained Z scaling values to calculations of a specific transition along the isoelectronic sequence, identifications can be obtained. The method is described in detail in [197] where it was given the name *line assist*.
2. Due to the magnetic field in the trap, transitions between states of different parity are split into multiple Zeeman components. By fitting the line shape given by the squared Clebsch-Gordan coefficients and calculated Landé factors g (see Sections 1 and 2.1.2), assuming a common Gaussian width for the individual components due to Doppler broadening and instrumental resolution, total angular momenta J of the upper and lower level can be deduced [15, 198] adding crucial additional information for the line identification.
3. Assuming some lines have been identified, the Rydberg-Ritz principle can be employed. The starting point is to find all combinations of at least three lines forming a closed loop. So when i. e. the photon energies of two lines add up to the energy of a third line and one of these lines was previously identified as the transition between two states A and B, there are in principle two energies at which a new level C could be placed. By including more of these Rydberg-Ritz combinations and selection rules to the picture, combinatorics can be used to determine the level scheme with the highest likelihood [156, 162].

The latter two methods will be referred to as the *Zeeman*, and *Rydberg-Ritz identification method* in this work.

To apply the line assist method, more experimental data is required. For the identified optical lines, spectra from neodymium-like tungsten ($Z = 74$), rhenium ($Z = 75$), osmium ($Z = 76$) and platinum ($Z = 78$) was available in addition to the iridium one. Zeeman splitting is expected to be in the order of 10^{-4} eV which is less than the resolution available. So this section will focus on the Rydberg-Ritz combination method.

Fortunately, a few optical lines have already been identified, so Rydberg-Ritz combinations of newly found lines including one of the identified lines are particularly interesting. A list of all identified lines including the identification methods can be found in Table 6.5. These are the same lines as shown in Figure 6.1.

Table 6.5: Previously identified lines in Ir^{17+}. A $*$ next to the reference denotes the identification method line assist. † refers to a closed Rydberg-Ritz loop and ‡ to the Zeeman method discussed above.

Transition	Line	λ (nm)	E (eV)	Reference
$4f^{12}\,5s^2\ {}^3P_1 \rightarrow {}^3F_2$	Line O1	226.630(20)	5.469 10(50)	[15]†
$4f^{12}\,5s^2\ {}^3H_4 \rightarrow {}^3H_5$	Line O30	324.609 90(40)	3.818 381 0(50)	[15, 197]*‡
$4f^{13}\,5s^1\ {}^1F_3^o \rightarrow {}^3F_4^o$	Line O32	329.302 50(40)	3.763 971 0(50)	[15, 197]*‡
$4f^{12}\,5s^2\ {}^1D_2 \rightarrow {}^3F_2$	Line O33	365.0318(10)	3.395 564 0(90)	[15, 197]* † ‡
$4f^{13}\,5s^1\ {}^1F_3^o \rightarrow {}^3F_3^o$	Line O36	390.6300(10)	3.173 060(10)	[15]‡
$4f^{12}\,5s^2\ {}^3F_3 \rightarrow {}^3F_4$	Line O37	391.823 70(40)	3.163 389 0(40)	[15, 197]* † ‡
$4f^{12}\,5s^2\ {}^3P_2 \rightarrow {}^1D_2$	Line O38	399.357 70(60)	3.103 712 0(40)	[15]‡
$4f^{12}\,5s^2\ {}^3H_5 \rightarrow {}^3H_6$	Line O40	422.895 00(30)	2.930 971 0(20)	[15, 197]*‡
$4f^{12}\,5s^2\ {}^1D_2 \rightarrow {}^3F_3$	Line O41	431.604 40(30)	2.871 827 0(20)	[15, 197]*‡
$4f^{12}\,5s^2\ {}^1G_4 \rightarrow {}^3F_4$	Line O42	435.634 80(50)	2.845 258 0(30)	[15, 197]* † ‡
$4f^{12}\,5s^2\ {}^3H_4 \rightarrow {}^1G_4$	Line O43	445.705 70(90)	2.780 970(60)	[15, 197]* † ‡
$4f^{13}\,5s^1\ {}^3F_2^o \rightarrow {}^3F_3^o$	Line O44	482.703 90(70)	2.567 818 0(40)	[15, 197]*‡
$4f^{12}\,5s^2\ {}^3H_4 \rightarrow {}^3F_3$	Line O45	503.2830(20)	2.462 820(10)	[15]†‡
$4f^{12}\,5s^2\ {}^3P_1 \rightarrow {}^1D_2$	Line O48	597.650(20)	2.073 950(70)	[15]†

As mentioned before, the Zeeman method only yields J for the upper and lower level and the optical lines at 390.6300(10) nm (O36: $4f^{13}\,5s^1\ {}^1F_3^o \rightarrow {}^3F_3^o$) and 399.357 70(60) nm (O38: $4f^{12}\,5s^2\ {}^3P_2 \rightarrow {}^1D_2$) were identified solely based on this method. For the latter, calculations agree quite well with each other, so the former is arguably the most unreliable identification in listed in Table 6.5.

When considering all sets of three lines, where $E_1 = E_2 + E_3$ is within 3.5σ of the largest uncertainty of the three, 327 Rydberg-Ritz combinations can be deduced from all experimentally known lines to date as given in Table B.5. Since most of the transitions within the two configurations $4f^{13}\,5s^1$ and $4f^{12}\,5s^2$ have been identified in previous works, it is useful to focus on transitions between two. This is done by discarding all combinations containing only unknown or only identified lines, so that each set has at least one identified and at least one unidentified transition. 62 combinations are left at this point. None of these is a set of two identified and one unidentified line that would make the identification of a third line trivial. Line V54 has a very large uncertainty due to close proximity to a Ir^{16+} line. After removing all sets including this particular line, 41 combinations are left. These are shown in Table 6.6.

Since each of the sets has two unidentified lines, at least two sets are needed to connect both configurations. The configuration $4f^{13}\,5s^1$ has only four levels and three transitions in the optical regime that have all been identified. This fact can be used to narrow the search down: there are only six sets in the list including a transition of that configuration (all of them being O44). Adding the constraint of $\Delta J = 0, \pm 1$ and assuming a second interconfiguration Rydberg-Ritz combination shares an unidentified line, with one of these six, the second combination would need to include one of these lines: $4f^{12}\,5s^2\ {}^1D_2 \rightarrow$

Table 6.6: Rydberg-Ritz combinations within the newly found lines. A confidence of 3.5σ for most uncertain line in the triplet was used as criterion.

E6, E24, and O44	V44, V74, and O43	V70, V111, and O34
E7, E23, and O46	V55, V84, and O46	V74, V107, and O44
E11, E29, and O46	V56, V97, and O39	V84, V119, and O37
E29, E41, and O41	V56, V107, and O31	V93, V120, and O38
V19, V26, and O44	V57, V102, and O33	V94, V119, and O45
V19, V29, and O41	V57, V110, and O31	V94, V123, and O34
V29, V74, and O2	V59, V105, and O33	V97, V120, and O42
V33, V80, and O2	V62, V103, and O39	V101, V120, and O45
V36, V63, and O31	V62, V105, and O37	V102, V123, and O44
V36, V84, and O2	V63, V101, and O41	V102, V125, and O37
V40, V59, and O41	V64, V102, and O42	V105, V124, and O42
V40, V62, and O38	V64, V107, and O39	V110, V124, and O44
V40, V63, and O34	V68, V110, and O37	V110, V127, and O41
V40, V68, and O33	V68, V114, and O31	

$^3F_2$ (corresponding to O33), $4f^{12}\,5s^2\ ^3F_3 \rightarrow\ ^3F_4$ (O37), $4f^{12}\,5s^2\ ^3P_2 \rightarrow\ ^1D_2$ (O38), $4f^{12}\,5s^2\ ^1D_2 \rightarrow\ ^3F_3$ (O41), or $4f^{12}\,5s^2\ ^3H_4 \rightarrow\ ^3F_3$ (O45). In principle, $4f^{12}\,5s^2\ ^3P_1 \rightarrow\ ^3F_2$, $4f^{13}\,5s^1\ ^1F_3^o \rightarrow\ ^3F_3^o$, or $4f^{12}\,5s^2\ ^3P_1 \rightarrow\ ^1D_2$ are valid choices as well, but there are no appropriate combinations in the list. There are only five pairs of Rydberg-Ritz combinations that match these criteria:

1. V19, V29, and O41 in conjunction with V19, V26, and O44
2. V57, V102, and O33 in conjunction with V102, V123, and O44
3. V68, V110, and O37 in conjunction with V110, V124, and O44
4. V102, V125, and O37 in conjunction with V102, V123, and O44
5. V110, V127, and O41 in conjunction with V110, V124, and O44

Assuming that $4f^{13}\,5s^1$ is the ground state excludes options 2 and 3. The remaining options 1, 4 and 5 are mutually exclusive and would place the $4f^{12}\,5s^2\ ^3H_6$ level at 18.885 eV, 11.168 eV, and 7.900 eV respectively. Comparing this with the most elaborate calculations published recently ([51], see Table 6.1), there is a disparity of 4.145 eV or 52 % for option number 5. Furthermore, the highest transition rates are expected for $^3H_4 \rightarrow\ ^3F_3^o$, $^3H_4 \rightarrow\ ^3F_4^o$, $^3P_2 \rightarrow\ ^1F_3^o$, and $^3P_2 \rightarrow\ ^3F_3^o$ [51]. Actual line intensities also depend on the upper level population and the exact plasma parameters, but a lack of the four most intense transitions, deviation from calculations and two other, conflicting matches are a good indication these are just coincidental matches. For line intensities, see [51] or Figure 6.3.

This is just an example for the most obvious approach to identify spectral lines using combinatorics. More advanced studies have been performed, including more complex schemes using sets of four lines instead of sets of three. However, this greatly increases the

number of possible combinations and therefore the number of false positives and conflicting matches. Another approach was to systematically assign spectral lines as interconfiguration transitions and thereby fixing the energy difference between both configurations. The resulting transition energies for the other lines were matched with the list of spectral lines.

Additionally, attempts have been made, omitting the identifications of $4f^{12}\,5s^2\ {}^3P_2 \rightarrow {}^1D_2$ and $4f^{13}\,5s^1\ {}^1F_3^o \rightarrow {}^3F_3^o$. However, especially removing the latter loosens the constraints for new identifications, resulting in even more ambiguity.

6.5 Summary

Neodymium-like iridium is one of the best-suited species for precision experiments on the variation of the fine-structure constant in the laboratory. However, knowledge about the level structure of this ion is limited. Calculations of the species are particularly challenging due to the open $4f$ shell and proximity to the $4f - 5s$ level crossing. In light of recent developments in metrology experiments, there is an exceptional demand for iridium spectra.

Previously, iridium has been studied at Heidelberg EBIT in the optical and EUV regime. However, a transition linking the configurations $4f^{13}5s^1$, $4f^{12}5s^2$, or $4f^{14}$ has not been found. Such an interconfiguration transition is crucial for future high-precision experiments. Recent calculations [51] predict these transitions at shorter wavelengths in the VUV range.

The experimental study of Ir^{17+} has successfully been transferred from Heidelberg EBIT to FLASH-EBIT in order to make use the new 3 m normal-incidence VUV spectrometer. Thorough comparison to existing data has confirmed the charge state identification and an estimate of the space-charge potential was obtained. Impurities were identified and successfully removed by optimisation methods. Calibration was performed using well-known spectra of O II through O V in a combined scan across the full spectrometer range.

After scanning the complete spectral range of the VUV spectrometer, 31 regions of interest were found that contained unknown transition lines of iridium. These regions were investigated further, using both the VUV normal-incidence spectrometer as well as the compact flat-field EUV spectrometer. In total, 68 emission lines were attributed to neodymium-like iridium. Artificial spectra based on the spectral lines attributed to the individual charge-states is presented in Figures 6.11, 6.12, and 6.13.

Furthermore, new FAC calculations for neodymium-like iridium are presented in Section 6.1, drastically reducing disparity to other atomic structure codes found in previous FAC results. A semi-empirical method was established to select the set of configurations to include in the calculation.

Despite almost doubling the number of known spectral lines in this work and extensive efforts, no identifications could be made using combinatorics, indicating more data is required in order to determine the urgently needed transition energies of the highly forbidden α sensitive transitions in neodymium-like iridium.

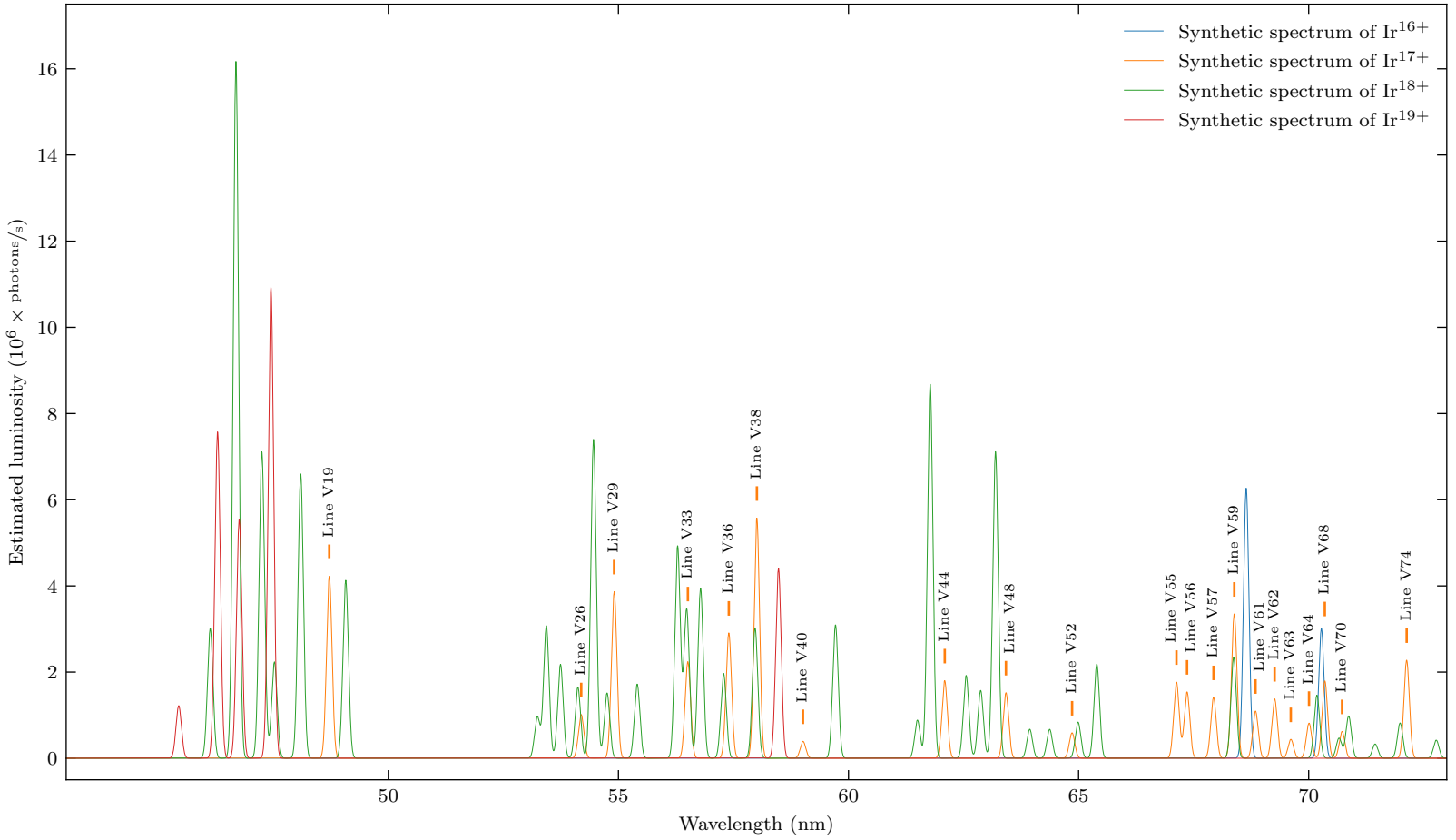

Figure 6.11: Synthetic spectrum of Ir^{16+}, Ir^{17+}, Ir^{18+}, and Ir^{19+} in the range of 43 nm to 73 nm. The spectra were generated by convolution of the values in Table 6.3 with a Gaussian kernel with typical line width. Peak heights were calculated using the sensitivity curve given in Figure 4.13 and the solid angle of the 3 m normal-incidence VUV spectrometer.

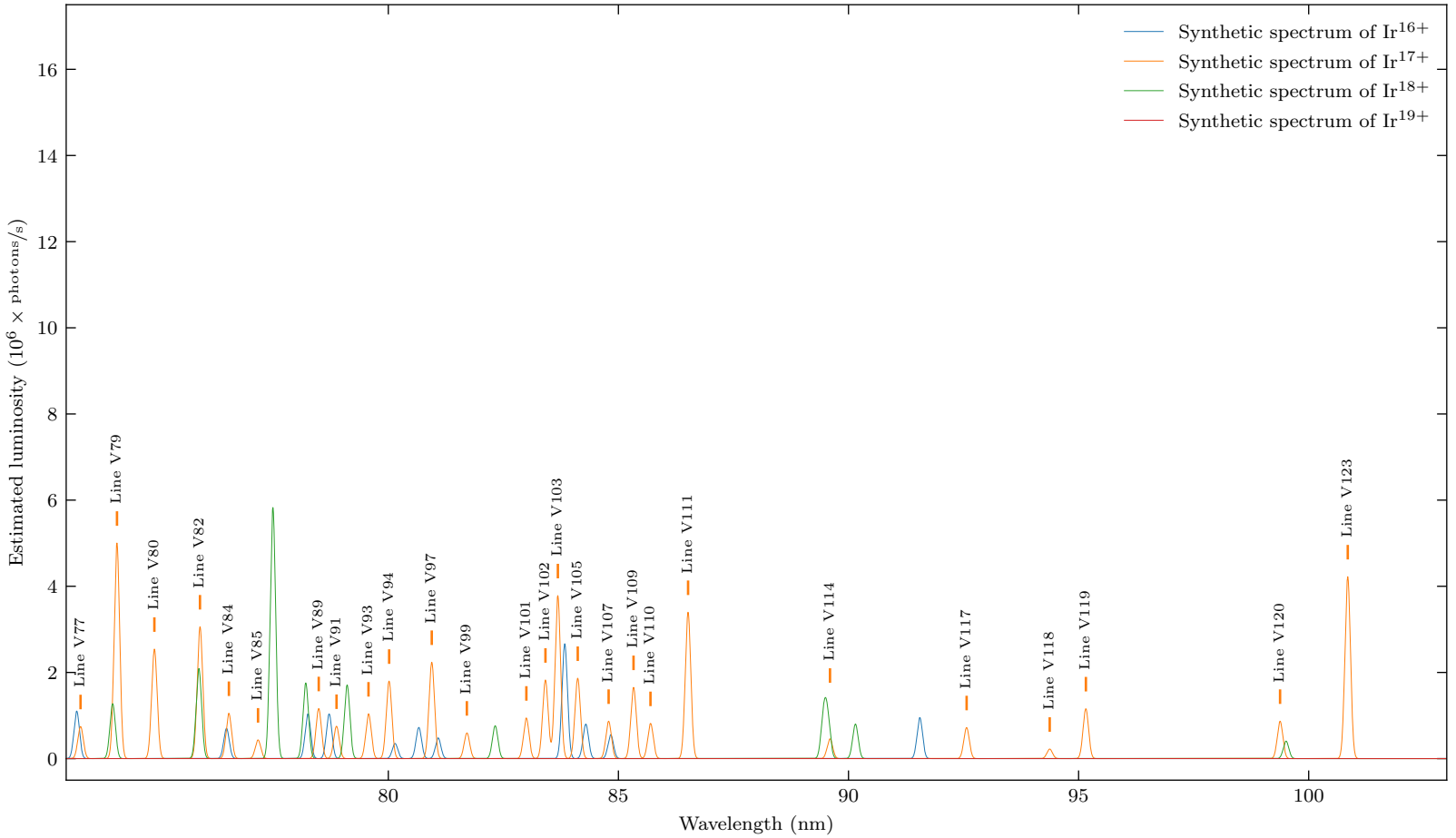

Figure 6.12: Synthetic spectrum of Ir^{16+}, Ir^{17+}, Ir^{18+}, and Ir^{19+} in the range of 73 nm to 103 nm. The spectra were generated by convolution of the values in Table 6.3 with a Gaussian kernel with typical line width. Peak heights were calculated using the sensitivity curve given in Figure 4.13 and the solid angle of the 3 m normal-incidence VUV spectrometer.

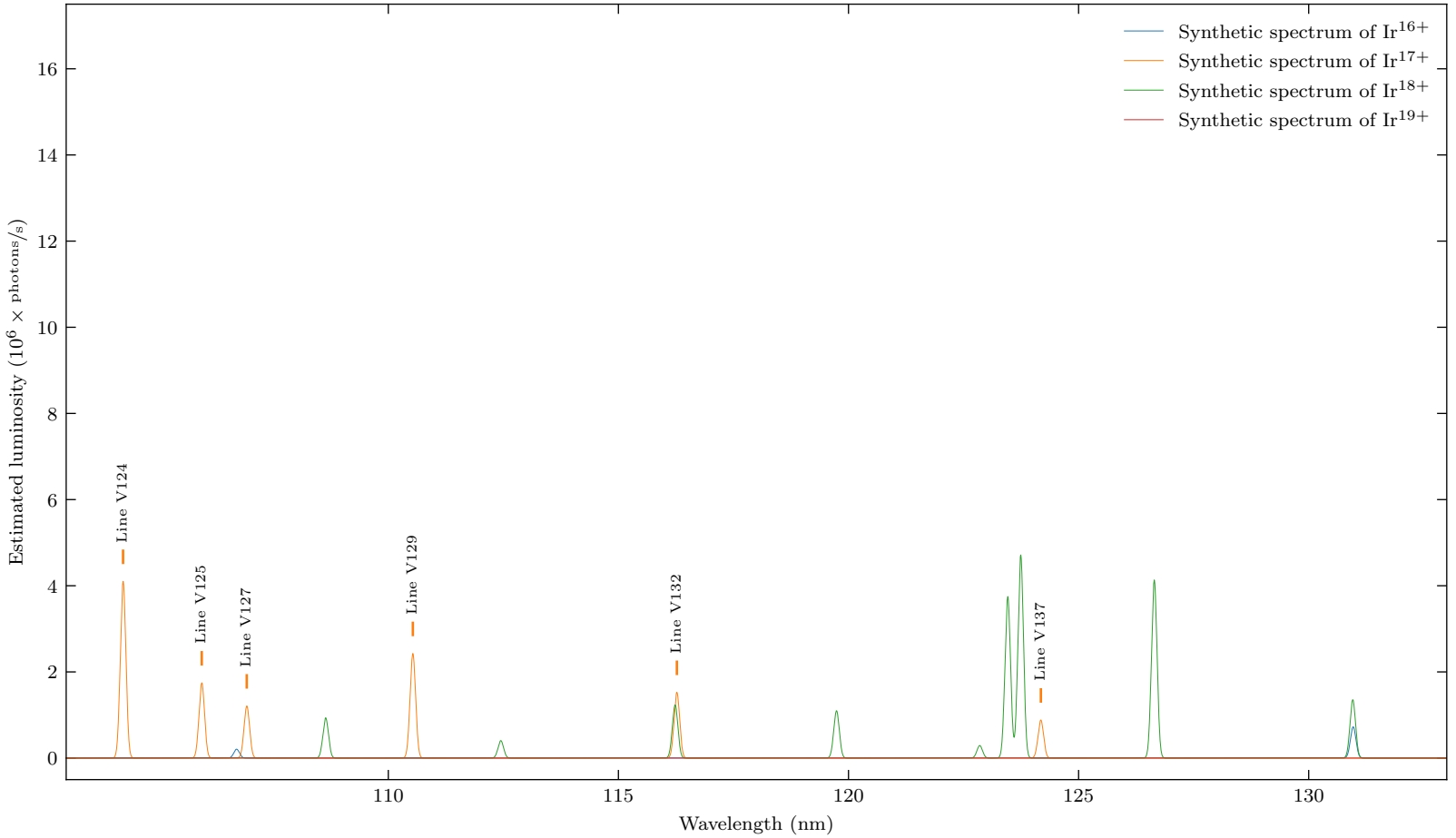

Figure 6.13: Synthetic spectrum of Ir^{16+}, Ir^{17+}, Ir^{18+}, and Ir^{19+} in the range of 103 nm to 133 nm. The spectra were generated by convolution of the values in Table 6.3 with a Gaussian kernel with typical line width. Peak heights were calculated using the sensitivity curve given in Figure 4.13 and the solid angle of the 3 m normal-incidence VUV spectrometer.

CHAPTER 7

Summary and Outlook

Two new devices were introduced in Chapters 3 and 4. Firstly, over the course of three years, a novel electron beam ion source (EBIS) was successfully co-developed, built, tested and commissioned for the new CANREB facility at TRIUMF for the production of highly charged rare-isotopes. Record-breaking specifications have been demonstrated amongst others by an electron beam current of 1 A. Secondly, a 3 m normal-incidence spectrometer sensitive in the wavelength range of 40 nm to 140 nm was adapted for spectroscopy of EBIT plasmas at FLASH-EBIT. Consequently, two pressing issues related to fine structure have been addressed that are discussed in more detail here.

Understanding fine-structure splitting in hydrogen has sparked the development of quantum electrodynamics (QED), which is one of the most precisely tested theories in atomic physics. As soon as experimental techniques were established to produce highly charged ions (HCIs) in the laboratory, interest in precision measurements of the Lamb shift was renewed. In the 1990s this culminated in the observation of hydrogen-like uranium in beam-foil experiments [27, 40].

So far, the best benchmark for theory is the lithium-like isoelectronic sequence, in which QED effects are particularly pronounced due to the interelectron interaction of the two core electrons with a single valence electron. Nevertheless, these systems are simple enough for accurate calculations. In argon, QED effects make up 11 % of the transition energy of $1s^2 2p\ ^2P_{1/2} \rightarrow 1s^2 2s\ ^2S_{1/2}$. Over the last decades, incremental advances have been made in accurate *ab initio* QED calculations for the lithium-like sequence alongside ever more precise experiments for heavy elements.

However, for species with moderate values of Z, there still is a lack of accurate laboratory data. In this work, the fine-structure doublet $1s^2 2p\ ^2P_{1/2} \rightarrow 1s^2 2s\ ^2S_{1/2}$ and $1s^2 2p\ ^2P_{3/2} \rightarrow 1s^2 2s\ ^2S_{1/2}$ has been observed for nitrogen, oxygen, neon, and argon (see Chapter 5). For neon, the accuracy of up to 0.15 eV (corresponding to 9.5 ppm) reported in the present work is similar to the best laboratory data from 1963 by Bockasten [32]. In the case of argon, so far only solar data from the 1970s have been available in literature and due to blending with a transition line of Fe^{14+} in the astronomical measurements, the values presented here are the most accurate ones to date [56, 169, 192]. The reported values are summarised in Table 7.1. For a detailed discussion of the results and their comparison to recent theory calculations, see Section 5.4.

For the elements nitrogen and oxygen, disparities were found, indicating more laboratory data are needed. The lack of independent measurements is most apparent for nitrogen, where data of four different instruments have been reported so far (including this work).

Table 7.1: Transition energies of the fine-structure doublets obtained in this work in units of eV. For wavelengths, see Table 5.6.

	$2p\ ^2P_{1/2} \to 2s\ ^2S_{1/2}$	$2p\ ^2P_{3/2} \to 2s\ ^2S_{1/2}$	$2p\ ^2P_{3/2} \to 2p\ ^2P_{1/2}$
Nitrogen ($Z = 7$)	9.976 87(36)	10.0089(36)	0.032 03
Oxygen ($Z = 8$)	11.950 96(42)	12.016 60(43)	0.065 64
Neon ($Z = 10$)	15.888 08(17)	16.093 32(15)	0.205 24
Argon ($Z = 18$)	31.867 86(77)	35.037 74(99)	3.169 88

The values reported here have reasonable agreement with the existing data and good agreement with calculations. However, the measurements previously reported deviate significantly from theory and each other.

Other elements potentially interesting for future measurements at the same instrument are fluorine, sodium, magnesium, aluminium, silicon, phosphor, sulphur, chlorine, potassium, and calcium. However, for some of these elements, injection of sufficient quantities into the EBIT could be challenging, but most can be injected either using a gaseous chemical compound or a metal-organic substance with low vapour pressure. When considering the sensitive range of the compact flat-field EUV spectrometer (see Section 4.2) more elements can be investigated at FLASH-EBIT. Worth mentioning are chrome, manganese, cobalt, gallium, germanium, arsenic, selenium, and bromide. For many of these, there are no experimental values available from literature for the lithium-like fine-structure splitting.

Despite two-loop QED being not as pronounced as for heavy elements, nonetheless this work provides a stringent benchmark for calculations of the Breit interaction, interelectronic QED interactions, one-loop QED effects, screening thereof and nuclear recoil effects. For argon, the uncertainties reported here are at the level of 0.59 % for the one-loop QED effects including screening.

Only in the last decade, state-of-the-art bound-state QED calculations have reached the level of accuracy reported in this work, demonstrating that there is an urgent need for ever more precise data to benchmark future advances in theory. After all, some of the most accurate predictions in physics have been obtained from QED. So in order to improve this essential tool not only for atomic structure calculations for the calibration of x-ray spectra or for modelling plasma processes in fusion reactors and astrophysical systems, experimental data along the isoelectronic sequence of lithium, such as the new values reported in this work, are desperately needed.

A second issue related to fine-structure has made an appearance in recent years: independent experiments in astronomy, geology and metrology have indicated a variation of the fine-structure constant α [93, 126, 158, 190, 195]. Despite strong evidence for a variation both in space and time across all of these measurements, there are still many unanswered questions that need to be addressed, before consequences can be drawn for the standard model or cosmology. From observations of quasars through absorbing gas clouds, a spatial dipole for variations of the fine-structure constant was deduced. When considering the movement of the earth with respect to the CMB and said dipole, an increase in α is expected [17]. However, the Oklo natural reactor in a uranium deposit in Gabon [126]

indicates a decrease of the terrestrial fine-structure constant over the course of two billion years.

In light of compelling improvements in metrology within the next years, such as a nuclear clock based on ^{229}Th [147, 173] or the very recent demonstration of quantum logic spectroscopy [142] enabling unprecedented precision experiments on forbidden transitions in highly charged ions (HCIs), there has been an ongoing effort in finding a suitable ion species with highest sensitivity for a measurement of the proposed fine-structure variation. Not only are highly charged ions less sensitive to external perturbations compared to atomic systems currently used for clocks, but it has also been shown that there are transitions in these systems much more sensitive to variations of α.

Among the most promising candidates, Ir^{17+} is expected to have two forbidden transitions that fulfil all the requirements for metrology experiments: there are no competing allowed decay channels broadening the transition and therefore compromising sensitivity. They have opposite signs in their dependency on changes of the fine-structure constant, enabling comparison experiments further boosting sensitivity. Finally, the transitions are expected to be in the optical regime which is critical for high-precision clock experiments [19].

A prerequisite for these, however, is good knowledge of the level scheme of Ir^{17+}. The proposed sensitive optical transitions arise from the $4f - 5s$ level crossing that has made atomic structure calculations challenging. Furthermore, the forbidden nature of the lines eliminates the opportunity of direct observation of fluorescence. Despite considerable experimental efforts in the past, no transition has been found linking the relevant configurations $4f^{13}\,5s^1$, $4f^{12}\,5s^2$, and $4f^{14}$ which would allow for an estimation of the clock transition energies. However, a few spectral lines within these configurations were observed and successfully identified [14, 15, 197, 198].

Very recently, large-scale CI calculations taking into account some closed subshells by including these electrons in the valence space [51], have found the configuration $4f^{12}\,5s^2$ at slightly higher energies with respect to the presumed ground state $4f^{13}\,5s^1$, potentially shifting the sought-after interconfiguration lines from the optical wavelength regime into the vacuum ultraviolet (VUV).

In Chapter 6, the new 3 m normal-incidence spectrometer was employed at FLASH-EBIT to investigate neodymium-like iridium. In this work a total of 68 previously unknown emission lines were found, almost doubling the amount of spectral lines available for this species. A complete list of all known lines is presented in the appendix in Table B.5. However, despite extensive efforts, none of these have been identified unambiguously.

The lack of interconfiguration lines could be explained by the gap of experimental data between 140 nm to 220 nm, a lack in sensitivity, or false assumptions for the identification procedure. These three aspects are discussed in more detail here.

The strongest interconfiguration transitions predicted by the most elaborate calculations yet, are in the range from 91 nm to 174 nm [51]. In the present work, a position-sensitive MCP detector was utilised. Sensitivity of the bare photocathode deteriorates with increasing wavelength by about 20 % per 10 nm (see Figure 4.12) and the available optical spectra start around 220 nm. For the identification process, more than one interconfiguration line is required without further information. So a lack of sensitivity of the 3 m VUV spectrometer in said range could explain the missing identification.

Of the 14 previously identified optical lines, only three were found using combinatorics. A description of the techniques used to identify the other lines can be found in Section 6.4. In summary, either Zeeman components were resolved and values of J for the upper and lower level of the transition were deduced or spectra of other elements along the neodymium-like isoelectronic sequence were used. For the newly found lines, however, Zeeman components of individual spectral lines are not resolved and there is no data available along the isoelectronic sequence yet.

In conclusion, more data is required for line identification. Future experiments could focus on improving sensitivity of the apparatus by using an appropriately coated MCP for the spectral range of 100 nm to 180 nm or other elements such as W, Re, Os, and Pt to resolve the issue.

Since the discovery of fine-structure splitting in hydrogen in 1887 [141], it has been an ongoing discussion to make use of the effect in metrology. Although, variation of the fine-structure constant α is not what Michelson and Morley originally intended when making that suggestion, first quantum logic experiments in the past months have demonstrated that the idea is getting closer to becoming a reality than ever before and dramatically increasing the urge for precise spectroscopic data on α sensitive species. Presupposing the variation of the fine-structure constant does not suffer the same fate as the luminiferous æther, a definitive measurement in a laboratory environment would have fundamental consequences for cosmology and the standard model: additional compact space dimensions, new weak scalar fields [190] and dark matter in the form of axion domain walls [157] have been proposed as cause for a variation of the fine-structure constant.

Bibliography

1. Amaro, Pedro, Sophie Schlesser, Mauro Guerra, Eric-Olivier Le Bigot, Jean-Michel Isac, Pascal Travers, José Paulo Santos, Csilla I. Szabo, Alexandre Gumberidze, and Paul Indelicato: 'Absolute Measurement of the Relativistic Magnetic Dipole Transition Energy in Heliumlike Argon'. *Physical Review Letters* (2012), vol. 109(4): p. 043005. doi: 10.1103/physrevlett.109.043005 (cit. on pp. 2, 100).
2. Andreev, O. V., D. A. Glazov, A. V. Volotka, V. M. Shabaev, and G. Plunien: 'Evaluation of the screened vacuum-polarization corrections to the hyperfine splitting of Li-like bismuth'. *Physical Review A* (2012), vol. 85(2): p. 022510. doi: 10.1103/physreva.85.022510 (cit. on p. 2).
3. Baumann, Thomas: 'Diploma Thesis'. Master's thesis. Universität Heidelberg, 2008 (cit. on pp. 57, 75).
4. Baumann, Thomas: 'Spektroskopische Untersuchungen resonanter Rekombinationsprozesse an hochgeladenem Silizium in einer Elektronenstrahl-Ionenfalle'. Doctoral dissertation. Universtät Heidelberg, 2012. doi: 10.11588/heidok.00013380 (cit. on pp. 57, 75).
5. Becker, R., O. Kester, and Th. Stoehlker: 'Simulation of charge breeding for trapped ions'. *Journal of Physics: Conference Series* (Mar. 2007), vol. 58: pp. 443–446. doi: 10.1088/1742-6596/58/1/102 (cit. on p. 30).
6. Beier, T., P. J. Mohr, H. Persson, and G. Soff: 'Influence of nuclear size on QED corrections in hydrogenlike heavy ions'. *Physical Review A* (1998), vol. 58(2): pp. 954–963. doi: 10.1103/physreva.58.954 (cit. on p. 23).
7. Beier, Thomas, Günter Plunien, Martin Greiner, and Gerhard Soff: 'Two-loop ladder diagram for the vacuum polarization contribution in hydrogen-like ions'. *Journal of Physics B: Atomic, Molecular and Optical Physics* (1997), vol. 30(12): pp. 2761–2772. doi: 10.1088/0953-4075/30/12/006 (cit. on p. 23).
8. Beiersdorfer, P., H. Chen, D. B. Thorn, and E. Träbert: 'Measurement of the Two-Loop Lamb Shift in Lithiumlike U^{89+}'. *Physical Review Letters* (2005), vol. 95(23): p. 233003. doi: 10.1103/physrevlett.95.233003 (cit. on pp. 2, 3).
9. Beiersdorfer, P., A. L. Osterheld, J. H. Scofield, J. R. Crespo López-Urrutia, and K. Widmann: 'Measurement of QED and Hyperfine Splitting in the $2s_{1/2}$–$2p3/2$ X-Ray Transition in Li-like $^{209}Bi^{80+}$'. *Physical Review Letters* (Apr. 1998), vol. 80(14): pp. 3022–3025. doi: 10.1103/physrevlett.80.3022 (cit. on pp. 2, 3, 35).

10. Beiersdorfer, P., T. Phillips, V. L. Jacobs, K. W. Hill, M. Bitter, S. von Goeler, and S. M. Kahn: 'High-resolution measurements, line identification, and spectral modeling of K-α transitions in Fe XVIII–Fe XXV'. *The Astrophysical Journal* (1993), vol. 409: p. 846. doi: 10.1086/172715 (cit. on p. 2).

11. Beiersdorfer, Peter, and Gregory V. Brown: 'Experimental study of the x-ray transitions in the heliumlike isoelectronic sequence: Updated results'. *Physical Review A* (2015), vol. 91(3): p. 032514. doi: 10.1103/physreva.91.032514 (cit. on p. 2).

12. Beiersdorfer, Peter, Joel Clementson, and Ulyana Safronova: 'Tungsten Data for Current and Future Uses in Fusion and Plasma Science'. *Atoms* (June 2015), vol. 3(2): pp. 260–272. doi: 10.3390/atoms3020260 (cit. on p. 35).

13. Beiersdorfer, Peter, Natalie Hell, Dmytro Panchenko, Greg V. Brown, Elmar Träbert, Richard L. Kelley, Caroline A. Kilbourne, and F. Scott Porter: 'Measurements of L-shell X-ray emission lines of neonlike europium on an electron beam ion trap'. *X-Ray Spectrometry* (June 2020), vol. 49(1): pp. 21–24. doi: 10.1002/xrs.3038 (cit. on p. 35).

14. Bekker, H., O. O. Versolato, A. Windberger, N. S. Oreshkina, R. Schupp, T. M. Baumann, Z. Harman, C. H. Keitel, P. O. Schmidt, J. Ullrich, and J. R. Crespo López-Urrutia: 'Identifications of $5s_{1/2}$–$5p_{3/2}$ and $5s^2$–$5s5p$ EUV transitions of promethium-like Pt, Ir, Os and Re'. *Journal of Physics B: Atomic, Molecular and Optical Physics* (2015), vol. 48(14): p. 144018. doi: 10.1088/0953-4075/48/14/144018 (cit. on pp. 104, 108, 109, 129).

15. Bekker, Hendrik: 'Optical and EUV spectroscopy of highly charged ions near the $4f - 5s$ level crossing'. Doctoral dissertation. Universtät Heidelberg, 2016. doi: 10.11588/heidok.00020759 (cit. on pp. 103, 104, 107–109, 120, 121, 129, 172–176).

16. Belic, D. S., Gordon H. Dunn, T. J. Morgan, D. W. Mueller, and C. Timmer: 'Dielectronic Recombination: A Crossed-Beams Observation and Measurement of Cross Section'. *Physical Review Letters* (1983), vol. 50(5): pp. 339–342. doi: 10.1103/physrevlett.50.339 (cit. on p. 29).

17. Berengut, J. C., V. A. Dzuba, and V. V. Flambaum: 'Enhanced Laboratory Sensitivity to Variation of the Fine-Structure Constant using Highly Charged Ions'. *Physical Review Letters* (2010), vol. 105(12): p. 120801. doi: 10.1103/physrevlett.105.120801 (cit. on pp. 4, 6, 7, 120, 128).

18. Berengut, J. C., V. A. Dzuba, and V. V. Flambaum: 'Transitions in Zr, Hf, Ta, W, Re, Hg, Ac, and U ions with high sensitivity to variation of the fine-structure constant'. *Physical Review A* (2011), vol. 84(5): p. 054501. doi: 10.1103/physreva.84.054501 (cit. on pp. 4, 7).

19. Berengut, J. C., V. A. Dzuba, V. V. Flambaum, and A. Ong: 'Electron-Hole Transitions in Multiply Charged Ions for Precision Laser Spectroscopy and Searching for Variations in α'. *Physical Review Letters* (2011), vol. 106(21): p. 210802. doi: 10.1103/physrevlett.106.210802 (cit. on pp. 4, 7, 103, 104, 120, 129).

20. Berengut, J. C., V. A. Dzuba, V. V. Flambaum, and A. Ong: 'Highly charged ions with E1, M1, and E2 transitions within laser range'. *Physical Review A* (2012), vol. 86(2): p. 022517. doi: 10.1103/physreva.86.022517 (cit. on pp. 4, 7, 120).

21. Berengut, J. C., V. A. Dzuba, V. V. Flambaum, and A. Ong: 'Optical Transitions in Highly Charged Californium Ions with High Sensitivity to Variation of the Fine-Structure Constant'. *Physical Review Letters* (2012), vol. 109(7): p. 070802. doi: 10.1103/physrevlett.109.070802 (cit. on pp. 4, 7).

22. Berengut, J. C., and V. V. Flambaum: 'Manifestations of a spatial variation of fundamental constants in atomic and nuclear clocks, Oklo, meteorites, and cosmological phenomena'. *EPL (Europhysics Letters)* (2012), vol. 97(2): p. 20006. doi: 10.1209/0295-5075/97/20006 (cit. on p. 4).

23. Bernitt, S. et al.: 'An unexpectedly low oscillator strength as the origin of the Fe XVII emission problem'. *Nature* (2012), vol. 492(7428): pp. 225–228. doi: 10.1038/nature11627 (cit. on p. 35).

24. Bethe, H.: 'Zur Theorie des Durchgangs schneller Korpuskularstrahlen durch Materie'. *Annalen der Physik* (1930), vol. 397(3): pp. 325–400. doi: 10.1002/andp.19303970303 (cit. on p. 27).

25. Beyer, H. F., R. D. Deslattes, F. Folkmann, and R. E. LaVilla: 'Determination of the 1*s* Lamb shift in one-electron argon recoil ions'. *Journal of Physics B: Atomic and Molecular Physics* (1985), vol. 18(2): pp. 207–215. doi: 10.1088/0022-3700/18/2/008 (cit. on pp. 1, 100).

26. Beyer, H. F., P. Indelicato, K. D. Finlayson, D. Liesen, and R. D. Deslattes: 'Measurement of the 1*s* Lamb shift in hydrogen-like nickel'. *Physical Review A* (1991), vol. 43(1): pp. 223–227. doi: 10.1103/physreva.43.223 (cit. on p. 1).

27. Beyer, H. F., G. Menzel, D. Liesen, A. Gallus, F. Bosch, R. Deslattes, P. Indelicato, Th. Stöhlker, O. Klepper, R. Moshammer, F. Nolden, H. Eickhoff, B. Franzke, and M. Steck: 'Measurement of the ground-state lambshift of hydrogen-like uranium at the electron cooler of the ESR'. *Zeitschrift für Physik D Atoms, Molecules and Clusters* (1995), vol. 35(3): pp. 169–175. doi: 10.1007/bf01437066 (cit. on pp. 2, 127).

28. Biedermann, Christoph, Rainer Radtke, Robert Seidel, and Thomas Pütterich: 'Spectroscopy of highly charged tungsten ions relevant to fusion plasmas'. *Physica Scripta* (2009), vol. T134: p. 014026. doi: 10.1088/0031-8949/2009/t134/014026 (cit. on p. 35).

29. Blessenohl, M. A., S. Dobrodey, C. Warnecke, M. K. Rosner, L. Graham, S. Paul, T. M. Baumann, Z. Hockenbery, R. Hubele, T. Pfeifer, F. Ames, J. Dilling, and J. R. Crespo López-Urrutia: 'An electron beam ion trap and source for re-acceleration of rare-isotope ion beams at TRIUMF'. *Review of Scientific Instruments* (2018), vol. 89(5): p. 052401. doi: 10.1063/1.5021045 (cit. on pp. 46, 49, 50, 52–54, 56).

30. Blessenohl, Michael Andreas: 'Master Thesis'. Master's thesis. Universität Heidelberg, 2015 (cit. on pp. 59, 65).

31. Blundell, Steven A.: 'Calculations of the screened self-energy and vacuum polarization in Li-like, Na-like, and Cu-like ions'. *Physical Review A* (1993), vol. 47(3): pp. 1790–1803. doi: 10.1103/physreva.47.1790 (cit. on pp. 95, 96, 98).

32. Bockasten, K., R. Hallin, and T. P. Hughes: 'The Spectra of Highly Ionized Light Elements in a High Temperature Plasma'. *Proceedings of the Physical Society* (Mar. 1963), vol. 81(3): pp. 522–530. doi: 10.1088/0370-1328/81/3/321 (cit. on pp. 89–91, 93, 95, 96, 99, 127).

33. Bosselmann, Ph., U. Staude, D. Horn, K.-H. Schartner, F. Folkmann, A. E. Livingston, and P. H. Mokler: 'Measurements of $2s\,^2S_{1/2} - 2p\,^2P_{1/2,3/2}$ transition energies in lithiumlike heavy ions. II. Experimental results for Ag^{44+} and discussion along the isoelectronic series'. *Physical Review A* (1999), vol. 59(3): pp. 1874–1883. doi: 10.1103/physreva.59.1874 (cit. on p. 2).

34. Bowen, I. S., and R. A. Millikan: 'Some Conspicuous Successes of the Bohr Atom and a Serious Difficulty'. *Physical Review* (1924), vol. 24(3): pp. 223–228. doi: 10.1103/physrev.24.223 (cit. on p. 89).

35. Bowen, I. S., and R. A. Millikan: 'Stripped Oxygen, O VI, the PP' Group in O V, and New Aluminum Lines in the Extreme Ultra-Violet'. *Physical Review* (1926), vol. 27(2): pp. 144–149. doi: 10.1103/physrev.27.144 (cit. on p. 91).

36. Brandau, C., T. Bartsch, A. Hoffknecht, H. Knopp, S. Schippers, W. Shi, A. Müller, N. Grün, W. Scheid, T. Steih, F. Bosch, B. Franzke, C. Kozhuharov, P. H. Mokler, F. Nolden, M. Steck, T. Stöhlker, and Z. Stachura: 'High Rydberg Resonances in Dielectronic Recombination of Pb^{79+}'. *Physical Review Letters* (2002), vol. 89(5): p. 053201. doi: 10.1103/physrevlett.89.053201 (cit. on p. 2).

37. Brandau, C., C. Kozhuharov, A. Müller, W. Shi, S. Schippers, T. Bartsch, S. Böhm, C. Böhme, A. Hoffknecht, H. Knopp, N. Grün, W. Scheid, T. Steih, F. Bosch, B. Franzke, P. H. Mokler, F. Nolden, M. Steck, T. Stöhlker, and Z. Stachura: 'Precise Determination of the $2s_{1/2}$–$2p_{1/2}$ Splitting in Very Heavy Lithiumlike Ions Utilizing Dielectronic Recombination'. *Physical Review Letters* (2003), vol. 91(7): p. 073202. doi: 10.1103/physrevlett.91.073202 (cit. on pp. 2, 3).

38. Bransden, Brian H., and Charles Jean Joachain: *Physics of Atoms and Molecules*. Second. Prentice Hall, 2006. isbn: 978-0582356924 (cit. on pp. 9, 15, 17, 25).

39. Briand, J. P., P. Charles, J. Arianer, H. Laurent, C. Goldstein, J. Dubau, M. Loulergue, and F. Bely-Dubau: 'Observation of the KLL Dielectronic Recombination Process in Highly Stripped Argon Ions'. *Physical Review Letters* (1984), vol. 52(8): pp. 617–620. doi: 10.1103/physrevlett.52.617 (cit. on p. 29).

40. Briand, J. P., P. Chevallier, P. Indelicato, K. P. Ziock, and D. D. Dietrich: 'Observation and measurement of $n = 2 \rightarrow n = 1$ transitions of hydrogenlike and heliumlike uranium'. *Physical Review Letters* (1990), vol. 65(22): pp. 2761–2764. doi: 10.1103/physrevlett.65.2761 (cit. on pp. 2, 127).

41. Briand, J. P., J. P. Mossé, P. Indelicato, P. Chevallier, D. Girard-Vernhet, A. Chetioui, M. T. Ramos, and J. P. Desclaux: 'Spectroscopy of hydrogenlike and heliumlike argon'. *Physical Review A* (1983), vol. 28(3): pp. 1413–1417. doi: 10.1103/physreva.28.1413 (cit. on pp. 1, 2, 100).

42. Briand, J. P., M. Tavernier, P. Indelicato, R. Marrus, and H. Gould: 'High-Precision Spectroscopic Studies of Lyman α Lines of Hydrogenlike Iron: A Measurement of the $1s$ Lamb Shift'. *Physical Review Letters* (1983), vol. 50(11): pp. 832–835. doi: 10.1103/physrevlett.50.832 (cit. on p. 1).

43. Briand, J. P., M. Tavernier, R. Marrus, and J. P. Desclaux: 'High-precision spectroscopic study of heliumlike iron'. *Physical Review A* (1984), vol. 29(6): pp. 3143–3149. doi: 10.1103/physreva.29.3143 (cit. on p. 2).

44. Bricault, Pierre G., Friedhelm Ames, Marik Dombsky, Peter Kunz, and Jens Lassen: 'Rare isotope beams at ISAC—target & ion source systems'. *Hyperfine Interactions* (2013), vol. 225(1-3): pp. 25–49. doi: 10.1007/s10751-013-0880-z (cit. on p. 31).

45. Brown, C. M.: 'On the $2s\ ^2S - 2p\ ^2P$ resonance lines of O VI and the $2s\ ^2S - 2p\ ^3P$ intercombination line of O V'. *Astronomy and Astrophysics* (1980), vol. 88(1–2): pp. 273–274. url: https://ui.adsabs.harvard.edu/abs/1980A&A....88..273B (cit. on pp. 92, 93).

46. Bruhns, H., J. Braun, K. Kubiček, J. R. Crespo López-Urrutia, and J. Ullrich: 'Testing QED Screening and Two-Loop Contributions with He-Like Ions'. *Physical Review Letters* (2007), vol. 99(11): p. 113001. doi: 10.1103/physrevlett.99.113001 (cit. on pp. 1, 2, 100).

47. Carlson, Thomas A., C. W. Nestor, Neil Wasserman, and J. D. Mcdowell: 'Calculated ionization potentials for multiply charged ions'. *Atomic Data and Nuclear Data Tables* (1970), vol. 2: pp. 63–99. doi: 10.1016/s0092-640x(70)80005-5 (cit. on pp. 103, 109).

48. Casini, R., and P. G. Nelson: 'On the intensity distribution function of blazed reflective diffraction gratings'. *Journal of the Optical Society of America A* (2014), vol. 31(10): p. 2179. doi: 10.1364/josaa.31.002179 (cit. on pp. 66, 67).

49. Chantler, C. T., M. N. Kinnane, J. D. Gillaspy, L. T. Hudson, A. T. Payne, L. F. Smale, A. Henins, J. M. Pomeroy, J. N. Tan, J. A. Kimpton, E. Takacs, and K. Makonyi: 'Testing Three-Body Quantum Electrodynamics with Trapped Ti^{20+} Ions: Evidence for a Z-dependent Divergence Between Experiment and Calculation'. *Physical Review Letters* (2012), vol. 109(15): p. 153001. doi: 10.1103/physrevlett.109.153001 (cit. on p. 2).

50. Chen, M. H., K. T. Cheng, W. R. Johnson, and J. Sapirstein: 'Relativistic configuration-interaction calculations for the n = 2 states of lithiumlike ions'. *Physical Review A* (1995), vol. 52(1): pp. 266–273. DOI: 10.1103/physreva.52.266 (cit. on pp. 95, 96).

51. Cheung, C., M. S. Safronova, S. G. Porsev, M. G. Kozlov, I. I. Tupitsyn, and A. I. Bondarev: 'Accurate Prediction of Clock Transitions in a Highly Charged Ion with Complex Electronic Structure'. *Physical Review Letters* (2020), vol. 124(16): p. 163001. DOI: 10.1103/physrevlett.124.163001 (cit. on pp. 103, 104, 106, 107, 122, 123, 129).

52. Cowan, Robert: *The theory of atomic structure and spectra*. Berkeley: University of California Press, 1981. ISBN: 9780520038219 (cit. on p. 18).

53. Davisson, C. J., and C. J. Calbick: 'Electron Lenses (Erratum)'. *Physical Review* (1932), vol. 42(4): pp. 580–580. DOI: 10.1103/physrev.42.580.

54. Davisson, C. J., and C. J. Calbick: 'Electron lenses'. *Physical Review* (Aug. 1931), vol. 38(Proceedings of the American Physical Society): p. 585.

55. Delaune, Boris Nikolaevich: 'Sur la sphère vide. A la mémoire de Georges Voronoï.' (June 1934), vol. VII(6): pp. 793–800. URL: http://mi.mathnet.ru/rus/izv/y1934/i6/p793 (cit. on p. 157).

56. Dere, Kenneth P.: 'Spectral lines observed in solar flares between 171 and 630 Angstroms'. *The Astrophysical Journal* (May 1978), vol. 221: pp. 1062–1067. DOI: 10.1086/156110 (cit. on pp. 97, 98, 127).

57. Derevianko, Andrei, V. A. Dzuba, and V. V. Flambaum: 'Highly Charged Ions as a Basis of Optical Atomic Clockwork of Exceptional Accuracy'. *Physical Review Letters* (2012), vol. 109(18): p. 180801. DOI: 10.1103/physrevlett.109.180801 (cit. on pp. 5, 120).

58. Deslattes, R. D., H. F. Beyer, and F. Folkmann: 'Precision X-ray wavelength measurements in helium-like argon recoil ions'. *Journal of Physics B: Atomic and Molecular Physics* (1984), vol. 17(21): pp. L689–L694. DOI: 10.1088/0022-3700/17/21/001 (cit. on pp. 2, 100).

59. Dirac, P. A. M.: 'The Cosmological Constants'. *Nature* (1937), vol. 139(3512): p. 323. DOI: 10.1038/139323a0 (cit. on p. 3).

60. Dittner, P. F., S. Datz, P. D. Miller, C. D. Moak, P. H. Stelson, C. Bottcher, W. B. Dress, G. D. Alton, N. Nešković, and C. M. Fou: 'Cross Sections for Dielectronic Recombination of B^{2+} and C^{3+} via $2s \rightarrow 2p$ Excitation'. *Physical Review Letters* (1983), vol. 51(1): pp. 31–34. DOI: 10.1103/physrevlett.51.31 (cit. on p. 29).

61. Dobrodey, Stepan: 'Charge-exchange studies of bare and hydrogen-like low-Z ions in the X-ray and extreme-ultraviolet ranges inside an electron beam ion trap'. Doctoral dissertation. Universtät Heidelberg, 2019. DOI: 10.11588/heidok.00027344 (cit. on p. 31).

62. Donets, E. D., V. I. Ilyushchenko, and V. A. Alpert: 'Ultrahigh vacuum electron beam source of highly stripped ions'. *Premiere Conference Internationale sur les Sources d'Ions, 18–20 Juin 1969*. 1970: pp. 635–642 (cit. on p. 31).

63. Dong, C. Z., D. H. Zhang, Th Stöhlker, S. Fritzsche, and B. Fricke: 'Relativity, electron correlation and QED effects in the $1s2s^2\ ^2S_{1/2}$ state of highly charged Li-like ions'. *Journal of Physics B: Atomic, Molecular and Optical Physics* (2006), vol. 39(14): pp. 3121–3129. doi: 10.1088/0953-4075/39/14/018 (cit. on p. 3).

64. Drake, Gordon W. F., ed.: *Atomic Structure: Multiconfiguration Hartree-Fock Theories*. Springer New York, 2006. doi: 10.1007/978-0-387-26308-3_21 (cit. on pp. 9, 17–19).

65. Dyson, Freeman J.: 'Time Variation of the Charge of the Proton'. *Physical Review Letters* (1967), vol. 19(22): pp. 1291–1293. doi: 10.1103/physrevlett.19.1291 (cit. on p. 4).

66. Dzuba, V. A., A. Derevianko, and V. V. Flambaum: 'High-precision atomic clocks with highly charged ions: Nuclear-spin-zero $f^1$2-shell ions'. *Physical Review A* (2012), vol. 86(5): p. 054501. doi: 10.1103/physreva.86.054501 (cit. on pp. 5, 120).

67. Dzuba, V. A., A. Derevianko, and V. V. Flambaum: 'Ion clock and search for the variation of the fine-structure constant using optical transitions in Nd^{13+} and Sm^{15+}'. *Physical Review A* (2012), vol. 86(5): p. 054502. doi: 10.1103/physreva.86.054502 (cit. on p. 7).

68. Dzuba, V. A., V. V. Flambaum, and Hidetoshi Katori: 'Optical clock sensitive to variations of the fine-structure constant based on the Ho^{14+} ion'. *Physical Review A* (2015), vol. 91(2): p. 022119. doi: 10.1103/physreva.91.022119 (cit. on pp. 7, 120).

69. Dzuba, V. A., V. V. Flambaum, and J. K. Webb: 'Calculations of the relativistic effects in many-electron atoms and space-time variation of fundamental constants'. *Physical Review A* (1999), vol. 59(1): pp. 230–237. doi: 10.1103/physreva.59.230 (cit. on p. 104).

70. Dzuba, V. A., M. S. Safronova, U. I. Safronova, and V. V. Flambaum: 'Actinide ions for testing the spatial α-variation hypothesis'. *Physical Review A* (2015), vol. 92(6): p. 060502. doi: 10.1103/physreva.92.060502 (cit. on p. 7).

71. Edlén, Bengt: 'Wellenlängen und Termsysteme zu den Atomspektren der Elemente Lithium, Beryllium, Bor, Kohlenstoff, Stickstoff und Sauerstoff'. *Nova acta Regiae Societatis Scientiarum Upsaliensis* (1934), vol. 9(6): p. 153. doi: 10.11588/heidok.00007493 (cit. on pp. 89–91, 93, 94).

72. Einstein, A.: 'Über einen die Erzeugung und Verwandlung des Lichtes betreffenden heuristischen Gesichtspunkt'. *Annalen der Physik* (1905), vol. 322(6): pp. 132–148. doi: 10.1002/andp.19053220607 (cit. on p. 27).

73. Eissner, W., M. Jones, and H. Nussbaumer: 'Techniques for the calculation of atomic structures and radiative data including relativistic corrections'. *Computer Physics Communications* (1974), vol. 8(4): pp. 270–306. doi: 10.1016/0010-4655(74)90019-8 (cit. on p. 18).

74. Eite Tiesinga Peter J. Mohr, David B. Newell, and Barry N. Taylor: *The 2018 CODATA Recommended Values of the Fundamental Physical Constants (Web Version 8.1). Database developed by J. Baker, M. Douma, and S. Kotochigova.* National Institute of Standards and Technology, 2018. url: http://physics.nist.gov/constants (cit. on pp. 2, 26).

75. Eliav, E., U. Kaldor, and Y. Ishikawa: *Tel-Aviv Relativistic Atomic Fock Space coupled cluster code (TRAFS-3C), available on request.* (Cit. on p. 18).

76. Eliav, Ephraim, Uzi Kaldor, and Yasuyuki Ishikawa: 'Ionization potentials and excitation energies of the alkali-metal atoms by the relativistic coupled-cluster method'. *Physical Review A* (1994), vol. 50(2): pp. 1121–1128. doi: 10.1103/physreva.50.1121 (cit. on p. 18).

77. Eliav, Ephraim, Uzi Kaldor, and Yasuyuki Ishikawa: 'Open-shell relativistic coupled-cluster method with Dirac-Fock-Breit wave functions: Energies of the gold atom and its cation'. *Physical Review A* (1994), vol. 49(3): pp. 1724–1729. doi: 10.1103/physreva.49.1724 (cit. on p. 18).

78. Epp, S. W., J. R. Crespo López-Urrutia, G. Brenner, V. Mäckel, P. H. Mokler, R. Treusch, M. Kuhlmann, M. V. Yurkov, J. Feldhaus, J. R. Schneider, M. Wellhöfer, M. Martins, W. Wurth, and J. Ullrich: 'Soft X-Ray Laser Spectroscopy on Trapped Highly Charged Ions at FLASH'. *Physical Review Letters* (2007), vol. 98(18): p. 183001. doi: 10.1103/physrevlett.98.183001 (cit. on pp. 2, 3).

79. Epp, S. W., J. R. Crespo López-Urrutia, M. C. Simon, T. Baumann, G. Brenner, R. Ginzel, N. Guerassimova, V. Mäckel, P. H. Mokler, B. L. Schmitt, H. Tawara, and J. Ullrich: 'X-ray laser spectroscopy of highly charged ions at FLASH'. *Journal of Physics B: Atomic, Molecular and Optical Physics* (2010), vol. 43(19): p. 194008. doi: 10.1088/0953-4075/43/19/194008 (cit. on pp. 2, 35).

80. Epp, S. W., R. Steinbrügge, S. Bernitt, J. K. Rudolph, C. Beilmann, H. Bekker, A. Müller, O. O. Versolato, H.-C. Wille, H. Yavaş, J. Ullrich, and J. R. Crespo López-Urrutia: 'Single-photon excitation of Kα in heliumlike Kr^{34+}: Results supporting quantum electrodynamics predictions'. *Physical Review A* (2015), vol. 92(2): p. 020502. doi: 10.1103/physreva.92.020502 (cit. on p. 2).

81. Epp, Sascha: 'Röntgen-Laserspektroskopie hochgeladener Ionen in einer EBIT am Freie-Elektronen-Laser FLASH'. Doctoral dissertation. Universtät Heidelberg, 2007. doi: 10.11588/heidok.00007493 (cit. on p. 57).

82. Erickson, Glen W.: 'Improved Lamb-Shift Calculation for All Values of Z'. *Physical Review Letters* (1971), vol. 27(12): pp. 780–783. doi: 10.1103/physrevlett.27.780 (cit. on p. 2).

83. Fawcett, B. C., B. B. Jones, and R. Wilson: 'Vacuum Ultra-violet Spectra of Multiply Ionized Inert Gases'. *Proceedings of the Physical Society* (1961), vol. 78(6): pp. 1223–1226. doi: 10.1088/0370-1328/78/6/318 (cit. on pp. 95, 96, 99).

84. Feili, D., Ph. Bosselmann, K.-H. Schartner, F. Folkmann, A. E. Livingston, E. Träbert, X. Ma, and P. H. Mokler: 'Measurements of $2s\,^2S_{1/2} - 2p\,^2P_{1/2}$ transition energies in lithiumlike heavy ions. III. Experimental results for Sn^{47+} and Xe^{51+}'. *Physical Review A* (2000), vol. 62(2): p. 022501. doi: 10.1103/physreva.62.022501 (cit. on p. 2).

85. Fischer, Charlotte: *Computational atomic structure: an MCHF approach*. Bristol, UK Philadelphia, Penn: Institute of Physics Publ, 1997. isbn: 0750303743 (cit. on p. 18).

86. Flambaum, V. V.: 'Enhanced Effect of Temporal Variation of the Fine Structure Constant and the Strong Interaction in Th^{229}'. *Physical Review Letters* (2006), vol. 97(9): p. 092502. doi: 10.1103/physrevlett.97.092502 (cit. on pp. 4, 5).

87. Fontes, C. J., K. A. Eriksen, J. Colgan, H. L. Zhang, and J. P. Hughes: 'Spectral modeling of supernova remnants'. *High Energy Density Physics* (2014), vol. 10: pp. 43–46. doi: 10.1016/j.hedp.2013.10.001 (cit. on p. 2).

88. Foot, Christopher J.: *Atomic physics*. Oxford master series in atomic, optical and laser physics. Oxford: Oxford University Press, 2007. isbn: 9780198506959 (cit. on p. 9).

89. Fraunhofer, Joseph: 'Bestimmung des Brechungs- und des Farbenzerstreungs-Vermögens verschiedener Glasarten, in Bezug auf die Vervollkommnung achromatischer Fernröhre'. *Annalen der Physik* (1817), vol. 56(7): pp. 264–313. doi: 10.1002/andp.18170560706 (cit. on p. 1).

90. Fraunhofer, Joseph: 'Kurzer Bericht von den Resultaten neuerer Versuche über die Gesetze des Lichtes, und die Theorie derselben'. *Annalen der Physik und der physikalischen Chemie* (1823), vol. 74(8): pp. 337–378. doi: 10.1002/andp.18230740802 (cit. on p. 1).

91. Gamow, G.: 'Electricity, Gravity, and Cosmology'. *Physical Review Letters* (1967), vol. 19(13): pp. 759–761. doi: 10.1103/physrevlett.19.759 (cit. on p. 4).

92. Gamow, G.: 'Erratum for Electricity, Gravity, and Cosmology'. *Physical Review Letters* (1967), vol. 19(17): p. 1000. doi: 10.1103/physrevlett.19.1000.4 (cit. on p. 4).

93. Godun, R. M., P. B. R. Nisbet-Jones, J. M. Jones, S. A. King, L. A. M. Johnson, H. S. Margolis, K. Szymaniec, S. N. Lea, K. Bongs, and P. Gill: 'Frequency Ratio of Two Optical Clock Transitions in $^{171}Yb^+$ and Constraints on the Time Variation of Fundamental Constants'. *Physical Review Letters* (2014), vol. 113(21): p. 210801. doi: 10.1103/physrevlett.113.210801 (cit. on pp. 5, 128).

94. Grant, I. P., B. J. McKenzie, P. H. Norrington, D. F. Mayers, and N. C. Pyper: 'An atomic multiconfigurational Dirac-Fock package'. *Computer Physics Communications* (1980), vol. 21(2): pp. 207–231. doi: 10.1016/0010-4655(80)90041-7 (cit. on p. 19).

95. Gu, Ming Feng: 'The Flexible Atomic Code'. *AIP Conference Proceedings*. AIP, 2004. doi: 10.1063/1.1824864 (cit. on p. 19).

96. Gu, Ming Feng: 'The Flexible Atomic Code'. *Canadian Journal of Physics* (2008), vol. 86(5): pp. 675–689. doi: 10.1139/p07-197 (cit. on pp. 9, 19).

97. Gumberidze, A., Th. Stöhlker, D. Banaś, K. Beckert, P. Beller, H. F. Beyer, F. Bosch, X. Cai, S. Hagmann, C. Kozhuharov, D. Liesen, F. Nolden, X. Ma, P. H. Mokler, A. Oršić-Muthig, M. Steck, D. Sierpowski, S. Tashenov, A. Warczak, and Y. Zou: 'Electron-Electron Interaction in Strong Electromagnetic Fields: The Two-Electron Contribution to the Ground-State Energy in He-like Uranium'. *Physical Review Letters* (2004), vol. 92(20): p. 203004. doi: 10.1103/physrevlett.92.203004 (cit. on p. 2).

98. Gumberidze, A., Th. Stöhlker, D. Banaś, K. Beckert, P. Beller, H. F. Beyer, F. Bosch, S. Hagmann, C. Kozhuharov, D. Liesen, F. Nolden, X. Ma, P. H. Mokler, M. Steck, D. Sierpowski, and S. Tashenov: 'Quantum Electrodynamics in Strong Electric Fields: The Ground-State Lamb Shift in Hydrogenlike Uranium'. *Physical Review Letters* (2005), vol. 94(22): p. 223001. doi: 10.1103/physrevlett.94.223001 (cit. on p. 2).

99. Hallin, Reinhold: 'The spectrum of N V'. *Arkiv för Fysik* (Nov. 1966), vol. 31(36): pp. 511–526 (cit. on pp. 90, 91).

100. Hanneke, D., S. Fogwell Hoogerheide, and G. Gabrielse: 'Cavity control of a single-electron quantum cyclotron: Measuring the electron magnetic moment'. *Physical Review A* (2011), vol. 83(5): p. 052122. doi: 10.1103/physreva.83.052122 (cit. on p. 19).

101. Harada, Tatsuo, and Toshiaki Kita: 'Mechanically ruled aberration-corrected concave gratings'. *Applied Optics* (1980), vol. 19(23): p. 3987. doi: 10.1364/ao.19.003987 (cit. on p. 75).

102. Herrmann, Gabriel: 'Optical Theory of Thermal Velocity Effects in Cylindrical Electron Beams'. *Journal of Applied Physics* (1958), vol. 29(2): pp. 127–136. doi: 10.1063/1.1723053 (cit. on p. 38).

103. Hertz, H.: 'Über einen Einfluss des ultravioletten Lichtes auf die electrische Entladung'. *Annalen der Physik und Chemie* (1887), vol. 267(8): pp. 983–1000. doi: 10.1002/andp.18872670827 (cit. on p. 27).

104. Hibbert, A.: 'CIV3 — A general program to calculate configuration interaction wave functions and electric-dipole oscillator strengths'. *Computer Physics Communications* (1975), vol. 9(3): pp. 141–172. doi: 10.1016/0010-4655(75)90103-4 (cit. on p. 18).

105. Hunter, W. R., D. W. Angel, and G. Hass: 'Optical properties of evaporated platinum films in the vacuum ultraviolet from 2200 Å to 150 Å'. (1979), vol. 69(12): p. 1695. doi: 10.1364/josa.69.001695 (cit. on p. 66).

106. Ichihara, Akira, and Jörg Eichler: 'Cross sections for radiative recombination and the photoelectric effect in the K, L, and M shells of one-electron systems with $1 \leq Z \leq 112$ calculated within an exact relativistic description'. *Atomic Data and Nuclear Data Tables* (2000), vol. 74(1): pp. 1–121. doi: 10.1006/adnd.1999.0825 (cit. on p. 28).

107. Ichihara, Akira, Toshizo Shirai, and Jörg Eichler: 'Radiative electron capture in relativistic atomic collisions'. *Physical Review A* (1994), vol. 49(3): pp. 1875–1884. doi: 10.1103/physreva.49.1875 (cit. on pp. 27, 30).

108. Indelicato, P., J. P. Briand, M. Tavernier, and D. Liesen: 'Experimental study of relativistic correlations and QED effects in heliumlike Krypton ions'. *Zeitschrift für Physik D Atoms, Molecules and Clusters* (1986), vol. 2(3): pp. 249–250. doi: 10.1007/bf01429081 (cit. on p. 2).

109. Janev, R. K., D. S. Belić, and B. H. Bransden: 'Total and partial cross sections for electron capture in collisions of hydrogen atoms with fully stripped ions'. *Physical Review A* (1983), vol. 28(3): pp. 1293–1302. doi: 10.1103/physreva.28.1293 (cit. on p. 30).

110. Jenkins, E. B., and D. A. Meloy: 'A survey with Copernicus of interstellar O VI absorption'. *The Astrophysical Journal* (1974), vol. 193: p. L121. doi: 10.1086/181647 (cit. on p. 91).

111. Kahl, E. V., and J. C. Berengut: 'AMBiT: A programme for high-precision relativistic atomic structure calculations'. *Computer Physics Communications* (2019), vol. 238: pp. 232–243. doi: 10.1016/j.cpc.2018.12.014 (cit. on p. 19).

112. Kaldor, Uzi: 'The Fock space coupled cluster method: theory and application'. *Theoretica Chimica Acta* (1991), vol. 80(6): pp. 427–439. doi: 10.1007/bf01119664 (cit. on p. 18).

113. Kaufman, V., and W. C. Martin: 'Wavelengths of the O VI $2s\ ^2Sp - 2p\ ^2P$ resonance-doublet lines'. *Journal of the Optical Society of America B* (1989), vol. 6(10): p. 1769. doi: 10.1364/josab.6.001769 (cit. on pp. 92, 93, 101, 165, 166).

114. Kim, Y.-K., D. H. Baik, P. Indelicato, and J. P. Desclaux: 'Resonance transition energies of Li-, Na-, and Cu-like ions'. *Physical Review A* (1991), vol. 44(1): pp. 148–166. doi: 10.1103/physreva.44.148 (cit. on pp. 90, 91, 93, 95, 96, 98, 99, 120).

115. Kim, Young Soon, and R. H. Pratt: 'Direct radiative recombination of electrons with atomic ions: Cross sections and rate coefficients'. *Physical Review A* (1983), vol. 27(6): pp. 2913–2924. doi: 10.1103/physreva.27.2913 (cit. on p. 30).

116. Kirchhoff, G.: 'Über die Fraunhofer'schen Linien'. *Monatsberichte der Königlichen Preußischen Akademie der Wissenschaften zu Berlin* (Oct. 1859), vol.: pp. 662–665. url: https://www.biodiversitylibrary.org/page/11070022 (cit. on p. 1).

117. Koscielniak, Shane: 'ARIEL e-linac'. *Hyperfine Interactions* (2013), vol. 225(1-3): pp. 263–273. doi: 10.1007/s10751-013-0907-5 (cit. on p. 31).

118. Kozhedub, Y. S., A. V. Volotka, A. N. Artemyev, D. A. Glazov, G. Plunien, V. M. Shabaev, I. I. Tupitsyn, and Th. Stöhlker: 'Relativistic recoil, electron-correlation, and QED effects on the $2p_j - 2s$ transition energies in Li-like ions'. *Physical Review A* (2010), vol. 81(4): p. 042513. doi: 10.1103/physreva.81.042513 (cit. on pp. 3, 7, 19–24, 95–98, 101).

119. Kozlov, A., V. A. Dzuba, and V. V. Flambaum: 'Transition amplitudes, polarizabilities, and energy levels within optical wavelength of highly charged ions Sm^{14+} and Sm^{13+}'. *Physical Review A* (2013), vol. 88(6): p. 062509. doi: 10.1103/physreva.88.062509 (cit. on p. 7).

120. Kozlov, M. G., M. S. Safronova, J. R. Crespo López-Urrutia, and P. O. Schmidt: 'Highly charged ions: Optical clocks and applications in fundamental physics'. *Reviews of Modern Physics* (2018), vol. 90(4): p. 045005. doi: 10.1103/revmodphys.90.045005 (cit. on pp. 2, 5).

121. Kramida, A. E., and M.-C. Buchet-Poulizac: 'Energy levels and spectral lines of Ne VIII'. *The European Physical Journal D* (2006), vol. 39(2): pp. 173–188. doi: 10.1140/epjd/e2006-00122-3 (cit. on p. 94).

122. Kramida, Alexander, and Yuri Ralchenko: *NIST Atomic Spectra Database, NIST Standard Reference Database 78*. eng. 1999. doi: 10.18434/T4W30F (cit. on pp. 84, 116, 163, 171).

123. Kubiček, K., J. Braun, H. Bruhns, J. R. Crespo López-Urrutia, P. H. Mokler, and J. Ullrich: 'High-precision laser-assisted absolute determination of x-ray diffraction angles'. *Review of Scientific Instruments* (2012), vol. 83(1): p. 013102. doi: 10.1063/1.3662412 (cit. on pp. 2, 100).

124. Kubiček, K., P. H. Mokler, V. Mäckel, J. Ullrich, and J. R. Crespo López-Urrutia: 'Transition energy measurements in hydrogenlike and heliumlike ions strongly supporting bound-state QED calculations'. *Physical Review A* (2014), vol. 90(3): p. 032508. doi: 10.1103/physreva.90.032508 (cit. on pp. 1, 2, 100).

125. Lamb, Willis E., and Robert C. Retherford: 'Fine Structure of the Hydrogen Atom by a Microwave Method'. *Physical Review* (1947), vol. 72(3): pp. 241–243. doi: 10.1103/physrev.72.241 (cit. on p. 1).

126. Lamoreaux, S. K., and J. R. Torgerson: 'Neutron moderation in the Oklo natural reactor and the time variation of α'. *Physical Review D* (2004), vol. 69(12): p. 121701. doi: 10.1103/physrevd.69.121701 (cit. on pp. 4, 5, 128).

127. Lapierre, A.: 'Electron-beam ion source/trap charge breeders at rare-isotope beam facilities'. *Review of Scientific Instruments* (2019), vol. 90(10): p. 103312. doi: 10.1063/1.5127203 (cit. on pp. 32, 33).

128. Leefer, N., C. T. M. Weber, A. Cingöz, J. R. Torgerson, and D. Budker: 'New Limits on Variation of the Fine-Structure Constant Using Atomic Dysprosium'. *Physical Review Letters* (2013), vol. 111(6): p. 060801. doi: 10.1103/physrevlett.111.060801 (cit. on p. 5).

129. Lestinsky, M., E. Lindroth, D. A. Orlov, E. W. Schmidt, S. Schippers, S. Böhm, C. Brandau, F. Sprenger, A. S. Terekhov, A. Müller, and A. Wolf: 'Screened Radiative Corrections from Hyperfine-Split Dielectronic Resonances in Lithiumlike Scandium'. *Physical Review Letters* (2008), vol. 100(3): p. 033001. doi: 10.1103/physrevlett.100.033001 (cit. on pp. 2, 3).

130. Levine, Morton A., R. E. Marrs, J. R. Henderson, D. A. Knapp, and Marilyn B. Schneider: 'The Electron Beam Ion Trap: A New Instrument for Atomic Physics Measurements'. *Physica Scripta* (1988), vol. T22: pp. 157–163. doi: 10.1088/0031-8949/1988/t22/024 (cit. on pp. 33, 35).

131. Lotz, Wolfgang: 'Electron-Impact Ionization Cross-Sections and Ionization Rate Coefficients for Atoms and Ions'. *The Astrophysical Journal Supplement Series* (1967), vol. 14: p. 207. doi: 10.1086/190154 (cit. on pp. 27, 33).

132. Lotz, Wolfgang: 'Electron-impact ionization cross-sections and ionization rate coefficients for atoms and ions from hydrogen to calcium'. *Zeitschrift für Physik* (1968), vol. 216(3): pp. 241–247. doi: 10.1007/bf01392963 (cit. on p. 27).

133. Machado, J., C. I. Szabo, J. P. Santos, P. Amaro, M. Guerra, A. Gumberidze, Guojie Bian, J. M. Isac, and P. Indelicato: 'High-precision measurements of $n = 2 \to n = 1$ transition energies and level widths in He- and Be-like argon ions'. *Physical Review A* (2018), vol. 97(3): p. 032517. doi: 10.1103/physreva.97.032517 (cit. on pp. 2, 100).

134. Mandal, P., G. Sikler, and M. Mukherjee: 'Simulation study and analysis of a compact einzel lens-deflector for low energy ion beam'. *Journal of Instrumentation* (2011), vol. 6(02): P02004. doi: 10.1088/1748-0221/6/02/p02004 (cit. on p. 42).

135. Marmar, E. S., J. E. Rice, K. Kallne, J. Kallne, and R. E. LaVilla: 'Precision measurement of the 1s Lamb shift in hydrogenlike argon'. *Physical Review A* (1986), vol. 33(1): pp. 774–777. doi: 10.1103/physreva.33.774 (cit. on pp. 1, 100).

136. Martin, Christopher, and Stuart Bowyer: 'Quantum efficiency of opaque CsI photocathodes with channel electron multiplier arrays in the extreme and far ultraviolet'. *Applied Optics* (1982), vol. 21(23): p. 4206. doi: 10.1364/ao.21.004206 (cit. on pp. 67, 68).

137. Massey, H. S. W., and D. R. Bates: 'The properties of neutral and ionized atomic oxygen and their influence on the upper atmosphere'. *Reports on Progress in Physics* (1942), vol. 9(1): pp. 62–74. doi: 10.1088/0034-4885/9/1/308 (cit. on p. 29).

138. Meitner, Lise: 'Über die Entstehung der β-Strahl-Spektren radioaktiver Substanzen'. *Zeitschrift für Physik* (1922), vol. 9(1): pp. 131–144. doi: 10.1007/bf01326962 (cit. on p. 29).

139. Mercadier, L., A. Benediktovitch, C. Weninger, M. A. Blessenohl, S. Bernitt, H. Bekker, S. Dobrodey, A. Sanchez-Gonzalez, B. Erk, C. Bomme, R. Boll, Z. Yin, V. P. Majety, R. Steinbrügge, M. A. Khalal, F. Penent, J. Palaudoux, P. Lablanquie, A. Rudenko, D. Rolles, J. R. Crespo López-Urrutia, and N. Rohringer: 'Evidence of Extreme Ultraviolet Superfluorescence in Xenon'. *Physical Review Letters* (2019), vol. 123(2): p. 023201. doi: 10.1103/physrevlett.123.023201 (cit. on pp. 59, 65).

140. Michelson, Albert A.: 'XXX. On the application of interference methods to spectroscopic measurements.—II'. *The London, Edinburgh, and Dublin Philosophical Magazine and Journal of Science* (1892), vol. 34(208): pp. 280–299. doi: 10.1080/14786449208620318 (cit. on p. 13).

141. Michelson, Albert A., and Edward W. Morley: 'LIX. On a method of making the wave-length of sodium light the actual and practical standard of length'. *The London, Edinburgh, and Dublin Philosophical Magazine and Journal of Science* (1887), vol. 24(151): pp. 463–466. doi: 10.1080/14786448708628131 (cit. on pp. 1, 12, 130).

142. Micke, P., T. Leopold, S. A. King, E. Benkler, L. J. Spiess, L. Schmöger, M. Schwarz, J. R. Crespo López-Urrutia, and P. O. Schmidt: 'Coherent laser spectroscopy of highly charged ions using quantum logic'. *Nature* (2020), vol. 578(7793): pp. 60–65. doi: 10.1038/s41586-020-1959-8 (cit. on pp. 5, 104, 129).

143. Mitchell, J. B. A., C. T. Ng, J. L. Forand, D. P. Levac, R. E. Mitchell, A. Sen, D. B. Miko, and J. Wm. McGowan: 'Dielectronic-Recombination Cross-Section Measurements for C^+ Ions'. *Physical Review Letters* (1983), vol. 50(5): pp. 335–338. doi: 10.1103/physrevlett.50.335 (cit. on p. 29).

144. Mohr, Peter J.: 'Self-energy correction to one-electron energy levels in a strong Coulomb field'. *Physical Review A* (1992), vol. 46(7): pp. 4421–4424. doi: 10.1103/physreva.46.4421 (cit. on p. 23).

145. Mohr, Peter J., Günter Plunien, and Gerhard Soff: 'QED corrections in heavy atoms'. *Physics Reports* (1998), vol. 293(5-6): pp. 227–369. doi: 10.1016/s0370-1573(97)00046-x (cit. on p. 2).

146. Pasternack, Simon: 'Note on the Fine Structure of Hα and Dα'. *Physical Review* (1938), vol. 54(12): p. 1113. doi: 10.1103/physrev.54.1113 (cit. on p. 1).

147. Peik, E., and Chr Tamm: 'Nuclear laser spectroscopy of the 3.5 eV transition in Th-229'. *Europhysics Letters (EPL)* (2003), vol. 61(2): pp. 181–186. doi: 10.1209/epl/i2003-00210-x (cit. on pp. 5, 129).

148. Penetrante, B. M., J. N. Bardsley, D. DeWitt, M. Clark, and D. Schneider: 'Evolution of ion-charge-state distributions in an electron-beam ion trap'. *Physical Review A* (1991), vol. 43(9): pp. 4861–4872. doi: 10.1103/physreva.43.4861 (cit. on p. 30).

149. Pierce, J. R.: 'Rectilinear Electron Flow in Beams'. *Journal of Applied Physics* (1940), vol. 11(8): pp. 548–554. doi: 10.1063/1.1712815 (cit. on p. 38).

150. Porter, Frederick Scott, Greg V. Brown, Kevin R. Boyce, Richard L. Kelley, Caroline A. Kilbourne, Peter Beiersdorfer, Hui Chen, Stephane Terracol, Steven M. Kahn, and Andrew E. Szymkowiak: 'The Astro-E2 X-ray spectrometer/EBIT microcalorimeter x-ray spectrometer'. *Review of Scientific Instruments* (2004), vol. 75(10): pp. 3772–3774. doi: 10.1063/1.1781758 (cit. on p. 35).

151. Pratt, R. H., Akiva Ron, and H. K. Tseng: 'Atomic Photoelectric Effect Above 10 keV'. *Reviews of Modern Physics* (1973), vol. 45(2): pp. 273–325. doi: 10.1103/revmodphys.45.273 (cit. on p. 27).

152. Pratt, R. H., Akiva Ron, and H. K. Tseng: 'Erratum: Atomic Photoelectric Effect above 10 keV'. *Reviews of Modern Physics* (1973), vol. 45(4): pp. 663–664. doi: 10.1103/revmodphys.45.663 (cit. on p. 27).

153. Pych, Wojtek: 'A Fast Algorithm for Cosmic-Ray Removal from Single Images'. *Publications of the Astronomical Society of the Pacific* (2004), vol. 116(816): pp. 148–153. doi: 10.1086/381786 (cit. on p. 78).

154. Reichardt, G., T. Noll, I. Packe, P. Rotter, J.-S. Schmidt, and W. Gudat: 'Adaption of the BESSY I-3m normal incidence monochromators to the BESSY II source'. *Nuclear Instruments and Methods in Physics Research Section A: Accelerators, Spectrometers, Detectors and Associated Equipment* (2001), vol. 467-468: pp. 458–461. doi: 10.1016/s0168-9002(01)00357-6 (cit. on pp. 59, 65).

155. Richard, Patrick, Martin Stockli, R. D. Deslattes, P. Cowan, R. E. La Villa, B. Johnson, K. Jones, M. Meron, Rido Mann, and K. Schartner: 'Measurement of the 1*s* Lamb shift in hydrogenlike chlorine'. *Physical Review A* (1984), vol. 29(5): pp. 2939–2942. doi: 10.1103/physreva.29.2939 (cit. on p. 1).

156. Ritz, W.: 'On a New Law of Series Spectra'. *The Astrophysical Journal* (1908), vol. 28: p. 237. doi: 10.1086/141591 (cit. on p. 120).

157. Roberts, Benjamin M., Geoffrey Blewitt, Conner Dailey, Mac Murphy, Maxim Pospelov, Alex Rollings, Jeff Sherman, Wyatt Williams, and Andrei Derevianko: 'Search for domain wall dark matter with atomic clocks on board global positioning system satellites'. *Nature Communications* (2017), vol. 8(1): p. 1195. doi: 10.1038/s41467-017-01440-4 (cit. on p. 130).

158. Rosenband, T., D. B. Hume, P. O. Schmidt, C. W. Chou, A. Brusch, L. Lorini, W. H. Oskay, R. E. Drullinger, T. M. Fortier, J. E. Stalnaker, S. A. Diddams, W. C. Swann, N. R. Newbury, W. M. Itano, D. J. Wineland, and J. C. Bergquist: 'Frequency Ratio of Al^+ and Hg^+ Single-Ion Optical Clocks; Metrology at the 17th Decimal Place'. *Science* (2008), vol. 319(5871): pp. 1808–1812. doi: 10.1126/science.1154622 (cit. on pp. 4, 5, 104, 128).

159. Rowland, Henry A.: 'XXIX. On concave gratings for optical purposes'. *The London, Edinburgh, and Dublin Philosophical Magazine and Journal of Science* (1883), vol. 16(99): pp. 197–210. doi: 10.1080/14786448308627419 (cit. on p. 59).

160. Rudolph, J. K., S. Bernitt, S. W. Epp, R. Steinbrügge, C. Beilmann, G. V. Brown, S. Eberle, A. Graf, Z. Harman, N. Hell, M. Leutenegger, A. Müller, K. Schlage, H.-C. Wille, H. Yavaş, J. Ullrich, and J. R. Crespo López-Urrutia: 'X-Ray Resonant Photoexcitation: Linewidths and Energies of $K\alpha$ Transitions in Highly Charged Fe Ions'. *Physical Review Letters* (2013), vol. 111(10): p. 103002. doi: 10.1103/physrevlett.111.103002 (cit. on p. 3).

161. Ryabtsev, A. N.: 'Wavelengths of the O VI resonance lines'. *Soviet Astronomy Letters* (1975), vol. 1: pp. 191–192 (cit. on pp. 91, 93).

162. Rydberg, J. R.: 'Researches sur la constitution des spectres d'émission des éléments chimiques'. *Kongliga Svenska Vetenskaps-Akademiens Handlingar* (Nov. 1889), vol. 23(11): pp. 1–177. url: https://www.biodiversitylibrary.org/page/41852974 (cit. on p. 120).

163. Safronova, M. S., V. A. Dzuba, V. V. Flambaum, U. I. Safronova, S. G. Porsev, and M. G. Kozlov: 'Atomic properties of Cd-like and Sn-like ions for the development of frequency standards and search for the variation of the fine-structure constant'. *Physical Review A* (2014), vol. 90(5): p. 052509. doi: 10.1103/physreva.90.052509 (cit. on pp. 7, 120).

164. Safronova, M. S., V. A. Dzuba, V. V. Flambaum, U. I. Safronova, S. G. Porsev, and M. G. Kozlov: 'Highly charged Ag-like and In-like ions for the development of atomic clocks and the search for α variation'. *Physical Review A* (2014), vol. 90(4): p. 042513. doi: 10.1103/physreva.90.042513 (cit. on pp. 7, 120).

165. Safronova, M. S., V. A. Dzuba, V. V. Flambaum, U. I. Safronova, S. G. Porsev, and M. G. Kozlov: 'Highly Charged Ions for Atomic Clocks, Quantum Information, and Search for alpha variation'. *Physical Review Letters* (2014), vol. 113(3): p. 030801. doi: 10.1103/physrevlett.113.030801 (cit. on p. 7).

166. Safronova, U. I., V. V. Flambaum, and M. S. Safronova: 'Transitions between the 4f-core-excited states in Ir16, Ir17+, and Ir18+ ions for clock applications'. *Physical Review A* (2015), vol. 92(2): p. 022501. doi: 10.1103/physreva.92.022501 (cit. on p. 104).

167. Safronova, U. I., and M. S. Safronova: 'Relativistic many-body calculations of energies for doubly-excited $1s2l2l'$ and $1s3l3l'$ states in Li-like ions'. *Canadian Journal of Physics* (2004), vol. 82(9): pp. 743–764. doi: 10.1139/p04-041 (cit. on p. 3).

168. Samson, James A. R.: *Techniques of vacuum ultraviolet spectroscopy*. eng. Wiley series in pure and applied spectroscopy. New York [u.a.]: Wiley, 1967: X, 348 S. (Cit. on p. 60).

169. Sandlin, G. D., G. E. Brueckner, V. E. Scherrer, and R. Tousey: 'High-temperature flare lines in the solar spectrum 171 A–630 A'. *The Astrophysical Journal* (Apr. 1976), vol. 205: pp. L47–L50. doi: 10.1086/182087 (cit. on pp. 97, 98, 127).

170. Sapirstein, J., and K. T. Cheng: 'Determination of the two-loop Lamb shift in lithiumlike bismuth'. *Physical Review A* (2001), vol. 64(2): p. 022502. doi: 10.1103/physreva.64.022502 (cit. on p. 3).

171. Sapirstein, J., and K. T. Cheng: 'S-matrix calculations of energy levels of the lithium isoelectronic sequence'. *Physical Review A* (2011), vol. 83(1): p. 012504. doi: 10.1103/physreva.83.012504 (cit. on pp. 96–98).

172. Schweppe, J., A. Belkacem, L. Blumenfeld, Nelson Claytor, B. Feinberg, Harvey Gould, V. E. Kostroun, L. Levy, S. Misawa, J. R. Mowat, and M. H. Prior: 'Measurement of the Lamb shift in lithiumlike uranium (U^{89+})'. *Physical Review Letters* (1991), vol. 66(11): pp. 1434–1437. doi: 10.1103/physrevlett.66.1434 (cit. on p. 2).

173. Seiferle, Benedict, Lars von der Wense, Pavlo V. Bilous, Ines Amersdorffer, Christoph Lemell, Florian Libisch, Simon Stellmer, Thorsten Schumm, Christoph E. Düllmann, Adriana Pálffy, and Peter G. Thirolf: 'Energy of the ^{229}Th nuclear clock transition'. *Nature* (2019), vol. 573(7773): pp. 243–246. doi: 10.1038/s41586-019-1533-4 (cit. on pp. 5, 129).

174. Shah, Chintan, Stepan Dobrodey, Sven Bernitt, René Steinbrügge, José R. Crespo López-Urrutia, Liyi Gu, and Jelle Kaastra: 'Laboratory measurements compellingly support a charge-exchange mechanism for the "dark matter" $\sim$ 3.5 keV X-ray line'. *The Astrophysical Journal* (2016), vol. 833(1): p. 52. doi: 10.3847/1538-4357/833/1/52 (cit. on p. 35).

175. Skinner, C. H.: 'Applications of EBIT to magnetic fusion diagnostics'. *Canadian Journal of Physics* (2008), vol. 86(1): pp. 285–290. doi: 10.1139/p07-100 (cit. on p. 35).

176. Stanyukovich, K. P.: 'Possible changes in the gravitational constant'. *Soviet Physics Doklay* (1963), vol. 7(12): pp. 1150–1152 (cit. on p. 4).

177. Staude, U., Ph. Bosselmann, R. Büttner, D. Horn, K.-H. Schartner, F. Folkmann, A. E. Livingston, T. Ludziejewski, and P. H. Mokler: 'Measurements of $2s\,^2S_{1/2} - 2p\,^2P_{3/2,1/2}$ transition energies in lithiumlike heavy ions: Experiments and results for Ni^{25+} and Zn^{27+}'. *Physical Review A* (1998), vol. 58(5): pp. 3516–3523. doi: 10.1103/physreva.58.3516 (cit. on p. 2).

178. Strüder, Lothar et al.: 'Large-format, high-speed, X-ray pnCCDs combined with electron and ion imaging spectrometers in a multipurpose chamber for experiments at 4th generation light sources'. *Nuclear Instruments and Methods in Physics Research Section A: Accelerators, Spectrometers, Detectors and Associated Equipment* (2010), vol. 614(3): pp. 483–496. doi: 10.1016/j.nima.2009.12.053 (cit. on p. 59).

179. Sugiyama, Jun: 'Spin polarized beam for battery materials research: $\mu^{\pm}$SR and β-NMR'. *Hyperfine Interactions* (2019), vol. 240(1): p. 17. doi: 10.1007/s10751-019-1560-4 (cit. on p. 32).

180. Tavernier, M., J. P. Briand, P. Indelicato, D. Liesen, and P. Richard: 'Measurement of the 1s Lamb shift of hydrogen-like krypton'. *Journal of Physics B: Atomic and Molecular Physics* (1985), vol. 18(11): pp. L327–L330. doi: 10.1088/0022-3700/18/11/004 (cit. on p. 1).

181. Teller, Edward: 'On the Change of Physical Constants'. *Physical Review* (1948), vol. 73(7): pp. 801–802. doi: 10.1103/physrev.73.801 (cit. on p. 4).

182. Thomson, J. J.: 'XLII. Ionization by moving electrified particles'. *The London, Edinburgh, and Dublin Philosophical Magazine and Journal of Science* (1912), vol. 23(136): pp. 449–457. doi: 10.1080/14786440408637241 (cit. on p. 26).

183. Tilford, S. G.: 'Rydberg Series in N V'. *Journal of the Optical Society of America* (1963), vol. 53(9): p. 1051. doi: 10.1364/josa.53.001051 (cit. on p. 92).

184. Tupitsyn, I. I., A. V. Volotka, D. A. Glazov, V. M. Shabaev, G. Plunien, J. R. Crespo López-Urrutia, A. Lapierre, and J. Ullrich: 'Magnetic-dipole transition probabilities in B-like and Be-like ions'. *Physical Review A* (2005), vol. 72(6): p. 062503. doi: 10.1103/physreva.72.062503 (cit. on p. 19).

185. Uzan, Jean-Philippe: 'The fundamental constants and their variation: observational and theoretical status'. *Reviews of Modern Physics* (2003), vol. 75(2): pp. 403–455. doi: 10.1103/revmodphys.75.403 (cit. on p. 4).

186. Vondrasek, Richard: 'On-line charge breeding using ECRIS and EBIS'. *Nuclear Instruments and Methods in Physics Research Section B: Beam Interactions with Materials and Atoms* (2016), vol. 376: pp. 16–23. doi: 10.1016/j.nimb.2015.11.043 (cit. on p. 33).

187. Wang, L. M., and Z.-C. Yan: 'Transition frequencies between the 2S and 2P states of the lithiumlike ion O^{5+}'. *Physical Review A* (2019), vol. 100(3): p. 032505. doi: 10.1103/physreva.100.032505 (cit. on pp. 93, 101).

188. Warnecke, Christian: 'Bachelor Thesis'. Master's thesis. Universität Heidelberg, 2017 (cit. on pp. 46, 47).

189. Webb, J. K., J. A. King, M. T. Murphy, V. V. Flambaum, R. F. Carswell, and M. B. Bainbridge: 'Indications of a Spatial Variation of the Fine Structure Constant'. *Physical Review Letters* (2011), vol. 107(19): p. 191101. doi: 10.1103/physrevlett.107.191101 (cit. on p. 4).

190. Webb, John K., Victor V. Flambaum, Christopher W. Churchill, Michael J. Drinkwater, and John D. Barrow: 'Search for Time Variation of the Fine Structure Constant'. *Physical Review Letters* (1999), vol. 82(5): pp. 884–887. doi: 10.1103/physrevlett.82.884 (cit. on pp. 4, 128, 130).

191. Wenander, Fredrik: 'Charge breeding of radioactive ions with EBIS and EBIT'. *Journal of Instrumentation* (2010), vol. 5(10): p. C10004. doi: 10.1088/1748-0221/5/10/c10004 (cit. on p. 33).

192. Widing, K. G., and J. D. Purcell: 'The lithium-like 2s 2S-2p 2P transition in solar flares'. *The Astrophysical Journal* (Mar. 1976), vol. 204: p. L151. doi: 10.1086/182076 (cit. on pp. 97, 98, 127).

193. Widmann, K., P. Beiersdorfer, V. Decaux, and M. Bitter: 'Measurements of the K*alpha* transition energies of heliumlike krypton'. *Physical Review A* (1996), vol. 53(4): pp. 2200–2205. doi: 10.1103/physreva.53.2200 (cit. on p. 2).

194. Widmann, K., P. Beiersdorfer, V. Decaux, S. R. Elliott, D. Knapp, A. Osterheld, M. Bitter, and A. Smith: 'Studies of He-like krypton for use in determining electron and ion temperatures in very-high-temperature plasmas'. *Review of Scientific Instruments* (1995), vol. 66(1): pp. 761–763. doi: 10.1063/1.1146281 (cit. on p. 2).

195. Wilczynska, Michael R., John K. Webb, Matthew Bainbridge, John D. Barrow, Sarah E. I. Bosman, Robert F. Carswell, Mariusz P. Dąbrowski, Vincent Dumont, Chung-Chi Lee, Ana Catarina Leite, Katarzyna Leszczyńska, Jochen Liske, Konrad Marosek, Carlos J. A. P. Martins, Dinko Milaković, Paolo Molaro, and Luca Pasquini: 'Four direct measurements of the fine-structure constant 13 billion years ago'. *Science Advances* (2020), vol. 6(17): eaay9672. doi: 10.1126/sciadv.aay9672 (cit. on pp. 4, 128).

196. Wilczynska, Michael R., John K. Webb, Julian A. King, Michael T. Murphy, Matthew B. Bainbridge, and Victor V. Flambaum: 'A new analysis of fine-structure constant measurements and modelling errors from quasar absorption lines'. *Monthly Notices of the Royal Astronomical Society* (2015), vol. 454(3): pp. 3082–3093. doi: 10.1093/mnras/stv2148 (cit. on p. 4).

197. Windberger, A., J. R. Crespo López-Urrutia, H. Bekker, N. S. Oreshkina, J. C. Berengut, V. Bock, A. Borschevsky, V. A. Dzuba, E. Eliav, Z. Harman, U. Kaldor, S. Kaul, U. I. Safronova, V. V. Flambaum, C. H. Keitel, P. O. Schmidt, J. Ullrich, and O. O. Versolato: 'Identification of the Predicted $5s$–$4f$ Level Crossing Optical Lines with Applications to Metrology and Searches for the Variation of Fundamental Constants'. *Physical Review Letters* (2015), vol. 114(15): p. 150801. doi: 10.1103/physrevlett.114.150801 (cit. on pp. 103, 104, 106, 120, 121, 129).

198. Windberger, Alexander: 'Identification of optical transitions incomplex highly charged ions forapplications in metrology and tests offundamental constants'. Doctoral dissertation. Universtät Heidelberg, 2015. doi: 10.11588/heidok.00018868 (cit. on pp. 104, 120, 129).

199. Yerokhin, V. A., A. N. Artemyev, and V. M. Shabaev: 'QED treatment of electron correlation in Li-like ions'. *Physical Review A* (2007), vol. 75(6): p. 062501. doi: 10.1103/physreva.75.062501 (cit. on p. 3).

200. Yerokhin, V. A., A. N. Artemyev, V. M. Shabaev, M. M. Sysak, O. M. Zherebtsov, and G. Soff: 'Two-Photon Exchange Corrections to the $2p_{1/2}$–$2s$ Transition Energy in Li-Like High-Z Ions'. *Physical Review Letters* (2000), vol. 85(22): pp. 4699–4702. doi: 10.1103/physrevlett.85.4699 (cit. on p. 3).

201. Yerokhin, V. A., P. Indelicato, and V. M. Shabaev: 'Nonperturbative Calculation of the Two-Loop Lamb Shift in Li-Like Ions'. *Physical Review Letters* (2006), vol. 97(25): p. 253004. doi: 10.1103/physrevlett.97.253004 (cit. on pp. 3, 20).

202. Yerokhin, V. A., and A. Surzhykov: 'Relativistic configuration-interaction calculation of energy levels of core-excited states in lithiumlike ions: Argon through krypton'. *Physical Review A* (2012), vol. 86(4): p. 042507. doi: 10.1103/physreva.86.042507 (cit. on pp. 3, 97–100).

203. Yerokhin, V. A., A. Surzhykov, and A. Müller: 'Relativistic configuration-interaction calculations of the energy levels of the $1s^22l$ and $1s2l2l'$ states in lithiumlike ions: Carbon through chlorine'. *Physical Review A* (2017), vol. 96(4): p. 042505. doi: 10.1103/physreva.96.042505 (cit. on pp. 3, 89–93, 95–97, 99, 100).

204. Yudin, V. I., A. V. Taichenachev, and A. Derevianko: 'Magnetic-Dipole Transitions in Highly Charged Ions as a Basis of Ultraprecise Optical Clocks'. *Physical Review Letters* (2014), vol. 113(23): p. 233003. doi: 10.1103/physrevlett.113.233003 (cit. on pp. 5, 120).

205. Zeeman, Pieter: 'Over den invloed eener magnetisatie op den aard van het door een stof uitgezonden licht.' (1896), vol. 5: 181–184 and 242–248. url: https://www.biodiversitylibrary.org/item/205530#page/217 (cit. on p. 25).

206. Zhang, Xuemei, Nobuyuki Nakamura, Chongyang Chen, Martin Andersson, Yong Liu, and Shunsuke Ohtani: 'Measurement of the QED energy shift in the $1s^22p_{3/2} - 1s^22s_{1/2}$ x-ray transition in Li-like $^{208}Pb^{79+}$'. *Physical Review A* (2008), vol. 78(3): p. 032504. doi: 10.1103/physreva.78.032504 (cit. on p. 2).

List of Figures

1.1 QED corrections to $1s^2 2p\ ^2P_{1/2} \to 1s^2 2s\ ^2S_{1/2}$ for different values of Z . . . 3
1.2 A few level crossings in the neodymium-like isoelectronic sequence 6

2.1 QED corrections to $1s^2 2p\ ^2P_{3/2} \to 1s^2 2s\ ^2S_{1/2}$ for different values of Z . . . 20
2.2 Electron structure contributions to $1s^2 2p\ ^2P_{1/2} \to 1s^2 2s\ ^2S_{1/2}$ for different values of Z . . . 21
2.3 Electron structure contributions to $1s^2 2p\ ^2P_{3/2} \to 1s^2 2s\ ^2S_{1/2}$ for different values of Z . . . 22
2.4 One-loop QED contributions to $1s^2 2p\ ^2P_{1/2} \to 1s^2 2s\ ^2S_{1/2}$ for different values of Z . . . 23
2.5 QED screening potential for different values of Z . . . 24
2.6 Nuclear recoil effect for different values of Z . . . 24
2.7 Schematic diagram of Radiative recombination . . . 28
2.8 Schematic diagram of Dielectronic recombination . . . 29

3.1 Panorama of the CANREB hall . . . 32
3.2 Schematic of an EBIS . . . 34
3.3 Time evolution of caesium ions during charge breeding . . . 35
3.4 Magnetic field of the CANREB magnet system . . . 37
3.5 Sectional view of the CANREB EBIS electron gun . . . 38
3.6 Herrmann radius and mean current density against residual magnetic field . 40
3.7 Sectional view of the CANREB EBIS trap centre . . . 41
3.8 Sectional view of the CANREB EBIS collector . . . 43
3.9 Three-dimensional model of the ion optics . . . 43
3.10 Schematic diagram of a PIN photodiode . . . 45
3.11 Schematic diagram of a Faraday cup and pickup ring . . . 45
3.12 Perveance of the electron gun . . . 46
3.13 X-ray spectra of radiative recombination in barium and tungsten ions . . . 48
3.14 KLL dr of argon . . . 49
3.15 Temporal evolution of an argon dr spectrum over time . . . 50
3.16 Temporal evolution of argon DR spectra over time for different injection pressures . . . 52
3.17 Temporal evolution of dielectronic recombination in iron injected from the laser ion source . . . 53
3.18 Extraction currents of argon ions for different injection pressures . . . 54
3.19 Extraction of ar ions for different beam energies . . . 55
3.20 Extraction of ar ions for different trap depths . . . 56

4.1 Side view of the EUV and VUV spectrometer attached to FLASH-EBIT . . 57
4.2 Bird's-eye view of FLASH-EBIT, EUV and VUV spectrometer 58
4.3 Schematic diagram of Rowland geometry 60
4.4 Detailed photograph of the linear stage for the MCP detector 61
4.5 Detailed photograph of the grating chamber 62
4.6 Rendered image of the grating mount 62
4.7 Schematic diagram of a micro-channel plate 63
4.8 Schematic diagram of a delay line anode 64
4.9 Scheme of the VUV control and data acquisition system 65
4.10 Reflectance of the grating in normal incidence 66
4.11 Estimated diffraction efficiencies 67
4.12 Quantum efficiency of an uncoated MCP photocathode such as the one used in this work 68
4.13 Estimated combined efficiencies for the VUV spectrometer 68
4.14 'start/stop sequence' used for the synchronisation of the VUV spectrometer 69
4.15 Pre-processing scheme for the VUV spectrometer in static mode 73
4.16 Pre-processing scheme for the VUV spectrometer in scanning mode 74
4.17 Section of the flat-field EUV spectrometer 76
4.18 Schematic diagram of a CCD sensor 77
4.19 Pre-processing of EUV spectra 79

5.1 Level scheme for lithium 81
5.2 VUV spectrum of nitrogen 85
5.3 VUV spectrum of oxygen 86
5.4 VUV spectrum of neon 87
5.5 VUV spectrum of argon 88
5.6 Fine-structure wavelengths of nitrogen 89
5.7 Comparison of the results for nitrogen with data found in literature 90
5.8 Fine-structure wavelengths of oxygen 92
5.9 Comparison of the results for oxygen with data found in literature 93
5.10 Fine-structure wavelengths of neon 95
5.11 Comparison of the results for neon with data found in literature 96
5.12 Fine-structure wavelengths of argon 97
5.13 Comparison of the results for argon with data found in literature 98

6.1 Grotrian diagram of Ir^{17+} 103
6.2 Extended Grotrian diagram of neodymium-like iridium 105
6.3 Transition rates as calculated using collisional-radiative modelling 107
6.4 Charge-state verification for iridium 109
6.5 Combined VUV spectrum of iridium and oxygen 111
6.6 Full-range scan of neodymium-like iridium 113
6.7 Detailed energy scan of iridium around 83.78 nm 117
6.8 Peak intensities of the lines found in Figure 6.7 plotted against beam energy 117
6.9 Direct comparison of the EUV and VUV spectrometer 118

6.10 Electron beam energy scan in the EUV range with iron injection 119
6.11 Synthetic spectrum of Ir^{16+}, Ir^{17+}, Ir^{18+}, and Ir^{19+} in the range of 43 nm to 73 nm 124
6.12 Synthetic spectrum of Ir^{16+}, Ir^{17+}, Ir^{18+}, and Ir^{19+} in the range of 73 nm to 103 nm 125
6.13 Synthetic spectrum of Ir^{16+}, Ir^{17+}, Ir^{18+}, and Ir^{19+} in the range of 103 nm to 133 nm 126

A.1 Non-linearity correction of the MCP data 158
A.2 Ballooning baseline example 161

B.1 Comparison of oxygen lines present as impurity in other spectra 166
B.2 Comparison of VUV spectra for different species in the range from 40 nm to 80 nm 167
B.3 Comparison of VUV spectra for different species in the range from 80 nm to 120 nm 168
B.4 Comparison of VUV spectra for different species in the range from 120 nm to 220 nm 169
B.5 Detailed energy scan of iridium around 31.74 nm 177
B.6 Peak intensities of the lines found in Figure B.5 plotted against beam energy 177
B.7 Detailed energy scan of iridium around 47.39 nm 178
B.8 Peak intensities of the lines found in Figure B.7 plotted against beam energy 178
B.9 Detailed energy scan of iridium around 55.03 nm 179
B.10 Peak intensities of the lines found in Figure B.9 plotted against beam energy 179
B.11 Detailed energy scan of iridium around 58.55 nm 180
B.12 Peak intensities of the lines found in Figure B.11 plotted against beam energy 180
B.13 Detailed energy scan of iridium around 63.43 nm 181
B.14 Peak intensities of the lines found in Figure B.13 plotted against beam energy 181
B.15 Detailed energy scan of iridium around 68.94 nm 182
B.16 Peak intensities of the lines found in Figure B.15 plotted against beam energy 182
B.17 Detailed energy scan of iridium around 69.01 nm 183
B.18 Peak intensities of the lines found in Figure B.17 plotted against beam energy 183
B.19 Detailed energy scan of iridium around 70.29 nm 184
B.20 Peak intensities of the lines found in Figure B.19 plotted against beam energy 184
B.21 Detailed energy scan of iridium around 73.21 nm 185
B.22 Peak intensities of the lines found in Figure B.21 plotted against beam energy 185
B.23 Detailed energy scan of iridium around 75.59 nm 186
B.24 Peak intensities of the lines found in Figure B.23 plotted against beam energy 186
B.25 Detailed energy scan of iridium around 78.23 nm 187
B.26 Peak intensities of the lines found in Figure B.25 plotted against beam energy 187
B.27 Detailed energy scan of iridium around 78.63 nm 188
B.28 Peak intensities of the lines found in Figure B.27 plotted against beam energy 188
B.29 Detailed energy scan of iridium around 80.62 nm 189
B.30 Peak intensities of the lines found in Figure B.29 plotted against beam energy 189
B.31 Detailed energy scan of iridium around 84.23 nm 190
B.32 Peak intensities of the lines found in Figure B.31 plotted against beam energy 190
B.33 Detailed energy scan of iridium around 87.73 nm 191
B.34 Peak intensities of the lines found in Figure B.33 plotted against beam energy 191
B.35 Detailed energy scan of iridium around 91.12 nm 192
B.36 Peak intensities of the lines found in Figure B.35 plotted against beam energy 192

B.37 Detailed energy scan of iridium around 91.52 nm 193
B.38 Peak intensities of the lines found in Figure B.37 plotted against beam energy 193
B.39 Detailed energy scan of iridium around 96.12 nm 194
B.40 Peak intensities of the lines found in Figure B.39 plotted against beam energy 194
B.41 Detailed energy scan of iridium around 100.91 nm 195
B.42 Peak intensities of the lines found in Figure B.41 plotted against beam energy 195
B.43 Detailed energy scan of iridium around 104.43 nm 196
B.44 Peak intensities of the lines found in Figure B.43 plotted against beam energy 196
B.45 Detailed energy scan of iridium around 107.90 nm 197
B.46 Peak intensities of the lines found in Figure B.45 plotted against beam energy 197
B.47 Detailed energy scan of iridium around 111.97 nm 198
B.48 Peak intensities of the lines found in Figure B.47 plotted against beam energy 198
B.49 Detailed energy scan of iridium around 118.22 nm 199
B.50 Peak intensities of the lines found in Figure B.49 plotted against beam energy 199
B.51 Detailed energy scan of iridium around 125.98 nm 200
B.52 Peak intensities of the lines found in Figure B.51 plotted against beam energy 200

List of Tables

2.1 Code letters used for the principal and orbital quantum number values. Some of the letters for l were originally abbreviations for names of spectral line series but later more values were added alphabetically. The last column denotes the number of electrons that can be in a given subshell (double the degeneracy of l). 11

3.1 Specification of the magnet system 37
3.2 Comparison of all materials used in the trap setup with respect to their thermal and electrical properties. MACOR is preferred over PTFE where rigidity is required. 40

5.1 Optimal EBIT parameters for fine-structure measurements 83
5.2 Comparison of nitrogen results with values available from literature 90
5.3 Comparison of oxygen results with values available from literature 93
5.4 Comparison of neon results with values available from literature 96
5.5 Comparison of argon results with values available from literature 98
5.6 Fine structure doublets of neon and argon 99
5.7 Accuracy of the results reported in this work compared to calculated contributions to the transition energies for $^2P_{3/2} \rightarrow {}^2S_{1/2}$ 100
5.8 Accuracy of the results reported in this work compared to calculated contributions to the transition energies for $^2P_{1/2} \rightarrow {}^2S_{1/2}$ 100

6.1 Comparison of different calculation results of the lowest levels in Ir^{17+} . . . 106
6.2 Optimal parameters determined for Ir^{17+} spectroscopy at FLASH-EBIT . . 110
6.3 New spectral lines found for neodymium-like iridium in the VUV range . . 114
6.4 New spectral lines found for neodymium-like iridium in the EUV range . . . 118
6.5 Previously identified lines in Ir^{17+} 121
6.6 Rydberg-Ritz combinations within the newly found lines 122

7.1 Transition energies of the fine-structure doublets obtained in this work . . . 128

B.1 Calibration lines used in the VUV range 163
B.2 Coefficients of the cubic calibration function $f(x)$ 170
B.3 Coefficients of the alternative calibration polynomial $f'(x)$ 170
B.4 Calibration lines used in the EUV range 171
B.5 Complete list of spectral lines attributed to Ir^{17+} 172

A Methods in data analysis

Some aspects of the data analysis described in Chapters 4, 5 and 6 are presented here.

A.1 Linearisation of the MCP data

In order to generate a lookup table for non-linearities of the MCP delay-line anode, the analogue amplifiers and ADCs used for data acquisition, a zero-order reference dataset was taken for several hours. Before starting the measurement, the zero-order line was placed on one side of the MCP. In regular time intervals the grating was rotated by 0.02° until the line had moved across the entire detector. This data set as well as the rest of the process is presented in Figure A.1.

After discarding all events outside the Region of interest, the events were rotated and binned into a two-dimensional histogram based on their coordinates. The area of the MCP was sliced into stripes of equal width that were projected. In each projection, individual Gaussian fits were performed to determine the line positions.

It was assumed that all the lines are parallel and equidistant. The averaged line position of the central line was used as a reference point. A two-dimensional lattice of points was defined with respect to this reference point such that the Y spacing is the width of the slices and the X spacing corresponds to the global average distance of two adjacent lines along the dispersive axis. For each point of this 'ideal lattice', the deviation was calculated where a fit result was available. Lastly, this table of distortions for certain positions was interpolated to create a full resolution lookup table.

The interpolation was performed by triangulating the lattice points using the Delaunay algorithm [55]. For each combination of X and Y coordinates within the range of the ADCs, a deviation is calculated. Inside the triangles the coordinates of the point P_X for which the interpolated value is calculated, are transformed into a coordinate system using an arbitrary point of the triangle P_0 as origin and two adjacent edges as basis. The length of these two edges is chosen to be one without loss of generality. These new coordinates c_1 and c_2 are used in conjunction with the distortion value at the origin v_0 and at the two other points of the triangle (v_1 and v_2) by plugging them into the following formula: $v_X = v_0 + (1 - c_1) \times (v_1 - v_0) + (1 - c_2) \times (v_2 - v_0)$. For points located outside any of the triangles, the closest point on the convex hull of the triangulated region is determined. By definition this is always an edge of a triangle so that 1D linear interpolation can be used to calculate the distortion value on the closest point of this facet.

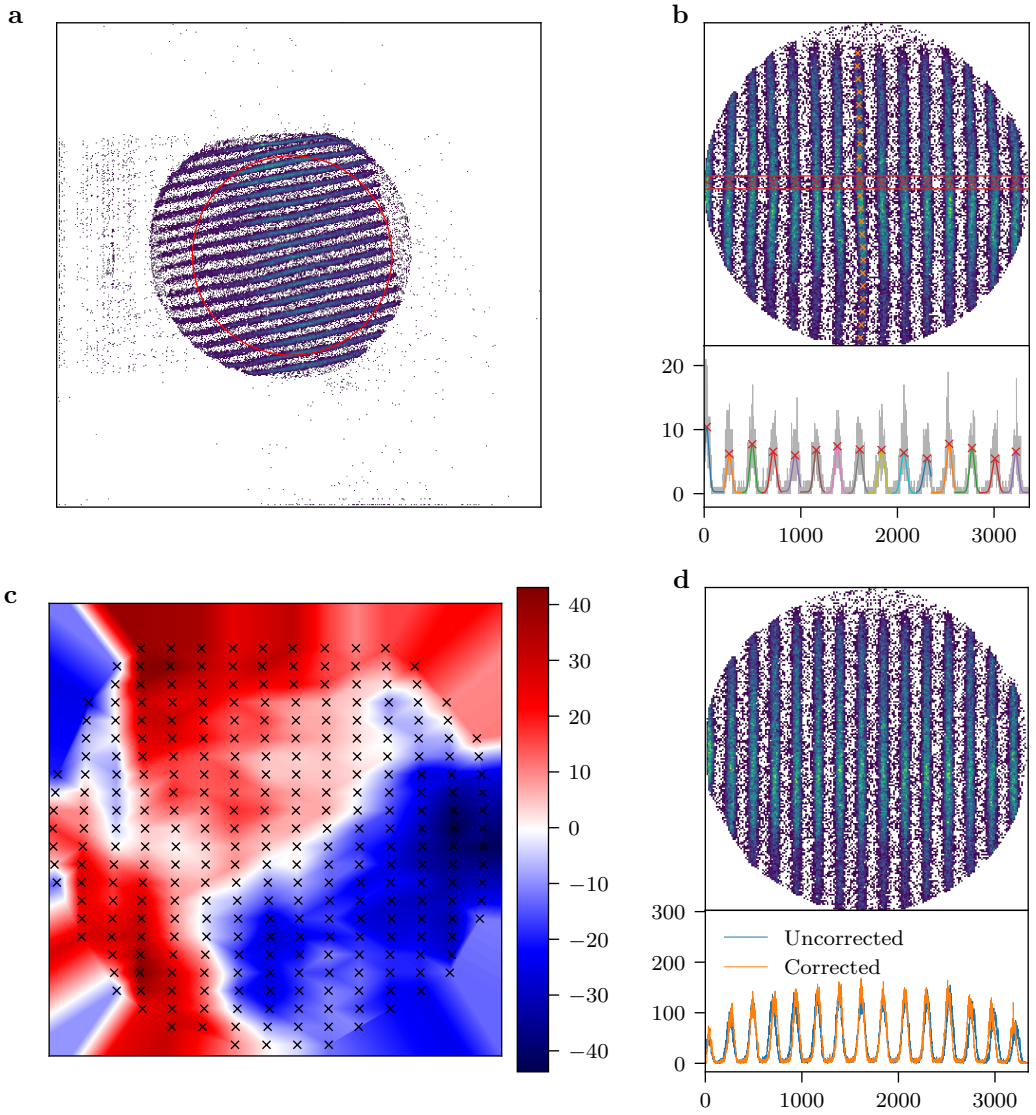

Figure A.1: Non-linearity correction of the MCP data. Two-dimensional data was binned by a factor of 16 for better visibility of the sparse data. The raw data used for the correction is shown in **a**. The red circle indicates the ROI used for this analysis. After discarding all data outside and rotation, the data is displayed in the upper part of Subfigure **b**. 23 narrow slices of the 2D histogram are projected and each line fitted individually in every slice using a Gaussian. For the slice highlighted in red, the projection as well as all the individual curves fitted to the lines are displayed in the lower part of the Subfigure. Maxima positions determined by these fits are displayed as red crosses in both the upper and lower part of the diagram. This process is repeated for all stripes of the same width along the Y axis. For a line close to the centre all these fit results are shown as orange crosses. It can clearly be seen that their position deviates from a straight line. Assuming all the lines should be equidistant and straight, a correction along the X axis for each of these points is calculated. Interpolation is performed as described in the text. In Subfigure **c** the result of the interpolation is presented which is then exported as a lookup table. Black crosses indicate where a maximum position was available. Please note the overall non-linearity is 1.0 % and therefore just slightly larger than one specified for the delay-line anode (0.75 % according to the manufacturer, see Section 4.1.3). Shifting each event according to the interpolated shift, Subfigure **d** is obtained. The individual lines are now straight and equidistant. Below, projections of the complete ROI are shown before and after linearisation of the data.

A.2 Ballooning baseline algorithm

Before using a peak finder on the spectrum or when compiling a two-dimensional spectrogram such as the one in Figure 6.4, a baseline subtraction was performed. Please refer to Figure 4.16 **c** for a representative example. Various popular methods were considered:

- Using a minimum, median or mean value as constant baseline cannot be applied, when it varies over the parameter range. Compare the baseline at 6000 mdeg with peak intensities around 3750 mdeg.
- Smoothing using convolution with various kernels was found to be inadequate. In spectra where the dynamic range is large (peaks close to each other with intensities different by three orders of magnitude) the peak finder will ignore the smaller peak. Other smoothing algorithms such as using a Savitzky-Golay filter suffer from the same problems. Please note the logarithmic scale in the example.
- Using deconvolution algorithms (such as Wiener deconvolution) in Fourier space was the most promising approach to remove the baseline because it can be fine-tuned to typical line shapes. However, deconvolution requires detailed modelling of noise. It was observed that the baseline is generally higher in segments of the spectra with many intense lines. So it is assumed, the main causes are so-called 'ghosts' caused by imperfections in the ruling process and diffuse scattering in the apparatus. The former were included in the deconvolution. Modelling reflections proved to be challenging, so the approach was abandoned due to artefacts causing false identifications for the peak finding.

A suitable baseline algorithm should approximate all broad features within the spectrum, but it should ignore narrow, high features, even if their local density is high. Please refer to Figure 4.16 **a** and **b** for an example: when the grating is rotated, spectral lines move across the detector, but this is not true for diffuse reflections such as the one caused by the zero order. After moving off the MCP detector, diffuse reflections cause a uniform increase in count rate across the entire detector (that is why the feature is not slanted in **a**). So after projecting the spectrum, a broad feature around 2100 mdeg remains. It is assumed that other intense lines cause similar features, causing the baseline to rise in parts of the spectrum with many intense lines.

PD Dr. José R. Crespo López-Urrutia proposed to model the baseline as a two-dimensional balloon with a certain pressure and elasticity that is initially located below the graph and as it extends up due to the internal pressure, the graph restricts further expansion. This will allow for the baseline to follow broad features, but expanding into a narrow peak is very costly due to the surface tension.

First, data is smoothed using a sliding average and downsampled to a few hundred values. This reduces computational effort. An initial baseline is generated as a flat line below the data. Each point of the baseline is then only allowed to move vertically but not horizontally by numerically solving a set of ordinary differential equations. A set of coordinates, velocities and accelerations is iteratively calculated until the system converges. At each time step, the area under the baseline is calculated and the initial 'pressure' is reduced by the ratio of the initial area to the current area under the curve. Then the

accelerating forces for each point are calculated by the distance and direction of the adjacent neighbours using Hooke's law and assuming a force proportional to the current pressure along the normal vectors of the adjacent facets. After the force vector was calculated, it is projected onto the vertical axis. As mentioned above, movement of these baseline points is also restricted by the data. Finally, the coordinates obtained are smoothed again by a moving average and linearly interpolated to match the X coordinates of the original dataset.

An example for such a baseline is shown in Figure A.2. It satisfies the objectives stated above quite nicely. A few disadvantages when comparing it this method to others are that it has quite a lot of parameters that need to be tuned for the specific problem: the smoothing window sizes for the initial (data) and final (baseline) smoothing, a value for the 'internal pressure', the 'surface tension' and the number of points used for modelling the balloon. Especially pressure and surface tension are correlated and can result in oscillations if chosen poorly. These can cause the solution to take many iteration steps until convergence or never converge at all. In future versions of the algorithm this could be mitigated by replacing them with a single parameter or by introducing some kind of friction to dissipate energy from the system and therefore dampen the oscillation. The datasets in this work are similar to each other, so it was sufficient to tune the parameters well, since it was only done once.

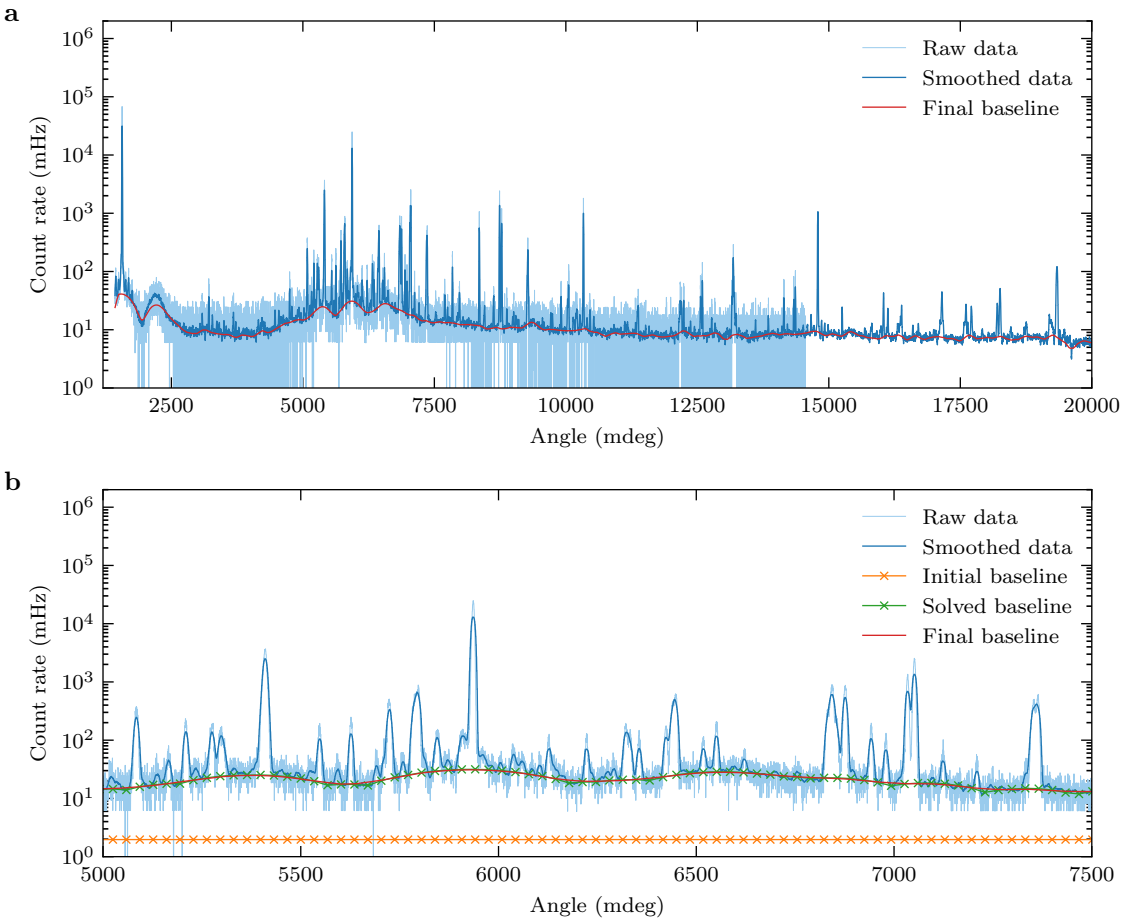

Figure A.2: Ballooning baseline example. (**a**) A spectrum of oxygen is shown including the final baseline across the whole spectral range. For better visibility, a smaller range is also provided (**b**). Individual points used by the algorithm are displayed in that graph. 'Final baseline' refers to the result of applying the final sliding average and linear interpolation. It is the same dataset as in Figures 4.16 and 5.3.

B Supplementary material

B.1 Fine-structure measurements

B.1.1 Calibration lines

The list of calibration lines used for the fine-structure measurements presented in Chapter 5 is given here. The data is from the NIST atomic spectra database [122].

Table B.1: Calibration lines used in the VUV range [122].

Species	Spectral orders	NIST wavelength (nm)
Ar XV	1st	22.115(3)
Ar XIV	1st	24.379(3)
N IV	1st	24.720(5)
N IV	1st	30.032(10)
N III	1st	37.4204(5)
Ar XV	1st	42.398(3)
Ar IX	1st	43.65(2)
N III	1st, 2nd	45.1869(5)
Ar IV	1st	45.1877(2)
N III	1st	45.2226(5)
O II	1st	45.8422(5)
Ne VII	1st, 2nd, 3rd, 4th	46.5221(10)
Ar VII	1st	47.5730(10)
Ar VII	1st	47.9379(10)
O III	1st	50.7683(5)
O II	1st	51.7937(5)
Ar II	1st	51.9329(3)
O III	1st	52.5795(5)
Ar VII	1st	52.6870(7)
N II	1st	53.3511(5)
O II	1st	53.8318(10)
Ar VI	1st	54.4730(10)
Ar VI	1st	54.8910(10)
Ar VI	1st, 2nd, 3rd	55.135(2)
O IV	1st, 3rd	55.3703(5)
O IV	1st	55.4075(5)
Ar VI	1st	55.5630(10)
Ar V	1st	55.8477(2)
Ne VI	1st	55.8600(5)
Ne V	1st	56.9830(5)

Table B.1 continued

Species	Spectral orders	NIST wavelength (nm)
Ne V	1st	57.2337(5)
Ar II	1st	58.0264(3)
Ar VII	1st, 2nd, 3rd, 4th	58.5748(4)
Ar VI	1st	58.891(2)
O III	1st, 2nd, 3rd	59.9598(5)
O IV	1st	60.9829(5)
O IV	1st	61.6992(5)
O V	1st, 2nd, 3rd, 4th	62.9730(5)
Ar XII	1st	64.9093(20)
N II	1st, 2nd, 3rd	64.4837(5)
N II	1st	66.0286(5)
Ar XII	1st	67.0302(10)
N II	1st	67.1386(5)
N III	1st, 2nd, 3rd	68.5513(5)
O I	1st	68.5544(5)
N III	1st	68.6335(5)
Ar VII	1st, 2nd, 3rd	70.0240(10)
O III	1st	70.3850(5)
Ar VIII	1st, 2nd	71.3802(7)
N V	1st	71.3860(5)
O II	1st	71.8534(5)
Ne I	1st	73.589 62(40)
N V	1st	74.8195(5)
N V	1st, 2nd	74.8291(5)
Ar II	1st	75.4824(3)
O V	2nd, 3rd	76.0228(5)
O V	1st	76.0445(5)
N IV	1st, 2nd, 3rd	76.5148(5)
N III	1st	77.2385(5)
O V	1st	77.4518(5)
N II	1st	77.5965(5)
O IV	1st	77.9821(5)
O IV	1st, 2nd, 3rd	78.7711(5)
O IV	1st, 2nd	79.0161(5)
Ar V	1st	82.7048(2)
O III	1st	83.5292(5)
Ar IV	1st	85.0607(2)
Ar VII	1st	87.792(3)
Ne VII	1st	89.512(5)
N IV	1st, 2nd	92.3057(5)

Table B.1 continued

Species	Spectral orders	NIST wavelength (nm)
O IV	1st	92.3367(5)
N IV	1st	92.4283(5)
N IV	1st	95.5335(5)
O I	1st	97.6448(5)
N III	1st	97.9842(5)
N III	1st	98.9799(5)
N III	1st	99.1514(5)
N II	1st	108.4580(5)
O II	1st	108.5056(5)
N II	1st	108.5701(5)

B.1.2 Systematic studies on the oxygen deviation

Additional analysis is provided here in order to narrow down the systematic deviation found in Chapter 5 for the fine-structure doublet in lithium-like oxygen compared to other laboratory measurements found in literature.

Comparison across different species

Three spectra have been recorded using oxygen gas injection. In the other fine-structure spectra recorded in this work, oxygen was present as an impurity. In particular the spectral line of O V around 62.9730(5) nm as well as both fine-structure lines in O VI could be identified in all of the spectra (see Figures B.2, B.3, and B.4). Due to low signal-to-noise ratio in measurements 'N 1', 'N 2', neon, and argon, these were not included in the results presented in Figure 5.8.

All spectra have been calibrated individually using spectral lines of the injected element (nitrogen, oxygen, neon and argon respectively). Consequently, the fine-structure lines were fitted using a Gaussian. A comparison of the O V calibration line and both fine-structure transitions across all the individual measurements can be found in Figure B.1.

When comparing the deviation of the calibration line at 62.9730(5) nm across the different measurements to the deviation of the fine-structure transitions, there is no obvious correlation between, that can be identified. However, the variance appears to be largest for nitrogen and oxygen, smaller for argon and smallest for neon. This could be related to the calibration lines used for the different species, or due to the trap depth. In Table 5.1 it can be seen that the axial trap depth was smallest for oxygen and nitrogen (20 V), larger for argon (60 V) and largest for neon (160 V). Furthermore, the radial trap depth is proportional to the electron beam current density which should be considerably higher for the measurements using neon and argon injection.

However, when calculating weighed average values for the oxygen fine-structure lines in the measurements for neon and argon, where the residuum of the oxygen calibration line is the lowest, the values are 103.1852(26) nm and 103.7487(39) nm which is still more than 2.8σ lower than the values reported by Kaufman and Martin [113] (103.192 60(50) nm and 103.762 00(50) nm).

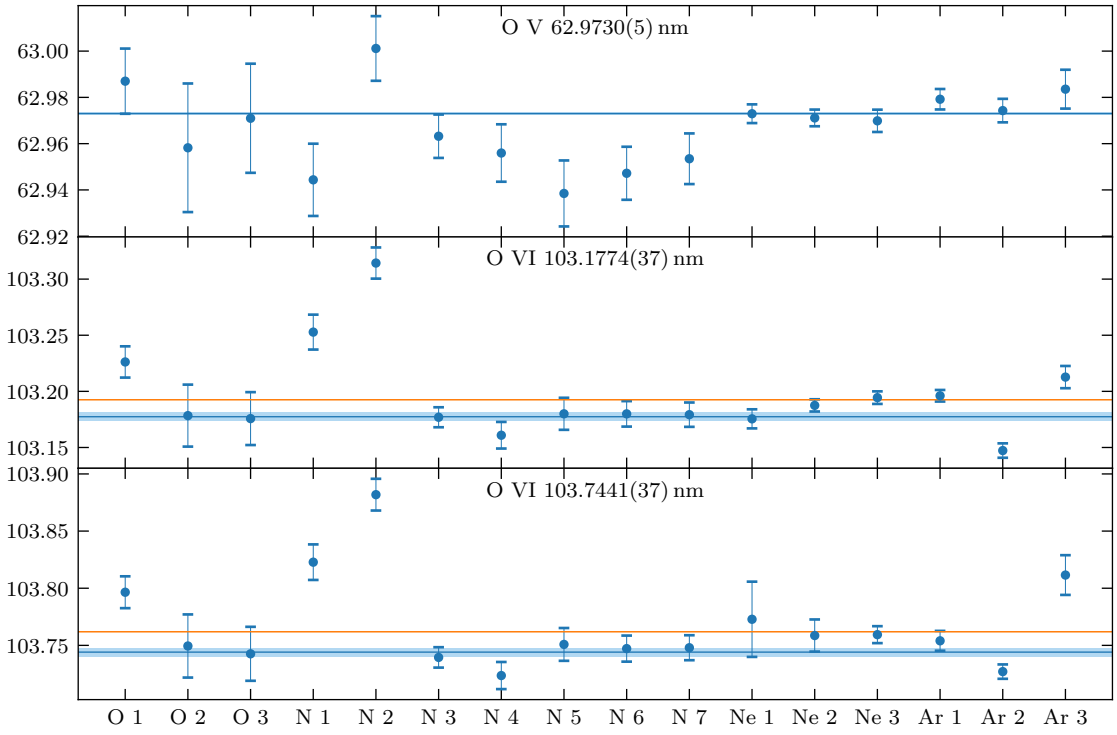

Figure B.1: Comparison of oxygen lines present as impurity in other spectra. The vertical blue line and confidence interval given as reference is the value given by the NIST database for the oxygen line around 62.9730(5) nm. Otherwise the weighed average results given in Chapter 5 were used. Higher spectral orders are not available for all measurements, so only first spectral orders are given. The orange line and shaded area represents the most accurate and recent experimental value by Kaufman and Martin [113].

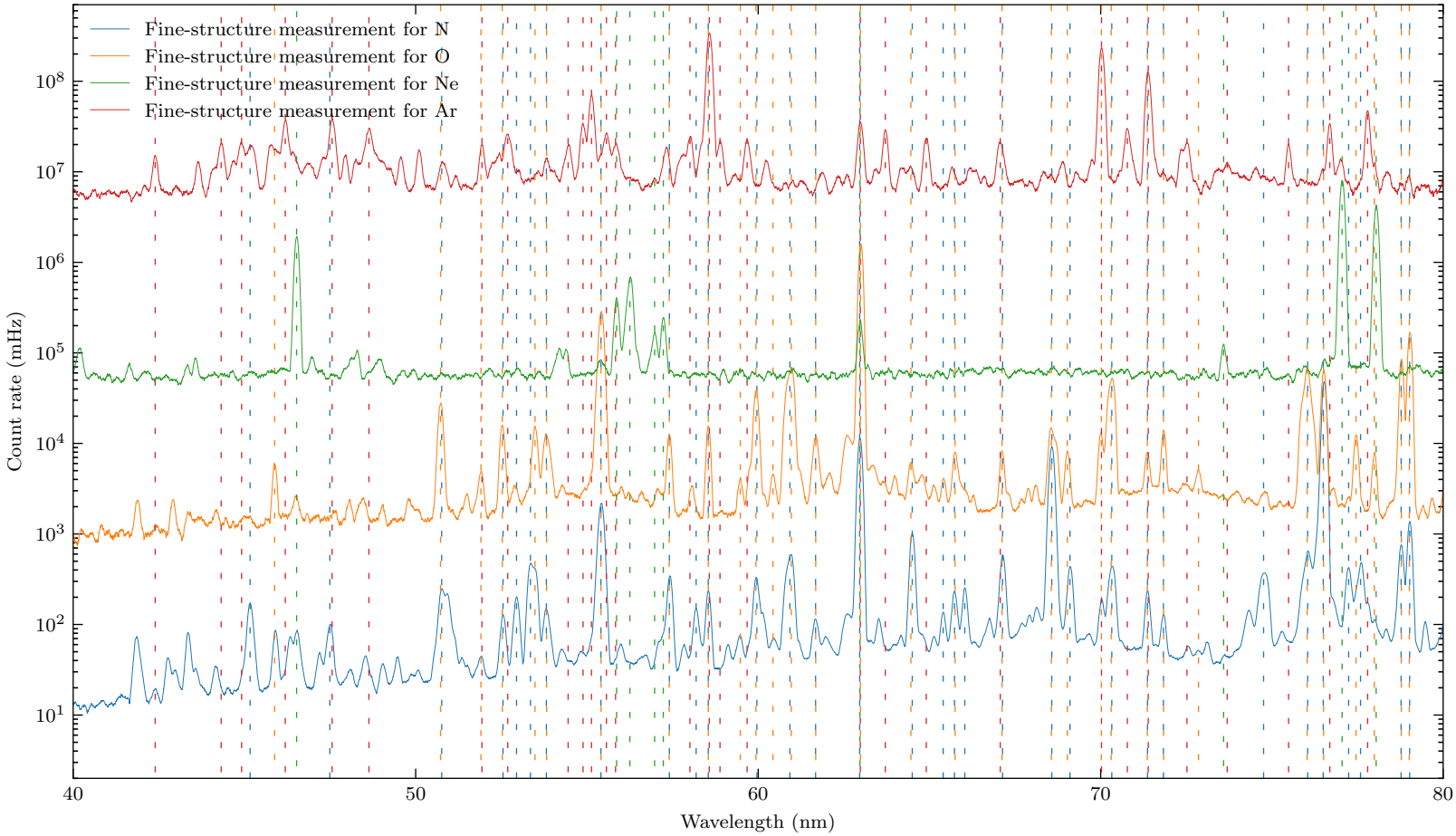

Figure B.2: Comparison of VUV spectra for different species in the range from 40 nm to 80 nm. All spectra are smoothed using a moving average for the visualisation and can also be found in Figures 5.2, 5.3, 5.4, and 5.5. Locations of peaks automatically found and fitted are indicated by dashed vertical lines in the colour of the respective spectrum. The O V line around 62.7930 nm was identified in the spectra of all four species.

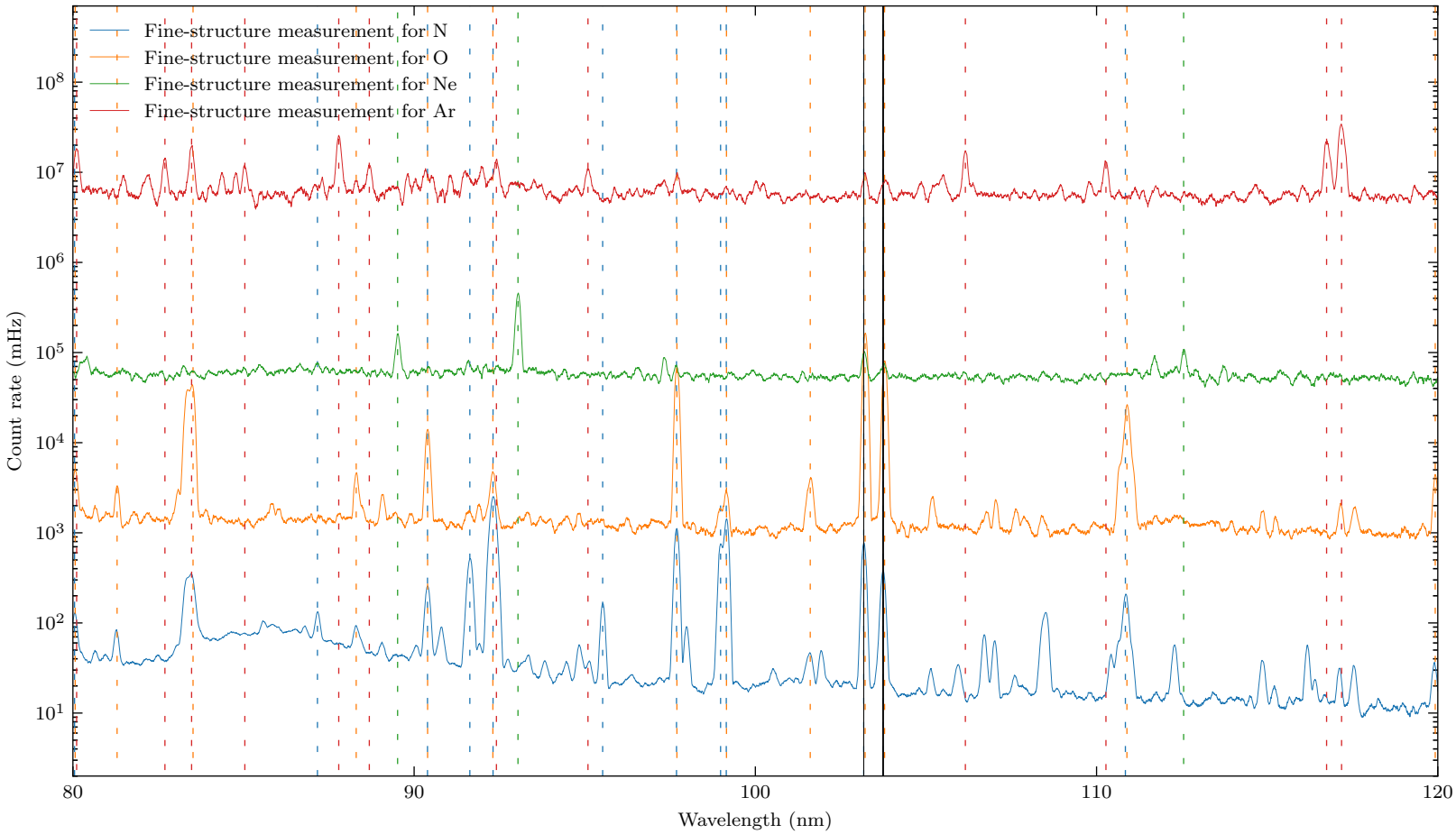

Figure B.3: Comparison of VUV spectra for different species in the range from 80 nm to 120 nm. All spectra are smoothed using a moving average for the visualisation and can also be found in Figures 5.2, 5.3, 5.4, and 5.5. Locations of peaks automatically found and fitted are indicated by dashed vertical lines in the colour of the respective spectrum. Two black vertical lines indicate the first spectral order of the oxygen fine-structure doublet.

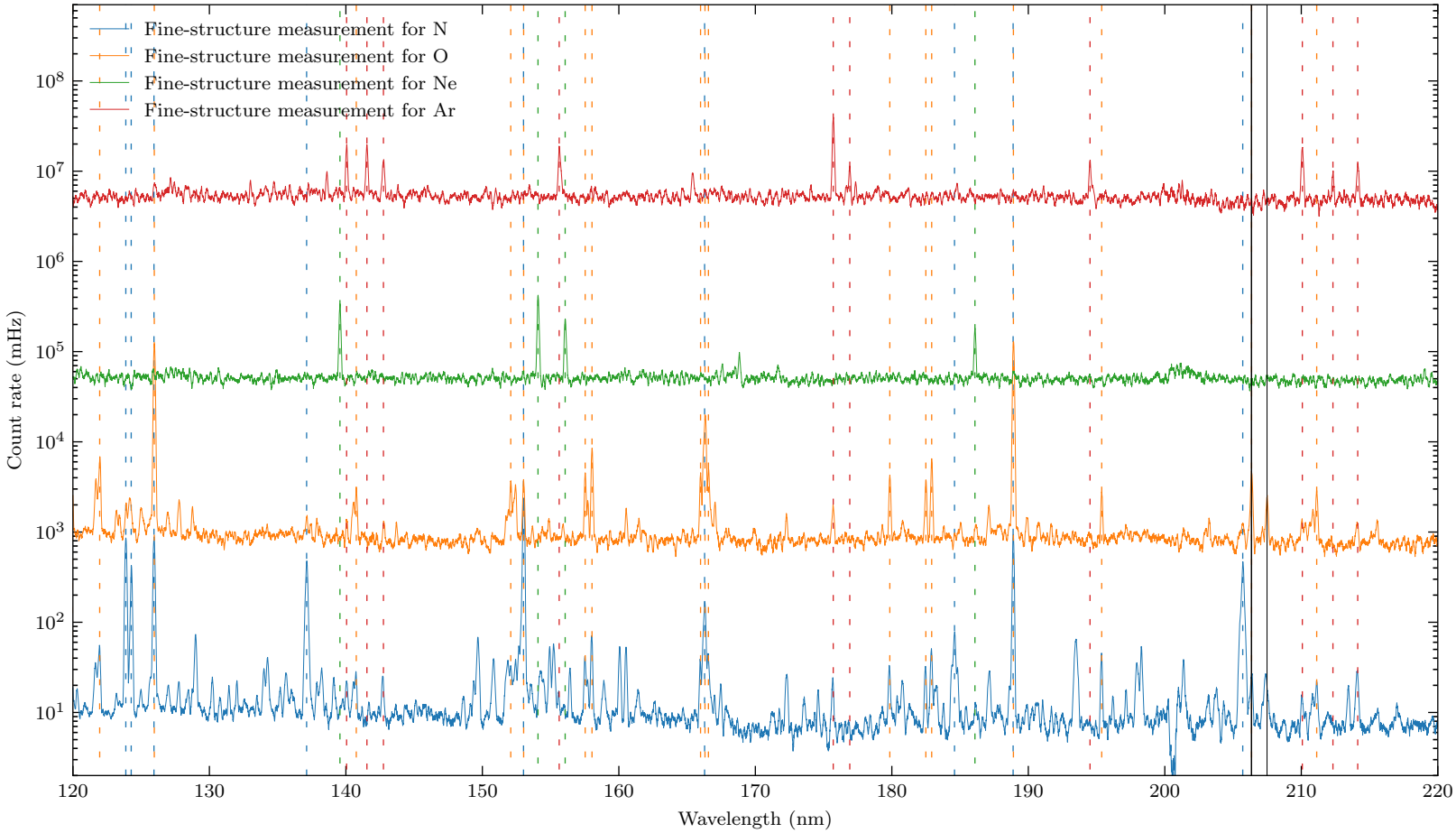

Figure B.4: Comparison of VUV spectra for different species in the range from 120 nm to 220 nm. All spectra are smoothed using a moving average for the visualisation and can also be found in Figures 5.2, 5.3, 5.4, and 5.5. Locations of peaks automatically found and fitted are indicated by dashed vertical lines in the colour of the respective spectrum. Two black vertical lines indicate the second spectral order of the oxygen fine-structure doublet.

Calibration function parameters

For all the fine-structure measurements presented in Chapter 5 the coefficients of the respective calibration polynomials $f(x) = ax^3 + bx^2 + cx + d$ are given in Table B.2.

Table B.2: Coefficients of the cubic calibration function $f(x)$.

Measurement	a	b	c	d
N 1	$5.8(39) \times 10^{-13}$	$-4.0(11) \times 10^{-8}$	0.014 85(11)	−23.88(32)
N 2	$4.4(44) \times 10^{-12}$	$-1.5(13) \times 10^{-7}$	0.015 90(12)	−26.84(36)
N 3	$-7.1(58) \times 10^{-13}$	$1.7(21) \times 10^{-9}$	0.014 422(23)	−22.564(76)
N 4	$-8.1(92) \times 10^{-13}$	$5.4(32) \times 10^{-9}$	0.014 383(34)	−22.44(11)
N 5	$-9.3(16) \times 10^{-13}$	$8.3(49) \times 10^{-9}$	0.014 363(48)	−22.31(15)
N 6	$-9.8(15) \times 10^{-13}$	$1.0(47) \times 10^{-8}$	0.014 339(46)	−22.20(14)
N 7	$-6.8(68) \times 10^{-13}$	$9.0(21) \times 10^{-10}$	0.014 429(21)	−22.455(62)
O 1	$-6.3(11) \times 10^{-13}$	$-2.1(39) \times 10^{-9}$	0.014 479(42)	−22.76(14)
O 2	$-6.1(51) \times 10^{-13}$	$-4.0(17) \times 10^{-9}$	0.014 47(18)	−11.22(55)
O 3	$2.1(61) \times 10^{-12}$	$-7.5(16) \times 10^{-8}$	0.015 04(12)	−12.64(30)
Ne 1	$-6.4(61) \times 10^{-13}$	$2.0(18) \times 10^{-10}$	0.014 432(16)	−22.474(47)
Ne 2	$-5.9(77) \times 10^{-13}$	$-1.0(22) \times 10^{-9}$	0.014 439(20)	−22.437(57)
Ne 3	$-8.0(12) \times 10^{-13}$	$5.3(36) \times 10^{-9}$	0.014 382(32)	−22.270(91)
Ar 1	$-8.7(23) \times 10^{-13}$	$6.8(71) \times 10^{-9}$	0.014 375 4(67)	−22.299(19)
Ar 2	$-2.0(79) \times 10^{-12}$	$2.3(13) \times 10^{-8}$	0.014 307(64)	−22.22(10)
Ar 3	$-8.3(44) \times 10^{-13}$	$5.5(14) \times 10^{-9}$	0.014 388(13)	−22.368(35)

It is apparent that the offset is changing from one measurement to the next. To facilitate comparison between the higher-order coefficients, the cubic functions in Table B.2 were converted to the calibration functions in the form of $f'(x) = a'(x-o)^3 + b'(x-o)^2 + c'(x-o)$. This was achieved by solving $f(o) = 0$ numerically for o. Then the other parameters are $a' = a$, $b' = b + 3a'o$, and $c' = c + 2b'o + 3a'o^2$. This set of coefficients is shown in Table B.3.

Table B.3: Coefficients of the alternative calibration polynomial $f'(x)$.

Measurement	a'	b'	c'	o
N 1	5.83×10^{-13}	-3.70×10^{-8}	1.47×10^{-2}	1.62×10^{3}
N 2	4.45×10^{-12}	-1.32×10^{-7}	1.55×10^{-2}	1.71×10^{3}
N 3	-7.06×10^{-13}	-1.58×10^{-9}	1.44×10^{-2}	1.56×10^{3}
N 4	-8.10×10^{-13}	1.65×10^{-9}	1.44×10^{-2}	1.56×10^{3}
N 5	-9.32×10^{-13}	3.98×10^{-9}	1.44×10^{-2}	1.55×10^{3}
N 6	-9.77×10^{-13}	5.61×10^{-9}	1.43×10^{-2}	1.55×10^{3}
N 7	-6.81×10^{-13}	-2.28×10^{-9}	1.44×10^{-2}	1.56×10^{3}
O 1	-6.33×10^{-13}	-5.08×10^{-9}	1.45×10^{-2}	1.57×10^{3}
O 2	-6.07×10^{-13}	-5.11×10^{-9}	1.45×10^{-2}	7.76×10^{2}
O 3	2.13×10^{-12}	-6.99×10^{-8}	1.49×10^{-2}	8.44×10^{2}

Table B.3 continued

Measurement	a'	b'	c'	o
Ne 1	-6.43×10^{-13}	-2.85×10^{-9}	1.44×10^{-2}	1.56×10^{3}
Ne 2	-5.90×10^{-13}	-3.76×10^{-9}	1.44×10^{-2}	1.55×10^{3}
Ne 3	-8.01×10^{-13}	1.57×10^{-9}	1.44×10^{-2}	1.55×10^{3}
Ar 1	-8.68×10^{-13}	2.72×10^{-9}	1.44×10^{-2}	1.55×10^{3}
Ar 2	-2.01×10^{-12}	1.39×10^{-8}	1.43×10^{-2}	1.55×10^{3}
Ar 3	-8.33×10^{-13}	1.62×10^{-9}	1.44×10^{-2}	1.55×10^{3}

B.2 Iridium spectroscopy

B.2.1 Detailed energy scans

All detailed energy scans related to the identification of new spectral lines in the VUV regime attributed to neodymium-like iridium are presented on the following pages with the exception of Figures 6.7 and 6.8. For a full list of lines, please refer to Table 6.3.

B.2.2 Calibration lines in the EUV range

Table B.4: Calibration lines used in the EUV range [122]. The last column indicates at which electron beam acceleration potentials the line was used for calibration.

Species	NIST wavelength (nm)	Observed at (V)
Fe XV	30.2334(10)	510, 530, 570, 590
Fe XIV	30.3573(10)	450, 470
Fe XV	30.4894(10)	510, 530, 550, 570, 590, 620
Fe XIV	30.773(10)	530, 550, 570, 590
Fe XI	30.8544(10)	450
Fe XIII	31.2164(10)	450, 470, 490
Fe XV	31.2556(10)	530, 550, 570, 590, 620
Fe XIII	31.821(10)	450, 470, 490
Fe XIII	32.0800(10)	450, 470, 490, 510, 530, 570
Fe XV	32.1771(10)	530, 570, 590, 620
Fe XVII	32.365(5)	450
Fe XV	32.4975(10)	570, 590
Fe XV	32.7024(10)	510, 530, 550, 570, 590, 620
Fe XV	33.1083(10)	550, 570
Fe XV	33.2854(10)	570
Fe XIV	33.4171(10)	450, 470, 490, 510, 530, 550, 570, 590, 620
Fe IX	33.5294(10)	450, 470
Fe XVI	33.5409(10)	550, 570, 590, 620
Fe XII	33.8263(10)	450, 470
Fe XII	34.6852(10)	450
Fe XIII	34.8184(10)	450, 470, 490, 510, 530
Fe XII	35.2107(10)	470

Table B.4 continued

Species	NIST wavelength (nm)	Observed at (V)
Fe XIV	35.3829(10)	450, 470, 490, 510, 530, 550, 570, 590, 620
Fe XIV	35.6505(10)	550
Fe XIV	35.660(10)	490, 510
Fe XIV	35.8681(10)	490, 510, 590
Fe XIII	35.963(10)	450, 470, 490, 510, 530
Fe XVI	36.0758(10)	450
Fe XV	36.0827(3)	590, 570, 620
Fe XII	36.4468(10)	450, 470
Fe XIII	36.812(10)	450, 470, 490, 510, 530
Fe XV	37.2798(10)	510, 530, 550, 570, 590
Fe XV	38.7086(10)	490, 550, 570
Fe XV	40.0851(10)	550, 570

B.2.3 Complete list of known spectral lines of Ir^{17+}

For future line identification efforts, a complete list of all known spectral lines of Ir^{17+} is given here.

Table B.5: Complete list of spectral lines attributed to Ir^{17+}. Lines found in this work are given without a reference. An $*$ next to the line indicates a previous identification (see Table 6.5). Please note that line intensities are only comparable within the same measurement (letter in the name of the line).

	λ (nm)	E (eV)	I (mHz/a. u.)	Ref.
Line A1	19.2222(12)	64.5005(40)	72	[15]
Line A2	19.271 74(18)	64.3347(59)	4	[15]
Line A3	19.3077(11)	64.2149(37)	14	[15]
Line A4	19.4073(10)	63.8853(33)	43	[15]
Line A5	19.4833(10)	63.6361(33)	23	[15]
Line A6	19.5715(10)	63.3494(32)	28	[15]
Line A7	19.616 90(80)	63.2027(26)	76	[15]
Line A8	19.664 40(90)	63.0501(29)	54	[15]
Line A9	19.7129(12)	62.8959(38)	24	[15]
Line A10	19.972 71(11)	62.0768(33)	3	[15]
Line A11	20.026 340(90)	61.9106(27)	5	[15]
Line A12	20.146 920(90)	61.5400(29)	6	[15]
Line A13	20.361 68(17)	60.8909(50)	6	[15]
Line A14	20.484 960(80)	60.5245(23)	7	[15]
Line A15	20.564 330(70)	60.2909(19)	15	[15]
Line A16	20.655 08(13)	60.0260(36)	3	[15]
Line A17	20.7598(10)	59.7232(29)	35	[15]
Line A18	20.809 29(30)	59.5812(85)	8	[15]

Table B.5 continued

	λ (nm)	E (eV)	I (mHz/a. u.)	Ref.
Line A19	20.845 04(23)	59.4790(64)	12	[15]
Line A20	20.948 53(17)	59.1852(49)	1	[15]
Line A21	21.025 27(10)	58.9691(29)	3	[15]
Line A22	21.082 58(10)	58.8088(27)	4	[15]
Line A23	21.143 16(15)	58.6403(42)	2	[15]
Line A24	21.587 90(80)	57.4323(21)	2	[15]
Line A25	21.767 10(80)	56.9594(21)	6	[15]
Line A26	21.867 40(90)	56.6982(23)	5	[15]
Line E6	30.1340(23)	41.1443(32)	0.0593	
Line E7	30.2291(25)	41.0175(34)	0.0329	
Line E9	30.3850(44)	40.8043(58)	0.0532	
Line E10	30.5084(28)	40.6394(37)	0.1838	
Line E11	30.6453(22)	40.4579(29)	0.2838	
Line E12	30.8825(23)	40.1471(30)	0.1545	
Line E23	31.9991(36)	38.7461(43)	0.3200	
Line E24	32.1406(23)	38.5755(28)	0.1047	
Line E29	32.4560(36)	38.2007(42)	0.0968	
Line E41	35.0890(31)	35.3342(31)	0.0271	
Line E48	37.5364(28)	33.0304(24)	0.0078	
Line E49	37.5390(28)	33.0281(24)	0.0193	
Line E51	37.9416(31)	32.6776(27)	0.0396	
Line E63	39.7908(44)	31.1590(34)	0.0272	
Line E65	40.1605(31)	30.8722(24)	0.0459	
Line V19	48.717(12)	25.4499(62)	5.38	
Line V26	54.1916(98)	22.8789(41)	3.60	
Line V29	54.9065(93)	22.5810(38)	14.84	
Line V33	56.5100(90)	21.9402(35)	10.03	
Line V36	57.3993(88)	21.6003(33)	13.93	
Line V38	58.0096(86)	21.3731(32)	27.73	
Line V40	59.0102(95)	21.0106(34)	2.06	
Line V44	62.0924(90)	19.9677(29)	10.11	
Line V48	63.4215(83)	19.5492(26)	8.54	
Line V52	64.859(90)	19.116(27)	3.27	
Line V55	67.1265(90)	18.4702(25)	9.47	
Line V56	67.3572(85)	18.4070(23)	8.22	
Line V57	67.9319(86)	18.2512(23)	7.49	
Line V59	68.3754(86)	18.1329(23)	16.53	
Line V61	68.3832(86)	18.1308(23)	17.68	
Line V62	69.2596(87)	17.9014(22)	7.24	
Line V63	69.611(12)	17.8111(30)	2.30	

Table B.5 continued

	λ (nm)	E (eV)	I (mHz/a. u.)	Ref.
Line V64	70.0072(88)	17.7102(22)	4.28	
Line V68	70.3505(88)	17.6238(22)	9.42	
Line V70	70.7255(89)	17.5303(22)	3.27	
Line V74	72.1295(90)	17.1891(22)	12.05	
Line V77	73.3123(93)	16.9118(22)	3.99	
Line V79	74.1041(92)	16.7311(21)	27.04	
Line V80	74.9165(93)	16.5497(21)	13.88	
Line V82	75.9073(94)	16.3336(20)	16.91	
Line V84	76.5360(96)	16.1995(20)	5.86	
Line V85	77.1691(96)	16.0666(20)	2.44	
Line V89	78.4882(96)	15.7965(19)	6.59	
Line V91	78.8750(97)	15.7191(19)	4.27	
Line V93	79.5693(97)	15.5819(19)	5.92	
Line V94	80.0180(98)	15.4945(19)	10.25	
Line V97	80.9440(98)	15.3173(19)	12.72	
Line V99	81.7068(99)	15.1743(18)	3.38	
Line V101	82.9999(99)	14.9379(18)	5.28	
Line V102	83.4146(99)	14.8636(18)	10.16	
Line V103	83.684(10)	14.8156(18)	20.98	
Line V105	84.116(10)	14.7396(17)	10.29	
Line V107	84.787(10)	14.6229(17)	4.74	
Line V109	85.328(10)	14.5302(17)	8.94	
Line V110	85.697(10)	14.4678(17)	4.39	
Line V111	86.514(10)	14.3311(17)	17.96	
Line V114	89.598(10)	13.8378(16)	2.27	
Line V117	92.5669(99)	13.3940(14)	3.32	
Line V118	94.372(10)	13.1378(14)	0.98	
Line V119	95.1586(98)	13.0292(13)	4.99	
Line V120	99.3781(95)	12.4760(12)	3.30	
Line V123	100.8492(93)	12.2940(11)	15.27	
Line V124	104.2361(91)	11.8946(10)	13.09	
Line V125	105.9458(90)	11.7026(10)	5.23	
Line V127	106.9240(90)	11.595 55(98)	3.47	
Line V129	110.5331(91)	11.216 92(93)	5.64	
Line V132	116.271(11)	10.663 40(97)	2.54	
Line V137	124.180(14)	9.9842(11)	0.79	
Line O1∗	226.630(20)	5.469 10(50)	0.003	[15]
Line O2	229.8270(50)	5.393 00(10)	—	[15]
Line O3	231.8760(50)	5.345 40(10)	—	[15]
Line O4	232.7750(30)	5.324 710(60)	—	[15]

Table B.5 continued

	λ (nm)	E (eV)	I (mHz/a. u.)	Ref.
Line O5	235.5820(30)	5.261 270(60)	—	[15]
Line O6	236.3240(20)	5.244 750(40)	—	[15]
Line O7	238.450(20)	5.198 00(40)	0.003	[15]
Line O8	240.0980(10)	5.162 330(20)	0.003	[15]
Line O9	243.4760(20)	5.090 710(40)	—	[15]
Line O10	244.2610(40)	5.074 350(80)	—	[15]
Line O11	248.0770(20)	4.996 300(40)	0.002	[15]
Line O12	252.3060(10)	4.912 560(20)	—	[15]
Line O13	255.868 40(30)	4.844 170 0(60)	0.003	[15]
Line O14	256.5530(30)	4.831 240(50)	—	[15]
Line O15	256.7670(30)	4.827 220(60)	—	[15]
Line O16	258.983 10(50)	4.785 915 0(90)	—	[15]
Line O17	271.690 90(20)	4.562 076 0(30)	0.005	[15]
Line O18	280.870(20)	4.413 00(30)	0.003	[15]
Line O19	289.490(10)	4.281 60(20)	0.005	[15]
Line O20	292.6340(40)	4.235 590(50)	0.014	[15]
Line O21	298.1420(10)	4.157 350(20)	0.007	[15]
Line O22	301.070(20)	4.116 90(30)	0.002	[15]
Line O23	304.240(20)	4.074 00(30)	0.008	[15]
Line O24	306.820(10)	4.039 80(10)	—	[15]
Line O25	314.950(20)	3.935 50(20)	0.006	[15]
Line O26	319.3420(20)	3.881 370(30)	—	[15]
Line O27	321.4640(50)	3.855 740(50)	—	[15]
Line O28	321.9130(30)	3.850 370(30)	0.008	[15]
Line O29	323.0220(70)	3.837 150(80)	0.006	[15]
Line O30∗	324.609 90(40)	3.818 381 0(50)	0.126	[15]
Line O31	327.7710(20)	3.781 560(30)	—	[15]
Line O32∗	329.302 50(40)	3.763 971 0(50)	0.299	[15]
Line O33∗	365.0318(10)	3.395 564 0(90)	0.053	[15]
Line O34	386.6550(50)	3.205 670(40)	—	[15]
Line O35	388.8240(10)	3.187 790(10)	0.018	[15]
Line O36∗	390.6300(10)	3.173 060(10)	—	[15]
Line O37∗	391.823 70(40)	3.163 389 0(40)	0.381	[15]
Line O38∗	399.357 70(60)	3.103 712 0(40)	0.065	[15]
Line O39	401.690(20)	3.085 70(20)	0.013	[15]
Line O40∗	422.895 00(30)	2.930 971 0(20)	1.000	[15]
Line O41∗	431.604 40(30)	2.871 827 0(20)	0.101	[15]
Line O42∗	435.634 80(50)	2.845 258 0(30)	0.191	[15]
Line O43∗	445.705 70(90)	2.780 970(60)	0.052	[15]
Line O44∗	482.703 90(70)	2.567 818 0(40)	0.052	[15]

Table B.5 continued

	λ (nm)	E (eV)	I (mHz/a. u.)	Ref.
Line O45∗	503.2830(20)	2.462 820(10)	—	[15]
Line O46	545.830(20)	2.270 850(80)	0.006	[15]
Line O47	577.570(20)	2.146 060(70)	0.006	[15]
Line O48∗	597.650(20)	2.073 950(70)	0.010	[15]

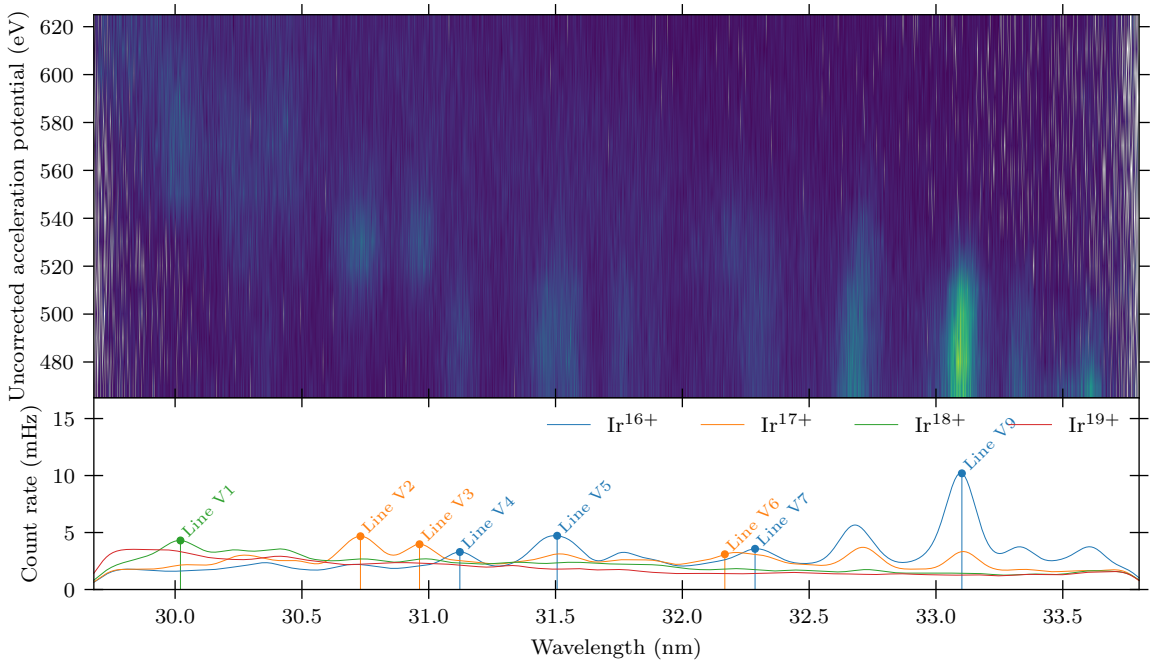

Figure B.5: Detailed energy scan of iridium around 31.74 nm. The upper part showing the two-dimensional spectrogram, while individual smoothed spectra at beam energies of 490 V, 530 V, 570 V, and 610 V are shown in the lower part. These values correspond to the ideal energies for measuring Ir^{16+}, Ir^{17+}, Ir^{18+}, and Ir^{19+} respectively. Sections through the data along the beam energy axis at the peak positions marked in the lower part can be found in Figure B.6.

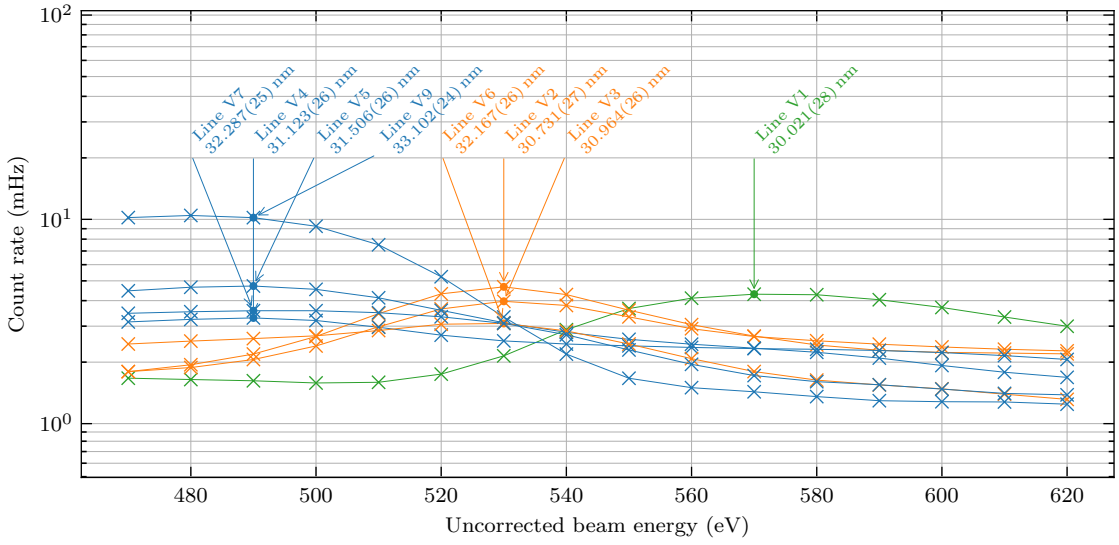

Figure B.6: Peak intensities of the lines found in Figure B.5 plotted against beam energy.

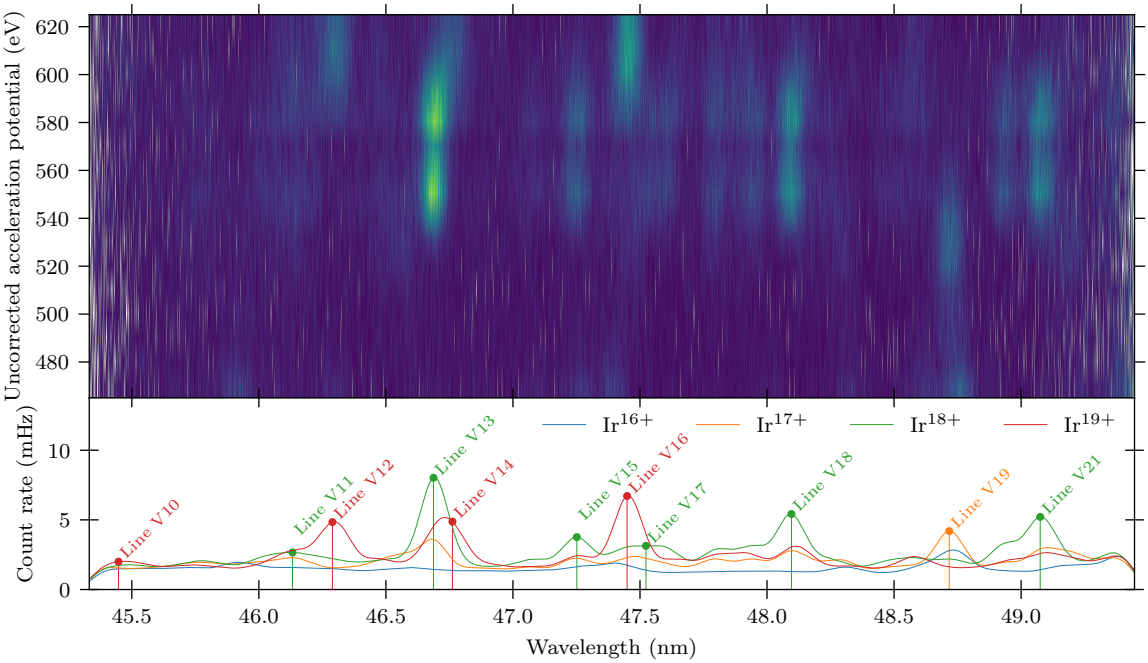

Figure B.7: Detailed energy scan of iridium around 47.39 nm. The upper part showing the two-dimensional spectrogram, while individual smoothed spectra at beam energies of 490 V, 530 V, 570 V, and 610 V are shown in the lower part. These values correspond to the ideal energies for measuring Ir^{16+}, Ir^{17+}, Ir^{18+}, and Ir^{19+} respectively. Sections through the data along the beam energy axis at the peak positions marked in the lower part can be found in Figure B.8.

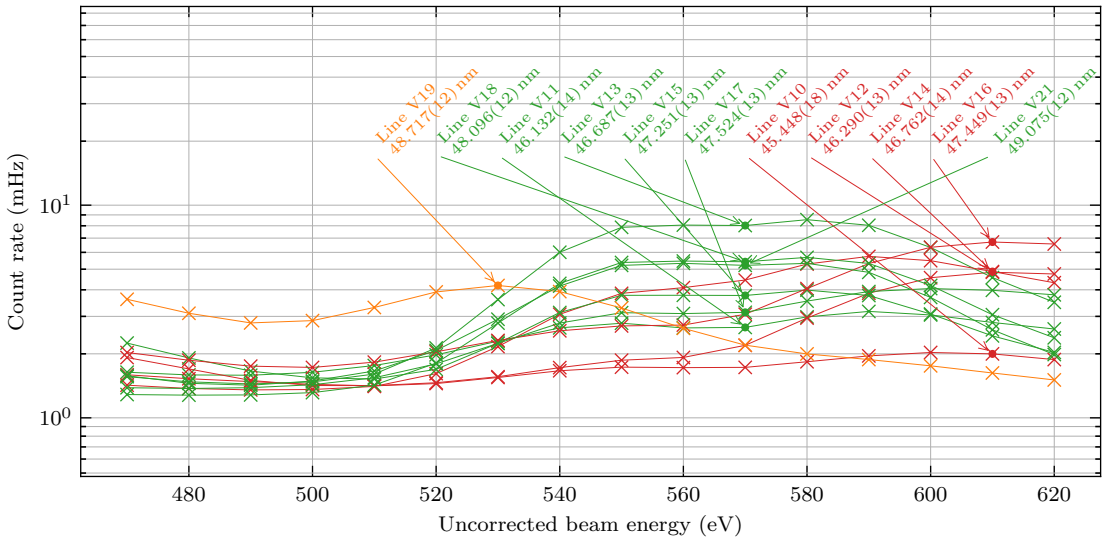

Figure B.8: Peak intensities of the lines found in Figure B.7 plotted against beam energy.

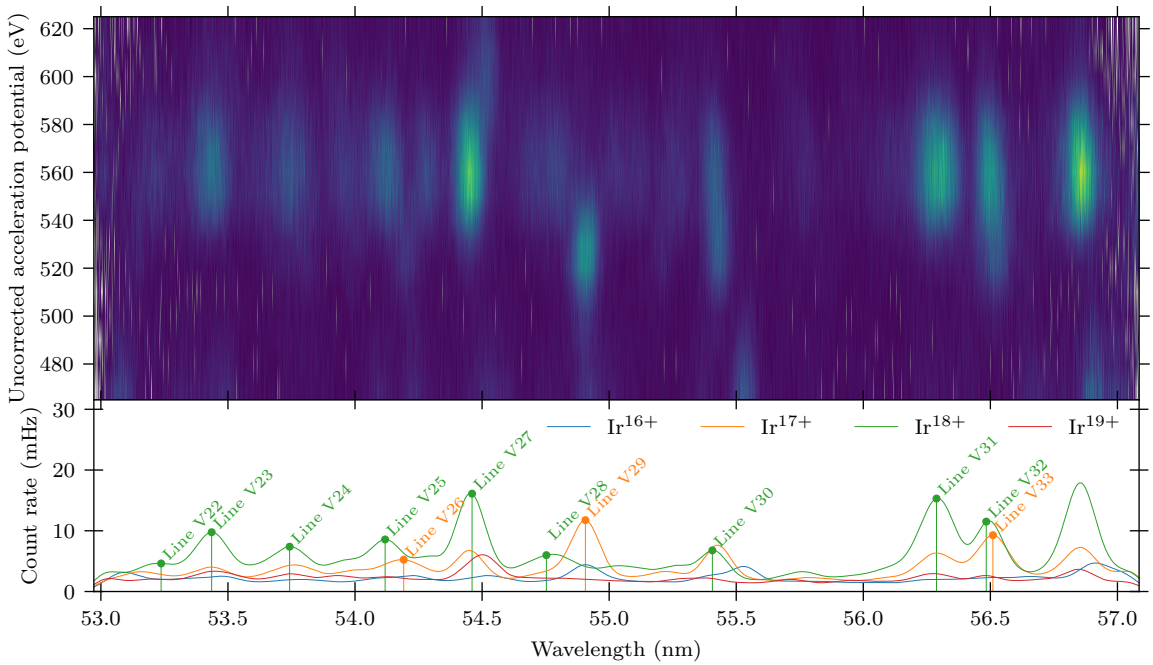

Figure B.9: Detailed energy scan of iridium around 55.03 nm. The upper part showing the two-dimensional spectrogram, while individual smoothed spectra at beam energies of 490 V, 530 V, 570 V, and 610 V are shown in the lower part. These values correspond to the ideal energies for measuring Ir^{16+}, Ir^{17+}, Ir^{18+}, and Ir^{19+} respectively. Sections through the data along the beam energy axis at the peak positions marked in the lower part can be found in Figure B.10.

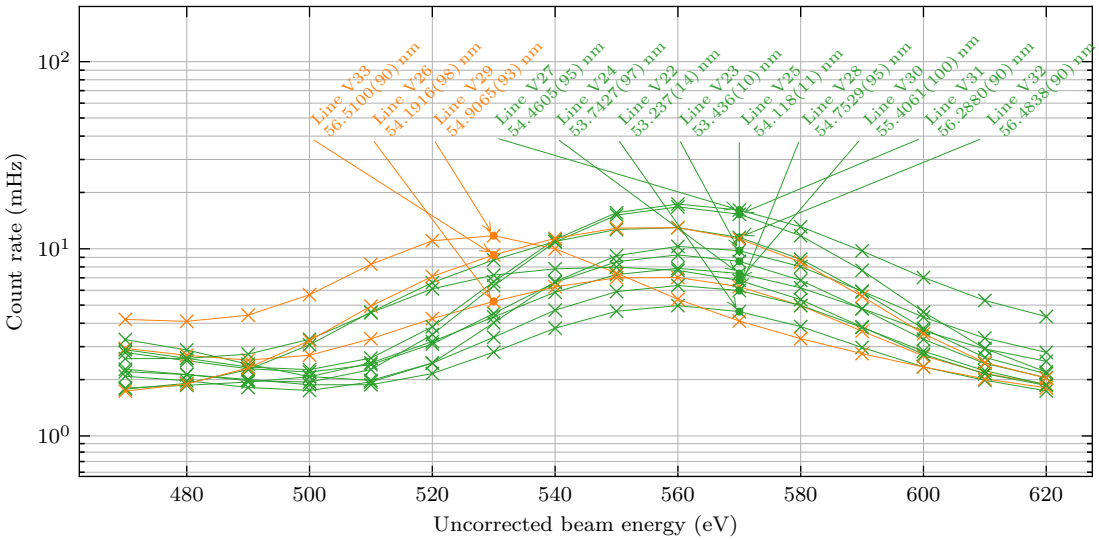

Figure B.10: Peak intensities of the lines found in Figure B.9 plotted against beam energy.

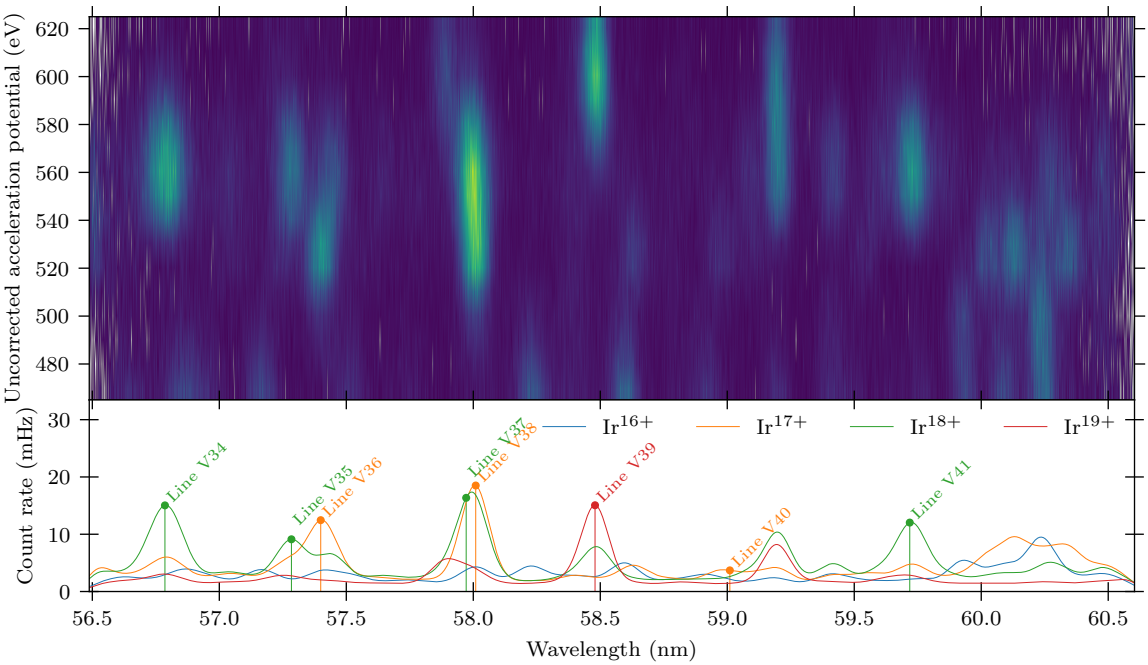

Figure B.11: Detailed energy scan of iridium around 58.55 nm. The upper part showing the two-dimensional spectrogram, while individual smoothed spectra at beam energies of 490 V, 530 V, 570 V, and 610 V are shown in the lower part. These values correspond to the ideal energies for measuring Ir^{16+}, Ir^{17+}, Ir^{18+}, and Ir^{19+} respectively. Sections through the data along the beam energy axis at the peak positions marked in the lower part can be found in Figure B.12.

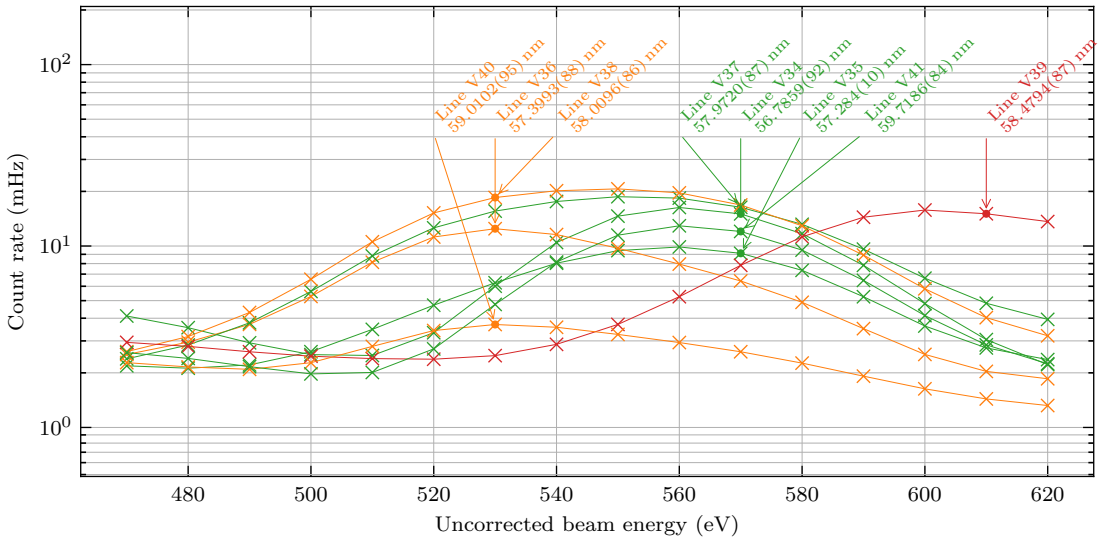

Figure B.12: Peak intensities of the lines found in Figure B.11 plotted against beam energy.

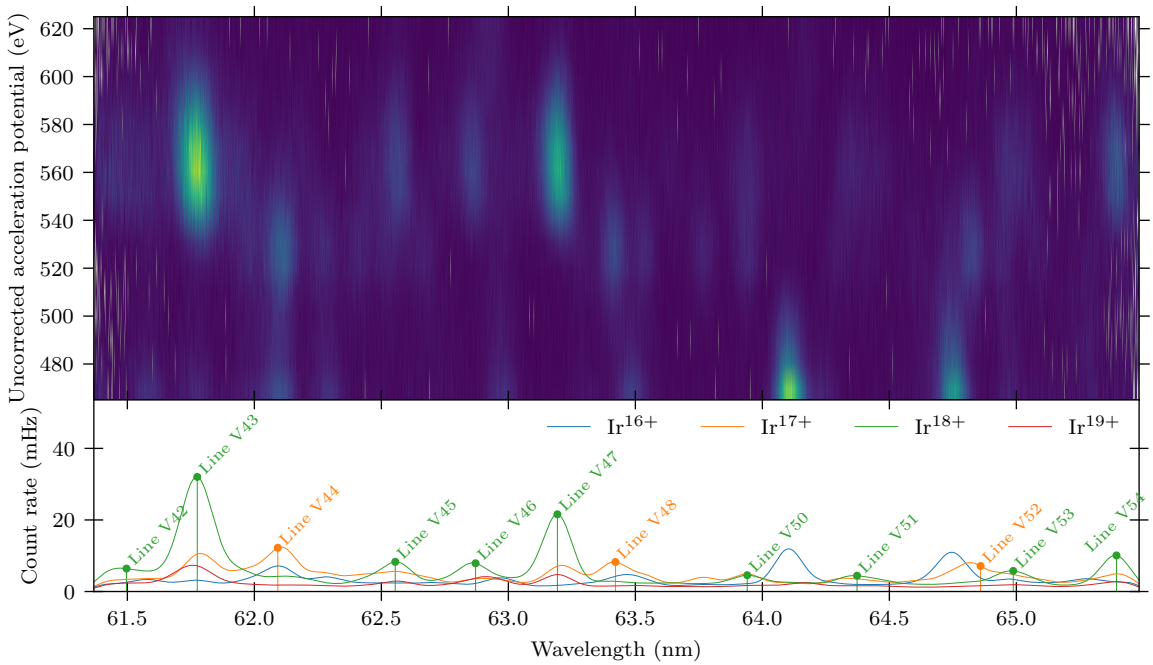

Figure B.13: Detailed energy scan of iridium around 63.43 nm. The upper part showing the two-dimensional spectrogram, while individual smoothed spectra at beam energies of 490 V, 530 V, 570 V, and 610 V are shown in the lower part. These values correspond to the ideal energies for measuring Ir^{16+}, Ir^{17+}, Ir^{18+}, and Ir^{19+} respectively. Sections through the data along the beam energy axis at the peak positions marked in the lower part can be found in Figure B.14.

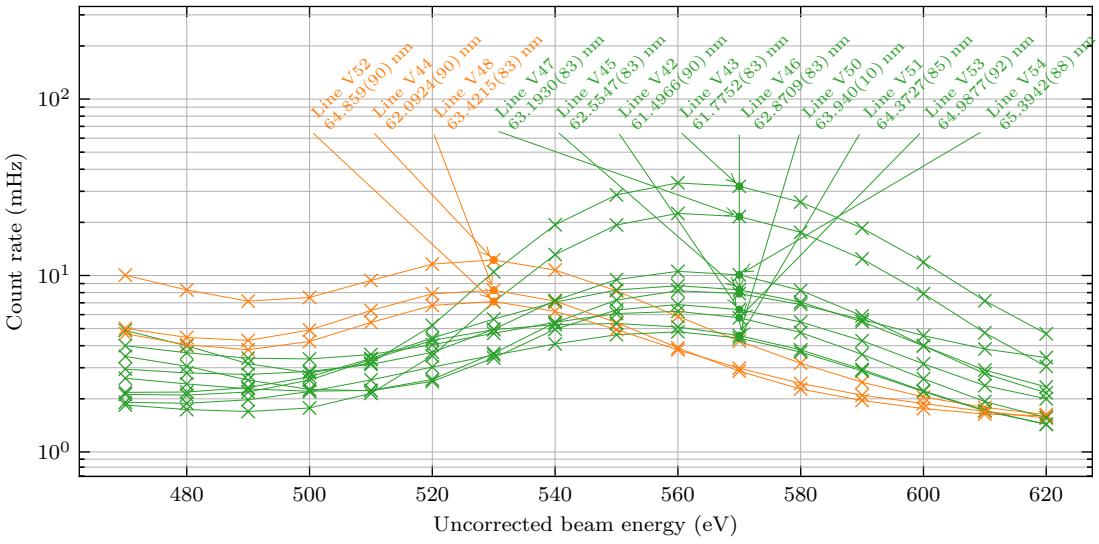

Figure B.14: Peak intensities of the lines found in Figure B.13 plotted against beam energy.

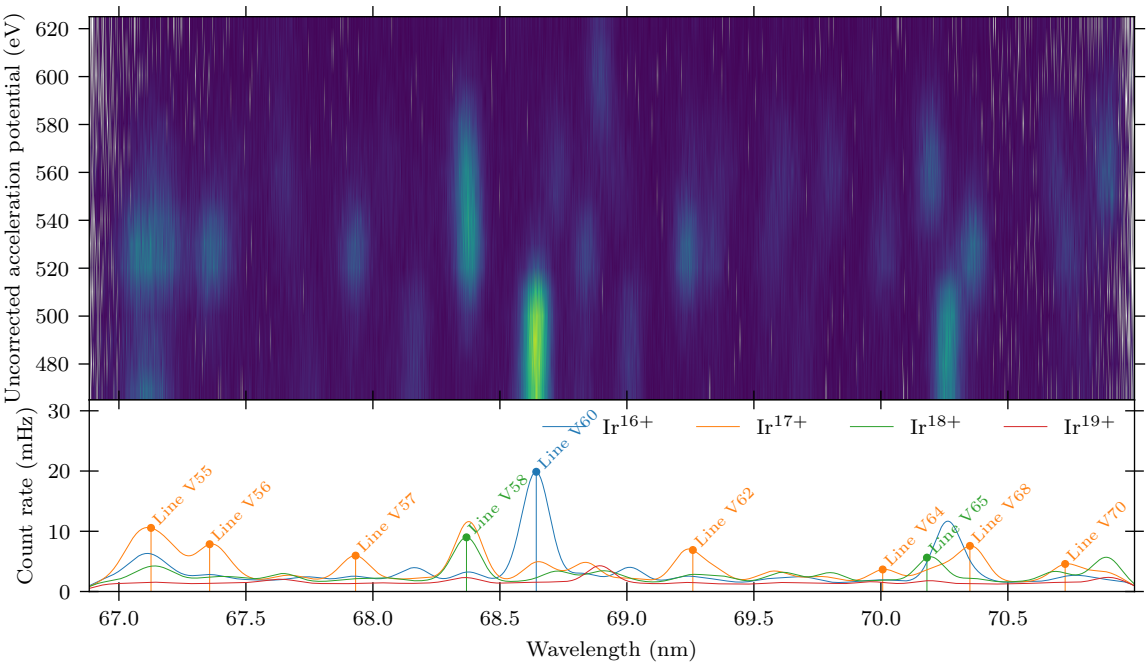

Figure B.15: Detailed energy scan of iridium around 68.94 nm. The upper part showing the two-dimensional spectrogram, while individual smoothed spectra at beam energies of 490 V, 530 V, 570 V, and 610 V are shown in the lower part. These values correspond to the ideal energies for measuring Ir^{16+}, Ir^{17+}, Ir^{18+}, and Ir^{19+} respectively. Sections through the data along the beam energy axis at the peak positions marked in the lower part can be found in Figure B.16.

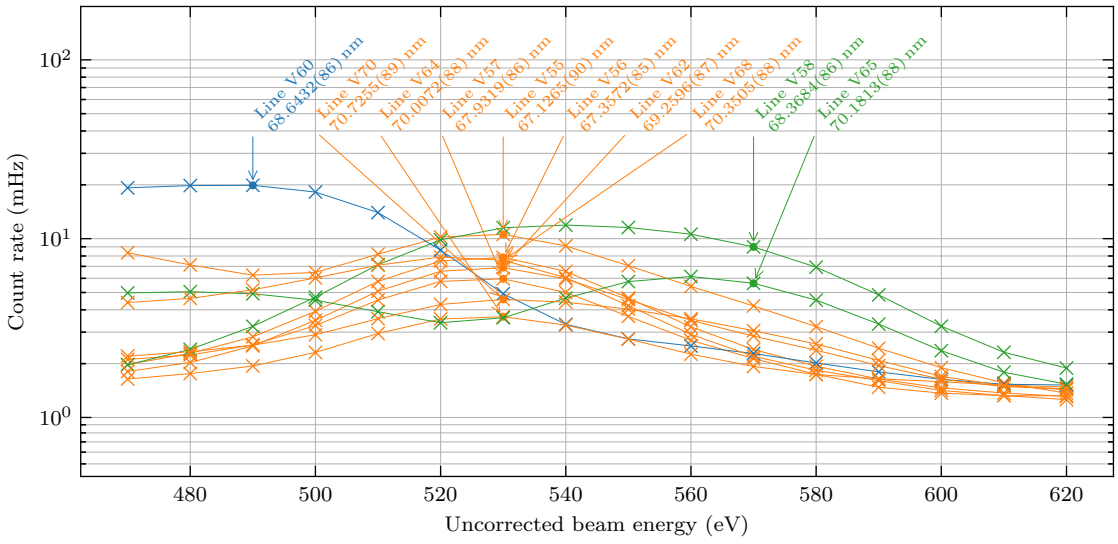

Figure B.16: Peak intensities of the lines found in Figure B.15 plotted against beam energy.

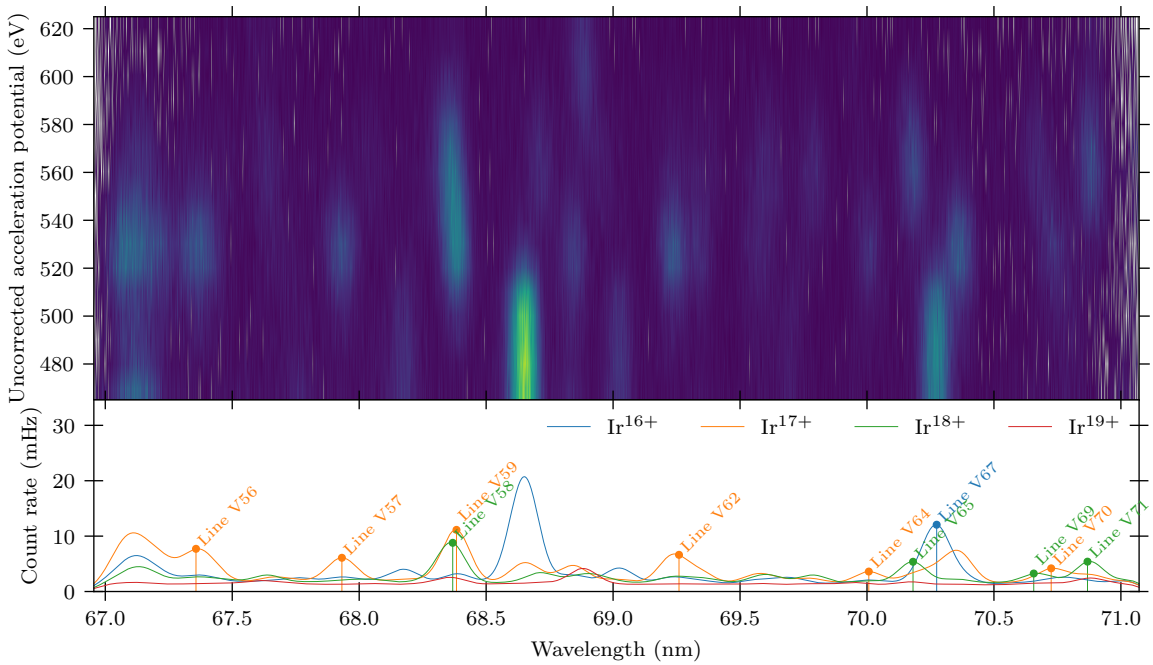

Figure B.17: Detailed energy scan of iridium around 69.01 nm. The upper part showing the two-dimensional spectrogram, while individual smoothed spectra at beam energies of 490 V, 530 V, 570 V, and 610 V are shown in the lower part. These values correspond to the ideal energies for measuring Ir^{16+}, Ir^{17+}, Ir^{18+}, and Ir^{19+} respectively. Sections through the data along the beam energy axis at the peak positions marked in the lower part can be found in Figure B.18.

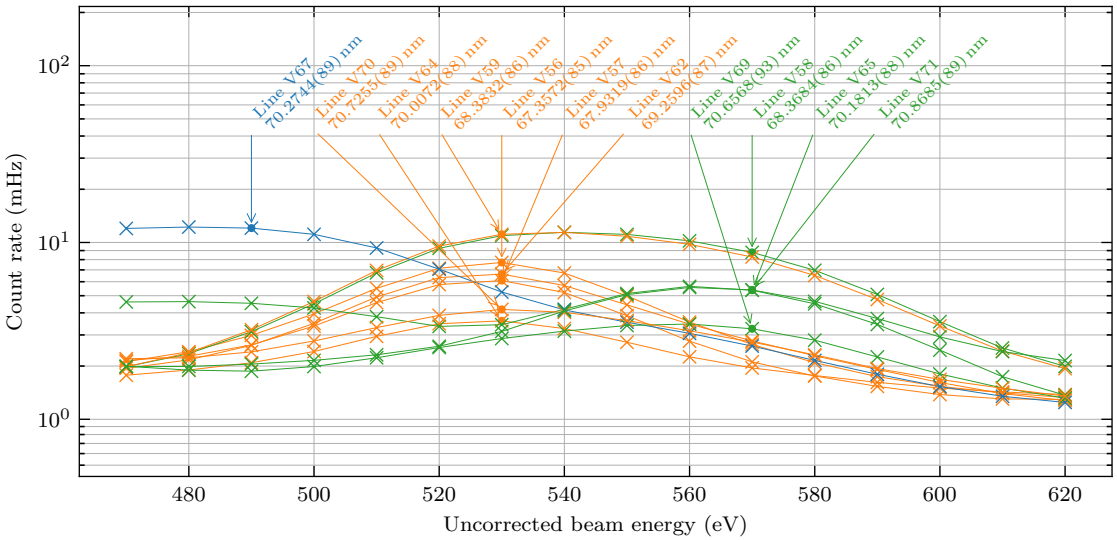

Figure B.18: Peak intensities of the lines found in Figure B.17 plotted against beam energy.

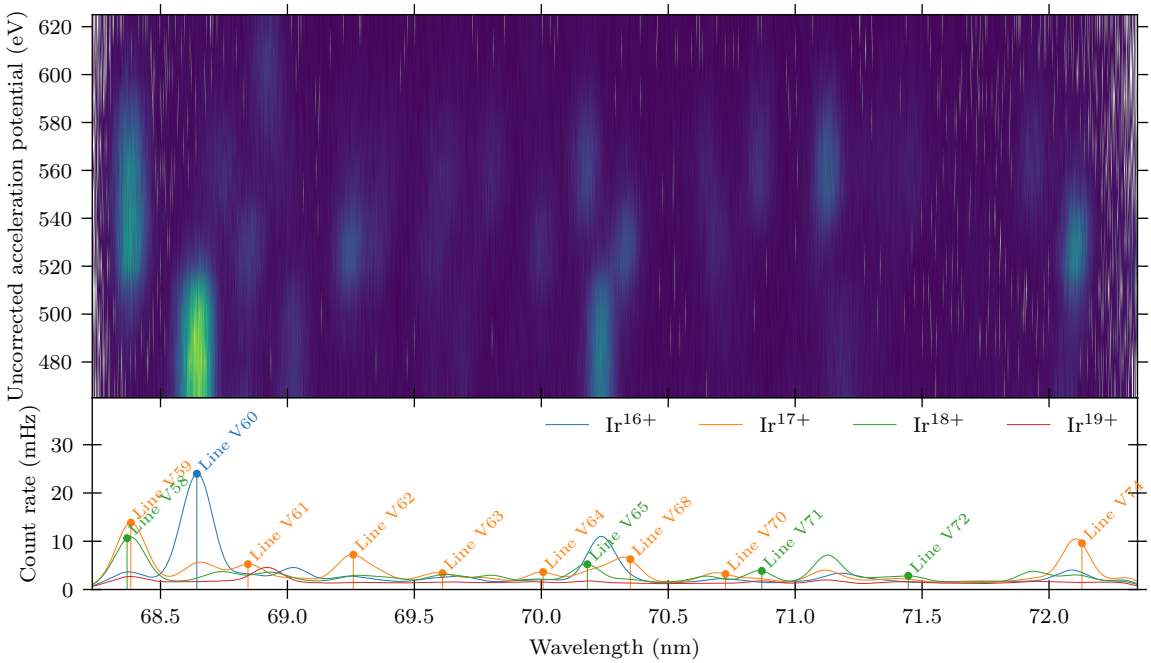

Figure B.19: Detailed energy scan of iridium around 70.29 nm. The upper part showing the two-dimensional spectrogram, while individual smoothed spectra at beam energies of 490 V, 530 V, 570 V, and 610 V are shown in the lower part. These values correspond to the ideal energies for measuring Ir^{16+}, Ir^{17+}, Ir^{18+}, and Ir^{19+} respectively. Sections through the data along the beam energy axis at the peak positions marked in the lower part can be found in Figure B.20.

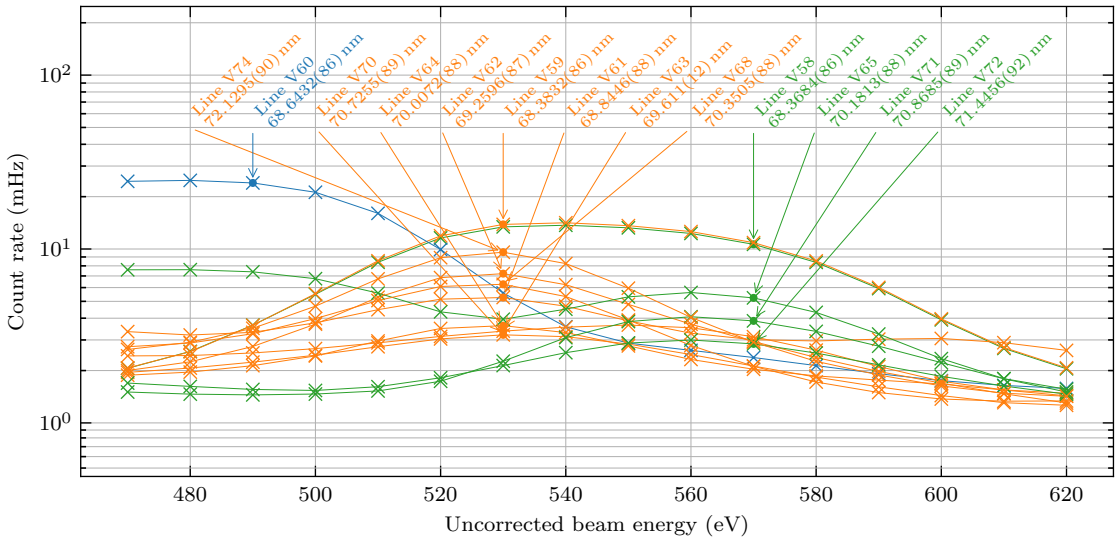

Figure B.20: Peak intensities of the lines found in Figure B.19 plotted against beam energy.

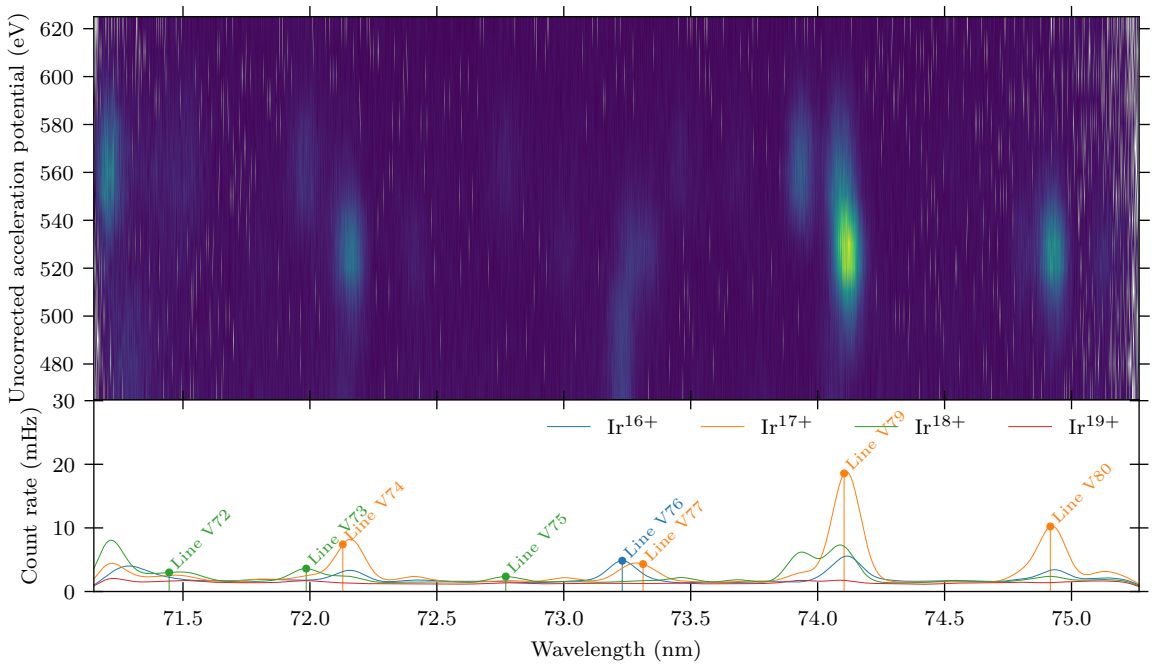

Figure B.21: Detailed energy scan of iridium around 73.21 nm. The upper part showing the two-dimensional spectrogram, while individual smoothed spectra at beam energies of 490 V, 530 V, 570 V, and 610 V are shown in the lower part. These values correspond to the ideal energies for measuring Ir^{16+}, Ir^{17+}, Ir^{18+}, and Ir^{19+} respectively. Sections through the data along the beam energy axis at the peak positions marked in the lower part can be found in Figure B.22.

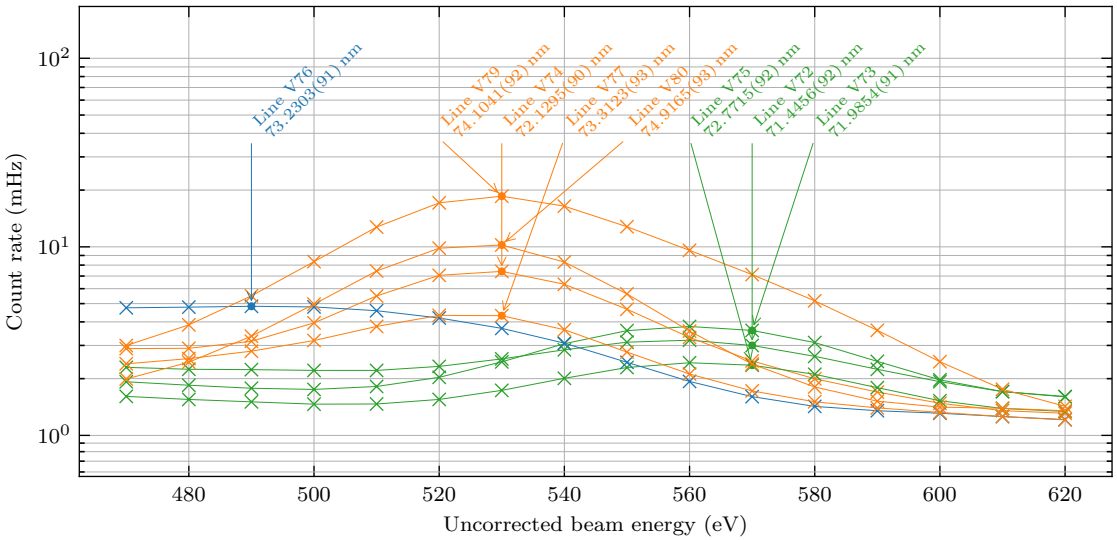

Figure B.22: Peak intensities of the lines found in Figure B.21 plotted against beam energy.

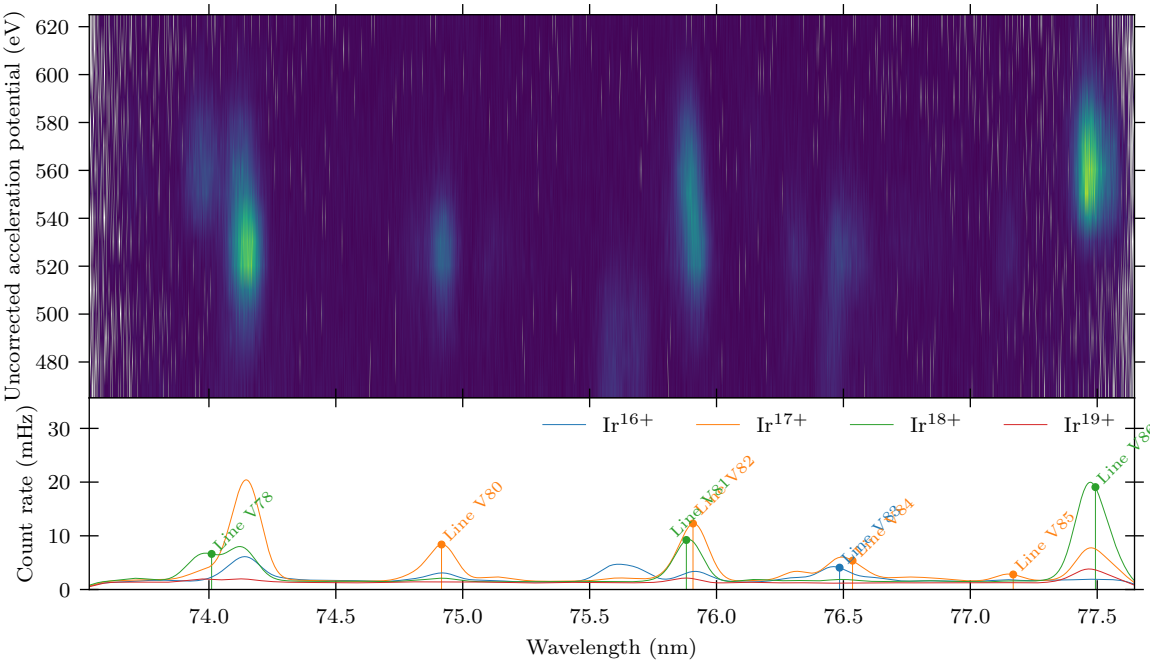

Figure B.23: Detailed energy scan of iridium around 75.59 nm. The upper part showing the two-dimensional spectrogram, while individual smoothed spectra at beam energies of 490 V, 530 V, 570 V, and 610 V are shown in the lower part. These values correspond to the ideal energies for measuring Ir^{16+}, Ir^{17+}, Ir^{18+}, and Ir^{19+} respectively. Sections through the data along the beam energy axis at the peak positions marked in the lower part can be found in Figure B.24.

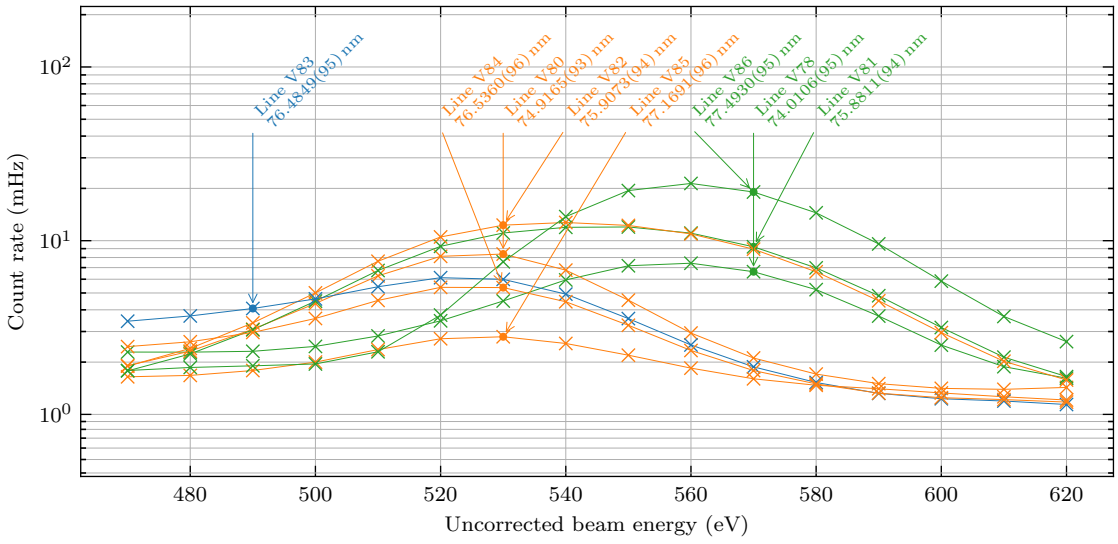

Figure B.24: Peak intensities of the lines found in Figure B.23 plotted against beam energy.

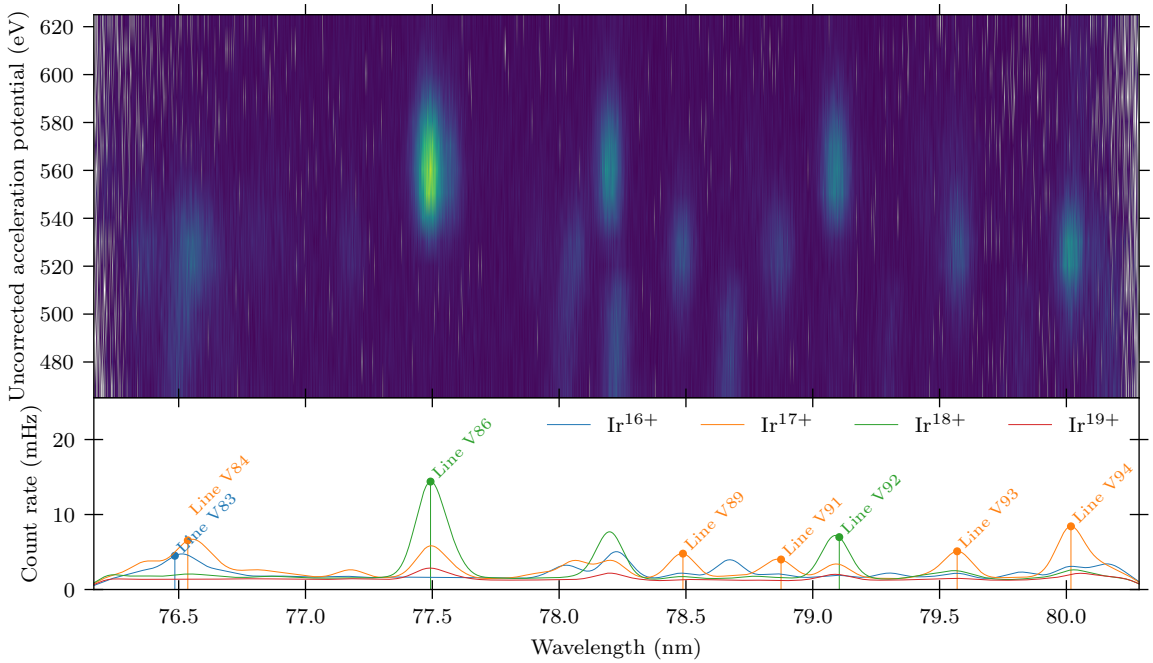

Figure B.25: Detailed energy scan of iridium around 78.23 nm. The upper part showing the two-dimensional spectrogram, while individual smoothed spectra at beam energies of 490 V, 530 V, 570 V, and 610 V are shown in the lower part. These values correspond to the ideal energies for measuring Ir^{16+}, Ir^{17+}, Ir^{18+}, and Ir^{19+} respectively. Sections through the data along the beam energy axis at the peak positions marked in the lower part can be found in Figure B.26.

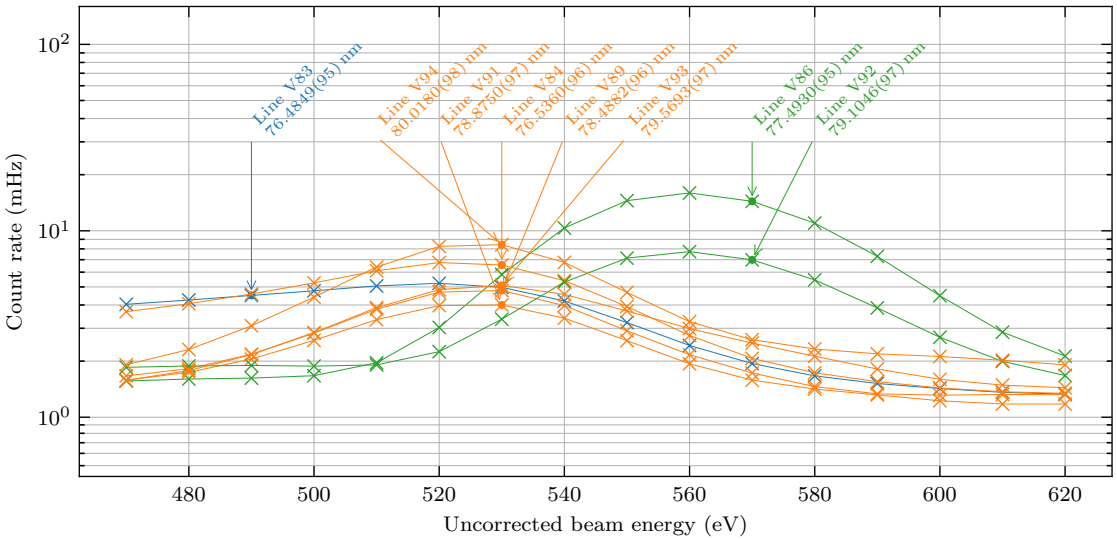

Figure B.26: Peak intensities of the lines found in Figure B.25 plotted against beam energy.

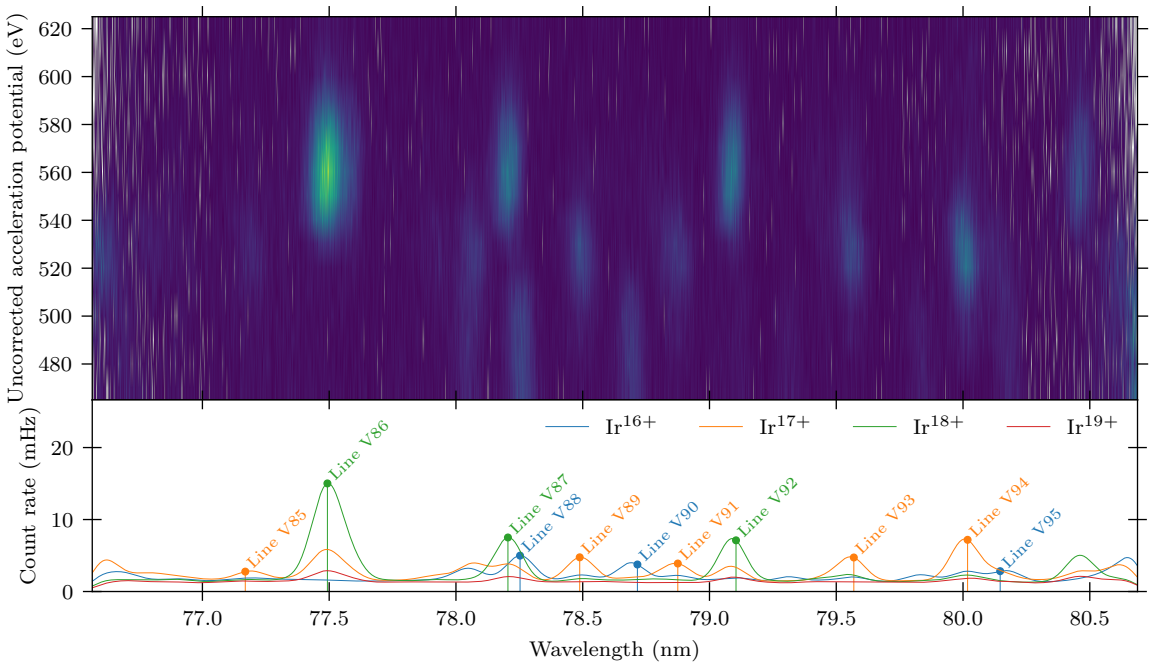

Figure B.27: Detailed energy scan of iridium around 78.63 nm. The upper part showing the two-dimensional spectrogram, while individual smoothed spectra at beam energies of 490 V, 530 V, 570 V, and 610 V are shown in the lower part. These values correspond to the ideal energies for measuring Ir^{16+}, Ir^{17+}, Ir^{18+}, and Ir^{19+} respectively. Sections through the data along the beam energy axis at the peak positions marked in the lower part can be found in Figure B.28.

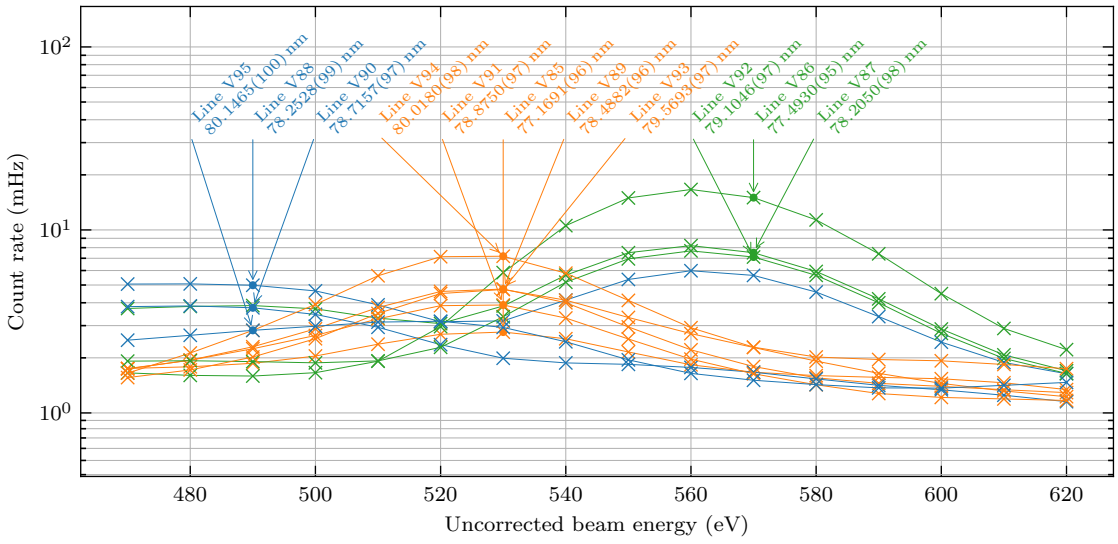

Figure B.28: Peak intensities of the lines found in Figure B.27 plotted against beam energy.

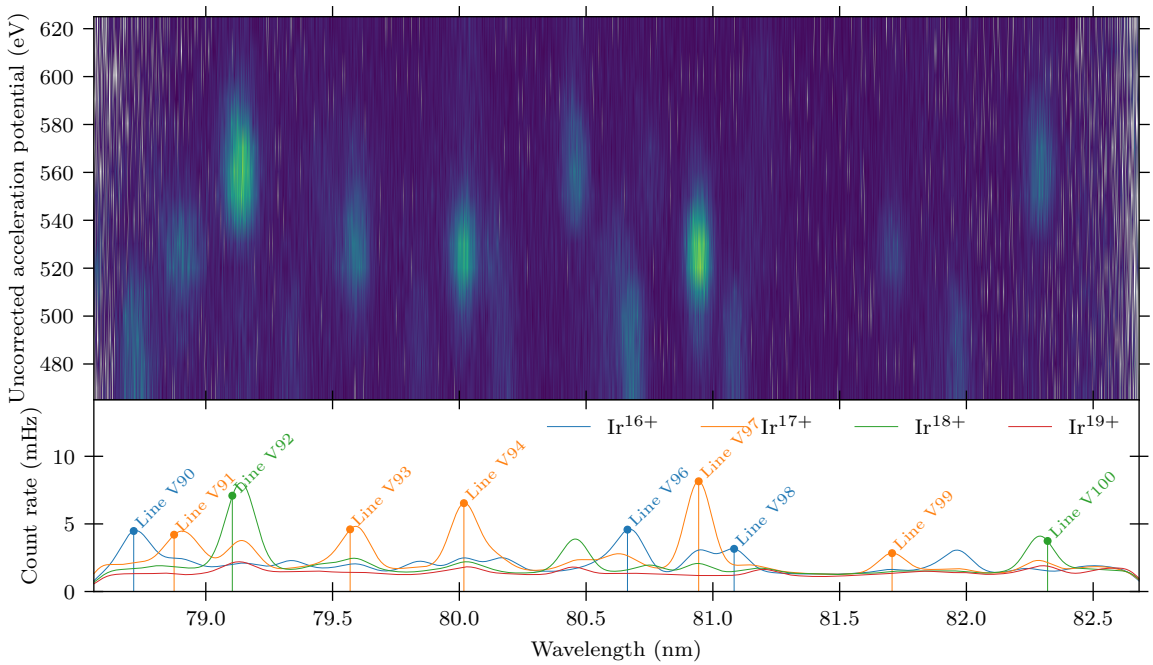

Figure B.29: Detailed energy scan of iridium around 80.62 nm. The upper part showing the two-dimensional spectrogram, while individual smoothed spectra at beam energies of 490 V, 530 V, 570 V, and 610 V are shown in the lower part. These values correspond to the ideal energies for measuring Ir^{16+}, Ir^{17+}, Ir^{18+}, and Ir^{19+} respectively. Sections through the data along the beam energy axis at the peak positions marked in the lower part can be found in Figure B.30.

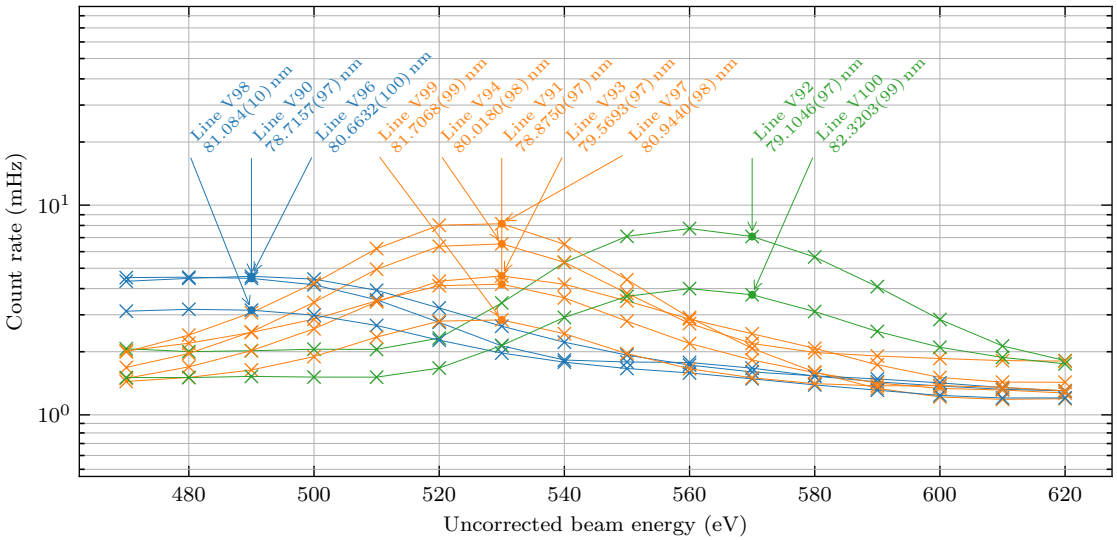

Figure B.30: Peak intensities of the lines found in Figure B.29 plotted against beam energy.

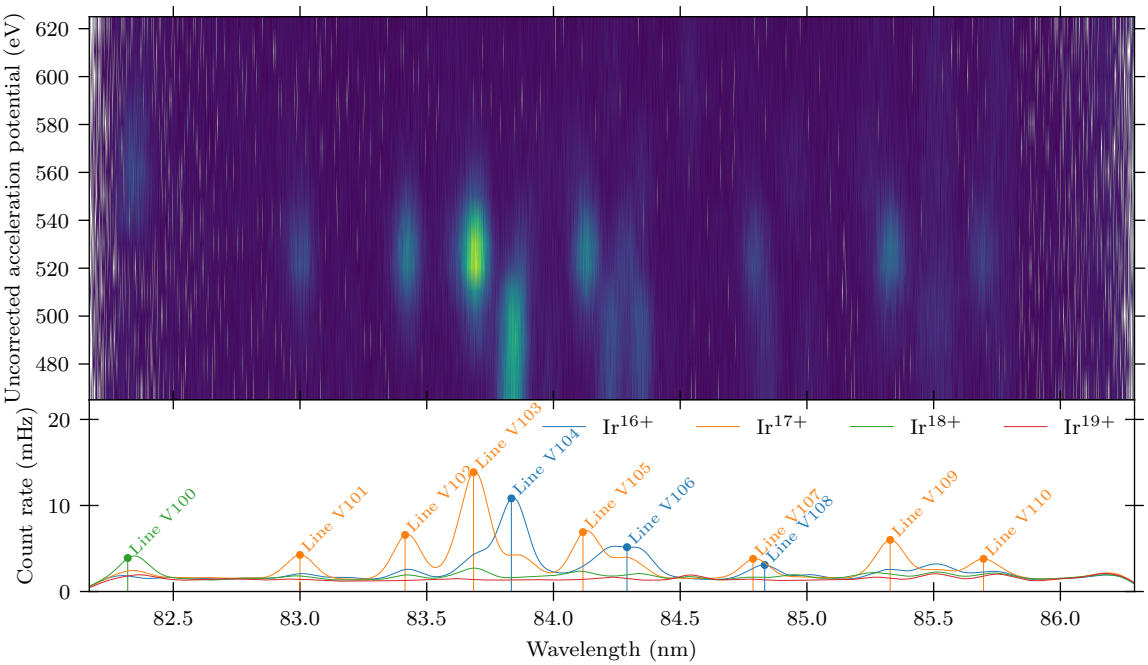

Figure B.31: Detailed energy scan of iridium around 84.23 nm. The upper part showing the two-dimensional spectrogram, while individual smoothed spectra at beam energies of 490 V, 530 V, 570 V, and 610 V are shown in the lower part. These values correspond to the ideal energies for measuring Ir^{16+}, Ir^{17+}, Ir^{18+}, and Ir^{19+} respectively. Sections through the data along the beam energy axis at the peak positions marked in the lower part can be found in Figure B.32.

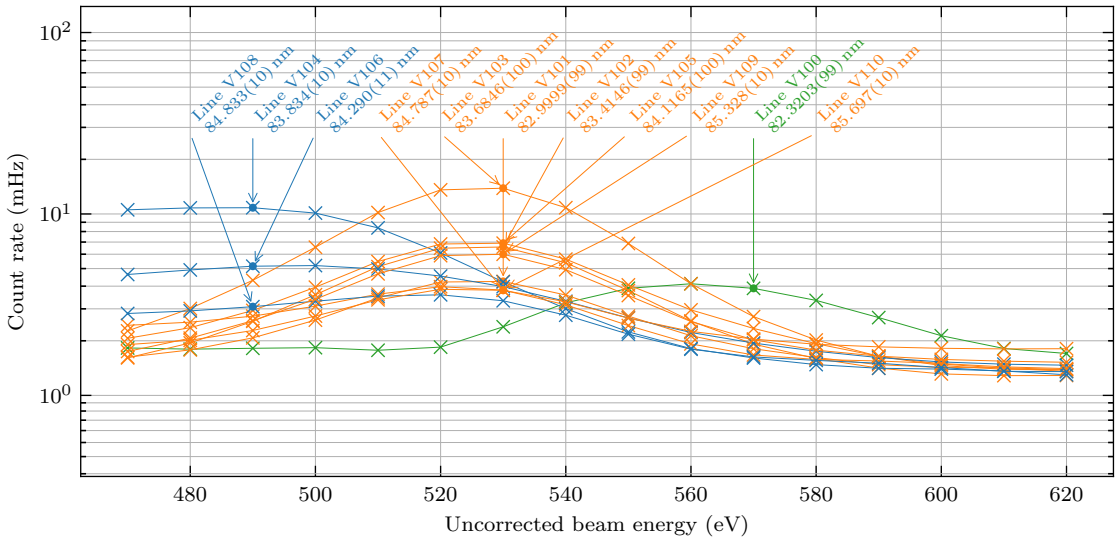

Figure B.32: Peak intensities of the lines found in Figure B.31 plotted against beam energy.

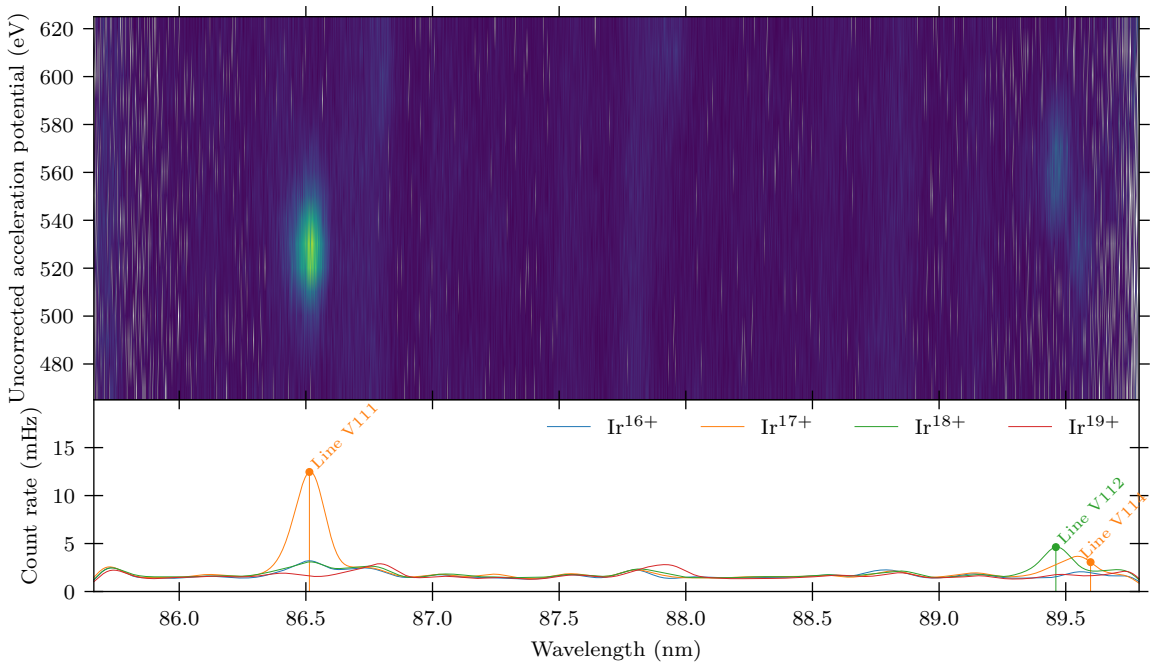

Figure B.33: Detailed energy scan of iridium around 87.73 nm. The upper part showing the two-dimensional spectrogram, while individual smoothed spectra at beam energies of 490 V, 530 V, 570 V, and 610 V are shown in the lower part. These values correspond to the ideal energies for measuring Ir^{16+}, Ir^{17+}, Ir^{18+}, and Ir^{19+} respectively. Sections through the data along the beam energy axis at the peak positions marked in the lower part can be found in Figure B.34.

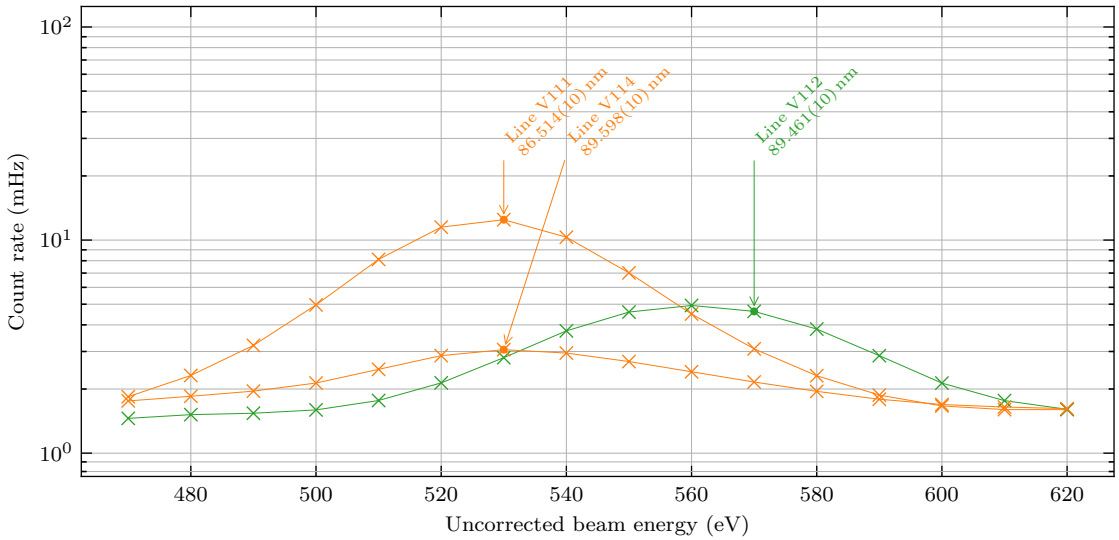

Figure B.34: Peak intensities of the lines found in Figure B.33 plotted against beam energy.

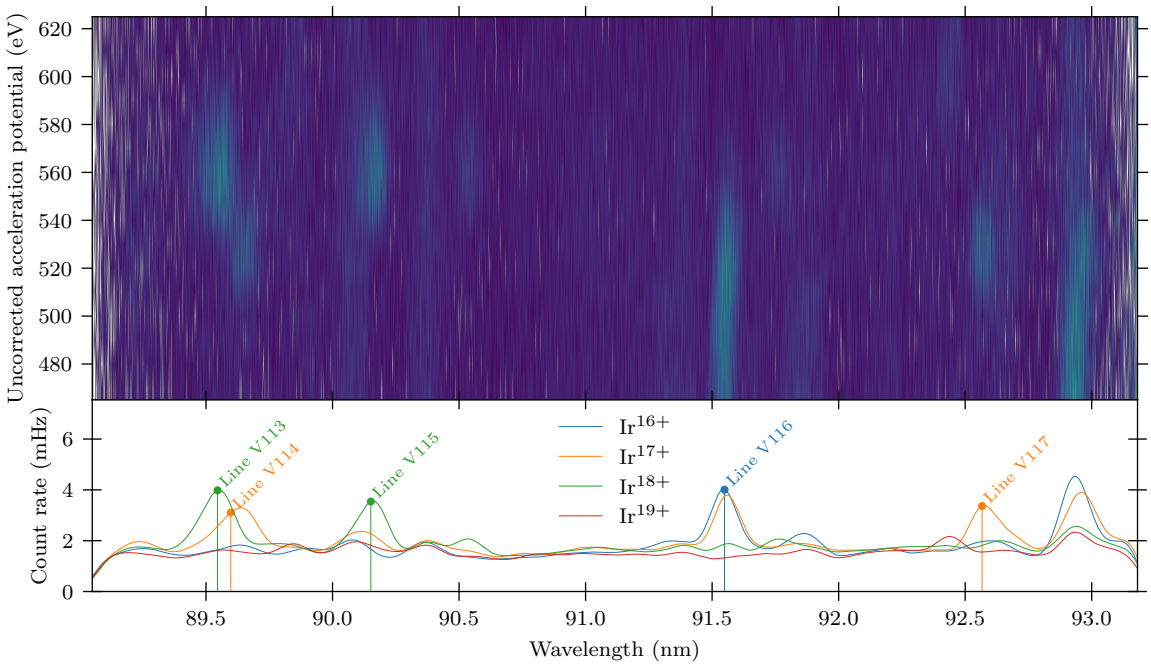

Figure B.35: Detailed energy scan of iridium around 91.12 nm. The upper part showing the two-dimensional spectrogram, while individual smoothed spectra at beam energies of 490 V, 530 V, 570 V, and 610 V are shown in the lower part. These values correspond to the ideal energies for measuring Ir^{16+}, Ir^{17+}, Ir^{18+}, and Ir^{19+} respectively. Sections through the data along the beam energy axis at the peak positions marked in the lower part can be found in Figure B.36.

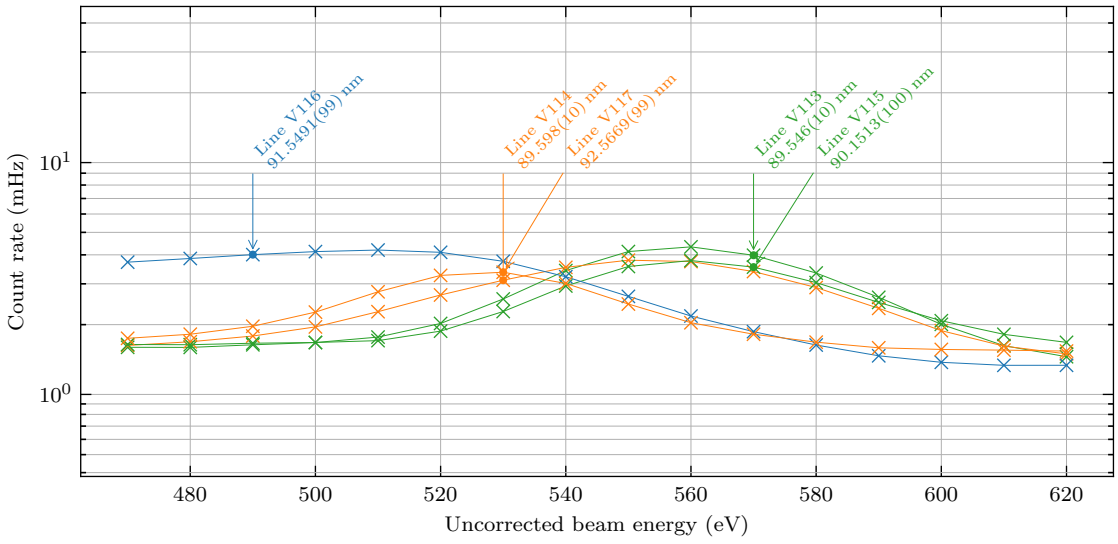

Figure B.36: Peak intensities of the lines found in Figure B.35 plotted against beam energy.

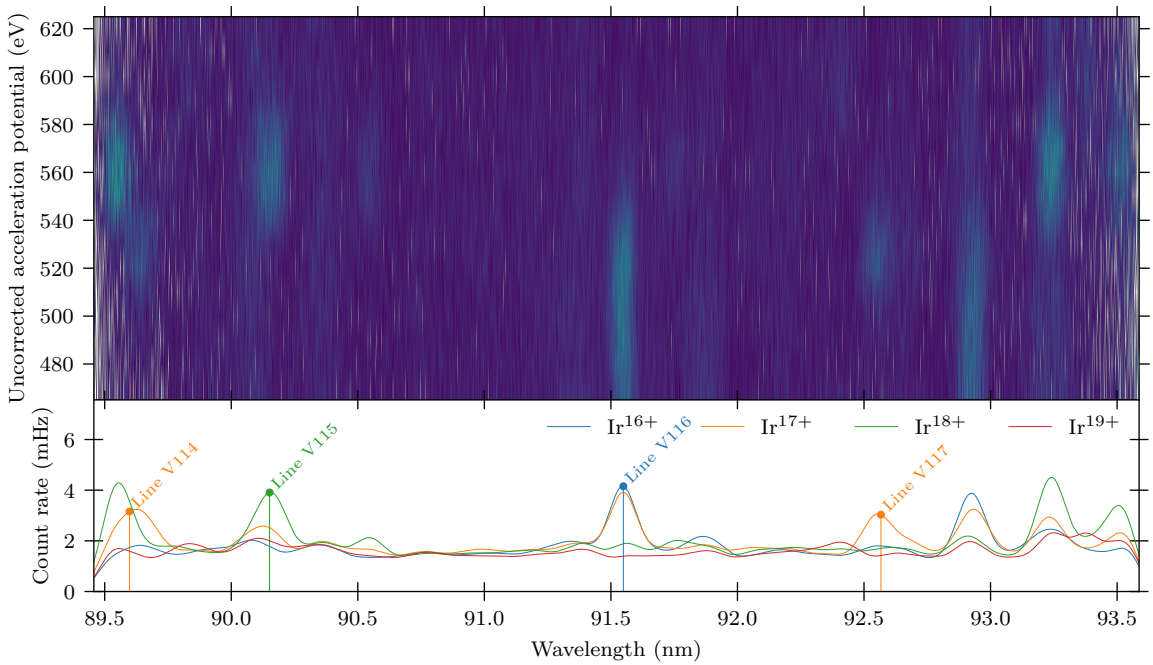

Figure B.37: Detailed energy scan of iridium around 91.52 nm. The upper part showing the two-dimensional spectrogram, while individual smoothed spectra at beam energies of 490 V, 530 V, 570 V, and 610 V are shown in the lower part. These values correspond to the ideal energies for measuring Ir^{16+}, Ir^{17+}, Ir^{18+}, and Ir^{19+} respectively. Sections through the data along the beam energy axis at the peak positions marked in the lower part can be found in Figure B.38.

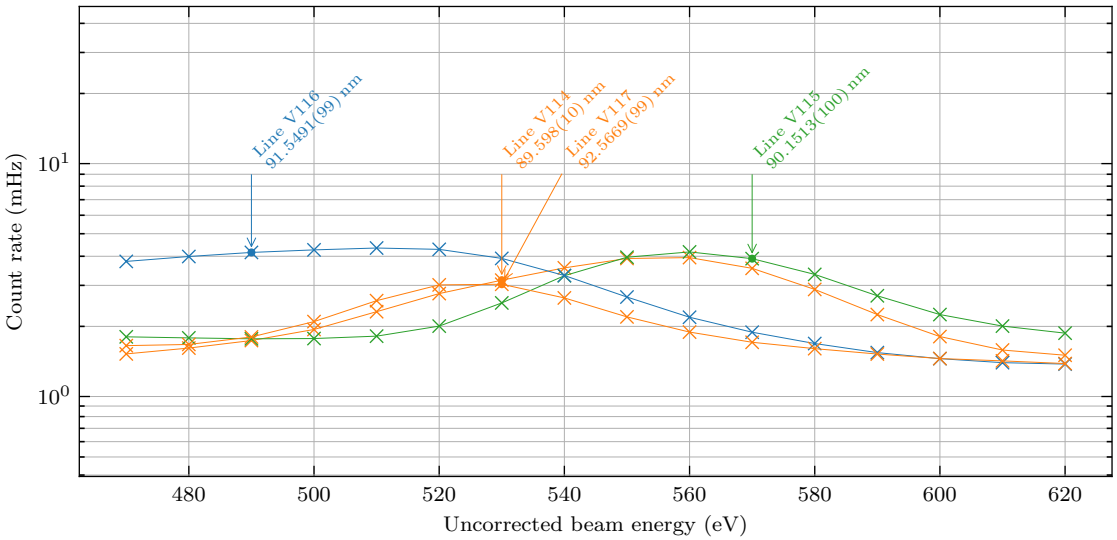

Figure B.38: Peak intensities of the lines found in Figure B.37 plotted against beam energy.

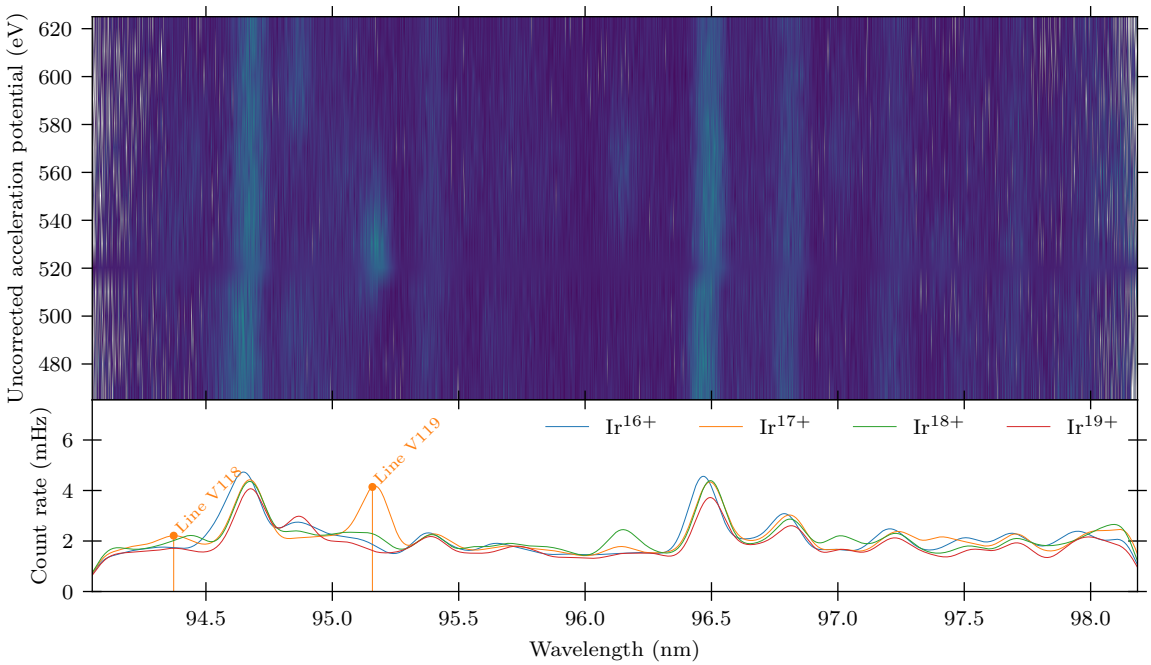

Figure B.39: Detailed energy scan of iridium around 96.12 nm. The upper part showing the two-dimensional spectrogram, while individual smoothed spectra at beam energies of 490 V, 530 V, 570 V, and 610 V are shown in the lower part. These values correspond to the ideal energies for measuring Ir^{16+}, Ir^{17+}, Ir^{18+}, and Ir^{19+} respectively. Sections through the data along the beam energy axis at the peak positions marked in the lower part can be found in Figure B.40.

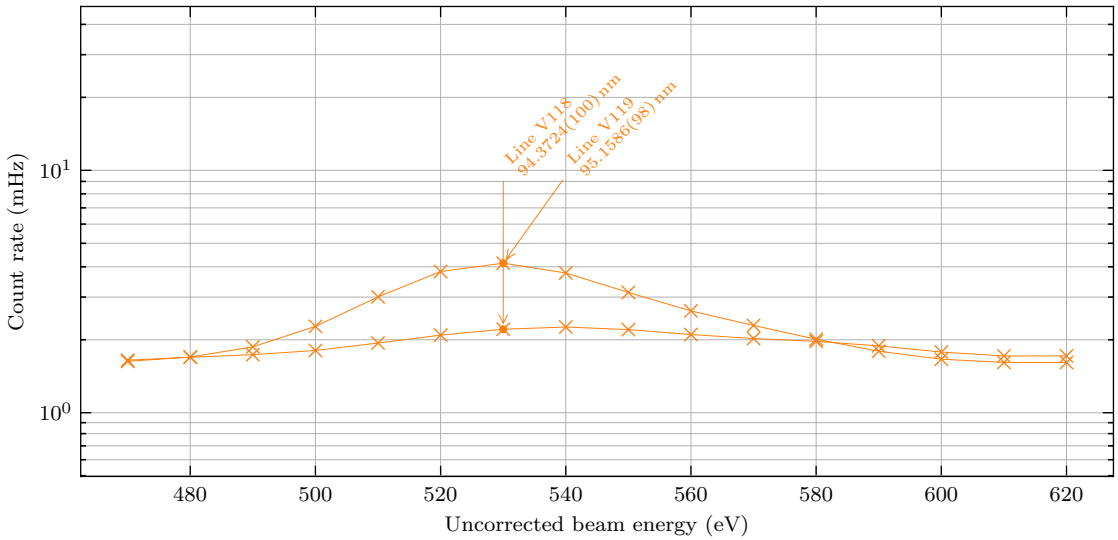

Figure B.40: Peak intensities of the lines found in Figure B.39 plotted against beam energy.

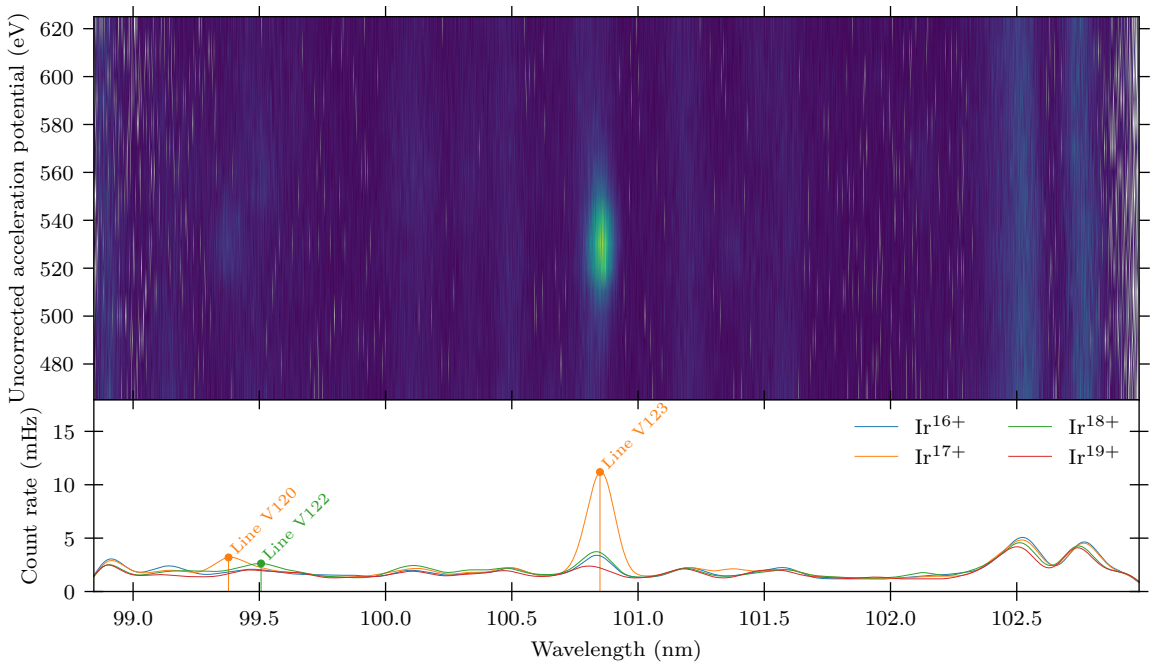

Figure B.41: Detailed energy scan of iridium around 100.91 nm. The upper part showing the two-dimensional spectrogram, while individual smoothed spectra at beam energies of 490 V, 530 V, 570 V, and 610 V are shown in the lower part. These values correspond to the ideal energies for measuring Ir^{16+}, Ir^{17+}, Ir^{18+}, and Ir^{19+} respectively. Sections through the data along the beam energy axis at the peak positions marked in the lower part can be found in Figure B.42.

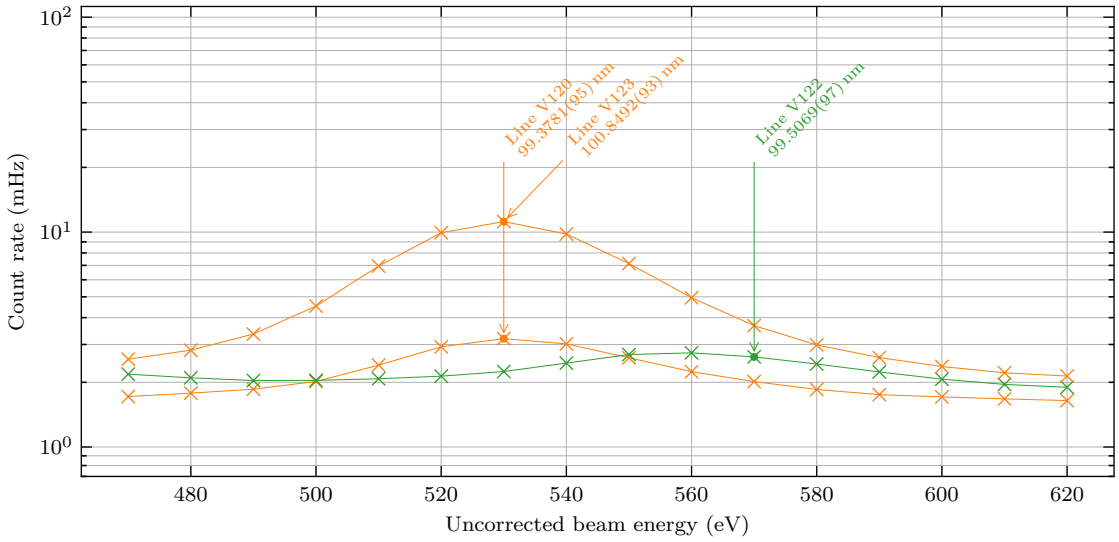

Figure B.42: Peak intensities of the lines found in Figure B.41 plotted against beam energy.

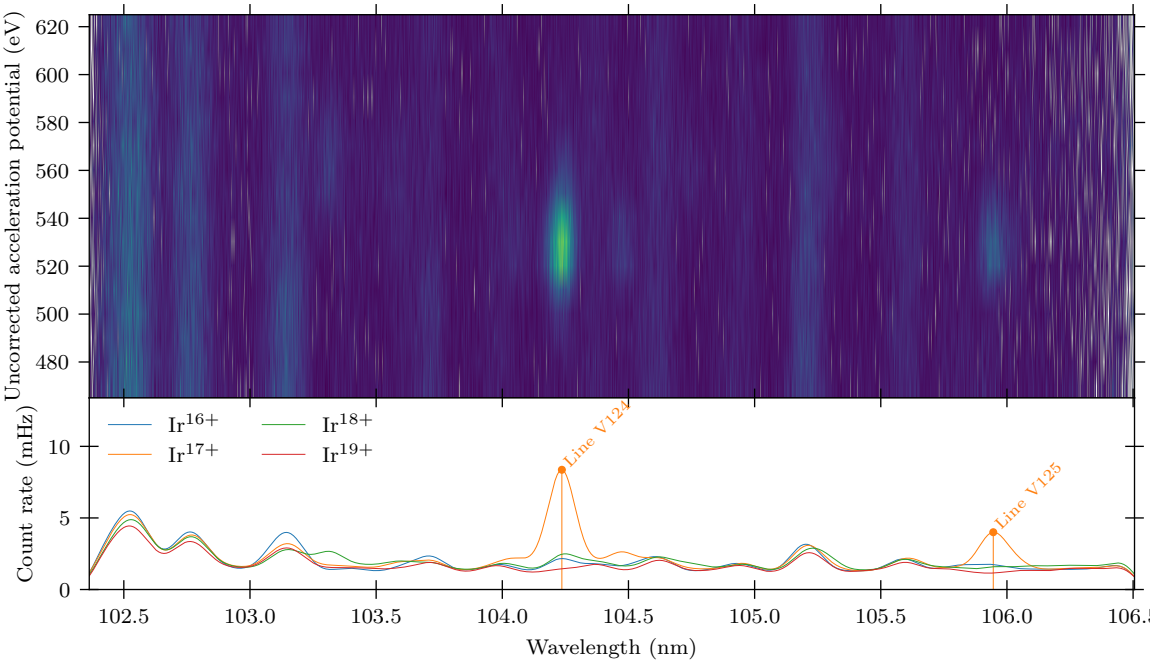

Figure B.43: Detailed energy scan of iridium around 104.43 nm. The upper part showing the two-dimensional spectrogram, while individual smoothed spectra at beam energies of 490 V, 530 V, 570 V, and 610 V are shown in the lower part. These values correspond to the ideal energies for measuring Ir^{16+}, Ir^{17+}, Ir^{18+}, and Ir^{19+} respectively. Sections through the data along the beam energy axis at the peak positions marked in the lower part can be found in Figure B.44.

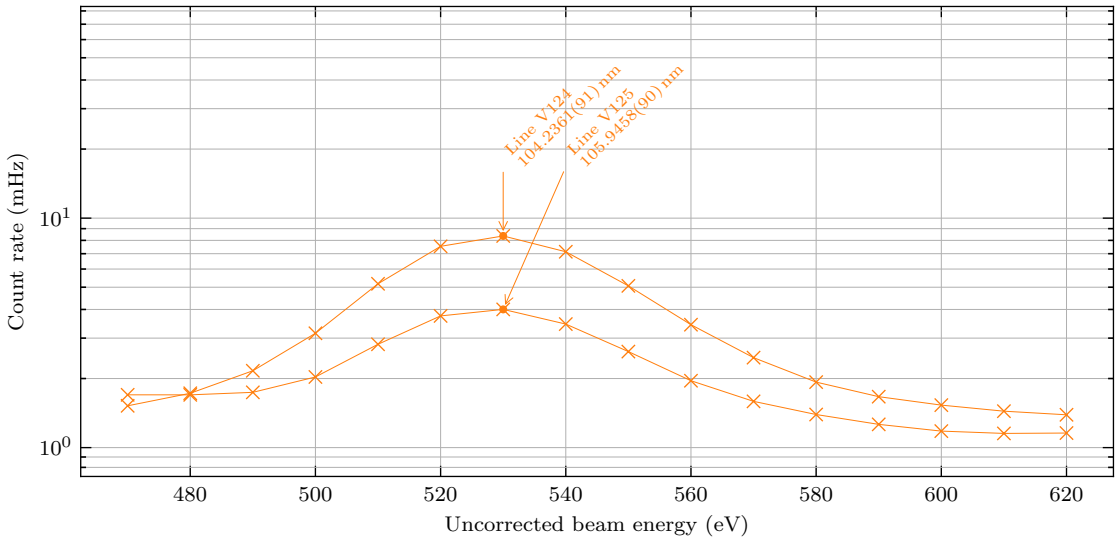

Figure B.44: Peak intensities of the lines found in Figure B.43 plotted against beam energy.

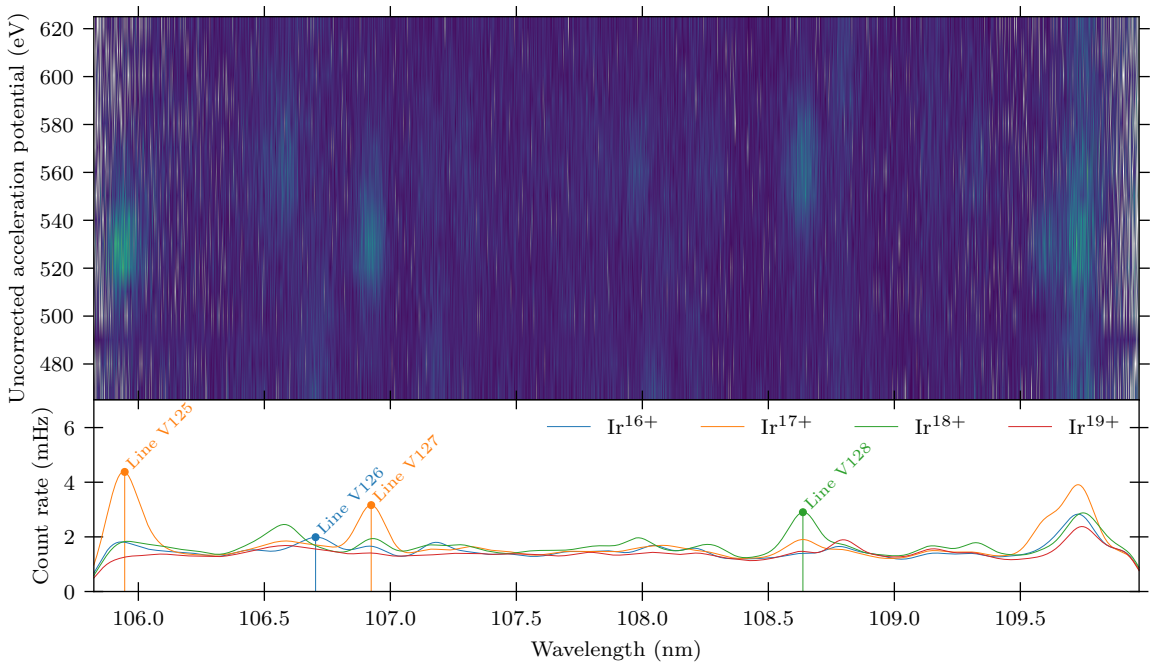

Figure B.45: Detailed energy scan of iridium around 107.90 nm. The upper part showing the two-dimensional spectrogram, while individual smoothed spectra at beam energies of 490 V, 530 V, 570 V, and 610 V are shown in the lower part. These values correspond to the ideal energies for measuring Ir^{16+}, Ir^{17+}, Ir^{18+}, and Ir^{19+} respectively. Sections through the data along the beam energy axis at the peak positions marked in the lower part can be found in Figure B.46.

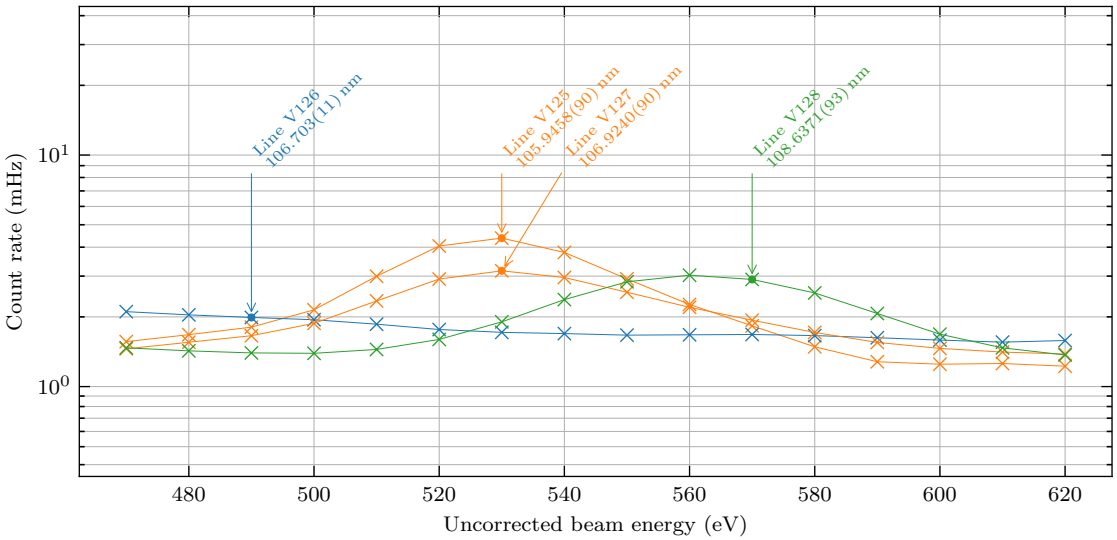

Figure B.46: Peak intensities of the lines found in Figure B.45 plotted against beam energy.

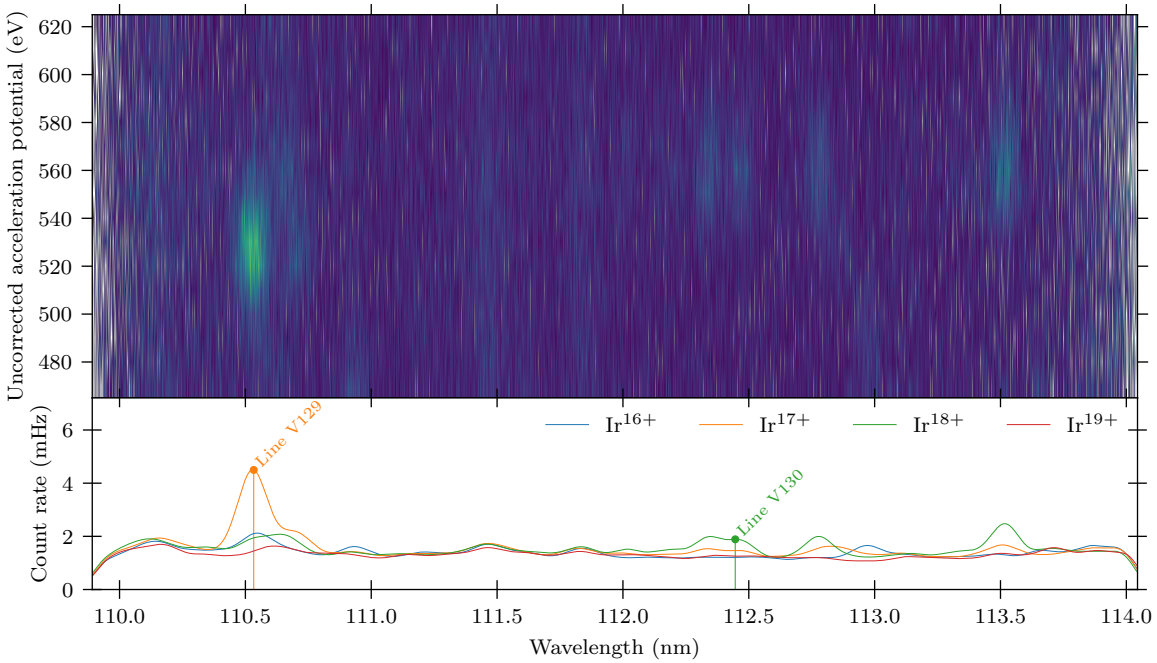

Figure B.47: Detailed energy scan of iridium around 111.97 nm. The upper part showing the two-dimensional spectrogram, while individual smoothed spectra at beam energies of 490 V, 530 V, 570 V, and 610 V are shown in the lower part. These values correspond to the ideal energies for measuring Ir^{16+}, Ir^{17+}, Ir^{18+}, and Ir^{19+} respectively. Sections through the data along the beam energy axis at the peak positions marked in the lower part can be found in Figure B.48.

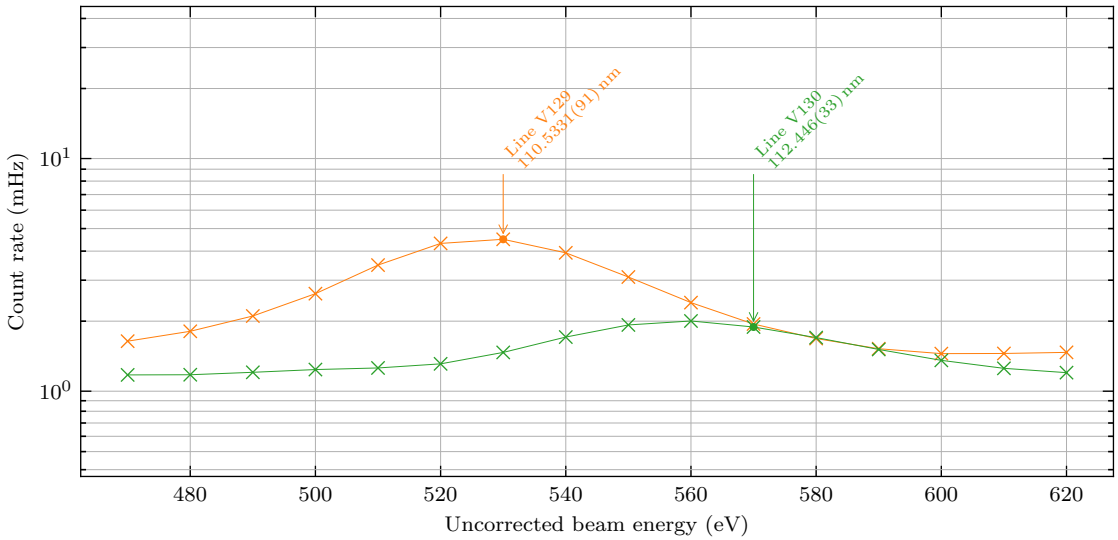

Figure B.48: Peak intensities of the lines found in Figure B.47 plotted against beam energy.

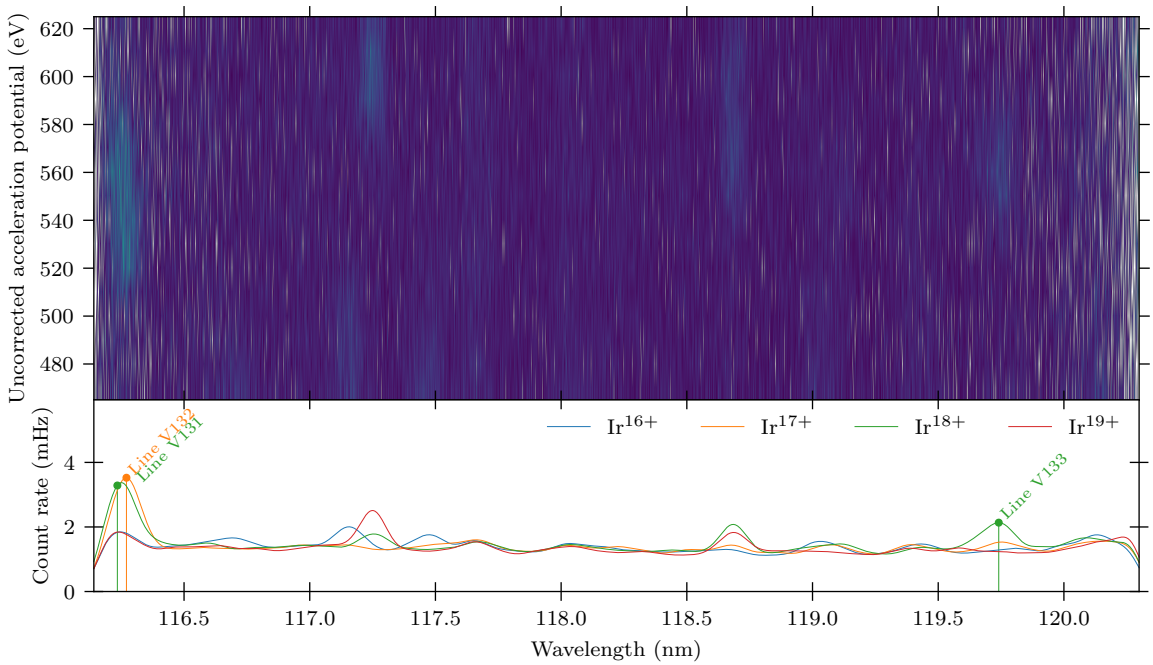

Figure B.49: Detailed energy scan of iridium around 118.22 nm. The upper part showing the two-dimensional spectrogram, while individual smoothed spectra at beam energies of 490 V, 530 V, 570 V, and 610 V are shown in the lower part. These values correspond to the ideal energies for measuring Ir^{16+}, Ir^{17+}, Ir^{18+}, and Ir^{19+} respectively. Sections through the data along the beam energy axis at the peak positions marked in the lower part can be found in Figure B.50.

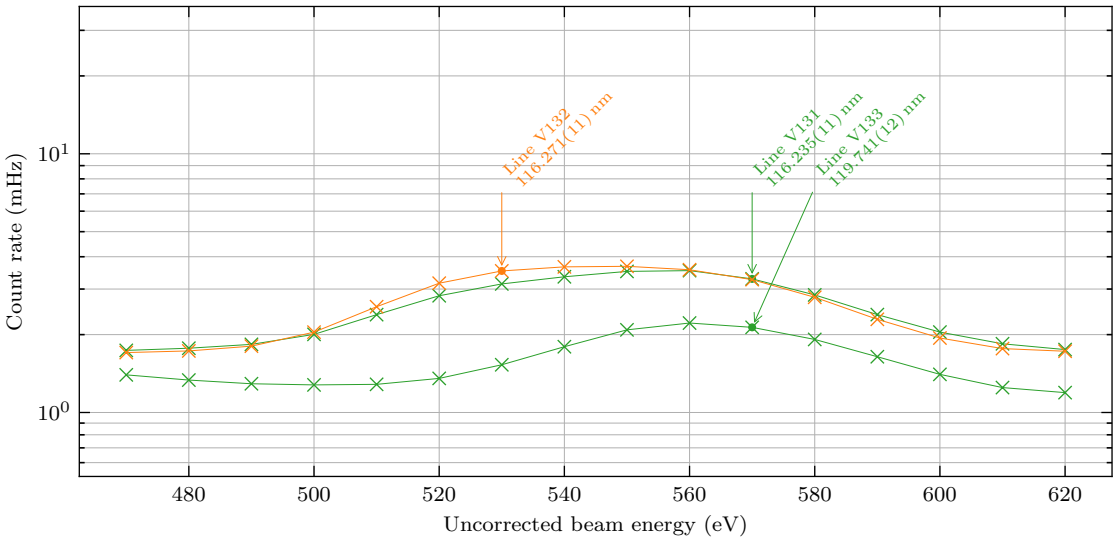

Figure B.50: Peak intensities of the lines found in Figure B.49 plotted against beam energy.

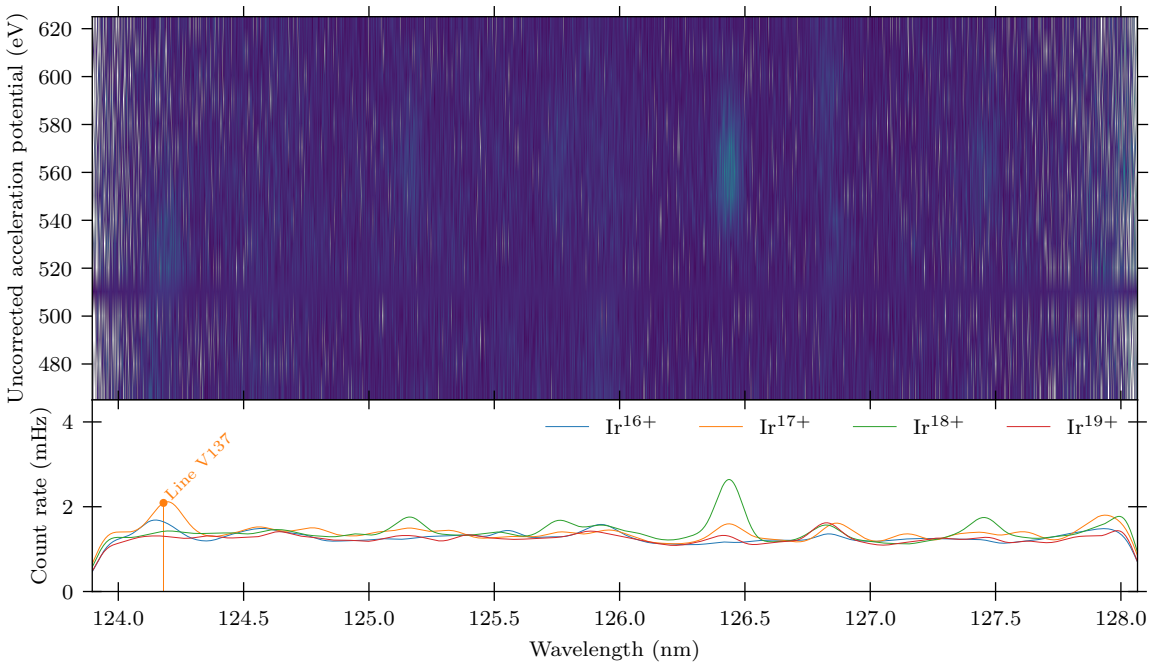

Figure B.51: Detailed energy scan of iridium around 125.98 nm. The upper part showing the two-dimensional spectrogram, while individual smoothed spectra at beam energies of 490 V, 530 V, 570 V, and 610 V are shown in the lower part. These values correspond to the ideal energies for measuring Ir^{16+}, Ir^{17+}, Ir^{18+}, and Ir^{19+} respectively. Sections through the data along the beam energy axis at the peak positions marked in the lower part can be found in Figure B.52.

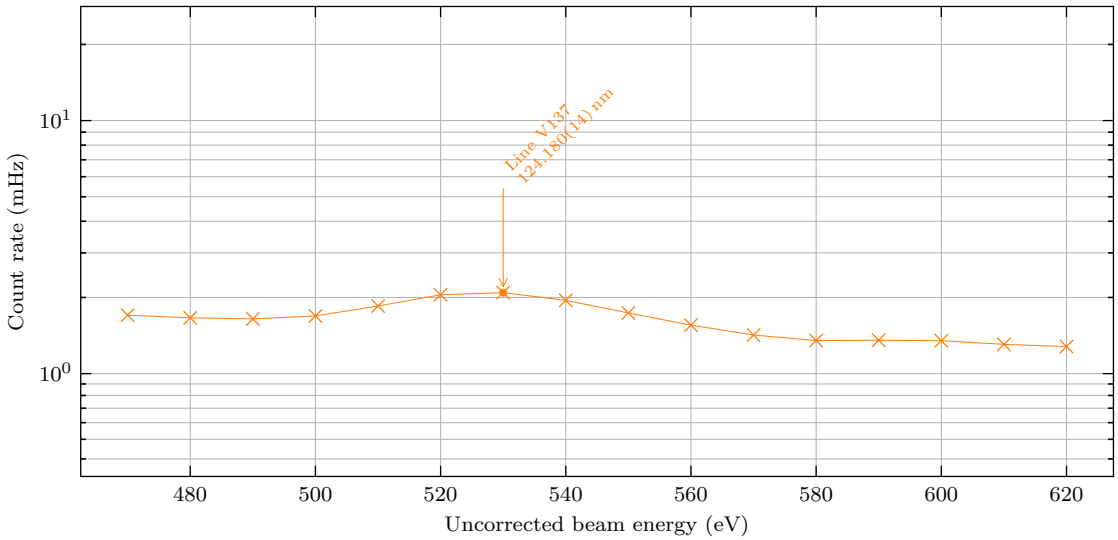

Figure B.52: Peak intensities of the lines found in Figure B.51 plotted against beam energy.

List of publications

1. **Blessenohl, M. A.**, S. Dobrodey, C. Warnecke, M. K. Rosner, L. Graham, S. Paul, T. M. Baumann, Z. Hockenbery, R. Hubele, T. Pfeifer, F. Ames, J. Dilling, and J. R. Crespo López-Urrutia: 'An electron beam ion trap and source for re-acceleration of rare-isotope ion beams at TRIUMF'. *Review of Scientific Instruments* (2018), vol. 89(5): p. 052401. doi: 10.1063/1.5021045.
2. Mercadier, L., A. Benediktovitch, C. Weninger, **M. A. Blessenohl**, S. Bernitt, H. Bekker, S. Dobrodey, A. Sanchez-Gonzalez, B. Erk, C. Bomme, R. Boll, Z. Yin, V. P. Majety, R. Steinbrügge, M. A. Khalal, F. Penent, J. Palaudoux, P. Lablanquie, A. Rudenko, D. Rolles, J. R. Crespo López-Urrutia, and N. Rohringer: 'Evidence of Extreme Ultraviolet Superfluorescence in Xenon'. *Physical Review Letters* (2019), vol. 123(2): p. 023201. doi: 10.1103/physrevlett.123.023201.
3. Jörg, H., Z. Hu, H. Bekker, **M. A. Blessenohl**, D. Hollain, S. Fritzsche, A. Surzhykov, J. R. Crespo López-Urrutia, and S. Tashenov: 'Linear polarization of x-ray transitions due to dielectronic recombination in highly charged ions'. *Physical Review A* (2015), vol. 91(4): p. 042705. doi: 10.1103/physreva.91.042705.
4. Benediktovitchy, A., L. Mercadier, O. Peyrusse, A. Przystawik, T. Laarmann, B. Langbehn, C. Bomme, B. Erk, J. Correa, C. Mossé, D. Rolles, S. Toleikis, M. Bucher, C. F. O. Bostedt, A. Sanchez-Gonzalez, S. Dobrodey, **M. A. Blessenohl**, A. Nelde, M. Müller, D. Rupp, T. Möller, J. R. Crespo López-Urrutia, and N. Rohringer: 'Amplified spontaneous emission in the extreme ultraviolet by expanding xenon clusters'. *Physical Review A* (2020), vol. 101(6): p. 063412. doi: 10.1103/physreva.101.063412.
5. Ames, F., R. Baartman, B. Barquest, C. Barquest, **M. A. Blessenohl**, J. R. Crespo López-Urrutia, J. Dilling, S. Dobrodey, L. Graham, R. Kanungo, M. Marchetto, M. R. Pearson, and S. Saminathan: 'The CANREB Project for Charge State Breeding at TRIUMF'. *AIP Conference Proceedings 2011* (2018): p. 070010-1. doi: 10.1063/1.5053352.
6. Brenner, G., S. Bernitt, S. Dobrodey, R. Steinbrügge, **M. A. Blessenohl**, A. Cieluch, Z. Hockenbery, S. Kühn, J. Nauta, M. A. Sanchez, S. W. Epp, and J. R. Crespo López-Urrutia: 'High-precision laser spectroscopy of the fine-structure transition $2s^2\ S_{1/2} - 2p^2\ P_{3/2}$ at 136 eV in lithiumlike Kr^{33+} using a free-electron laser'. *Physical Review A* (2020). *In peer-review process.*

In this work, reference [1] has been utilized in the chapter about the setup and characterization of the CANREB EBIS with a more detailed description.

Addendum

After submission of this work, the author was made aware that the lithium-like fine-structure doublet was previously measured in the laboratory by Biedermann *et al.* using a 2 m grazing-incidence spectrometer at Berlin EBIT calibrated by the Lyman series of singly charged helium. Their values are (35.3921 ± 0.0006) nm and (38.9108 ± 0.0007) nm:

Biedermann, C., R. Radtke, G. Fussmann, and F.I. Allen: 'Extreme ultraviolet spectroscopy of highly charged argon ions at the Berlin EBIT'. *Journal of Physics: Conference Series* (2007), vol. 72: p. 012004. doi: 10.1088/1742-6596/72/1/012004.